CO_2 CORROSION MECHANISTIC MODELING IN HORIZONTAL SLUG LOW

A Dissertation Presented to

The Faculty of the

Fritz J. and Dolores H. Russ

College of Engineering and Technology

Ohio University

In Partial Fulfillment

Of the Requirements for the Degree

Doctor of Philosophy in Chemical Engineering

by

Hongwei Wang

March, 2002

ACKNOWLEDGEMENTS

The author dedicates this dissertation to his parents in gratitude for their love and encouragement throughout his entire graduate study and his journey to and in the USA.

The author would like to take this opportunity to express his gratitude to Professor W. Paul Jepson, for his steady influence in the commencement, continuation, and completion of this dissertation. Under his supervision in the Institute for Corrosion and Multiphase Technology, the author developed an industrially oriented vision on science and engineering research and practice, which will guide him in his future endeavors after completing his graduate studies at Ohio University.

The additional guidance of Dr. Madan Gopal, Dr. Ji Yong Cai, Dr. Tao Hong, and Dr. Christoph Bosch are also greatly appreciated. They have always been very supportive. Without their expert support in regards to the multiphase flow experiment, corrosion theory, and theoretical computation, the author would not have been able to quickly accomplish this dissertation which covers a broad topics.

The author would also like to acknowledge the helpful guidance from his Ph.D. Advisory Committee, Professor Howard D. Dewald, Professor Wen-Jia Chen, and Professor Daniel A. Gulino from the initiation to the accomplishment of the entire dissertation.

The author would also like to acknowledge the assistance from the technical staff at Ohio University which is comprised of Mr. Al Schubert, Mr. Jim McKnight,

Mr. Bruce Brown, and Mr. John Goettge in regards to the experimental system construction and maintenance.

This occasion is also used to acknowledge fellow graduate students, visiting scholars, and industrial board members of the Institute in appreciation of their ready assistance as well as their different cultural perspectives. Ms. Andrea Zheng has given significant help regarding this dissertation, the author is indebted deeply.

Finally, the author would like to extend his gratitude to Professor Hwa-Wei Lee, Professor Hugh M. Culbertson, Professor Wen-Jia Chen, Professor Xiaozhuo Chen, Dr. Liren Zheng, and Professor Valerie Young. Their guidance encouraged him to have a diversified life as a member of the Ohio University community, and their advice regarding the author's career and overall life philosophy will forever have a far-reaching impact on him.

TABLE OF CONTENTS

LIST OF TABLES

LIST OF FIGURES

CHAPTER 1

INTRODUCTION

In the majority of cases offshore exploration, crude oil and natural gas outputs are transported from the drilling platform by a subsea pipeline. Depending on the pipe diameter, length, need for burial, need for coatings, cathodic protection, water depth, and various construction factors, a subsea pipeline can be the single most expensive element of an offshore installation (Bradley, 1987). Thus carbon steels are used extensively in the design of subsea pipelines for multiphase transportation. These steels are inexpensive, but they usually exhibit poor internal corrosion resistance properties.

In recent years, the presence of carbon dioxide is encountered more frequently through the use of enhanced oil recovery (EOR) techniques involving CO_2 injection into reservoirs and water-injection. Carbon dioxide dissolves in the brine to form carbonic acid that ionizes to yield a weak acid with a low pH. This solution with dissociated carbonic acid consequently corrodes well tubulars and flow lines. Carbon dioxide (CO_2) corrosion has become a well-known problem in the oil and gas production industry (Hausler 1984, Burke 1985).

Many oil fields are located in remote areas, e.g. subsea, which makes the maintenance of the pipelines costly. Every year corrosion related problems result in economic losses worth millions of dollars because of production shutdown, efficiency losses, and environment pollution factors.

CO_2 corrosion can be broadly categorized into three types. These types are uniform corrosion, localized corrosion, and erosion corrosion. Uniform or general corrosion causes overall metal loss and general thinning of metal. Localized corrosion has the appearance of pits or grooves. Erosion corrosion is defined as the deterioration of the metal surface due to the relative motion between the metal wall and the corrosive fluid.

Under the right conditions, three types of corrosion product scale can form on carbon steel along the pipelines and pipe fittings. Under low temperatures, the corrosion product scale is mainly composed of iron carbide (Fe_3C) which is very porous and non-protective. Under intermediate temperatures, it will be mainly composed of iron carbonate ($FeCO_3$) which is protective. Under high temperatures (e.g. 100 °C) or higher, iron oxide will be the main component of the product layer and it is also protective.

The presence of a protective corrosion product layer can dramatically decrease the corrosion rate by protecting the steel from the corroding media. The formation and properties of the corrosion product layer are highly dependent on environmental factors and the microstructure of the carbon steel being used. The corrosion scale can be destroyed in certain conditions. These conditions include being removed by the action of flow because of the shear stress and other forces.

In offshore exploration, it is often uneconomical for every well to have its own platform from the view of design. Hence, it is a common practice to transport the gas-liquid mixture from several wells through a large diameter pipe (e.g. 10 inch I.D.) to a

central gathering station on the platform where the separation takes place. Because of the special turbulence, multiphase flow will further influence the internal corrosion rate.

Figure 1.1 shows the various flow regimes in a gas/liquid two-phase system. Different liquid and gas velocities will determine different flow regimes. These regimes include smooth, wavy stratified, rolling wave, plug flow, slug flow, and annular flow. Each flow regime will have a different influence on the corrosion rate.

At low gas and liquid velocities, the interface between the two layers is a smooth stratified flow. An increase in the gas velocity leads to the formation of regular two-dimensional waves at the interface. This regime is called a wavy-stratified flow. With a further increase in the gas velocity, the two dimensional waves grow in height and begin to roll over, which is called a rolling wave regime. At a higher liquid velocity, there is a transition from a stratified flow to an intermittent flow pattern. The waves on the liquid layer grow to bridge the pipe. Two types of intermittent flow are possible, plug flow and slug flow. At low gas velocities, the waves form lumps of liquid called plugs. The plug flows over the liquid film intermittently between the elongated gas bubbles with very little turbulence. At a higher gas velocity, the front of the plug begins to overrun the liquid film and assimilates it into the structure. This results in acceleration of the slug front and a highly turbulent slug flow is formed. With a further increase in the gas velocity, large three-dimensional roll waves start to appear on the liquid film between the slugs. The slugs are highly aerated at this point and this regime is called a pseudo-slug flow. With a further increase in the gas

velocity, the slugs are not able to hold the gas and the gas starts to flow into the central core of the pipe with a thin layer of liquid flowing in the annulus around it, thus called annular flow.

These flow patterns become more complicated with the addition of oil to the water phase as shown in Figure 1.2. The transitions of flow patterns are similar to those obtained in the gas/liquid two-phase as shown in Figure 1.1. However, a distinct oil layer in between the gas and seawater is seen in a smooth, wavy stratified, and rolling wave flow. In a plug flow, the seawater mainly forms a stratified layer in contact with the bottom of the pipe wall. The oil phase forms a layer at the top of this and also bridges the pipe in the intermittent plugs. In the slug flow, more mixing between the oil and the seawater is seen. The continuous phase in contact with the pipe wall depends on the oil, the seawater compositions, and flow velocities. Annular flow is characterized by a well mixed oil-seawater liquid phase near the pipe walls.

Slug flow always exists in oil and gas pipelines with the presence of a higher oil and gas production rates. The high turbulence in slug flow causes a high corrosion rate of carbon steel, which was first reported by Green et al. (1990). Jepson showed that the turbulence of slug flow is associated with pulses of gas bubbles reaching the bottom surface of the pipe in 1987. Through the visualization of flow, Gopal and Jepson (1998a) showed that the gas bubbles trapped in the mixing zone are forced down towards the wall surface, where they are released in the form of pulses of bubbles. Gas bubbles result with a high degree of turbulence, and destroy the hydrodynamic boundary layer within the mixing zone.

The prediction of corrosion rates in oil and gas production has attracted significant attention and extensive research have been carried out to investigate the corrosion mechanisms and to develop the corrosion prediction model utilizing a rotating cylinder electrode, jet impingement, and a small diameter flow loop. These systems can provide easy and inexpensive tests under controlled conditions. However, these methods do not take into account the effect of flow on corrosion in the large diameter horizontal pipeline. The extrapolation of these results including the corrosion mechanisms and the corrosion prediction models to multiphase flow can lead to large error.

Up to now the study of the influence of multiphase flow on corrosion has been limited. The current corrosion prediction models usually do not consider the influence of multiphase flow on corrosion. Pots (1995) developed a corrosion mechanistic model under multiphase slug flow. A limiting corrosion rate model and a numerical method were proposed. This initial work found that further modeling, plus more extensive experimental data were needed.

The study of CO_2 corrosion in horizontal slug flow requires an understanding of the effects that gas bubble formation, bubble collapsing, oil/water composition, oil droplets, and flow regime characteristics have on corrosion rates. The model for the prediction of uniform corrosion has been developed for full pipe flow and water/oil two-phase flow (Zhang, 1997). The effect of the gas bubble formation and the oil phase will be added to Zhang's model to develop a corrosion mechanistic model for slug flow utilizing the strategy shown in Figure 1.3.

The model developed in this dissertation takes into account the slug flow hydrodynamics, the mass transfer characteristics, and the electrochemical corrosion kinetics. The effect of the corrosion product film was also included in the model. This model will be verified by the experimental data previously generated in the multiphase flow loops and other corrosion prediction models extensively used in the oil and gas industry.

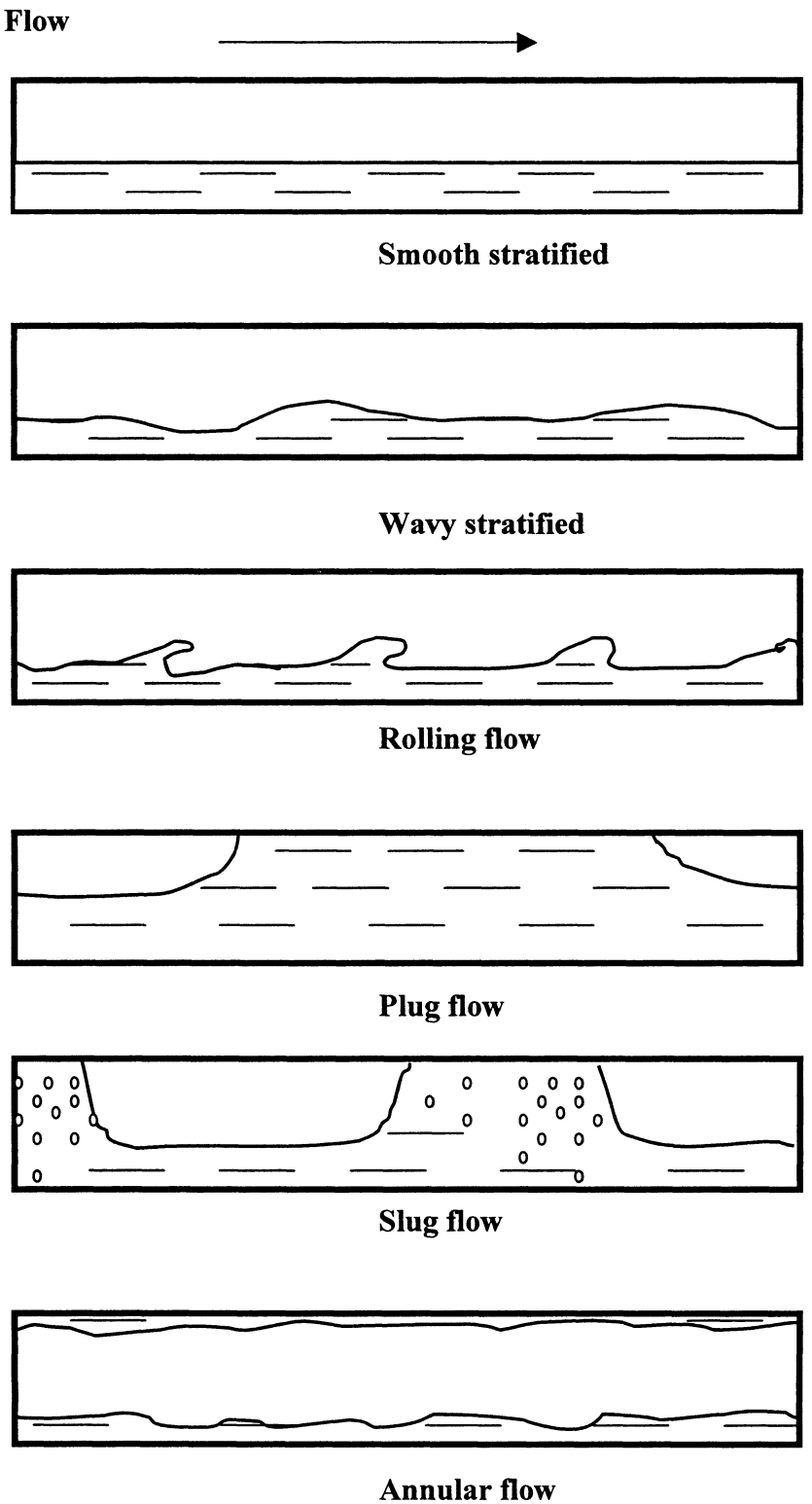

Figure 1.1 Gas/liquid two-phase flow patterns

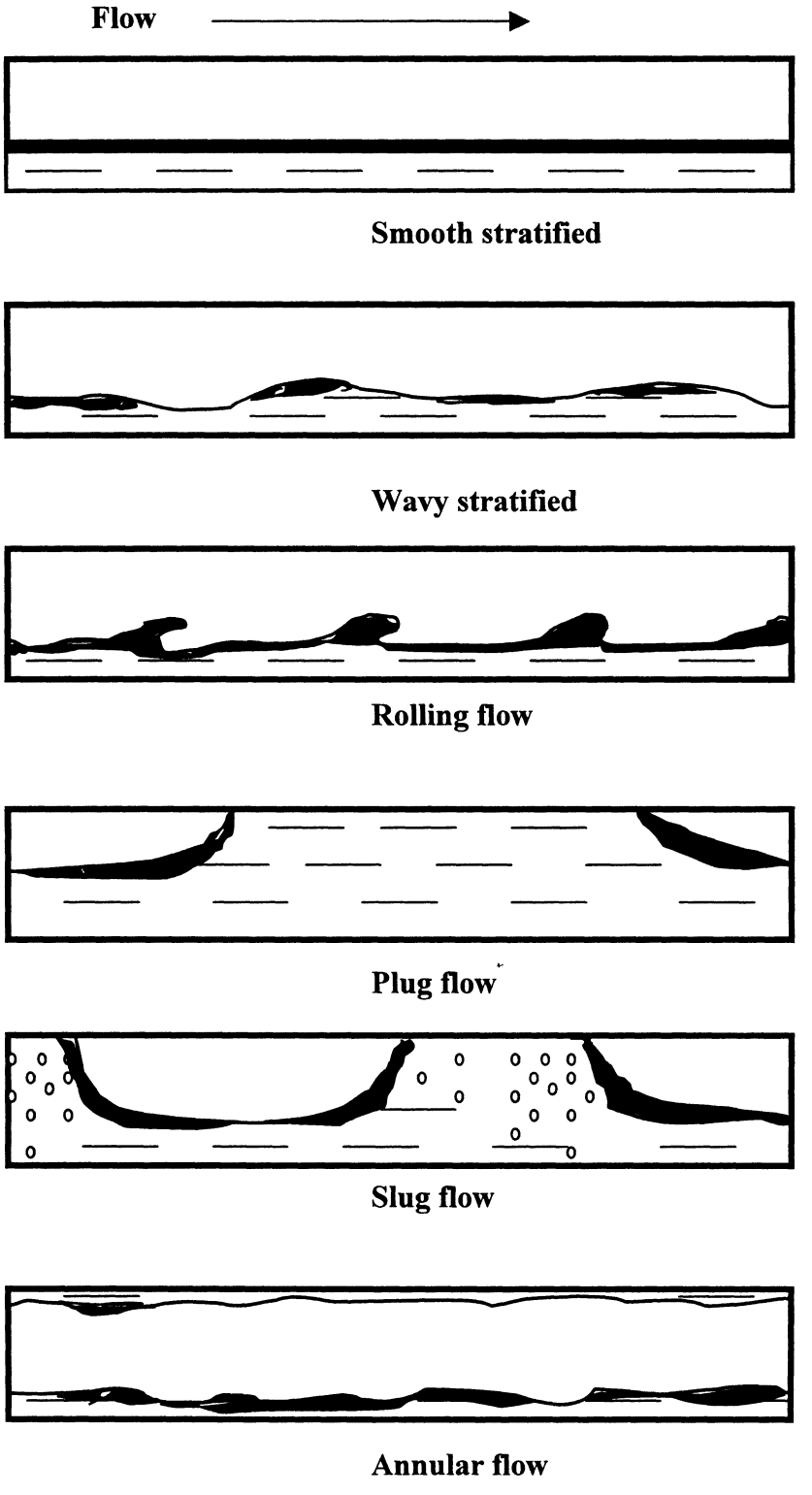

Figure 1.2 Gas/oil/liquid three-phase flow patterns

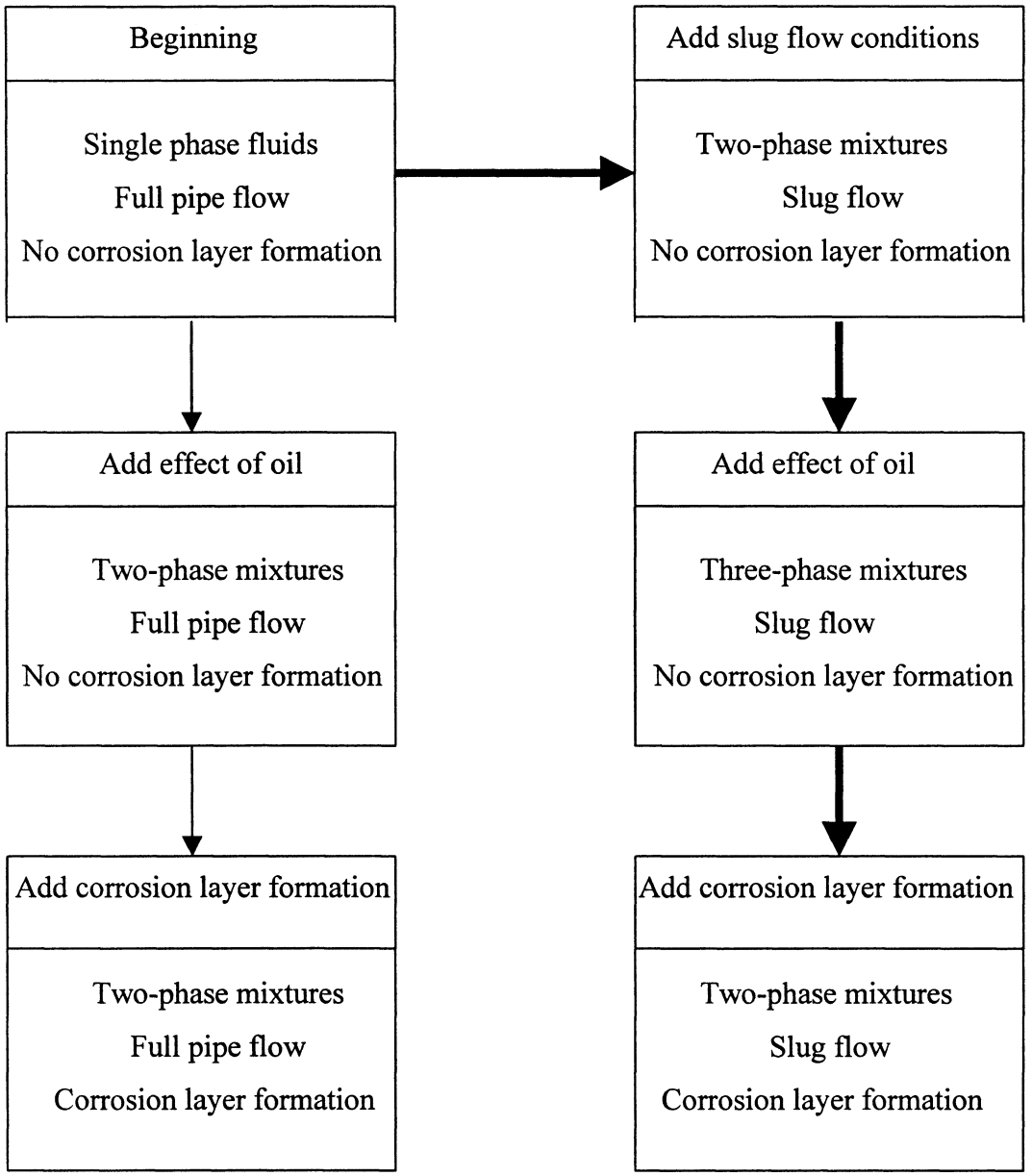

Figure 1.3 Proposed stages of model development

CHAPTER 2

LITERATURE REVIEW

A review of the literature was conducted to show the current understanding of the carbon dioxide corrosion occurring in oil and gas production. It covers the CO_2 corrosion mechanism, the carbon dioxide corrosion prediction model, the hydrodynamics of horizontal slug flow, and the mass transfer study in multiphase flow using the electrochemical limiting current density technique.

2.1 Carbon Dioxide Corrosion Mechanism

2.1.1 Forms of Corrosion

Jones (1991) discussed various forms of corrosion and their mechanisms. Corrosion can be broadly categorized into uniform corrosion, pitting corrosion, and erosion corrosion.

Uniform or general corrosion involves the constant removal of metal from a surface. It requires the corrosive environment to have the same access to all parts of the metal surface. Moreover, the metal surface should be metallurgically and compositionally uniform.

Pitting corrosion has been defined as a localized attack on an otherwise resistant surface. It results from a failure of a passive film. The passive film might be in the form of corrosion product deposits or a corrosion inhibitor film. Under many conditions of practical interest in oil and gas production in a carbon dioxide

environment, a protective iron carbonate scale can form on the surface of the steel piping and tubing. Depending on the environmental factors and the characteristics of the steel, the presence of the scale can reduce the corrosion rates dramatically. Pitting corrosion requires that corrosion product layers have local defects (Schmitt 1984b). Pits are initiated by a number of surface discontinuities. These include insufficient inhibitor coverage, scratches in coatings, and deposits such as dust, mud, or sand. The shape of these pits depends on the metallurgy of the corroding surface and the chemistry of the environment. They may be shallow, deep, undercut, or subsurface.

Chloride is usually present as an essential ingredient to break down a passive film and to initiate localized corrosion. Chloride ions destroy passivity by penetrating pores in the film or colloidally dispersing it. These ions preferentially adsorb in favored areas and alter the electron configuration of metal atoms on the surface so that a reaction can occur. Pitting of iron typically takes place in alkaline chloride solutions.

Erosion corrosion results from a combination of the corrosive fluid and a high flow velocity. The protective corrosion product film is removed physically by the rapid movement of the corrosive fluid. The iron carbonate crystals are weakened by the action of flow via the shear stress and turbulence. This results in very high corrosion of the exposed surface. The attack is seen to follow the directions of the localized flow and turbulence.

Erosion corrosion can be a costly problem and occurs in many industries. In oil and gas production, sand is sometimes encountered and produced along with the liquid and gas. If the flow stream velocity is high enough, the sand can erode the production

tubing, pipelines, fittings, and valves since the sand can mechanically remove the protective corrosion product films. This enables corrosion to occur at an accelerated rate.

2.1.2 Carbon Dioxide Corrosion Mechanism

Extensive research has been done in the past to investigate the corrosion mechanisms of carbon steel in carbon dioxide systems. Most of it has been based on experiments carried out in stirred beakers, rotating cylinder electrodes, autoclave, and small diameter flow loops.

De Waard and Milliams (1975) studied the mechanisms of carbon dioxide corrosion of carbon steel under various conditions of pH, temperature, and pressure. They performed experiments using brine in a stirred beaker and proposed a model to predict the corrosion rates. The undissociated carbonic acid molecule in Equation 2.1 is directly adsorbed on the metal surface and then reduced as shown in Equation 2.2. This is the rate-determining step. The corrosion rate is directly related to the concentration of the undissociated carbonic acid in the solution. The recombination of the bicarbonate ion in the second step (Equation 2.3) and the combination of hydrogen ions to form hydrogen atom in the third step (Equation 2.4) are much faster and therefore not the rate determining steps. The concentration of hydrogen ion determines the pH of the solution.

In the bulk:

$$CO_2 + H_2O \rightarrow H_2CO_3 \quad (2.1)$$

At the metal surface, the cathodic reactions are:

$$2H_2CO_3 + 2e^- \rightarrow H_2 + 2HCO_3^- \quad (2.2)$$

$$HCO_3^- + H^+ \rightarrow H_2CO_3 \quad (2.3)$$

$$2H^+ + 2e^- \rightarrow H_2 \quad (2.4)$$

The anodic reaction is given by:

$$Fe \rightarrow Fe^{2+} + 2e^- \quad (2.5)$$

Bockris et al. (1962) showed that the rate controlling step depends upon the pH. The overall reaction is given by:

$$Fe + H_2CO_3 \rightarrow FeCO_3 + H_2 \quad (2.6)$$

Nesic et al. (1996) proposed a model for carbon dioxide corrosion, based on the modeling of individual electrochemical reactions occurring in water-carbon dioxide systems. In their model, they began with Equation (2.1) to describe the

formation of carbonic acid in an aqueous solution. The carbonic acid is then dissociated in two steps:

$$H_2CO_3 \rightarrow H^+ + HCO_3^- \quad (2.7)$$

$$HCO_3^- \rightarrow H^+ + CO_3^{2-} \quad (2.8)$$

At the surface, the reduction of hydrogen ions to hydrogen was given by:

$$H^+ + e^- \rightarrow H \quad (2.9)$$

Equation 2.9 dominates for pH < 4. At an intermediate pH (4 < pH < 6), which is the range of primary interest, in addition to the reduction of hydrogen ions, the direct reduction of carbonic acid also becomes important. This reaction is given by:

$$H_2CO_3 + e^- \rightarrow H + HCO_3^- \quad (2.10)$$

Herce et al. (1995) measured corrosion rates in single-phase flow using NaCl solutions. They studied the effect of carbon dioxide partial pressure and solution chemistry under turbulent pipe flow conditions. They proposed that the combined effects of carbon dioxide partial pressure, ionic strength, temperature, and initial bicarbonate ion concentration, i.e. solution chemistry, may be described by a single

variable pH. They combined the effects of fluid flow with pH to define the hydrogen ion flux, which they related to the corrosion rates under a variety of conditions.

Dayalan et al. (1995) proposed a mechanistic model for the carbon dioxide corrosion of steel in pipe flow. They suggested that the overall corrosion process can be divided into four steps. The first step is the dissolution of carbon dioxide in the aqueous solution to form the various reactive species, which take part in the corrosion reaction. The second step is the transportation of these reactants to the metal surface. The third step involves the electrochemical reactions (anodic and cathodic) taking place at the metal surface. The fourth step is the transportation of the corrosion products to the bulk of the solution. This can be shown schematically as:

1. Formation of reactive species in the bulk

$$CO_2 + H_2O \rightarrow H_2CO_3 \quad (2.1)$$

$$H_2CO_3 \rightarrow H^+ + HCO_3^- \quad (2.7)$$

$$HCO_3^- \rightarrow H^+ + CO_3^{2-} \quad (2.8)$$

2. Transportation of reactants from bulk to surface

$$H_2CO_3\ (bulk) \rightarrow H_2CO_3\ (surface) \quad (2.11)$$

$$HCO_3^-\ (bulk) \rightarrow HCO_3^-\ (surface) \quad (2.12)$$

$$H^+ \quad (bulk) \quad \rightarrow \quad H^+ \quad (surface) \qquad (2.13)$$

3. Electrochemical reactions at the surface

$$2H_2CO_3 + 2e^- \rightarrow H_2 + 2HCO_3^- \qquad (2.2)$$

$$2HCO_3^- + 2e^- \rightarrow H_2 + 2CO_3^{2-} \qquad (2.14)$$

$$2H^+ + 2e^- \rightarrow H_2 \qquad (2.4)$$

$$Fe \rightarrow Fe^{2+} + 2e^- \qquad (2.5)$$

4. Transportation of products from surface to bulk

$$Fe^{2+} \quad (surface) \quad \rightarrow \quad Fe^{2+} \quad (bulk) \qquad (2.15)$$

$$CO_3^{2-} \quad (surface) \quad \rightarrow \quad CO_3^{2-} \quad (bulk) \qquad (2.16)$$

2.1.3 Factors Controlling CO_2 Corrosion

Increased interest in the CO_2 corrosion on carbon steels, also called sweet corrosion, has promoted extensive research in the past few decades. These efforts have resulted in a good understanding of the sweet corrosion (De Waard and Milliams 1975, Schmitt 1984, Ogundele and White 1986, Gray et al. 1989, Gray et al. 1990, Dugstad et al. 1994, Nesic et al. 1996, Linter and Burstein 1999). The sweet corrosion is related to many factors associated with material and environmental characteristics.

The former is related to microstructure, chemical composition, and protective film solubility. The latter is related to carbon dioxide partial pressure, temperature, pH, fluid composition, and flow velocity. Therefore, it is important to have a thorough picture of these variables when studying sweet corrosion. Schmitt (1984a) depicted the major factors of CO_2 corrosion as shown in Figure 2.1. So far the effects of the individual parameters can be summarized as follows.

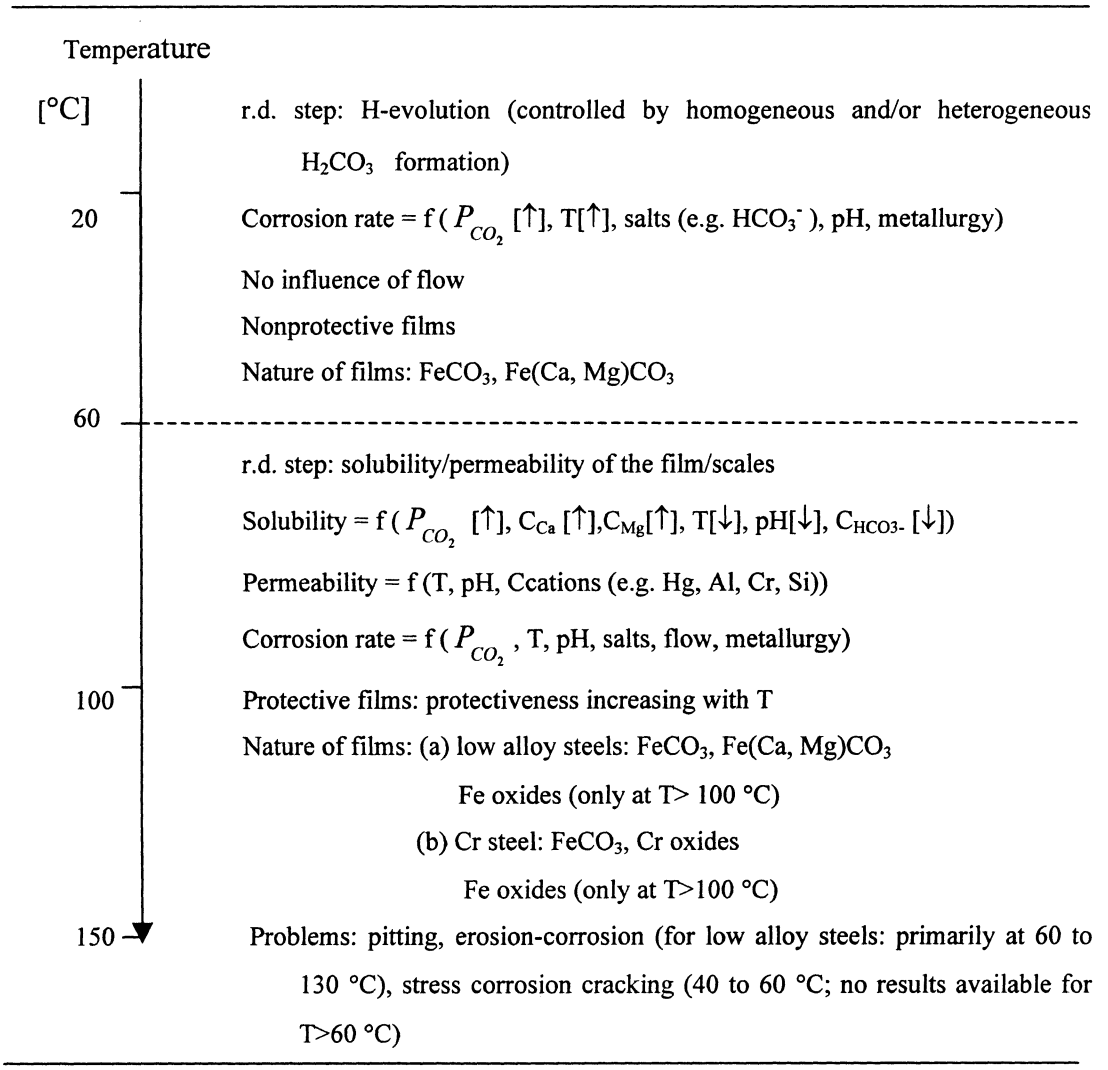

r.d.: rate determining

Figure 2.1 Schematic of CO_2 corrosion of carbon steel (Schmitt, 1984a)

2.1.3.1 Corrosion Product Film

Usually, the main corrosion product found in carbon dioxide related corrosion in oil and gas pipelines is iron carbonate. The reaction is:

$$Fe^{2+} + CO_3^{2-} \rightarrow FeCO_3 \qquad (2.17)$$

De Waard and Milliams (1975) showed the solubility of iron carbonate, which is usually the main corrosion product, is low and decreases with an increase in temperature. The iron carbonate dissolves in the solution until its solubility limit is reached. When the solubility limit for iron carbonate ($FeCO_3$) is exceeded it precipitates onto the metal surface forming a protective film at a higher temperature (> 60 °C). Due to the fact that precipitation does not occur instantaneously when the thermodynamic saturation is reached, it is possible to exceed the solubility limit in a corroding system (super-saturation). The degree of super-saturation is primarily a function of the iron carbonate concentration, temperature, and pH (Jasinski and Tomson, 1991). Iron carbonate ($FeCO_3$) films are considered to be protective in many cases and to reduce the corrosion rate by limiting the transport of chemical species involved in the electrochemical reactions. However, the presence of iron carbide (Fe_3C) in the film is considered to increase the corrosion reaction when corrosion proceeds in a lower temperature (< 60°C) by selectively increasing the cathodic

reaction rate (galvanic effect) (Jasinski, 1987). Iron carbide is left from the metal composition when the iron leaves the metal surface.

Vuppu and Jepson (1994b) performed studies on the characteristics of the protective iron carbonate film formed on the metal surface under various conditions of temperature, pressure, oil/water fraction, and flow conditions. It was found from scanning electron microscopy (SEM) studies, that at temperatures below 60 °C, the corrosion deposit formed under a full pipe flow for brine was of uniform thickness. The formation of protective iron carbonate scales was found to occur at 70 °C for brine. It was also found that under the slug flow conditions, at a high pressure, and Froude numbers, the corrosion product is broken into small flakes. This is possible due to the high shear and turbulence associated with the slug flow.

Heuer and Stubbins (1999) reported that the effect of temperature, pressure, slug flow Froude number, and water cut on the corrosion products formed in horizontal multiphase flow. They found that coupons exposed under a full pipe flow, have much thicker films than specimens exposed to a slug flow. The average thickness in a full pipe flow is about three times greater than that for a slug flow. They determined the thickness of corrosion film for various full pipe flow and slug flow conditions. The thickness of the corrosion product film is about 30 to 50 micrometers for the full pipe flow, but for the slug flow the average thickness of the corrosion product film is about 6 to 14 micrometers. This indicates the possible stripping of the protective film of corrosion products on the metal surface due to higher levels of shear stress and turbulence under slug flow conditions.

2.1.3.2 pH

The pH affects the corrosion rate by changing the reaction mechanisms. The increased pH gives a lower corrosion rate due to a lower availability of H^+ ions and a lower rate of the hydrogen reduction reaction. A higher pH also means a lower solubility of iron carbonate giving a higher probability of a protective film formation (Nesic and Lunde, 1993, Nesic et al. 1996).

Nesic et al. (1996) distinguished the direct influence of pH on the electrochemical reactions. At the surface, the reduction of the hydrogen ions to hydrogen given by Equation 2.9 dominates for pH < 4. At an intermediate pH (4 < pH < 6), in addition to the reduction of the hydrogen ions, the direct reduction of the carbonic acid also becomes important as shown by Equation 2.10. At a higher pH (pH>6), in addition to the above two reactions, the reduction of bicarbonate acid as shown in Equation 2.8 also becomes important.

2.1.3.3 CO_2 Partial Pressure

A higher CO_2 partial pressure gives a higher corrosion rate due to a reduction in pH, and due to the increased rate of the carbonic acid reduction reaction (De Waard et al. 1995).

2.1.3.4 Temperature

A higher temperature directly causes a higher corrosion rate due to the acceleration of the electrochemical and chemical reactions. However, precipitation rates also increase at a higher temperature, so the protective films form more easily and can lead to a reduction in the corrosion rate (Ikeda et al. 1984, Jasinski and Tomson, 1991).

It appears that the temperature is obviously one of the most important parameters. Detailed studies revealed that there is a qualitative change in the corrosion kinetics at temperatures around 60°C. Ikeda et al. (1984) has classified the three types of corrosion according to temperature:

Low temperature (~ 40°C)	general corrosion
Intermediate temperature (~100°C)	deep pitting
High temperature (~150°C)	anti-corrosion

2.1.3.5 Flow

It is appropriate to include a few earlier historical notes. The understanding of the basic processes of flow-accelerated corrosion was tremendously stimulated by the introduction of the rotating disc for use in laboratory studies in the 1960s (Levich, 1962). Articles on flow effects on corrosion first appeared in the 1950s and 1960s and they still contain usable material (Laque, 1957, Copson, 1960, Ross and Hitchen, 1961). Principles derived from transport processes as treated in chemical engineering were introduced in the 1960s and 1970s (Mahato et al. 1968, Ellison and Schmeal, 1978).

Within the last 20 years a large number of fundamental studies by laboratory methods, e.g. jet impingement and rotating cylinder electrode, have continuously addressed the CO_2 mechanism (Gray et al. 1989, Gray et al. 1990, Nesic et al. 1996, Linter and Burstein 1999). Efird (1977) published the first paper about the effect of fluid dynamics on the corrosion of copper-base alloys in seawater through the analysis of a transport parameter, i.e. shear stress. Ahmed et al. (1994) reviewed the application of closed-loop systems in flow-induced corrosion. In a power plant, the flow-accelerate corrosion (FAC) is also an important branch of corrosion engineering (Chexal et al. 1996).

There are several important reviews discussing the flow effect on corrosion by Poulson (1993) and Heitz (1991). Poulson examined the hydrodynamic parameters influencing erosion corrosion in a two-phase gas-liquid system, e.g. velocity, surface shear stress, intensity of turbulence, and mass transfer coefficient. Heitz considered that there are a number of mechanisms of conjoint action of flow and corrosion that result in four types of flow-induced corrosion: (1) mass transport-controlled corrosion, (2) phase transport-controlled corrosion, (3) erosion-corrosion, and (4) cavitation corrosion. These mechanisms are schematically represented in a simplified fashion in Figure 2.2.

From a microscopic view, the flow induced localized corrosion can also be caused by the momentum exchange of near-wall turbulence elements and subsequent fatigue cracking of corrosion product scales as shown in Figure 2.3

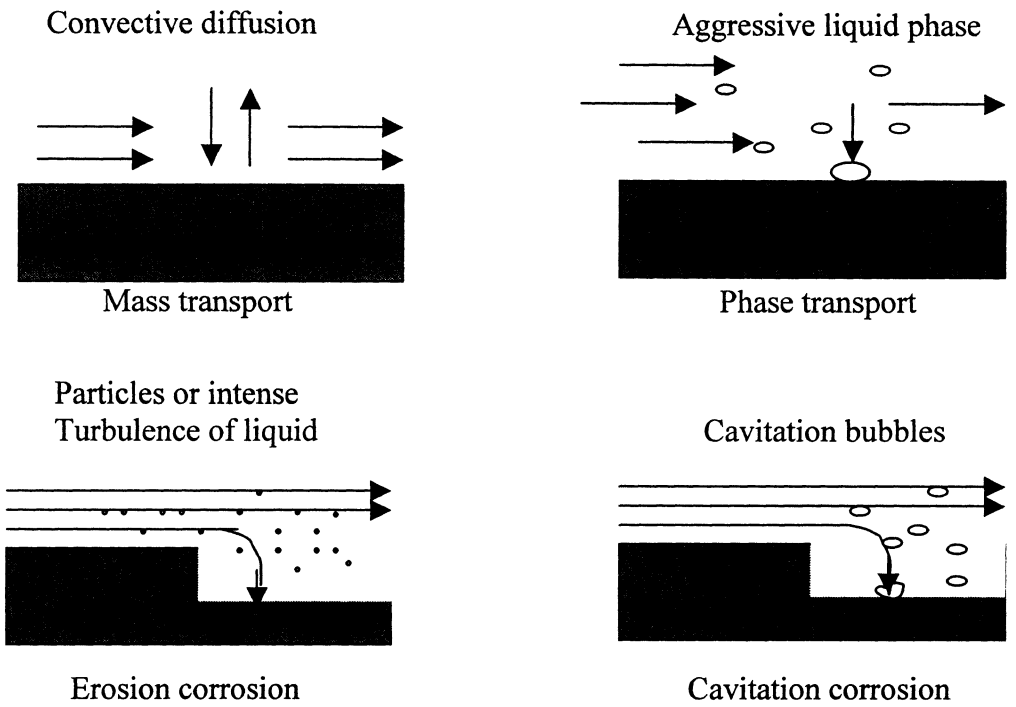

Figure 2.2 Schematic of the four main types of flow-accelerated corrosion (Poulson, 1993)

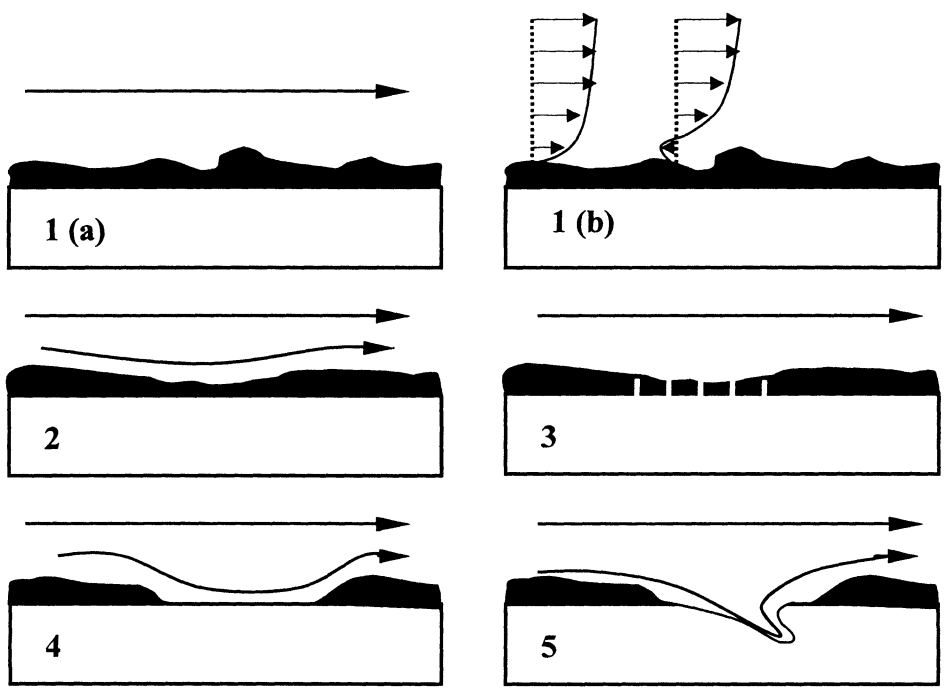

Figure 2.3 Development of flow induced localized corrosion (FILC) mechanism (Schmitt et al. 1999)

(Schmitt et al. 1999). These studies indicated the significant effect of flow on corrosion; therefore, the study of flow becomes very important.

The above studies did not consider or only partially considered the effect of practical multiphase flow on corrosion. Different flow regimes, such as a stratified flow, a plug flow, a slug flow, a wavy stratified flow, an annual flow, and a bubbly flow will appear at a specific liquid and gas velocity. Figures 2.4 and 2.5 show a typical flow regime map in a gas/liquid two-phase and a gas/oil/liquid three-phase flow in a 4-inch diameter horizontal pipeline, respectively. Mass transfer of corrosive components to the corroding surface, as well as wall shear stresses which might influence the mechanical wear on possible protective layers on the steel surface, can be much higher in the actual multiphase pipelines than can be simulated with a rotating disk electrode in water solutions. In addition, phenomena related to water separation from the flowing oil/water/gas mixture, high turbulent slug flow, and annular flow in the pipelines cannot be studied in simple experiments with only a water phase or in a laboratory cell containing oil, water, and gas.

Therefore, in recent years, the effects of multiphase flow on sweet corrosion have been studied extensively in large flow loops, e.g. 4 inch, 10 inch I.D. pipeline (Sun and Jepson, 1992, Chen and Jepson, 1999) via advanced hydrodynamics measurement techniques and electrochemical corrosion test methods. Table 2.1 further shows some typical flow loop studies conducted over the last 20 years that highlight the effect of a multiphase flow on CO_2 corrosion.

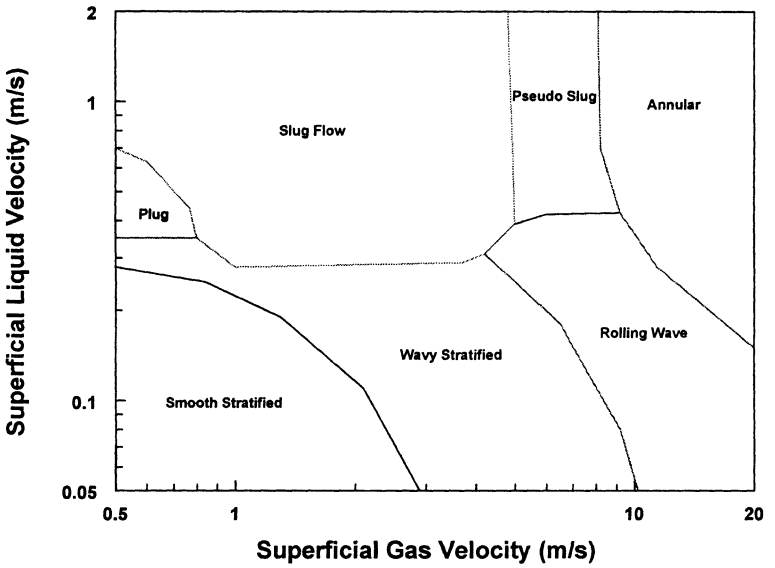

Figure 2.4 A typical flow regime map for gas/liquid two-phase flow in horizontal pipes (Lee, 1993)

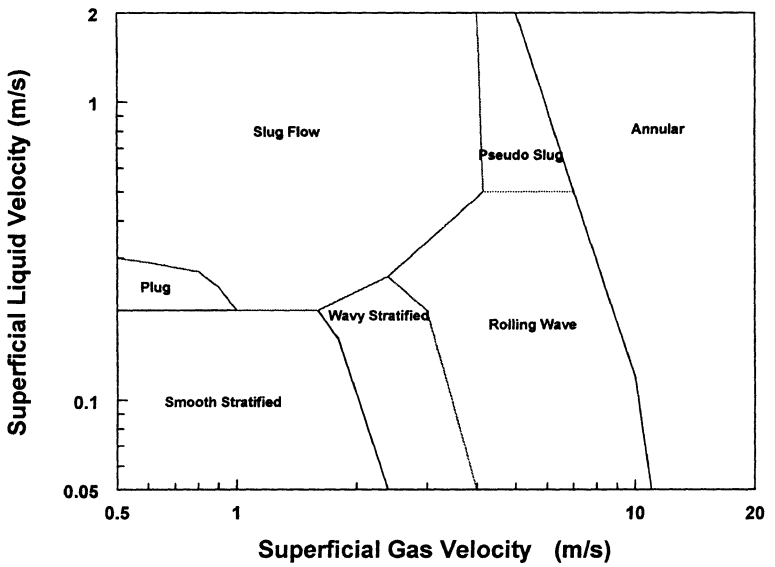

Figure 2.5 A typical flow regime map for gas/oil/liquid three-phase flow in horizontal pipes (Lee, 1993)

Table 2.1 Comparison of the studies on the effect of flow on CO_2 corrosion

Year	Authors	P CO_2 (bar)	pH	T (°C)	Flow	Loop I.D. (cm)	Significance
1984	Eriksrud and Sontvedt	1-2	3.8, 8	20, 60	Water/oil Slug flow Elongated bubble flow	2.4	First study on multiphase flow effect on corrosion
1989	Choi et al.	20-41	-	49-93	Brine/crude oil water cut: 1-60%	-	Study the effect of crude oil in two-phase flow
1993	Denpo and Ogawa	1, 10, 40	-	80	Water fully pipe	-	Comparison of pipe and rotating cylinder
1993	Efird et al.	1.3	6	50	Water	1.27 and 2.54	Comparison of pipe flow, jet impingement and rotating cylinder
1993	Nesic and Lunde	1-2	4-7	20 to 80	Two-phase flow (slug flow), single phase, and stratified flow	3.2	Quantify the influence of two-phase flow
1993	Dayalan et al.	11.2	3.4 and ♦	93	Single and two-phase flows	2.54	Correction of the API correlation of fluid erosion velocity
1994	Dugstad et al.	0.5, 21.4	3.5 to 6	20 to 90	Water	8.0	corrosion prediction model in single phase flow
1994	Fu and Bluth	2.07 to 7.58	4.5 to 5.5	38 to 60	Water/oil (kerosene 30%), water	2.54	Inhibitor study in pipeline
1995	Herce et al.	0.14, 0.7, 1.4	♦	30 to 115	Water	1.27, 2.54	Corrosion prediction model in single phase flow
1995	De Waard et al.	0, 3, 20	3.7-6.5	20 to 90	Water	-	Corrosion prediction model from data in single-phase flow
1992	Sun and Jepson	2	♦	35	0% oil, 20% oil, 40% oil and 100% oil, Stationary slug	10	Slug flow characteristics and effect on corrosion rate
1994 a, b	Vuppu and Jepson	2.75, 4.6	♦	40, 60, 80	Full pipe and slug flow, water cut: 0, 20, 40, 60, 80, 100%	10	Effect of multiphase flow, temperature, and other factors on corrosion rate and inhibitor performance

Continue Table 2.1

1994	Kanwar and Jepson	2.75, 4.6, 8.06	♦	40	Water/oil, water cut: 100, 80, 40, 20 and 0%	10	Prediction model for water/oil flow based on shear stress correlation with corrosion rate
1995	Gopal et al.	1.4	♦	40	Water/oil/gas slug flow	7.5, 10	Confirm the relation between the bubble mechanism and the enhanced corrosion rate
1996	Jepson and Bhongale	2.75, 4.6, 8.06	♦	40 to 90	Water/oil/gas slug flow, Water cut: 20, 40, 60, 80, 100%	10	Study the effect of temperature, CO2 partial pressure, and oil composition on corrosion rate
1997	Jepson et al.	1.32, 2.75, 4.6, 8.06	♦	40	Water cut: 20, 40, 60, 80, 100%, three-phase slug flow, horizontal	10	Study the effect of slug frequency, crude oil on the corrosion model (Jepson et al, 1996)
1998	Jepson et al.	2.75, 4.6, 8.06	♦	40 to 80	Water cut: 40 and 80%	10	Study the effect of gas density on the corrosion model (Jepson et al, 1996)

♦: pH not controlled

Extensive studies have been carried out in the past few years to study CO_2 corrosion in multiphase flow such as a water/oil two-phase flow, a water/gas two-phase flow, a water/oil/gas three-phase flow, and different flow regimes not only including the stratified flow, the slug flow, and the annual flow (Sun and Jepson, 1992, Zhou and Jepson, 1994, Gopal et al. 1995, Jepson et al. 1996, Kang et al. 1996, Jepson et al. 1997, Jepson et al. 1998).

In the slug flow the effects of parameters such as the Froude number, slug frequency, water cut, liquid viscosity, gas density, oil type, temperature, pressure, and pipeline inclination on CO_2 corrosion have been studied extensively. These corrosion

experiments provided important information towards understanding the effect of slug flow on CO_2 corrosion in pipelines.

The mechanism of corrosion enhancement of the slug flow can be explained through the extensive experimental methods, such as a surface analysis of coupons, visualization of slug flow, shear stress and single pressure measurements, and mass transfer measurements. The enhancement of corrosion in a slug flow can be attributed to the impact and subsequent collapse of the gas bubbles as they hit the bottom of the pipe (Gopal et al. 1995). These pulses of bubbles are generated within the mixing zone of the slug. In water/oil flow, the effects of flow regime, water cut, and phase inversion on the corrosion have been studied (Kanwar and Jepson, 1993, Vuppu and Jespon, 1994a, b, Kanwar and Jepson, 1994).

2. 2 Carbon Dioxide Corrosion Prediction Model

2.2.1 Theoretical Model for CO_2 Corrosion Prediction

There are a large number of CO_2 corrosion models available in the literature. These models can be classified as electrochemical mechanistic models (models describing the mechanism of the underlying corrosion process that have a strong theoretical background), semi-empirical models (models based only partially on a firm theoretical background), and empirical models (most of the constants used have little physical meaning). These models are compared in Table 2.2.

Table 2.2 Comparison of different CO_2 corrosion prediction models

Author	Model type	Significance & drawback	Year
Dayalan et al.	Mechanistic	Corrosion model for single phase flow	1993
De Waard and Milliams	Mechanistic	Does not consider flow	1975
De Waard et al.	Semi-empirical	Starting from a "worst case" corrosion rate, correction factors are included to quantify the influence of environmental parameters and product scale	1991
De Waard and Lotz	Semi-empirical	New model included the effect of flow	1993
De Waard et al.	Semi- empirical	Updated the corrosion mechanistic model which includes the effect of single phase flow	1995
Dugstad et al.	Empirical model	CO_2 corrosion in single phase flow	1994
Gray et al.	Mechanistic	An electrochemical model with limited consideration of single phase flow	1989, 1990
Jepson et al.	Semi-empirical	Corrosion rate prediction in slug flow	1998
Nesic et al.	Mechanistic	A model developed in rotating cylinder	1996
Pots	Mechanistic	Mechanistic model for CR in multiphase flow	1995
Zhang et al.	Mechanistic	Used for water/oil flow	1997

Corrosion is a very complex phenomenon involving the surface electrochemical reaction and the transport process of reactants and corrosion products to and from the metal surface. A mechanistic model is based on the rate equations of anodic dissolution of metals and of cathodic reductions of oxidants (e.g. H^+, H_2CO_3, and H_2O) combined with transport equations for reactants and products. All kinetic parameters and transport coefficients have physical meaning and are obtainable from experimental measurements.

De Waard and Milliams (1975) were the first to develop an mechanistic model for predicting iron corrosion in a CO_2 system. They derived the rate equation of anodic dissolution of iron based on the pH-dependent mechanism proposed by Bockris et al. (1961). For the mechanism of cathodic reaction, they suggested the reduction of undissociated carbonic acid as the rate-determining step. The resulting model could quantitatively explain their own experimental results and predict the effects of temperature and CO_2 partial pressure on the corrosion rate. De Waard et al. (1991) extended the model to wet natural gas pipelines after including the effects of new parameters, e.g. total pressure, protective film, pH, oil, condensation factor, etc. Such a semi-empirical model does not lend itself to extrapolation easily. These correction factors further obscure the underlying corrosion mechanism and that can have dubious interactions when more than one correction factor is applied. De Waard et al. (1993, 1995) added the mass transfer factor into the 1991 model by using the resistance model adopting the principle of series reactions in chemical engineering as follows.

$$\frac{1}{V_{cor}} = \frac{1}{V_r} + \frac{1}{V_m} \tag{2.18}$$

Where,

V_{cor} = corrosion rate (mm/year)

V_r = reaction rate term (mm/year)

V_m = mass transfer term (mm/year)

$$V_m = 2.45 \frac{U^{0.8}}{d^{0.2}} P_{CO_2} \quad (2.19)$$

Where,

V_m = mass transfer term (mm/year)

U = liquid velocity (m/s)

P_{CO_2} = carbon dioxide partial pressure (bar)

d = hydraulic diameter (m)

$$\log(V_r) = 4.93 - \frac{1119}{T} + 0.58 \log(P_{CO_2}) - 0.34 (pH_{actual} - pH_{CO_2}) \quad (2.20)$$

Where,
$$pH_{CO_2} = 3.82 + 0.00384T - 0.5 \log(P_{CO_2}) \quad (2.21)$$

V_r = reaction rate (mm/year)

P_{CO_2} =carbon dioxide partial pressure (bar)

pH_{actual} = actual pH in the presence of dissolved salts

pH_{CO2} = pH of dissolved CO_2 in pure water

T = temperature (K)

Gray et al. (1989, 1990) presented an electrochemical model as part of their experimental studies of CO_2 corrosion. The cathodic reduction reactions taken into account include H^+, H_2CO_3, and water reduction. The anodic dissolution reaction which is considered is the oxidation of Fe to Fe^{2+} based on a pH-dependent mechanism (Bockris et al. 1961). The electrochemical model has been used successfully to calculate the active dissolution rate of carbon steel at 25°C. The model

could also be used to predict the effect of the partial pressure of CO_2 and the fluid rate on the corrosion rate.

Nesic et al. (1996) conducted a study on CO_2 corrosion in a rotating cylinder. The cathodic reactions considered include H^+ reduction, O_2 reduction, direct reduction of H_2CO_3, and water. The charge transfer controlled oxidation of Fe to Fe^{2+} was used for the dissolution of iron. When modeling the limiting current density of H^+ reduction and O_2 reduction reactions, the correlation of Berger and Hau (1977), and of Eisenberg et al. (1954) were used for straight pipe flow and rotating cylinder systems respectively. Nesic et al. (1996) reported that the developed corrosion model could be used to predict the corrosion rate and to determine the governing corrosion mechanism (charge transfer control, mass transfer control, reaction or mixed control).

Dayalan et al. (1995) developed a corrosion model based on the corrosion mechanism introduced in Chapter 2.1.2. The API N-80 carbon steel used in these experiments corrodes uniformly and no corrosion product scales ($FeCO_3$) were observed in the range of low pH conditions in the experiments carried out in the study. Therefore, they suggested that the observed changes in the corrosion rates represent the true effects of velocity and carbon dioxide partial pressure on the corrosion rates given these scale-free conditions.

Figure 2.6 shows a schematic of the corrosion contribution of each cathodic reactant to the total corrosion rate. The three reactants are H^+, H_2CO_3, and HCO_3^-. The dotted lines represent the variation of corrosion rate with velocities due to these three cathodic reactants individually. These lines were obtained from theory by assuming

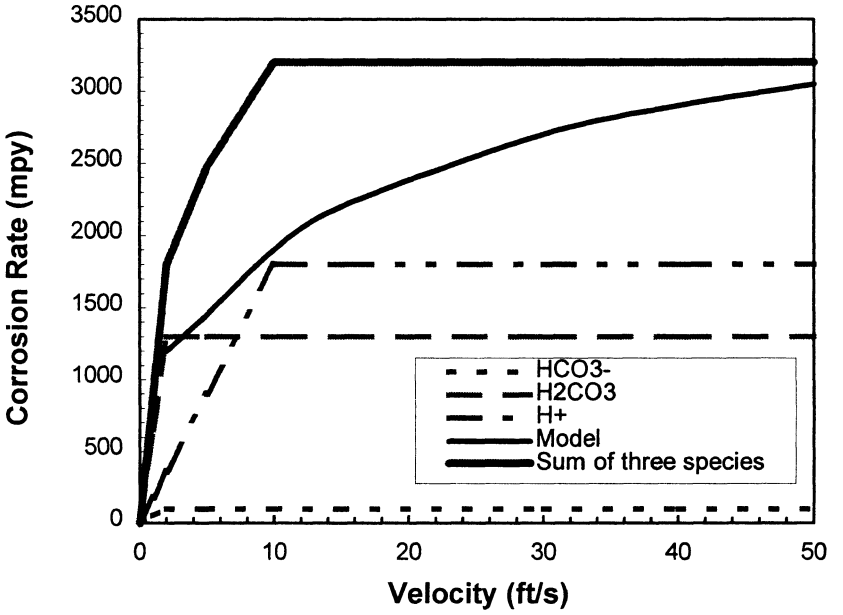

Figure 2.6 Schematic of corrosion concentration of various cathodic reactants and comparison with the model (Dayalan et al. 1995)

the total mass transfer controlled and the total electrochemical reaction rate controlled corrosion. For each species, the slanting line represents the mass transfer controlled region and the horizontal line represents the electrochemical reaction rate controlled region. The top solid line represents the total corrosion rate line, which is the sum of the corrosion rates of the three cathodic reactants. There are different slopes in this line because the rates of these cathodic reactions contributing to the total corrosion are controlled by different mechanisms at different velocities.

It is seen that the corrosion rate is mass transfer controlled at very low velocities and that becomes an electrochemical reaction controlled at high velocities. The heavy solid line represents the corrosion rates calculated by the model. The model takes into account all of the three cathodic reactions. At very low velocities, this line

asymptotically approaches the mass transfer controlled region of the total corrosion rate line and at very high velocities it asymptotically approaches the reaction rate controlled line. The model shows that in practical situations the carbon dioxide corrosion takes place under mixed control, that is, the corrosion is neither completely mass transfer rate controlled nor completely reaction rate controlled.

Figure 2.7 shows the model prediction at different velocities. It is seen that the increase in the corrosion rate with velocity is nonlinear. A linear relation is typical of a corrosion process being limited by a mass transfer rate. The model predicts a curved line that is a representation of a mixed control of mass transfer and surface reaction. Figure 2.8 shows the effect of pH on the corrosion rate. It is seen that an increase in pH decreases the corrosion rate.

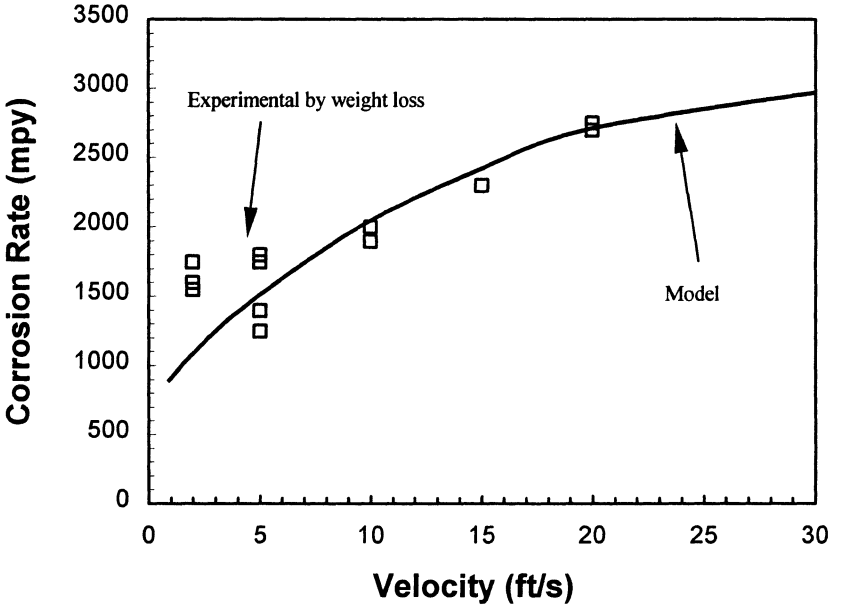

Figure 2.7 Comparison of corrosion rates from model predictions and experiments at 150 psig CO_2 partial pressure, 160 °F, and 3.4 pH as a function of velocity in 1" pipe (Dayalan et al. 1995).

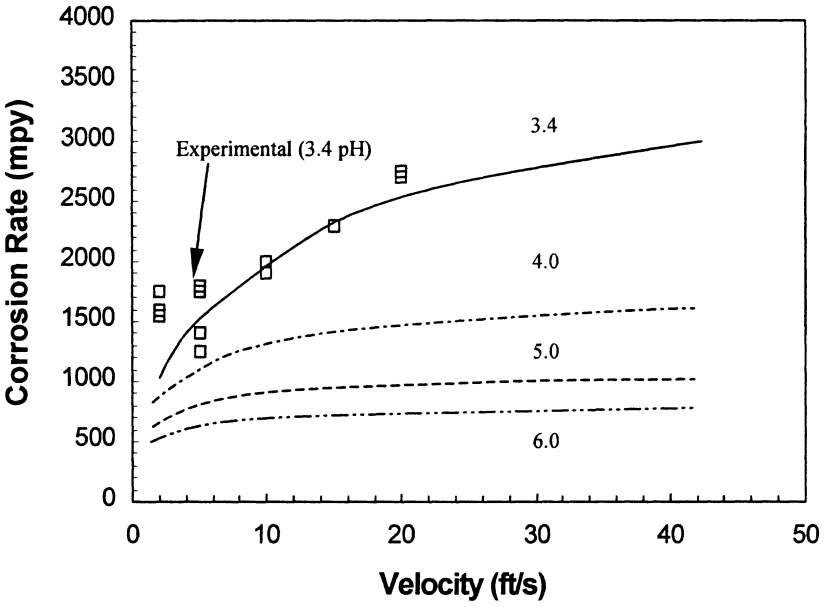

Figure 2.8 Comparison of corrosion rates from model predictions and experiments with E/CRC experimental data at 150 psig CO_2 partial pressure, 160 °F, and 3.4 pH as a function of velocity in 1" pipe (Dayalan et al. 1995).

Dayalan assumed that three species (H^+, H_2CO_3, and HCO_3^-) undergo reduction at the metal surface and contribute to corrosion. Apart from the surface reactions, mass transfer is also an important parameter to be considered in the corrosion process. There are fifteen unknowns in their study. The fifteen unknowns are the six surface concentrations (H_2CO_3, HCO_3^-, CO_3^{2-}, H^+, Fe^{2+}, and OH^-), four equilibrium potentials for reactions 2.2, 2.14, 2.4, and 2.5, the corrosion potential, and currents due to these four reactions. Fifteen equations are needed to solve these fifteen unknowns. These fifteen equations are coupled and most of them are non-linear. The Newton-Raphson method was used for solving the equations. It is not easy to make the program converge. They only studied brine with a 3% NaCl solution. There was no

evaluation of the corrosion product film effect. They also limited their work to 1-inch diameter pipe single-phase flow, without any comparison to experimental data for larger diameter pipes.

The model described in this dissertation follows the same principle steps as described by Dayalan et al. (1995). The number of cathodic reactions in the corrosion process is simplified according to the gas condensed slug flow with a low pH (pH < 4). Hence, only two reactions that are of interest in this corrosion model are represented below: the reduction of the hydrogen ion as the cathodic reaction and the oxidation of iron to the ferrous ion as the anodic reaction as shown in Equations 2.4 and 2.5.

Cathodic reaction: $2H^+ + 2e^- \rightarrow H_2$ (2.4)

Anodic reaction: $Fe \rightarrow Fe^{2+} + 2e^-$ (2.5)

The proposed transfer scheme is shown in Figure 2.9 without the build up of a corrosion product layer. The reactant (H^+) passes from the bulk solution to the metal surface through a mass transfer region, and the product (Fe^{2+}) moves from the metal surface towards the bulk solution. In the case where a corrosion film forms, the mass transfer is described schematically in Figure 2.10. The mass transfer region exists between a corrosion layer and the bulk solution, and the additional transport through the corrosion film must be also considered. For simplicity only the movement of the

ferrous ion and hydrogen ion will be considered in this layer since only these two ions are of interest in regards to the surface reactions.

Based on the above strategy, Zhang (1997) already produced a mechanistic model for full pipe oil-water flow as shown in Figure 1.3. Studies with and without a corrosion product layer were performed. Following this strategy, a corrosion mechanistic model for slug flow will be developed with a full consideration of hydrodynamics in slug flow.

2.2.2 Commercial Model for CO_2 Corrosion Prediction in Slug Flow

Table 2.3 shows the most popular corrosion prediction models currently used in the oil and gas industry. Most of models can be used for corrosion in turbulent flow or gas well and could be extended to multiphase flow with some doubtful assumptions. Three models, HYDROCOR (Shell), Model (IFE), and Ohio model (Ohio University) have specifically discussed the application of a corrosion prediction model in water/gas and water/oil/gas multiphase slug flow.

It is not possible to use the same model or correlation for the prediction of the corrosion for both gas lines and oil lines or for wells and flow lines due to the fact that corrosive mediums and flow regimes are quite different (Gunaltun, 1996). For each case, parameters to be used need to be identified and calculated separately for the specified conditions.

In the model by IFE, slug flow is divided into a bubble part and a stratified/annular part. The wall shear stress and liquid velocity averaged over the two

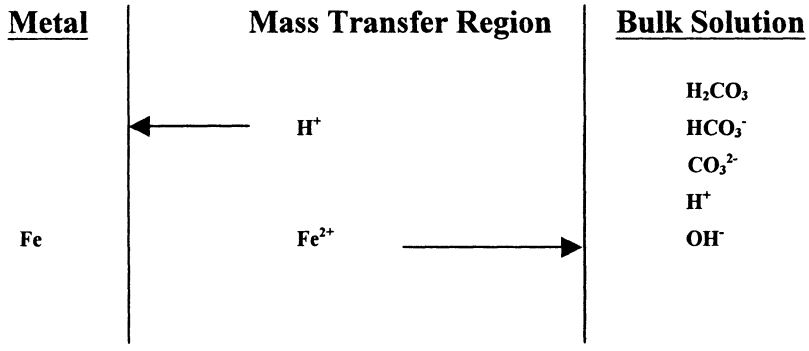

Figure 2.9 Transfer of ions between the metal surface and the bulk solution

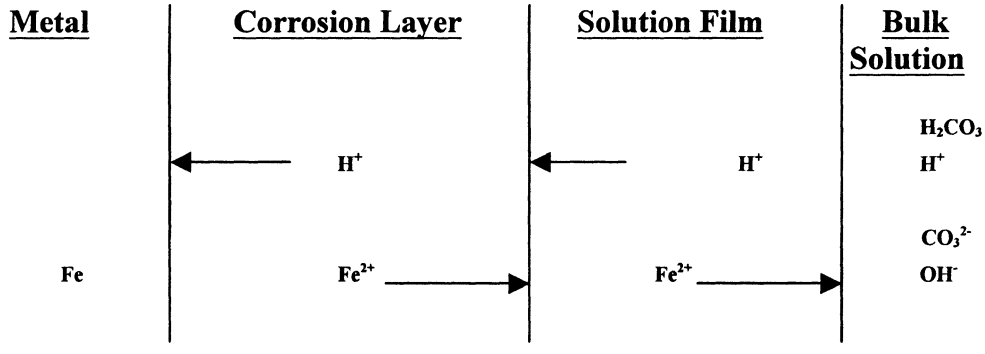

Figure 2.10 Effect of a corrosion product layer on the transfer of ions between the metal surface and the bulk solution

Table 2.3 Comparison of commercial CO_2 corrosion prediction models for carbon steel

Name	Year	Availability	Model Type	Flow	Reference
De Waard et al. (Shell)	1975-1995	Open	Semi-empirical model	Turbulent flow (single phase)	De Waard et al. (1995)
LIPUCOR (Total)	1979-1996	N/A	Empirical model	Gas line/wells, oil lines/wells	Gunaltun (1996)
NORSOK M-506 model (Statoil, Saga, Hydro)	1998	Open	Empirical model	Turbulent flow (single phase)	Norwgian Technology Standards Institution (1998)
HYDROCOR (Shell)	1995	N/A	Mechanistic model	Extend to slug flow	Pots (1995)
KSC Model (IFE)	1998	N/A for JIP only	Mechanistic model, with scale formation	Turbulent flow	Nyborg et al. (1998)
Model (IFE)	2000	N/A	De Waard + NORSOK M-506	Extend to slug flow (Use OLGA Three-phase fluid flow model)	Nyborg et al. (2000)
PREDICT (InterCorr)	1996-2000	Demo	De Waard model	Multiphase flow	Jangama et al. (1996)
Tulsa model (University of Tulsa)	1995	N/A for JIP only	Mechanistic, no scale formation	Turbulent flow (single phase)	Dayalan et al. (1995)
Ohio model (Ohio University)	1995-2001	N/A for JIP only	Mechanistic and empirical, scale formation	Applied to multiphase flow	Zhang et al. (1998) Jepson et al. (1997)
USL model (Univ. of Southwestern Louisiana)	1984-2000	N/A for JIP only Demo	N/A	Gas-condensate wells	Garber et al. (1998)
DREAM (Oklahoma State University)	1996-2000	N/A for JIP only	Mechanistic model, no scale formation	Down hole gas well	High et al. (2000)

parts is then used as input to the corrosion model. The HYDROCOR (Shell) model uses the same method as the IFE model. They divided the slug flow pattern into a film zone and a slug zone. Corrosion rates are then calculated separately for film and slug zones. For the film zone the same relations are used as for the separated flow. For the slug zone, the relevant flow velocity is the mixture velocity, which is the sum of the superficial liquid velocity and the superficial gas velocity. The hydraulic diameter equals the pipe

diameter. The overall corrosion rate is calculated from averaging over the two zones. This approach ignores the highly turbulent flow conditions that exist in the slug zone.

The Ohio model has been developed over past several years. This model combines the fluid dynamic models and corrosion prediction models. Fluid dynamic models include flow regime prediction, water/oil flow, and slug flow tracking. Corrosion prediction models include a specific corrosion mechanistic model for turbulent flow and water/oil flow (Zhang, 1997), and a semi-emipirical corrosion model for multiphase slug flow (Jepson et al. 1997).

The semi-emipirical corrosion model was developed from a large amount of experimental data at Ohio University from the relationship between wall shear stress and corrosion rate (Jepson et al., 1997). This model considers many variables in the multiphase flow conditions as shown in Equation 6.3. The comparison shows that this model can repeat the experimental data in the laboratory very well. In this model including the effects of the new parameters, it is possible only through new correction

factors that further obscure the underlying corrosion mechanisms and that can have dubious interactions once more than one correction factor is applied.

$$CR = 31.15 C_{oil} C_{freq} (\frac{\Delta P}{L})^{0.3} \upsilon^{0.6} P_{CO_2}{}^{0.8} T \exp(\frac{-2671}{T}) \qquad (2.22)$$

Where,

C_{oil} = normalized factor to account for crude oil type and $0<C_{oil}<1$

$$C_{oil} = 10^{(\log(acidnumber \times \%nitrogen)+0.38)} / 24000$$

C_{freq} = normalized factor to account for slug frequency and $0<C_{freq}<1$

$$C_{freq} = 0.023\ F + 0.214$$

$\frac{\Delta P}{L}$ = pressure drop through the slug flow (KPa/m)

$$\frac{\Delta P}{L} = 0.38 \times Froude$$

ν = the water cut, $0< \nu <1$

P_{CO_2} = partial pressure of CO_2 (MPa)

T = temperature (K)

The earlier models, i.e. HYDROCOR (Shell) and IFE model, have ignored the highly turbulent flow conditions that exists in the slug zone because little information about the slug zone was available due to the complex hydrodynamics inside the slug zone. The current investigation of the mass transfer coefficient in slug flow will provide a better understanding with the help of the earlier studies of slug

characteristics by Gopal (1994, 1997, 1998) and Maley and Jepson (1998), which will be further discussed in Chapter 2.3.

This dissertation aims to develop a mechanistic CO_2 corrosion model in slug flow taking into account the effect of mass transfer in slug flow on CO_2 corrosion. These well established theoretical paths developed or used by De Waard and Milliams (1975, 1991, 1995), Dayanan et al. (1996), Pots (1995), Nesic et al. (1996), Zhang et al. (1998) will be adopted into this study. The tremendous amount of corrosion data in slug flow produced in the Institute of Corrosion and Multiphase Technology will be used to validate the prospective corrosion mechanistic model developed for slug flow.

2.3 Hydrodynamics of Horizontal Slug Flow

CO_2 corrosion research in the last decades has been concerned with multiphase-phase flow as shown in Table 2.1. Advanced research and development focuses on multiphase flow largely stimulated by oil and gas production. Hydrodynamic conditions in multiphase slug flow are much more complicated than in single-phase flow. It is important to understand the hydrodynamics of slug flow in order to understand the corrosion mechanism in slug flow. Sydberger and Lotz proved a strong relationship between corrosion rate and hydrodynamics in 1982. In 1991 Heitz considered that the control of flow-induced corrosion requires analysis of the systems with regard to the nature of the flow, possible mechanical actions of the liquid, wall geometry changes during the erosion-corrosion process, and the characteristics of the electrochemical/chemical corrosion behavior of the material

itself. Corrosion control by flow mechanical measures and appropriate material selection has the greatest potential. Poulson (1993) examined the possible hydrodynamic parameters controlling the occurrence and rate of erosion corrosion.

2.3.1 Experimental Study of Slug Flow

Slug flow characteristics have been experimentally studied for many years. Kordyban (1963) presented experimental techniques used to study the mechanism of two-phase slug flow in a horizontal tube. This result showed that the velocity of the slug appeared to be a stronger function of air flow rate than of liquid flow rate. The magnitude of pressure fluctuations varied considerably from slug to slug for a given value of air water total flow rate. A schematic of slug flow is shown in Figure 2.11.

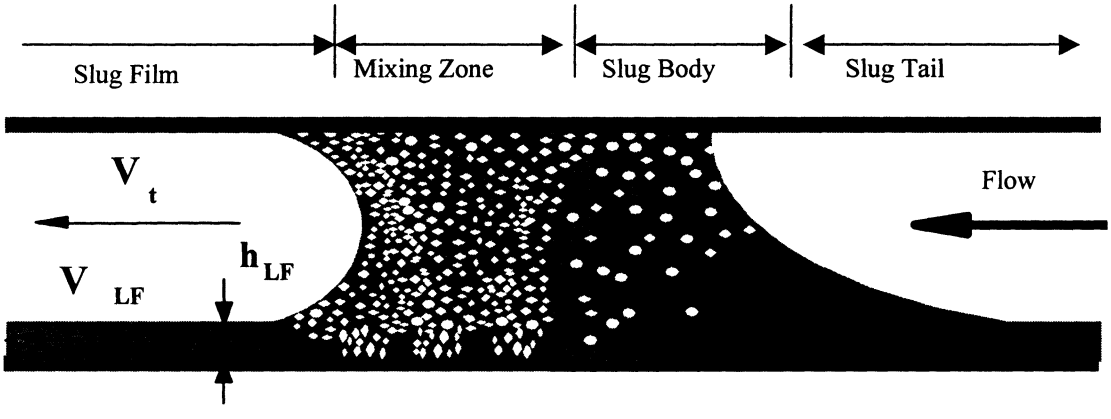

Figure 2.11 Schematic of horizontal slug flow

Crowley (1984) studied the effects of liquid viscosity and gas densities on slug characteristics. Experiments were conducted on a horizontal, 17 cm I.D. pipe for

superficial gas velocities of 1.2, 2.4, 3.6 m/s and superficial liquid velocities of 0.6, 1.2, 1.8 m/s, respectively. The fluids used were water (1 cp in viscosity, Newtonian liquid 400 cp) and gas (hydrogen, Freon 12). The results showed that liquid viscosity has a significant effect on two-phase slug flow characteristics while gas density has only a slight effect.

Due to the high velocity and transient nature of slug flow, it is very difficult to take accurate measurements on real moving slugs. Jepson et al. (1987, 1989) showed that the mixing zones in moving slugs and stationary hydraulic jumps are identical at the same Froude number. Stationary slugs are much easier to study than true moving slugs. The stationary slug formed by a hydraulic jump can accurately show the mechanisms in certain regions of true slug flow, and the measurements in a stationary slug are much easier than in a fast moving real slug.

Kouba and Jepson (1989) examined the Froude number both in the film ahead of slug and in the slug body from the measurements of liquid fraction, translational velocity of slug, slug length, and slug frequency. Experiments were carried out for gas and liquid superficial velocities ranging from 0.8 to 20 m/s and 0.3 to 3 m/s respectively. Typical results showed that the Froude number was basically less than unity after the front. This proves that a slug is a hydraulic jump that propagates along a pipe.

Zhou and Jepson (1994) carried out an experimental study of flow characteristics in stationary slug flow. The slug characteristics such as slug length, velocity, frequency, void fraction, and pressure drop are important parameters in

investigating flow characteristics in multiphase pipelines. It was found that shear stress increases with an increase in the Froude number. Shear stress also increases with an increase in oil fraction, while turbulent intensity decreases. Shear stress and turbulent intensity change rapidly within the mixing zone of the slug. The fluid composition and the Froude number can change the void fraction and the pressure drop around a stationary slug. It was found that the void fraction at the bottom of the pipe is always smaller than at the top of the pipe, and the void fraction increases with an increase in the Froude number and the oil concentration. The pressure drops across the slug front and within the slug body increase with an increase in the Froude number and decrease in the oil fraction.

2.3.2 Modeling of Slug Flow

The first realistic model of slug flow was proposed by Dukler and Hubbard (1975). They found that liquid is entrained at the slug front, accelerated to the slug velocity and then passed back through the slug. Jepson (1989) developed a mechanistic model for the prediction of transition to slug flow. Jepson's model assumes that the slug forms as a result of a hydraulic jump, which just touches the top wall of the conduit. This provides the necessary and sufficient conditions for the formation of a stable slug together with a " breaking dam" assumption at the rear of the slug.

There are several different types of slug. Their 'strength' is proportional to the Froude number calculated in the liquid film ahead of the slug, a parameter defined by

Jepson (1989) as shown in Equation 2.23. Jepson demonstrated that at low Froude numbers, there is some mixing at the front of the slug. When the gas and liquid flow rates are increased, the intensity of the mixing region increases and a strongly turbulent zone is formed at the slug front. In high Froude numbers, the film ahead of the slug is subjected to extremely high shear stresses. These high shearing forces may destroy inhibitor layers close to the wall.

$$Fr = \frac{V_t - V_{LF}}{\sqrt{(g \cdot h_{EF})}} \tag{2.23}$$

Where,

V_t = translation velocity = (1+ C)(V_{sl} + V_{sg}) (m/s)

V_{LF} = liquid film velocity = superficial liquid velocity = V_{sl} (m/s)

h_{EF} = effective liquid film height (m)

V_{sg} = superficial gas velocity (m/s)

V_{sl} = superficial liquid velocity (m/s)

C = constant =1.25

F_r = slug flow dimensionless Froude number

Maley (1997) developed a correlation and a mechanistic model for predicting the length of the mixing zone (LMZ) in the horizontal slug flow as shown in the following two equations.

$$LMZ = 0.051\ Fr + 0.18 \tag{2.24}$$

or

$$LMZ = 1.5D + \frac{h_{ls} \times Fr_s \times \sqrt{gD}}{v_b} \tag{2.25}$$

Where,

$$v_b = 1.53\left[\frac{\sigma \times g \times \Delta\rho}{\rho^2}\right]^{1/4} \tag{2.26}$$

v_b = rise velocity of a moderate bubble calculated from equations (Harmathy, 1960) (m/s)

h_{ls} = liquid height to gas/liquid interface, i.e. vertical traverse distance for bubbles (m)

Fr_s = Froude number for the slug front: $Fr_s = \frac{v_t - v_m}{\sqrt{g \times D}}$ (2.27)

v_m = mixture velocity with respect to pipe wall (m/s)

Laws (1999) developed a model predicting the slug freqency as follow.

$$\text{Log}\,(f \times D/V_{sl}) = m \times V_m + b \tag{2.28}$$

$$m = 4 \times 10^{-5}\theta^3 + 5 \times 10^{-4}\theta^2 - 2.5 \times 10^{-2}\theta + 0.7 \tag{2.29}$$

$$b = -4 \times 10^{-4}\theta^3 - 4.1 \times 10^{-3}\theta^2 + 2\theta - 1.7 \tag{2.30}$$

Where,

f = slug frequency (s)

V_m = total gas/oil/water velocity (m/s)

V_{sl} = superficial liquid velocity (m/s)

D = pipeline diameter (m)

θ = pipeline inclination (degree)

2.4 Mass Transfer Study in Multiphase Flow

Mass transfer coefficient is studied as a very important parameter in electrochemical processes (electroplating, corrosion) and chemical processes. The mass transfer process can exist at the interfaces among liquid, second liquid, gas, and solid phases. The multiphase flow can be water/gas two-phase flow, water/solid two-phase flow, water/oil two-phase flow, water/solid/gas, and water/oil/gas three-phase flow. This review will cover the mass transfer experimental measurement methods and their applications.

2.4.1 Electrochemical Limiting Current Technique

The electrochemical limiting current technique has become a standard method to measure mass transfer coefficient during the past 40 years. Two important articles have reviewed this method and its applications in studying mass transfer and shear stress (Mizushina, 1971, Selman and Tobias, 1978). The main equation for calculation of the mass transfer coefficient is given as follows.

$$K = I_L / (n F A C_b) \qquad (2.31)$$

Where K = mass transfer coefficient (m/s)

I_L = limiting current (A)

n = number of moles reacted

F = Faraday's constant = 96500 (C/mol)

A = surface area of the electrode (m^2)

C_b = bulk concentration of the potassium ferrocyanide (mol/m^3)

A series of published papers discussed the theoretical analysis. Deslous et al. (1990, 1993) studied the frequency response of electrochemical sensors to hydrodynamic fluctuations. They considered that the analysis of the statistics of the flow fluctuation requires knowledge of the transfer function between the mass flux and the velocity gradient. Calculations of these functions in the stream wise and in the span wise directions, with respect to the average flow direction, were reported. Van Steenhoven and Van De Beucken (1991) performed a dynamic analysis of the electrochemical wall shear rate measurements. They found that an electrochemical wall shear rate probe could be successfully applied to a flow situation where low frequency, high amplitude fluctuations, without backflow are present. Mao and Hanratty (1991, 1992) analyzed the probe design and calibration relationships necessary for the interpretation of the results of wall shear rate in large amplitude unsteady flow with flow reversal.

2.4.2 Effect of Bubble on Mass Transfer in the Ultrasound Systems

Several studies in ultrasound sonochemistry have investigated the effect of the collapsing of gas bubbles on the mass transfer to a solid surface. Tomita and Shima (1990) have studied the bubble collapsing process as shown in Figure 2.12. The interval between the numbered frames is 10 μms and the frame width is 1.4 mm. These microjets or forced convection when impinging on or near the microelectrode will increase the mass transport of electrolyte to the electrode. Birkin and Silva-Matinez (1996) studied the important effect of ultrasound on mass transport with the microelectrode. They recorded the current as a function of time at 25 μm diameter gold microelectrode electrode. The presence of ultrasound produces microjets due to collapsing/cavitating bubbles directed at the solid-liquid boundary. Well resolved current spikes were obtained as shown in Figure 2.13, which were about two-orders of magnitude higher than the steady state mass transport current produced in the absence of forced convection. The potential of the electrode was held potentiostatically at + 600 mV vs. Ag in a methanol solution containing 5.2 $mmol \cdot dm^{-3}$ ferrocene and 0.1 $mol \cdot dm^{-3}$ tetraethylammonium tetrafluoroborate ($C_8H_{20}BF_4N$, TEATFB) supporting electrolyte. The dotted line indicates the steady state mass transport current recorded for a static solution at +600 mV vs. Ag in a static solution. They found that increasing the intensity of the ultrasound source or decreasing the separation between the ultrasonic horn and electrode resulted in an increase in the frequency and magnitude of the observed events.

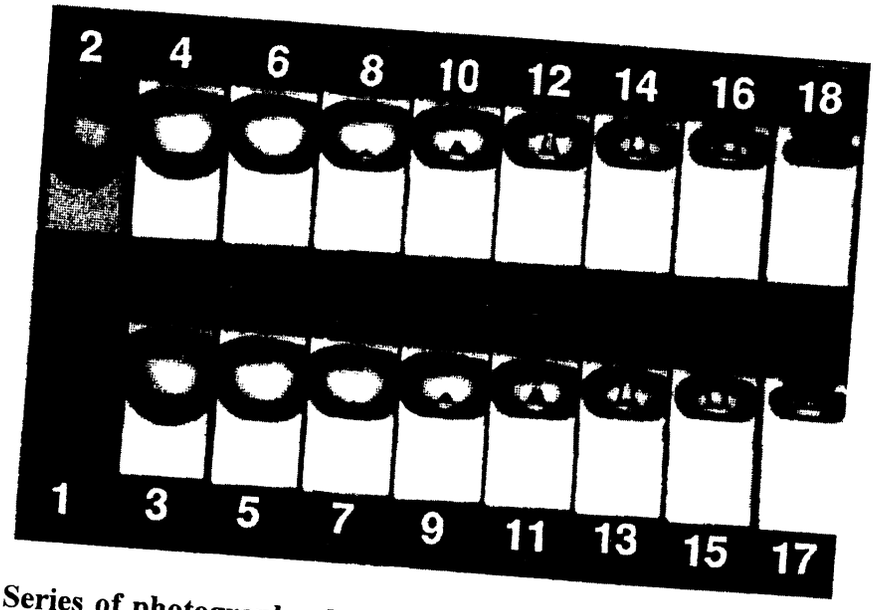

Figure 2.12 Series of photographs showing the development of the microjet in a bubble collapsing very close to a wall (Tomita and Shima, 1990)

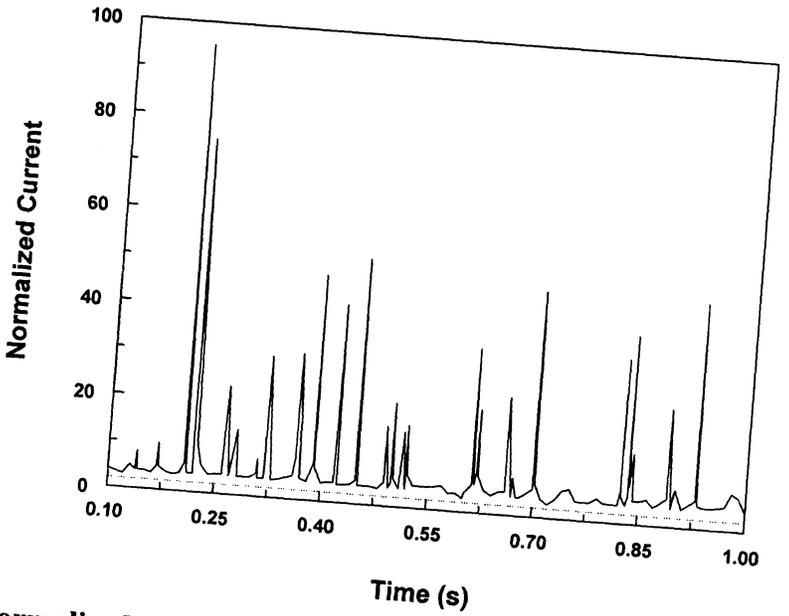

Figure 2.13 Normalized current recorded at a 25 μm diameter Au microelectrode exposed to ultrasound (Birkin and Silva-Martinez, 1996)

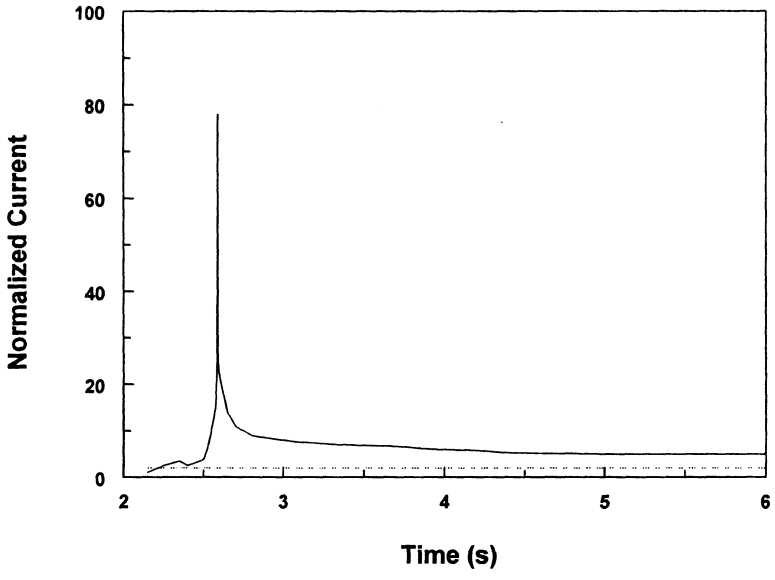

Figure 2.14 A single normalized current-time transient recorded at a 25 μm diameter Au microelectrode exposed to ultrasound (Birkin and Silva-Martinez, 1996)

Clear current spikes and decay transients due a single bubble back to the steady state can be seen, shown in Figure 2.14 by Birkin and Silva-Matinez (1996) and Ben Youssef et al. (1994). Current transients in the order of 80 – 100 times normalised height were observed under the condition stated. Birkin and Silva-Matinez (1996) showed that the magnitude of normalised current was altered by the potential applied to the electrode. Hence the events observed, attributed to cavitation events, are not the result of erroneous noise phenomena but only exist if the potential is in the correct region for the redox couple employed. In the same way if the solution is not excited by ultrasound to produce the cavitation events, then no transient events are observed.

These observations show that the events (current transients) are the result of the cavitation enhanced forced mass transfer.

They attributed these events to the impacts of microjets, caused by the collapse of transient cavitation bubbles, directly above or in the proximity of the microelectrode diffusion field. Direct hits or near-misses are recorded as current spikes of different normalised height. Figure 2.15 shows the scheme proposed by Birkin and Silva-Martinez (1996). Figure 2.15(a) shows the hemispherical diffusion field of a microelectrode held at the steady state mass transport limited condition in the absence of forced convection. Figure 2.15(b) shows the impact and subsequent compression of the diffusion field produced as a result of forced convection due to the microjet impact. After the cavitation event is over, Figure 2.15(c) shows how the diffusion sphere of the microelectrode will relax back to the non-convective steady state. This relaxation of the diffusion sphere is analogous to a potential step at the same microelectrode from a potential insufficient to oxidize the redox species to a potential sufficient to oxidize the redox species at the mass transport limited condition.

The presumption in the above studies was that the jet passes through a liquid layer. This is based on the following observations. Firstly, if the bubble were to occur immediately on the electrode, we would expect the current to fall to zero prior to the event. Secondly, on the reconnection of the electrode with the electrolytes (as the jet impacts) we would expect a contribution to the current-time transient from the capacitive charging of the electrode. This capacitive charging would be identical to that recorded for the chronoamperometric experiment. If these two characteristics have

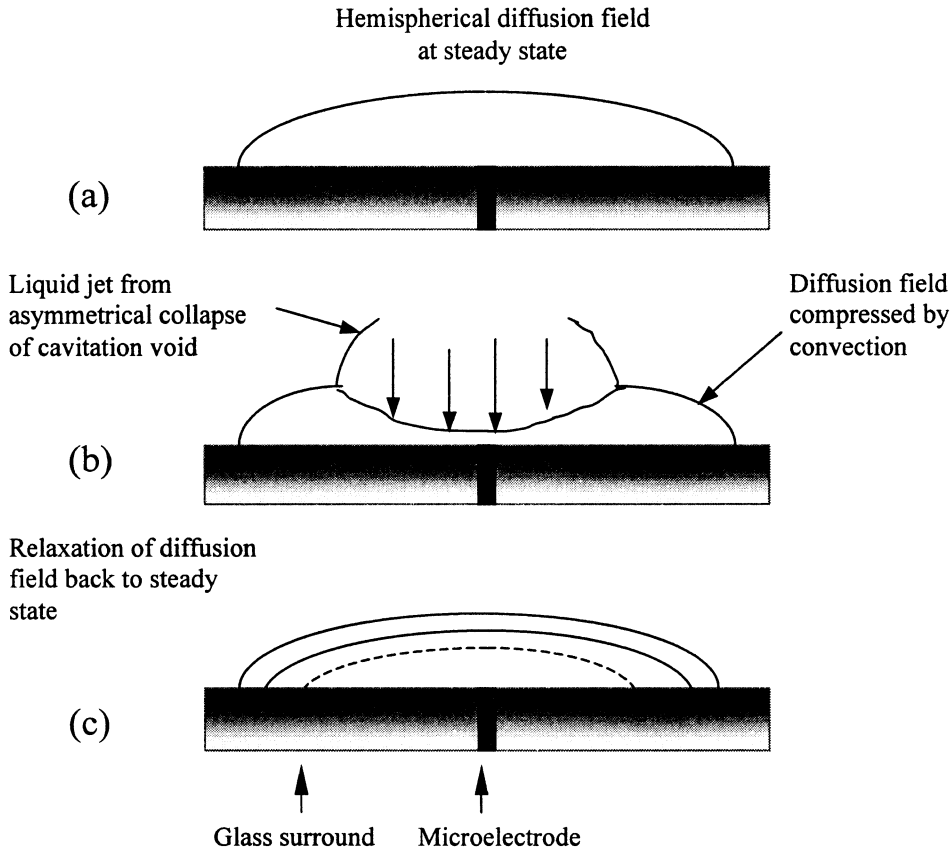

Figure 2.15 Schematic model of the proposed sequence of events, (a) The diffusion field at equilibrium prior to the caviatation event, (b) The impact of a microjet as a result of asymmetric collapse of a cavitation bubble over the electrode surface, (c) The relaxation of the diffusion field after the cavitation event is over (Birkin and Silva-Martinez, 1996)

not been observed, it is concluded that the electrode is continuously in contact with the electrolyte.

The direct effect of ultrasound on mass transfer can arise due to three major mechanisms. These mechanisms are acoustic streaming, microstreaming, and microjetting. Basically, acoustic streaming arises from attenuation of the sound field

within the liquid, resulting in a pressure gradient and subsequent liquid motion. Microstreaming occurs close to a forced oscillating bubble or some other vibrating body. Microjetting occurs when a cavitation bubble collapses asymmetrically next to a solid/liquid interface. It is also likely that ultrasound can indirectly produce mass transfer effects due to bubble formation or motion within the diffusion field of the electrode.

Marken et al. (1995) summarized the effect of ultrasound on the electro-chemical process as follows: i) mass transfer is observed experimentally to be strongly enhanced near the electrode surface. Possible processes that contribute to mass transport are acoustic streaming, cavitation or micro streaming at the electrode surface. ii) cavitation has a considerable cleaning effect on the electrode but also erodes away the surface material. ii) radical species formed in the cavitation event are highly reactive and may participate in the electrode process. iv) ultrasound enhances the rate of certain chemical reactions, such as disproportionations, coupled to the heterogeneous electrode transfer.

It has been demonstrated that for the chosen example of heterogeneous electron transfer reactions no obvious direct effect of intense ultrasound on the rate of simple electron transfer processes for fast and quasi-reversible system exists. The dominating effect caused by ultrasound is the strongly enhanced mass transport resulting from a very thin diffusion layer thickness.

Considering the cavitation process in slug flow, it is believed that the electrochemical study is also important to understand the nature of the bubble impact and the collapse in slug flow and its effect on mass transfer and on corrosion rate.

Hagenson and Doraiswamy (1998) compared the effects of ultrasound and mechanical agitation on a reacting solid-liquid system. When solid particles are in the vicinity of the cavitation bubble the implosion may occur symmetrically or asymmetrically, depending on the proximity of the solids. Symmetric cavitation creates shock waves that propagate to the surrounding solids causing microscopic turbulence and/or thinning of the solid-liquid film. This phenomenon is called microstreaming and is thought to be responsible for increasing the rate of mass transfer of reactor and products through the film. When solid particles are in close proximity to the bubble, it is unable to collapse symmetrically. This is known as asymmetric cavitation and is responsible for the formation of microjets of solvents, which bombard the solid surface, leading to pitting and corrosion.

Enhancement of ultrasound may be attributed to its chemical or mechanical effects or to both simultaneously. The chemical effects of ultrasound are due to the implosion of microbubbles, generating free radicals with a great propensity for reaction. Mechanical effects are caused by shock waves formed during symmetric cavitation. Hagenson found that the most important of these are that ultrasound increases 1) the intrinsic mass transfer coefficient of the liquid reactant through the interfacial film by a factor ~ 2. 2) the effective diffusivity of the liquid reactant through the product layer surrounding the unreacted core by a factor of 3.3.

Li et al. (1997ab) studied the potential and current oscillation in the reduction of $Fe(CN)_6^{3-}$ ions involving convection mass transfer. It was found that the convection mass transfer, which is induced by hydrogen evolution, plays an important role in the oscillations. It is seen that the convection mass transfer induced by the gas bubbles plays an important role in the oscillation of limiting current in the slug flow.

Apfel (1984) defines acoustic cavitation as a process will encompass any observable activity involving a bubble or population of bubble stimulated into motion by an acoustic field. He emphasized that an important class of acoustic phenomena involving bubbles arises from the passive emission of pre-existing macroscopic bubbles which are mechanically excited to undergo shape or volume changes of relatively small amplitude. Such processes, where the bubbles excited the sound wave rather than vice versa, might be classed as passive acoustic cavitation.

It is reasonably to consider that passive acoustic cavitation exists in slug flow, e.g. mixing zone and slug body. The macroscopic bubbles arise from slug flow and further strengthen the cavitation. When fluid flows, the pressure often decreases. When the pressure decreases to the fluid vapor pressure at the local temperature of the fluid, the fluid will change phase. That is, bubbles will form. This is known as cavitation. Engineers generally wish to design systems to avoid cavitation because it can produce the effects of noise, vibration, and erosion or damage to the valve and downstream piping.

The effect of bubble motion on mass transfer has been studied by Shah and Jorne (1989) and Whitey and Tobias (1988). Birkin and Silva-Martinez (1995, 1996,

and 1997) studied the effects of bubbles generated by an acoustic field, like ultrasound, specifically on mass transfer to an electrode. However, the effects of bubbles generated by slug flow on mass transfer to an electrode have, to our knowledge, not been studied extensively. Jiang and Gopal (1998) only reported that the phenomena existed, but the mechanism has not been studied yet.

2.4.3 Study of Mass Transfer in the Multiphase Reactor

Legrand et al. (1997) used electrochemical sensors for the determination of wall turbulence characteristics in annular swirling decaying flows. The mean value of the diffusional current leads to the mean wall velocity gradient, and the power spectral density of the current fluctuations is linked, via a transfer function, to the velocity gradient fluctuations. The wall turbulence was characterized by both the turbulence intensity and the cutoff frequency as defined by the transition between the low-frequency plateau and the inertial subrange of the power spectral density. Dumont et al. (2000a,b) used an electrochemical technique to measure the local and instantaneous wall shear rates in a scraped surface heat exchange (SSHE). In the general case of scraping, the flow was unsteady, and very fast, large fluctuations of the limiting diffusion current were measured. The shear rate at the wall of the stator of the SSHE appeared fully controlled by the rotation of the blades. Wall shear rates appear ten to a hundred times greater in an SSHE than in an annulus.

Rode et al. (1994a, b, c) used an electrochemical technique to study the hydrodynamics and liquid/solid mass transfer mechanisms in packed beds operating in

a concurrent gas-liquid downflow. The local instantaneous hydrodynamics were analyzed using electrochemical shear sensors. This study explains the gas-liquid flow mechanisms, especially in high-interaction regimes. In the dispersed bubble flow and in the liquid rich slugs of pulse flow, the local instantaneous liquid-solid shear rate is characterized by high-amplitude-high-frequency fluctuations. The study indicates the flow mechanism in dispersed bubble flow. Viscous forces dominate the liquid flow, whereas the gas bubbles pass through the packed bed by pressure pulses. Seguin et al. (1998a, b) used the electrochemical sensors to characterize the flow regimes (laminar flow and turbulent flow) in various porous media, e.g. a packed bed.

Perez-Herranz et al. (1999) studied the mass transfer in an annular electrodialysis cell in a pulsating flow. From their experimental results and numerical calculations, an enhancement of mass transfer, due to superimposed pulsation, can take place in the case of a reversing flow. The results indicate that the fluid velocity, the pulsation amplitude, and the pulsation frequency, influence the limiting current, giving an increase of 400% with respect to the steady state. For a given amplitude, the dimensionless velocity, α_0 ($\alpha_0 = \alpha\omega/\upsilon$), can be taken as a representative parameter of the pulsation effect on the mass transfer. The fractional increase in the Sherwood number in pulsating flow with respect to the steady state has been correlated in terms of the dimensionless velocity, α_1 ($\alpha_1 = D_{eq}(\omega\upsilon)^{1/2}$), giving the correlation:

$$\frac{Sh_p - Sh_0}{Sh_0} = 0.192(\alpha_0\alpha_1)^{0.377} \qquad (2.32)$$

Sh_p is the time-averaged Sherwood number in a pulsating flow and Sh_0 is the Sherwood number in a steady state.

Nishimura et al. (2000) studied the influence of imposed oscillatory frequency on mass transfer enhancement of grooved channels for pulstile flow using electrochemical technique. Transport enhancement by means of fluid oscillation is found to be higher in laminar than in turbulent flow. There is a noticeable enhancement at intermediate Strouhal numbers, depending on the cavity length and the net flow Reynold numbers. The electrochemical sensors have been also used to study liquid-wall shear stress in stratified liquid/gas flow (Rosant 1994) and in stratified/atomization flow (Vlachos et al. 1997).

Fenton and Alkire (1984) studied the mass transfer in two-phase liquid-liquid flow in the flow-through porous electrode cell. The liquid system is composed of water and toluene. The overall mass transfer rate was found to be a combination of four effects: (i) the single-phase mass transfer rate associated with the liquid as if it were flowing alone across the porous electrode, (ii) the decrease in mass transfer owing to coverage of the electrode surface by dispersed liquid droplets, (iii) the mass transfer exchange rate between the two liquids, and (iv) the further enhancement owing to penetration of the mass transfer boundary layer by the addition of an inert second phase.

The enhancement of mass transfer by inert suspended solids was found using a rotating-disk electrode (Anderson et al. 1989). Solid particles the same size as, or

smaller than, the thickness of the mass transfer boundary layer, create small-scale micro convective vortices. Particles much larger than the boundary-layer thickness appear to enhance transport by a different mechanism, possibly involving the formation of particle-free wall layers. The higher shear rate may reduce the thickness of the mass transfer boundary layer, thereby increasing the rate of mass transfer to the surface.

Mass transfer studies have two major industrial objectives (Selman and Tobias, 1978). One major objective is to clarify the mass transfer enhancement in multiphase electrochemical reactors, thus improving the reactor productivity as shown by the above research. Another objective is to clarify the mass transfer effect and the mechanical effect in a multiphase pipeline, thus increasing the understanding of the influences of multiphase systems on the corrosion mechanism and having better corrosion prediction and control.

The mass transfer study in multiphase pipelines received attention for a few years. The mass transfer change under disturbed flow conditions, such as near pits, weld beads, etc. has been examined in the presence of fully developed flow, slug flow, and annular flow (Langsholt et al. 1997, Jiang and Gopal 1998). The direct comparison of steady state mass transfer coefficients in these situations indicates that the weld beads and pits could increase the mass transfer coefficient and the corrosion rate. It was also found that slug flow usually results in a higher mass transfer coefficient, which contributes to a high corrosion rate. Jiang and Gopal (1998) reported large limiting current peaks in slug flow and slug-annular flows and

hypothesized their existence as the reason for enhanced corrosion in slug flow. However, a complete understanding of the mass transfer enhancement mechanism by multiphase flow in horizontal pipelines has not yet been seen in the literature, and it becomes one of subjects in this dissertation and elsewhere (Wang et al. 1999, 2000a, b, 2001)

2.4.4 Mass Transfer Correlation in Pipeline

The electrochemical limiting current technique has been used to obtain local and average mass transfer coefficients under a large variety of hydrodynamic conditions, e.g. laminar flow, free convection mass transfer at a plate, cylinder, forced convection mass transfer in a tube flow, agitated vessel, oscillating flow, and stirred cells. Selman and Tobias (1978) compiled over one hundred mass transport correlation pertaining to different transports, flows, and agitation configurations.

For fully developed turbulent mass transfer in a horizontal pipeline, several important empirical correlations for mass transfer coefficient have been developed by Chilton and Colburn (1934), Deissler (1955), and Vieth et al. (1963). The most recent correlation was proposed by Berger and Hau (1977) for mass transfer in fully developed flow in smooth pipes over a range of Reynolds number ($8 \times 10^3 < Re < 2 \times 10^5$) at Schmidt numbers varying between 1000 and 6000. It was found that a mass transfer correlation study has never been done in multiphase flow.

In the work of Berger and Hau, mass transfer was measured by the electrochemical limiting current density method in a 54.8 mm I.D. pipe. The

electrochemical system used in their experiments was the well-known aqueous solution of potassium ferro/ferricyanide with an addition of sodium hydroxide as the inert electrolyte. The mass transfer coefficient in fully developed flow was determined from the limiting current density on a 293 mm long cathode for Reynolds numbers ranging from 1×10^4 to 2×10^5 and Schmidt numbers from 1160 to 5900.

Sedahmed et al. (1994) studied mass transfer at rough gas-sparged electrodes. This study was done to help enhance the production in electrochemical reactors with diffusion-controlled reactions. Mass transfer data at the smooth surface were correlated according to the expression:

$$j = 0.126(Fr\,\mathrm{Re})^{-0.226} \tag{2.33}$$

Where:

j = mass transfer factor = $StSc^{0.66}$

Fr = Froude number = $\dfrac{V_g^{\,2}}{d_e g}$

Re = Reynolds number = $\dfrac{\rho_L V_g d_e}{\mu}$

St = Stanton number = $\dfrac{Sh}{\mathrm{Re}\,Sc}$

Sh = Sherwood number = $\dfrac{Kd_e}{D}$

Sc = Schmidt number = $\dfrac{\upsilon}{D}$

So far there are four typical correlations for calculation of the mass transfer coefficient for single-phase flow in pipeline. They are:

1) Chilton-Colburn: (1934)

$$S_t = \frac{1}{2} f Sc^{-2/3} \tag{2.34}$$

2) Deissler: (1955)

$$Sh = 0.0789 f^{1/2} \mathrm{Re}(Sc)^{1/3}, \qquad f = F(\mathrm{Re}, e/d) \tag{2.35}$$

3) Vieth: (1963)

$$Sh = 4.586 \frac{V_{max}}{V_{avg}} \frac{f}{2} \mathrm{Re}(Sc)^{1/3} \tag{2.36}$$

$$\text{If } \mathrm{Re} \le 3200, \ \frac{V_{max}}{V_{avg}} = \frac{1}{0.0425 \log \mathrm{Re} + 0.6172} \tag{2.37}$$

$$\text{If } \mathrm{Re} > 3200, \ \frac{V_{max}}{V_{avg}} = \frac{1}{1.0319 \log \mathrm{Re} - 2.8880} \tag{2.38}$$

$$(4f)^{-1/2} = -1.8 \log_{10}\left[\frac{6.9}{\mathrm{Re}} + \frac{(e/d)^{1.11}}{3.7}\right] \tag{2.39}$$

Where,

f = Fanning friction factor

e = roughness of the pipe

d = diameter of the pipe (m)

Re = Reynolds number

4) Berger & Hau: (1977)

$$St = 0.0165\,\mathrm{Re}^{-0.14}\,Sc^{-2/3}, \qquad St = \frac{Sh}{\mathrm{Re}\,Sc} \tag{2.40}$$

Lei and Gopal (1998) have studied the influence of weld and pit on mass transfer in full pipe flow, slug flow and annular flow. However, a conclusive mass transfer correlation has not been obtained yet. So this current study will develop a mass transfer correlation, which is necessary to calculate mass transfer coefficients for various reactive species used in the corrosion prediction model in horizontal slug flow.

In summary, the following objectives will be studied in this dissertation:

1. Develop a successful method to measure the mass transfer coefficient by the electrochemical limiting current density technique in multiphase flow.
2. Explain the relationship between bubble collapsing and mass transfer oscillation in slug flow.
3. Develop a mass transfer correlation for slug flow.
4. Develop a CO_2 corrosion mechanistic model for horizontal slug flow.

CHAPTER 3

EXPERIMENTAL DESIGN

This chapter describes the experimental techniques and equipment that were employed to measure the mass transfer coefficient in the multiphase slug flow.

3.1 Design of the Mass Transfer Multiphase Flow Apparatus

The experiments were carried out in 10 cm I.D. and 15 meter long Plexiglas™ pipe. The overall layout of the system is shown in Figure 3.1. The solution used in the experiments was 0.01 M potassium ferri/ferrocyanide in 1.0 M NaOH electrolyte, stored in a 1.8 m^3 stainless steel tank. The solution was pumped through a 10 cm I.D. PVC pipe by a variable speed Moyno™ multiphase pump. The liquid flow rate was measured by means of an orifice plate.

LVT 200 oil was used which includes 60% cycloparaffinic hydrocarbon, 20% isoparaffinic hydrocarbon, 19% normal parraffinic hydrocarbon and 1% other hydrocarbon. It has 3 cp viscosity and 850 kg/m^3 density at 25°C. Nitrogen gas, stored in pressurized cylinders, was used for water/oil/gas three-phase flow. Gas flow rate was controlled by a regulator and valve. Its flow rate was measured using an OMEGA® flow meter. The gas was injected into the system at a T-junction as shown in Figure 3.1. The liquid and gas were mixed at this junction and the mixture then flowed through a 15 m long pipeline before entering the storage tank. The storage tank

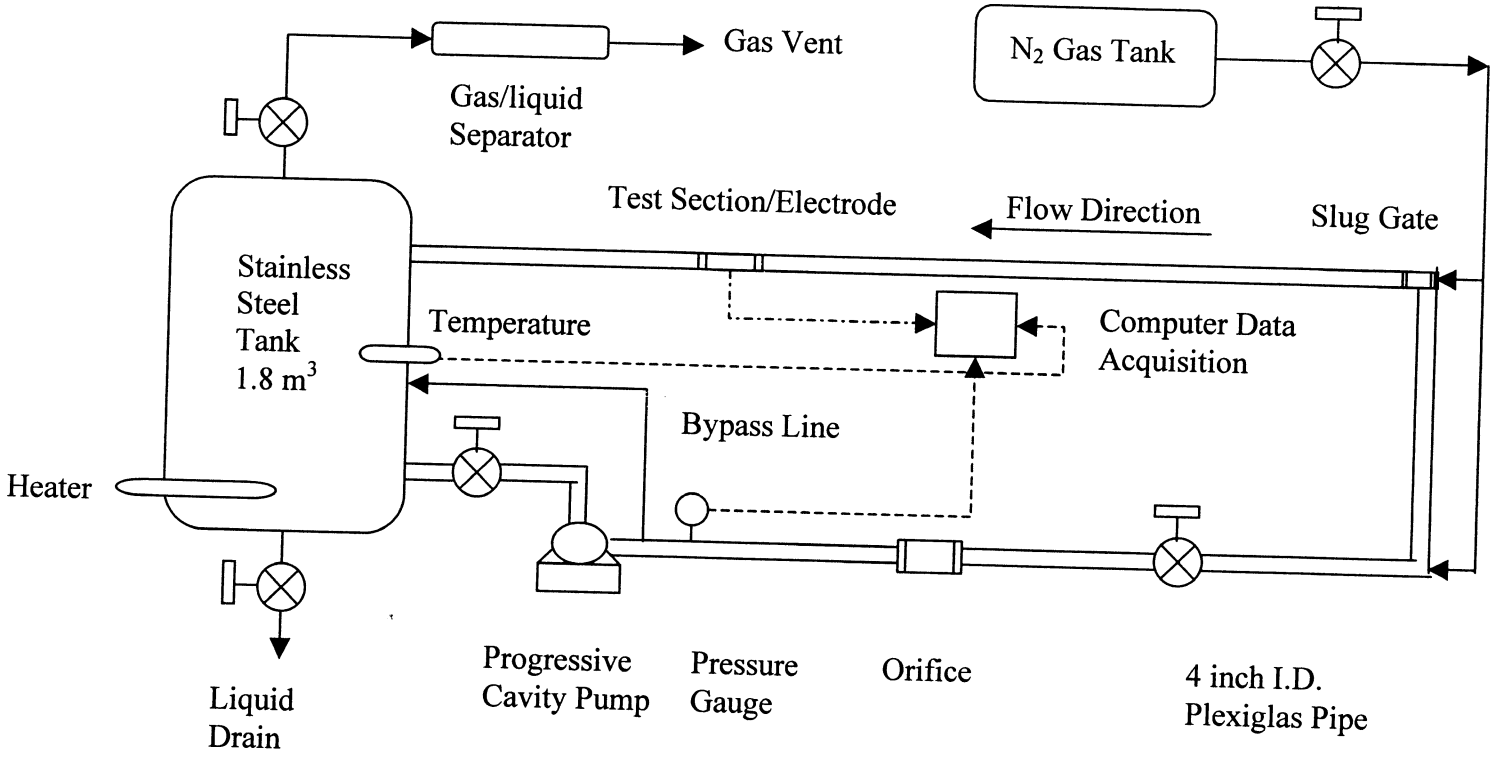

Figure 3.1 Schematics layout of mass transfer experimental multiphase flow system

also acts as a primary separator for the liquid and gas. The gas was vented from the top and sent to a vertical separator where it was stripped of the entrained liquid before being vented. In horizontal pipes at moderate liquid and gas flow rates the flow regime is slug flow.

The test section is shown in Figure 3.2. The reference electrode, five working electrodes, and counter electrode were placed in the direction of the flow, respectively. All electrodes were made from Hastelloy C-276. The counter was a ring electrode mounted flush with the pipe wall. The working and reference electrode pins were inserted in the Plexiglas block along a line at the bottom of the pipe wall. The diameter of each pin was 1.5 mm and the distance between the consecutive working electrodes was 4.5 mm.

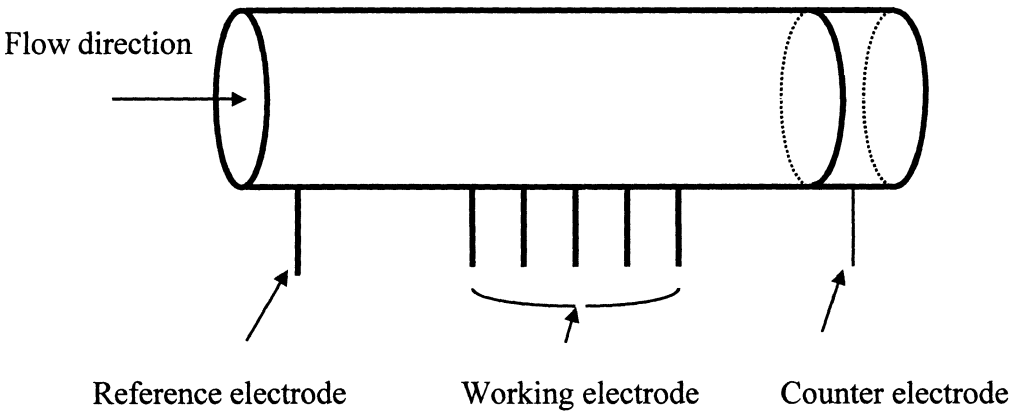

Figure 3.2 Test section used for mass transfer measurement in multiphase flow

In multiphase systems, once the standard reference electrode becomes filled with oil, it is just about impossible to get valid readings. Therefore, pseudo reference electrodes are becoming increasingly popular in multiphase systems, *e.g.* 316L

stainless steel has been recommended as a pseudo reference electrode in electrical impedance spectrum (EIS) studies in multiphase flow conditions (Chen et al. 2000). Sedahmed et al. (1994) have used nickel wire as a pseudo reference electrode in the mass transfer study at rough gas-sparged electrodes. The dimensionally stable anode (DSA) has been applied as a pseudo reference electrode in the study of two-phase mass transfer in channel electrolyzers with gas-liquid flow (Economou and Alkire, 1985). In the present electrolyte solution, the Hastelloy C-276 can also provide a stable potential considering that it is better than stainless steel or nickel in terms of metal stability. Thus it was employed in the mass transfer studies in water/oil/gas multiphase flow in a large diameter pipeline.

3.2 Experimental Technique

The electrochemical limiting current technique is used quite frequently for measuring mass transfer rates and shear stress between a fluid and a solid surface. The measured quantity is the electric current produced by the transfer of certain reacting ions to electrodes. Various systems have been suggested, but the most frequently applied in practice is an aqueous solution of the redox couple potassium ferro/ferricyanide with an added non-reacting electrolyte, usually NaOH (Berger and Ziai, 1983). The NaOH was added to reduce the ionic migration effects and to increase the conductivity of the solution.

The studied surface is located in working electrodes, where anodic reaction $Fe(CN)_6^{4-} = Fe(CN)_6^{3-} + e$ takes place, and the reaction in cathode is $Fe(CN)_6^{3-} + e =$

$Fe(CN)_6^{4-}$. The limiting current is obtained from the potentiodynamic measurements of the electric current as a function of the potential applied between the working electrode and reference electrode. The current increases exponentially with increasing potential until it approaches a constant value, i.e. the limiting current. The instantaneous limiting current is measured from the potentionstatic curve at a given potential corresponding to the limiting current density plateau.

The transfer of electrons produces a current which is related to the molar flux by Equation (3.1)

$$I_L = n\ F\ A\ N \qquad (3.1)$$

The mass transfer coefficient is defined as

$$K = N / (C_b - C_w) \qquad (3.2)$$

If the chemical reaction proceeds rapidly, the reaction rate at the cathode is diffusion limited and $C_w=0$. The mass transfer coefficient can be determined from

$$K = I_L / (n\ F\ A\ C_b) \qquad (3.3)$$

Where,

K = mass transfer coefficient (m/s)

I_L = limiting current (A)

n = number of moles reacted

F = Faraday's constant (=96500C/mol)

A = surface area of the electrode (m^2)

C_b = the bulk concentration of the potassium ferrocyanide (mol/m^3)

C_w = the concentration at the wall (mol/m^3)

Gamry software CMS 105 was used for the potentiodynamic and potentiostatic measurements. All experiments were performed at 20°C. The limiting current density can be obtained through the potentiodynamic and potentiostatic measurements. Correspondingly the average mass transfer coefficient and instantaneous mass transfer coefficient can be calculated by above equation.

3.3 Experimental Setup

3.3.1 Preparation of the Electrolyte Solution

The electrolyte solution used in this study was made from reagent grade $K_3Fe(CN)_6$, $K_4Fe(CN)_6$ from the Aldrich Chemical, NaOH (50% liquid soda) from Ashland Chemicals, and deionized water. Approximately 700 Litres of deionized water was placed in the storage tank of the system, and the required amount of sodium hydroxide solution was added. After thorough mixing of the solution, weighted amounts of potassium ferricyanide and ferrocyanide were added and the solution was mixed again. The nominal concentration of the electrolyte solution was:

1 mol/L NaOH

0.01 mol/L $K_3Fe(CN)_6$

0.01 mol/L $K_4Fe(CN)_6$

3.3.1.1 Titration of NaOH with HCl

A 25 mL sample was withdrawn and titrated with standard 1 mol/L hydrochloric acid according to the following equation, using phenolphthalein as an indicator (Jandau and Blasius, 1977):

$$NaOH + HCl \rightarrow NaCl + H_2O \qquad (3.4)$$

3.3.1.2 Titration of Potassium Ferricynide

The ferricynide was analyzed iodometrically using the procedures commonly described (Rosin, 1946, Kolthoff and Sandell, 1955). A 10 mL sample was acidified with concentrated 20 mL 1 M HCl and about 2 g potassium iodide (KI). The contents mixed and allowed to react for about 1 minute. A solution of 10mL 0.05 M zinc sulphate was added. Then the solution was titrated with standardized 0.01 M sodium thiosulfate, using starch as reaction indicator. The blue starch-iodine color was titrated to a colorless endpoint. The zinc serves to combine with the ferrocyanide as soon as the latter is formed. By the virtue of the insolubility of zinc ferrocyanide, the $Fe(CN)_6^{4-}$ is removed from reaction and the following reactions are completed. As it is common practice, at least three titrations were performed and the average volume was used to calculate the ferricyanide ion concentration.

$$2\ Fe(CN)_6^{3-} + 2\ I^- \rightarrow\ 2\ Fe(CN)_6^{4-} + I_2 \qquad (3.5)$$

$$I_2 + 2\ S_2O_3^{2-} \rightarrow\ S_4O_6^{2-} + 2\ I^- \qquad (3.6)$$

$$2\ Fe(CN)_6^{4-} + 2K^+ + Zn^{2+} \rightarrow\ K_2ZnFe(CN)_6 \qquad (3.7)$$

3.3.1.3 Titration of Potassium Ferrocynide

The ferrocyanide concentration was determined by using permanganometric (Rosin, 1946, Kolthoff and Snadell, 1955). A 25 mL sample was drawn and neutralized with concentrated 2 M sulfuric acid. After adding 10 mL of concentrated H_2SO_4, the well mixed solution was titrated with standardized 0.01 M potassium permanganate to a slight reddish color. The reaction equation for this titration process can be written as the following equation:

$$5\ K_4Fe(CN)_6 + KMnO_4 + 4\ H_2SO_4 \rightarrow\ 5\ K_3Fe(CN)_6 + MnSO_4 + 3\ K_2SO_4 + 4H_2O \qquad (3.8)$$

Again each titration was repeated at least 3 times and the average was taken to calculate the ferrocyanide concentration. After about 10 days with continuous experiments, a full set of analyses were carried out in order to determine the concentration of individual electrolyte components (NaOH, $K_3Fe(CN)_6$, and $K_4Fe(CN)_6$). Nitrogen gas was used to deoxygenate the solution in the system, thus maintaining the concentration of each component and preventing them from other reaction.

3.3.2 Electrode Preparation Procedure

Prior to each set of experiments, the working electrodes were prepared using a combination of several techniques. First the electrode surface was sanded with progressively finer grades of 600 and 1500 grit paper (Master Mechanic), followed by 45 and 9 μm Metadi diamond compound (Buehler), and finally polished with 1.0 μm γ-alumina micropolish (Buehler). Next the electrodes were rinsed with dilute H_2SO_4. Then each electrode was treated cathodically at 20 mA/cm^2 for 20 min. with 5% H_2SO_4 as an electrolyte. The test section was then installed into the system after rinsing with demineralized distilled water.

3.3.3 Preliminary Experiments in Electrochemical Cell

Figure 3.3 shows the 25 mL electrochemical cell. The working electrode, reference electrode, and auxiliary electrode are made of nickel. The cross-sectional area of working electrode is 0.072 cm^2. It was filled by 20 mL 2N NaOH and 0.01 M potassium ferro/ferricyanide solution. The nitrogen is bubbled through the solution beneath the working electrode from the nitrogen cylinder. The bubbling frequency of nitrogen is controlled by the regulator and needle valve. The magnetic bar is used in the oil test, and the speed is controlled by the speed switch. The cell is put on the Type 10100 stirring hot plate with speed range from 1 to 5; however, magnetic bar is not used in the case of bubble study in the cell.

3.4 Test Matrix

Table 3.1 shows the test matrix for the mass transfer measurements in electrochemical cell. Tables 3.2 and 3.3 shows the test matrix for the two types of mass transfer measurements in multiphase flows. Full pipe flow and slug flow experiments were conducted for the different LVT in situ oil percentage.

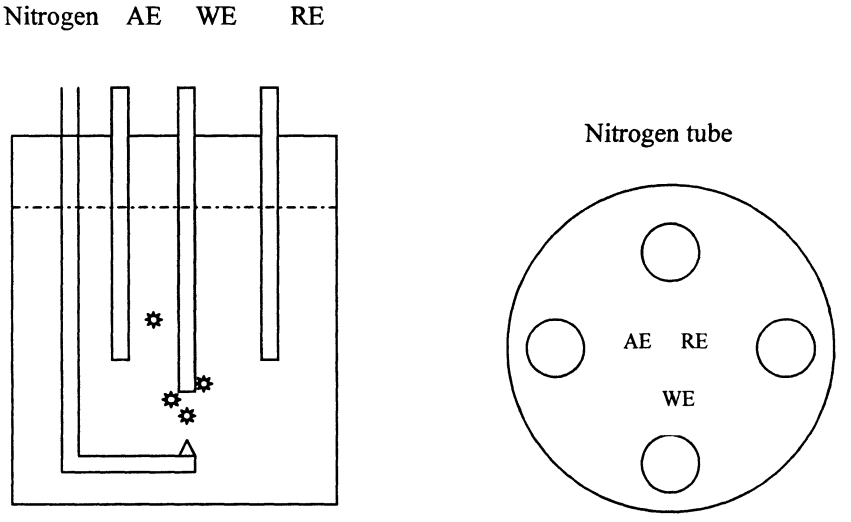

Figure 3.3 Schematic of electrochemical cell

Table 3.1 Test matrix for bubble study in electrochemical cell

Frequency of single bubble (hz)	0. 2, 0.03
Electrode	Nickel
Gas	Nitrogen
Solution	2 N NaOH, 0.01 M $K_4Fe(CN)_6$ and 0.01 M $K_3Fe(CN)_6$
Temperature (°C)	20

Table 3. 2 Experimental test matrix in slug flow with different oil percentages

Slug flow superficial gas velocity (m/s)	1.4, 2.4, 3.6, 4.8
Slug flow superficial liquid velocity (m/s)	1.5
Test section	Smooth section
Electrode	1, 2, 3, 4, 5
Gas	Nitrogen
Liquid	Potassium ferro/ferricyanide, sodium hydroxide and LVT oil
Temperature (C)	20
LVT oil cut in tank	0%, 25 %, 75%
Full pipe flow velocity (m/s)	0.7, 1.0, 1.5, 2.0

Table 3.3 Experimental test matrix in multiphase flow with 0%, 20%, and 40% input Oil

Superficial liquid velocity (m/s)	0.2, 0.5, 0.8, 1.0, 1.2, 1.5
Superficial gas velocity (m/s)	0, 0.4, 0.6, 0.8, 1.0, 1.4, 2.4, 3.0, 3.6, 4.8
Test section	Smooth section
Electrode	1, 2, 3, 4, 5
Gas	Nitrogen
Liquid	0.01 M potassium ferro/ferricyanide and 1.0 N sodium hydroxide, with 0%, 20% and 40% input LVT oil,
Temperature (°C)	20

CHAPTER 4

MASS TRANSFER EXPERIMENTAL RESULTS AND MODELING

4.1 Effect of Gas Bubble on Mass Transfer

Table 4.1.1 and Table 4.1.2 shows the experimental test matrix in electrochemical cell and stationary slug, respectively.

Table 4.1.1 Test matrix for bubble study in electrochemical cell

Frequency of single bubble (Hz)	0. 2, 0.03
Electrode	Nickel
Gas	Nitrogen
Solution	2 N NaOH, 0.01 M $K_4Fe(CN)_6$ and $K_3Fe(CN)_6$
Temperature (°C)	20

Table 4.1.2 Test matrix for bubble study in stationary slug flow

Liquid velocity (m/s)	0.55	0.70	0.85	1.0
Froude number	4	5	6	7
Electrode	Nickel			
Gas	Nitrogen			
Solution	2 N NaOH, 0.01 M $K_4Fe(CN)_6$ and $K_3Fe(CN)_6$			
Temperature (°C)	20			

4.1.1 Experimental Results in Electrochemical Cell

Figure 4.1.1 and 4.1.2 show the potentiostatic curve and Fast Fourier Transform (FFT) analysis results when the bubbling frequency is 0.2 Hz. Regular peaks at intervals of approximately 5 seconds can be seen in Figure 4.1.1. The results

are also summarized in Table 4.1.3. The potentiostatic curve quantitatively represents the transient limiting current density at an applied potential of 0.4 volts. It confirms the relationship between the oscillation and the physical bubble movement. The negative current corresponds to the cathodic current. The absolute maximum limiting current density $|I_{max}|$ is 4.50×10^{-4} (A/cm^2) corresponds to the condition at which a bubble just detaches from the working electrode. When a bubble attaches to the working electrode for about 5 seconds, the $Fe(CN)_6^{3-}$ ion in the interface film between the electrode and bubble is consumed very quickly, and thus the limiting current density decreases to the lowest value close to zero. When the gas bubble attaches to the surface of the working electrode, the limiting current decreases at different rates based on the duration of bubble attachment. The diffusion sphere of the electrode will relax back to the non-convective steady state after the bubble impact event is over, as shown in Figure 2.13. This relaxation of the diffusion sphere is analogous to a step at

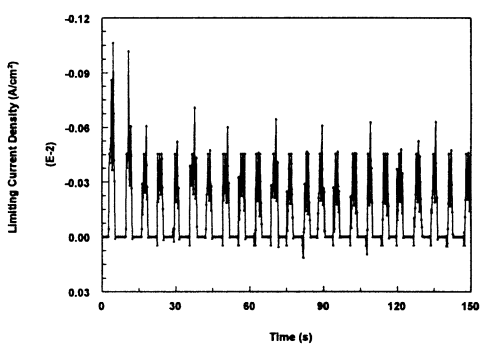

Figure 4.1.1 Instantaneous limiting current density for 0.2 Hz bubble in electrochemical cell

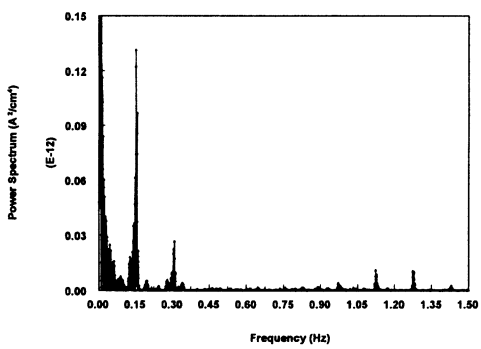

Figure 4.1.2 Power spectrum of the instantaneous limiting current density at 0.2 Hz bubble in the electrochemical cell

the same electrode from a potential insufficient to reduce the redox species to a potential sufficient to reduce the redox species at the mass transport limited condition. When the bubble detaches from the electrode again, the concentration of $Fe(CN)_6^{3-}$ ions is renewed, and the limiting current reaches the peak value.

Table 4.1.3 Comparison of bubble study in electrochemical cell

Frequency (Hz)	0.2	0.03
Chronoamperometry	Figure 4.1.1	Figure 4.1.3
FFT	Figure 4.1.2	Figure 4.1.4
$\lvert I_{max} \rvert$ (A/cm^2)	4.50e-4	8.25e-4
$\lvert I_{min} \rvert$ (A/cm^2)	0	0
FFT, f1 (Hz)	0.15	0.033
FFT, f2 (Hz)	0.3	0.073
FFT, f3 (Hz)	1.13	0.106

Through Fast Fourier Transform (FFT) analysis it can be seen from Figure 4.1.2 that the dominant frequency occurs at 0.15 Hz and is close to the 0.2 Hz bubbling frequency. The frequency f1 shown in Table 4.1.3 therefore represents the bubbling frequency, f2 and f3 are second and third harmonics, respectively.

The results for 0.03 Hz bubbling test are also shown in Table 4.1.3. Figure 4.1.3 and Figure 4.1.4 represent the results at 0.03 Hz bubbling in cell. It is seen that the dominant frequency of 0.033 Hz is close to the 0.03 Hz bubbling frequency. It is seen from Figure 4.1.3 that between the time interval of 30 to 60 second, four continuous peaks are seen. The peaks are associated with the phenomenon that the first four small gas bubbles attach to the working electrode and coalesce to a single and larger bubble on the surface of the working electrode. When the fifth bubble

further attaches to the big bubble, the large internal pressure thins the diffusion layer and the current decreases to the lowest value, close to zero, because of the complete consumption of $Fe(CN)_6^{3-}$ ions in the boundary layer. Until the ninth bubble attaches to the surface of the working electrode, the current stays very close to zero. When the ninth bubble attaches to the electrode, the whole bubble detaches from the electrode. The cycle of oscillation repeats itself.

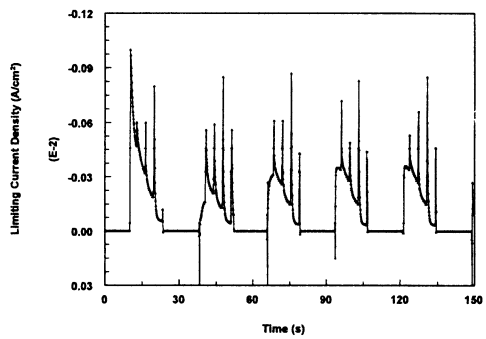

Figure 4.1.3 Instantaneous limiting current density for 0.03 Hz bubble in electrochemical cell

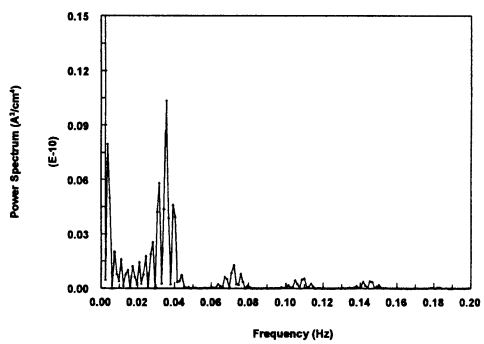

Figure 4.1.4 Power spectrum of the instantaneous limiting current density at 0.03 Hz bubble in the electrochemical cell

4.1.2 Experimental Results in Stationary Slug Flow

Figures 4.1.5, 4.1.6, 4.1.7, and 4.1.8 show the results of limiting current density measurements in stationary slug flow at Fr number 4, 5, 6, and 7, respectively. The sampling rate is 50Hz. Comparison of Figures 4.1.5, 4.1.6, 4.1.7, and 4.1.8 shows that the number of spikes and the magnitude all increase with the increase of Froude number which represents the turbulence of slug flow. For example, in Froude number 4 shown in Figure 4.1.5 only few of spikes exist and the peak value of limiting current density is 0.0095 A/cm^2. More spikes appear in slug flow with Froude number 5

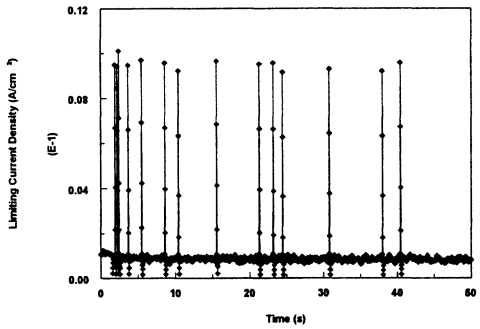

Figure 4.1.5 Instantaneous limiting current density in stationary slug with Froude 4

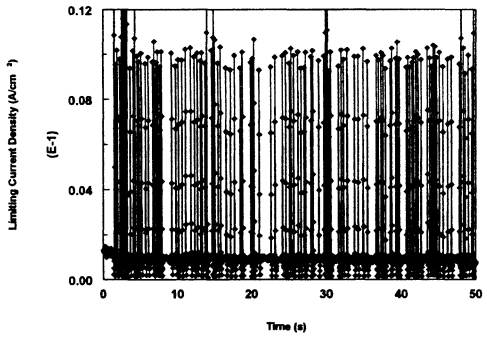

Figure 4.1.6 Instantaneous limiting current density in stationary slug with Froude 5

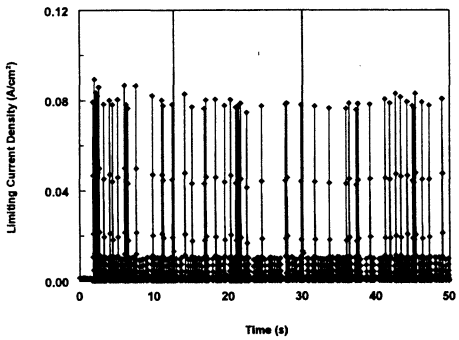

Figure 4.1.7 Instantaneous limiting current density in stationary slug with Froude 6

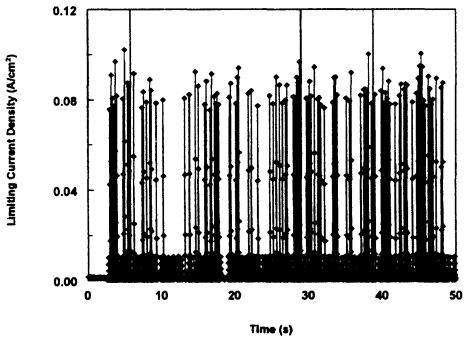

Figure 4.1.8 Instantaneous limiting current density in stationary slug with Froude 7

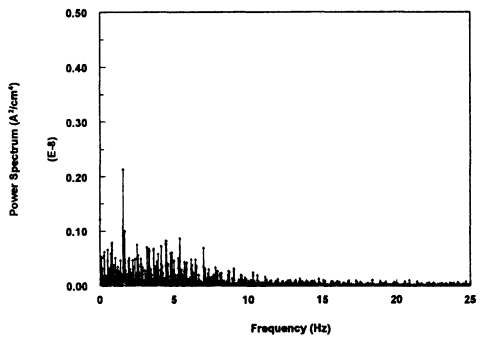

Figure 4.1.9 Power spectrum of the instantaneous limiting current density in stationary slug with Froude 4

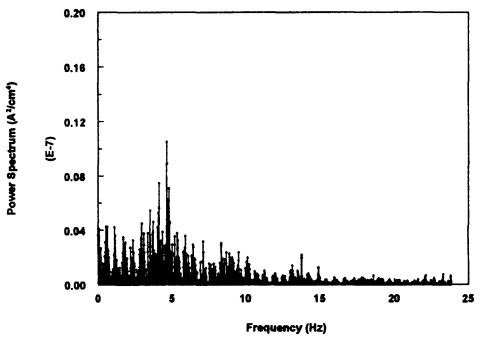

Figure 4.1.10 Power spectrum of the instantaneous limiting current density in stationary slug with Froude 5

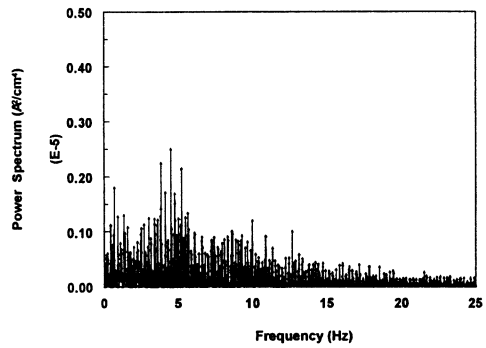

Figure 4.1.11 Power spectrum of the instantaneous limiting current density in stationary slug with Froude 6

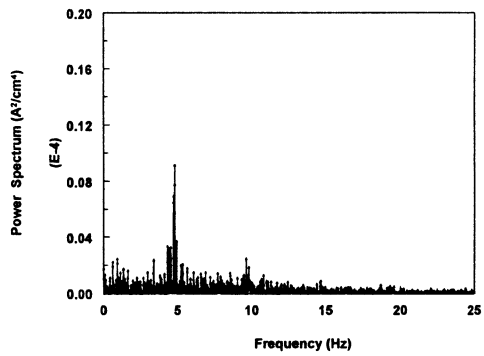

Figure 4.1.12 Power spectrum of the instantaneous limiting current density in stationary slug with Froude 7

shown in Figure 4.1.6. In Froude number 6 more spikes appear and the peak value has reached 0.08 A/cm^2, which is about 8.4 times enhancement compared to that at Froude number 4. Hence the different amount and magnitude of the limiting current density spikes could directly indicate the relation between physical phenomenon of bubble movement and mass transfer enhancement, considering the conclusion drawn from the experiments in electrochemical cell. In slug flow with a lower Froude fewer bubbles touch to bottom, whereas more and more can move toward and collapse on the bottom of the pipe in slug flow with a higher Froude.

Based on the present data acquisition method, these spikes never appear in full pipe flow where no bubbles exist. The fluctuation of limiting current density in full pipe flow would follow the base line in Figure 4.1.5. Hence, such large limiting current density spike becomes a footprint to detect the existence of bubbles collapsing on the bottom of a pipe in multiphase flow, e.g. slug flow and bubbly flow.

Figures 4.1.9, 4.1.10, 4.1.11, and 4.1.12 show the power spectrum of the instantaneous limiting current density as a function of frequency. It can also be seen that the amplitude gradually increases with the increase of Froude number.

The amplitude of peak value represents the energy level of bubbles in stationary slug flow. It can be assumed that three kinds of bubbles exist. Above some high energy level, the bubbles can collapse on the bottom surface of a pipe, and completely destroy the mass transfer boundary layer. Immediately after this event, the electrode experiences a surge in electrolyte concentration approaching bulk concentration, which greatly increases the mass transfer rate. This process is related with microjetting, which occurs when a bubble collapses asymmetrically next to a solid/liquid interface. At the intermediate energy level of bubbles, the gas bubbles can enter the mass transfer boundary layer, but does not collapse on the wall because of a lower energy. This process could be related with microstreaming, which occurs close to forced oscillating bubbles or some other vibrating bodies, e.g. a small oil droplet. At a lower energy level, the gas bubble cannot enter the mass transfer boundary layer and its direct influence on mass transfer is negligible. However, it can produce turbulence and further influence the pressure gradient and wall shear stress. In the slug flow with different Froude numbers, these three kinds of bubbles can co-exist. In addition, the distribution of these bubbles is closely related to the change of Froude number.

It has been found in the pressure drop measurement in slug flow that the dominant frequency occurs at about 5 Hz (Maley, 1997). This dominant frequency is associated with the frequency of pulses of bubbles in the mixing zone of slug flow.

The dominant frequency of 5 Hz is apparent in Figure 4.1.9, 4.1.10, 4.1.11, and 4.1.12. In this manner the mass transfer study provides a tool to detect the bubble hydrodynamics in multiphase flow.

The effect of the viscosity of oil on corrosion in three-phase flow has been studied previously (Jepson and Menezes, 1995). Oils with 2 cp and 96 cp have been used in experiments. The water cut ranged from 0 to 100 %. It was found that the oil with a lower viscosity entrains more gas in the slug than the oil with a higher viscosity. The pressure drop across the slug is larger for the higher viscosity oil. It was also found that the corrosion rate in 96 cp oil/water mixture is higher than in 2 cp oil/water mixture in slug flow. In the study of cavitation pitting and erosion of aluminum 6061-T6 in mineral oil and water, it was found that the cavitation effect is stronger in a higher viscosity liquid (Rao and Buckley, 1983). Hence, it is concluded that higher liquid viscosity and higher cavitation increase the corrosion rate. Thus it is derived that a cavitation type phenomenon probably exists in slug flow. Furthermore, the bubble effect on mass transfer in slug flow could also be confirmed again by above phenomena, considering the known mechanism of bubble effect on mass transfer by ultrasound and cavitation (Ben Youssef et al. 1994, Birkin and Silva-Martinez, 1995, 1996, 1997).

4.1.3 Experimental Results in Full Pipe Flow and Slug Flow

Figures 4.1.13, 4.1.14, and 4.1.15 are selected to show the instantaneous mass transfer coefficient in full pipe flow and slug flow. Figure 4.1.13 obtained in full pipe

flow without bubbles is a blank test to confirm the bubbles' contribution to the mass transfer spikes in Figures 4.1.14 and 4.1.15 obtained in slug flow, Figures 4.1.5, 4.1.6, 4.1.7, and 4.1.8 for stationary slug flow. With the increase of Froude number, the mass transfer spikes increase in amount and amplitude significantly.

These corresponding FFT results are also available in Figure 4.1.16, 4.1.17, and 4.1.18. The dominant frequency is close to 5 Hz. It was also found that the dominant frequency of pulses of bubbles in a vertical slug flow equals the dominant frequency of the instantaneous pressure (Fabre et al. 1992, Mercier-Bonin et al. 2000).

4.1.4 Mechanism of Mass Transfer Oscillation by Gas Bubble

Several recent studies have addressed the effects of ultrasound induced bubbles and bubble sparging on mass transfer (Ben Youssef et al. 1994, Birkin and Silva-Martinez, 1995, 1996, 1997). In those studies it was found that the collapsing bubbles renewed the surface concentration, which was not zero during the period of bubble formation and collapse. In addition it was shown that microjets or forced convection produced when cavitation bubbles impinge on, or near, the electrode will increase the mass transport of electrolyte to the electrode. Table 4.1.4 compares the basic nature of bubble movement in the cell and slug flow. In the cell a bubble slowly collapses on the surface of the electrode. However, bubbles could quickly collapse in either stationary

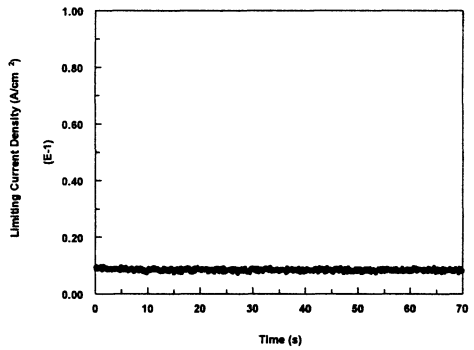

Figure 4.1.13 Instantaneous mass transfer coefficient in full pipe flow with Vsl=1.5 m/s and Vsg=0 m/s

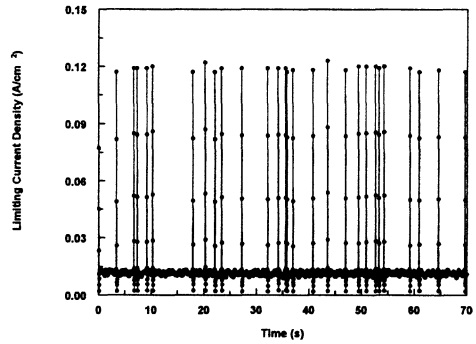

Figure 4.1.14 Instantaneous mass transfer coefficient in slug flow with Vsl=1.5 m/s and Vsg=1.4 m/s

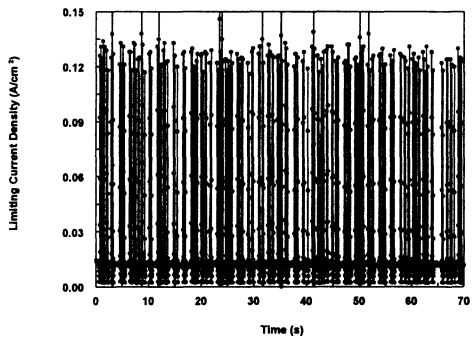

Figure 4.1.15 Instantaneous mass transfer coefficient in slug flow with Vsl=1.5 m/s and Vsg=4.8 m/s

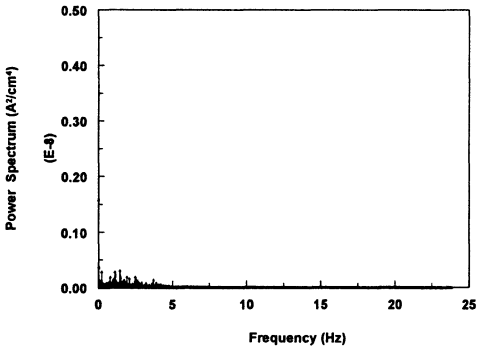

Figure 4.1.16 Power spectrum of the instantaneous limiting current density in full pipe flow with Vsl=1.5 m/s

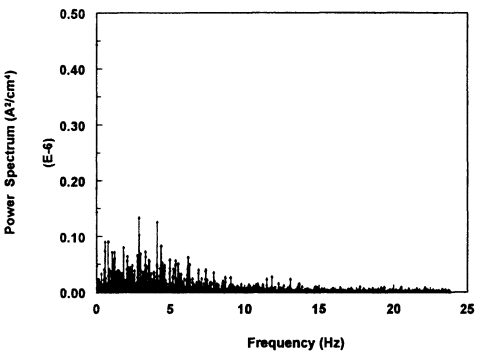

Figure 4.1.17 Power spectrum of the instantaneous limiting current density at slug flow with Vsl=1.5 m/s and Vsg=1.4 m/s

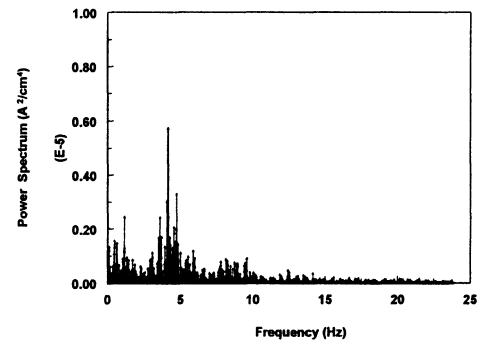

Figure 4.1.18 Power spectrum of the instantaneous limiting current density at slug flow with Vsl=1.5 m/s and Vsg=4.8 m/s

slug flow or moving slug flow. Because of the short duration of collapse in slug flow, the current can hardly decrease to a very low value. The microjet and microstreaming effects are considered to be effective in slug flow and contribute to the mass transfer enhancement.

Table 4.1.4 Comparison of the bubble characteristics in cell and slug flow

	Energy	Physical phenomena	Mechanism
Cell	low	block the surface of electrode (there is still liquid at the interface between bubble and electrode surface, however the redox reaction is quickly finished and the current decreases to zero because of long duration of bubble), renew the solution around the electrode surface after bubbles move away.	slow collapse
Slug flow	a distribution of bubbles with three energy levels	quick collapse on the surface of electrode (there are still liquid at the interface of bubble and electrode surface, however the redox material can not be consumed because of short duration of collapse and the current can hardly decrease to very low value close to zero), renew the solution around the electrode surface after bubbles move away.	i) microjet resulting from bubble collapse. ii) micro-streaming

The previously mentioned relaxation mechanism of the diffusion sphere in the electrochemical cell as shown in Figure 2.15 could also be used to explain the mass transfer enhancement mechanism in stationary slug flow and moving slug flow.

Similar current spikes (or oscillatory phenomena) to those observed in Figures 4.1.5, 4.1.6, 4.1.7, 4.1.8, 4.1.14, and 4.1.15 in the oxidation of $Fe(CN)_6^{4-}$ ions have been observed by Li *et al.* (1997). However, their experiments were performed in quiescent solutions. They considered that oscillations would disappear with agitation. In the present full pipe flow under higher turbulence, the low level of fluctuation of current oscillations exists and can only be attributed to the fluctuation of turbulent flow itself in water flow and possibly the influence of a surface film on the electrode

(Figure 4.1.13). Li et al. considered that the oscillations are attributed to the occurrence of bistability, *i.e.* $Fe(CN)_6^{4-}$ oxidation and oxygen production at different potentials, coupled with convective feedback induced by oxygen evolution. This bistability theory considered that it is the overlap of the positive and negative feedbacks between the bistable states ($Fe(CN)_6^{4-}$ oxidation and oxygen production) that accounts for the oscillations. It had been described through a circuit model in Figure 4.1.19. The positive feedback emphasizes the determination of oxygen evolution to raise the limiting current to the level of the peaks under the initial high voltage. This is because the growth, detachment, and movement of oxygen bubbles produce a forced convection, which replenishes the surface concentration of the anions. However, the oscillation found in a water/gas system does not include the influence of oxygen evolution because no oxygen was produced under the voltage corresponding to the limiting current. Therefore, the high frequency and high magnitude current oscillations encountered in water/gas flow (Figures 4.1.5, 4.1.6, 4.1.7, 4.1.8, 4.1.14, and 4.1.15) are attributed to the entrained gas bubbles and cannot be explained directly by this bistability theory (Wang et al. 1999, 2000a).

A new qualitative explanation may be given, as follows, after considering the influence of entrained gas bubbles and revising Li's bistability theory. When a constant voltage (V) is imposed in the circuit in Figure 4.1.19, it is divided into two parts: one part, $I \times (R_e + R_s)$, where I is the circuit current, R_e is the external series resistance and R_s is the solution resistance, and the other part is E, the potential of the cell. At the beginning of the imposition of the potential, E will drive the current over

the limiting value of the $Fe(CN)_6^{4-}$ anions in a stationary state, so the surface concentration of the anions is depleted and maintained at zero because this potentiostatic experiment is carried out at the selected voltage E_A. The movement of gas bubbles produces a forced convection, which replenishes the surface concentration of the $Fe(CN)_6^{4-}$ anions and raises the limiting current plateau over the stationary one to the spiked level. This may be called a positive feedback because it increases the current. In the meanwhile, a negative feedback comes from two aspects: one is the depletion of the surface concentration of the $Fe(CN)_6^{4-}$ anions by oxidation; and the other is a decrease in E because of an increase in I (remembering that V = 0.25 volts = $I \times (R_e + R_s) + E$). This reduces the current to the minimum until the bubble influences it again. It is believed that the combination of positive feedback and negative feedback accounts for the oscillation of the instantaneous limiting current.

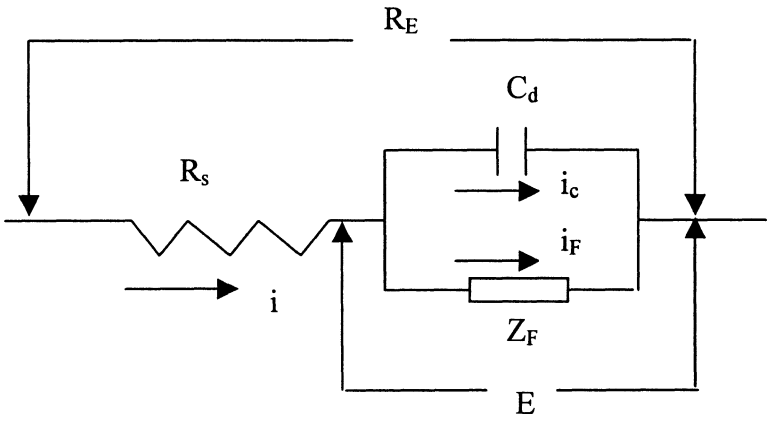

Figure 4.1.19 Schematic of circuit for mass transfer enhancement mechanism by gas bubble or oil droplet

4.2 Effect of Oil Phase on Mass Transfer

4.2.1 Average Mass Transfer Coefficient

Mass transfer experiments were conducted in full pipe and slug flow with different oil percentages. Table 4.2.1 and Table 4.2.2 shows the experimental test matrix for full pipe flow and slug flow, respectively. Data were obtained using Gamry CMS 105 electrochemical software package. Anodic limiting current density was determined using potentiodynamic measurements. All experiments were performed at 20° C. The potentiodynamic test was conducted through the range from 0 to 480 mV with the sweep rate of 4 mV/s. Figure 4.2.1 shows the potentiodynamic sweep in full pipe flow at liquid velocity of 1 m/s.

Table 4.2.1 Experimental test matrix for full pipe flow

Liquid velocity (m/s)	0.7,	1.0,	1.5,	2.0
Electrode	1, 2, 3, 4, 5			
Oil percentage in tank (v./v.)	0%,	25%,		75%

Table 4.2.2 Experimental test matrix for slug flow

Superficial gas velocity (m/s)	1.4,	2.4,	3.6,	4.8
Superficial liquid velocity (m/s)	1.5			
Electrode	1, 2, 3, 4, 5			
Oil percentage in tank (v./v.)	0%,	25%,		75%

4.2.1.1 Water and Water/Oil Full Pipe Flow

Figure 4.2.2 shows the local mass transfer coefficient at five electrodes at different velocities in single-phase flow. The five mass transfer coefficients show negligible difference. The error in mass transfer measurement is about 3.3%. Figure

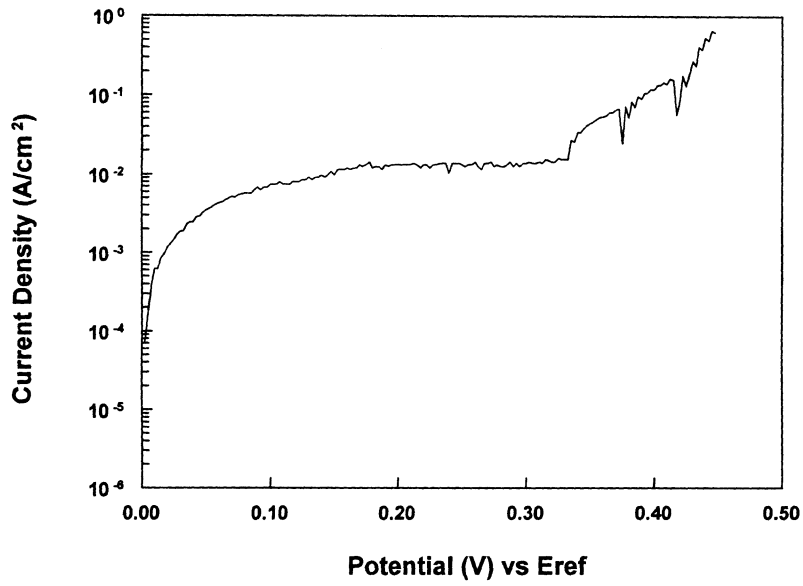

Figure 4.2.1 Limiting current density at liquid velocity of 1 m/s in full pipe flow without oil

4.2.3 shows the local mass transfer coefficient of five electrodes at different velocities in full pipe flow with 75% oil. The corresponding mass transfer measurement error is about 7.4%. In addition, there is approximately 3.9% measurement error in full pipe flow with 25% oil.

The average mass transfer coefficients in single-phase flow are obtained as 1.09×10^{-4}, 1.25×10^{-4}, 1.63×10^{-4}, 1.84×10^{-4} m/s at 0.7, 1.0, 1.5, and 2.0 m/s liquid velocity, respectively, from these local mass transfer coefficients. The average mass transfer coefficients in 25% and 75% oil full pipe flow can be calculated similarly. All average mass transfer coefficients are shown in Figure 4.2.4 and Table 4.2.3. The average mass transfer coefficient increases with increase in liquid velocity. For example, with 25% oil in the tank, the mass transfer coefficient are 1.01×10^{-4}, 1.10×10^{-4}, 1.45×10^{-4} to 1.79×10^{-4} m/s, respectively at a liquid velocity of 0.7, 1.0, 1.5 and

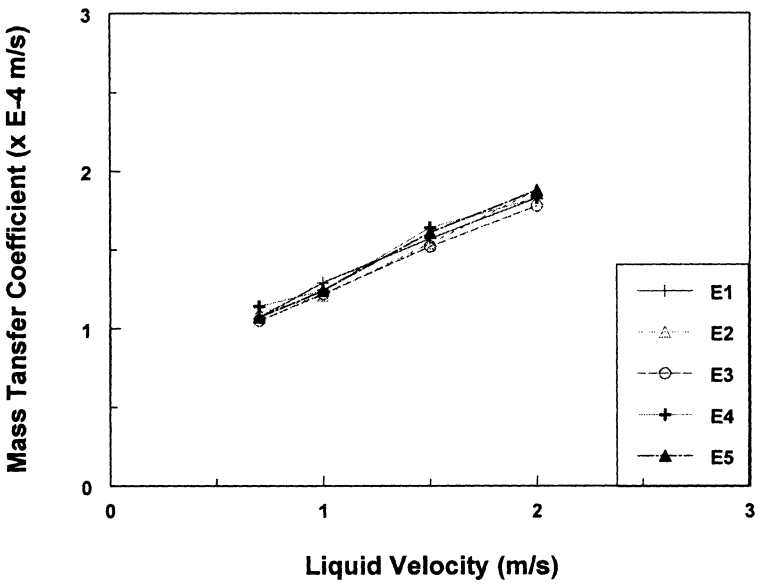

Figure 4.2.2 Local mass transfer coefficient of five electrodes vs liquid velocity in full pipe flow without oil

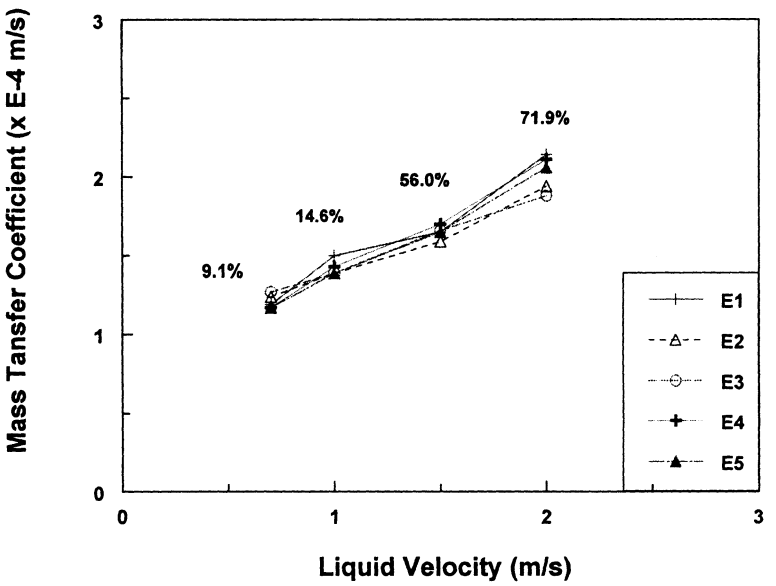

Figure 4.2.3 Local mass transfer coefficient of five electrodes vs liquid velocity in full pipe flow with 75% oil

Table 4.2.3 Average mass transfer coefficients in full pipe flow

Mass transfer coefficient (m/s)		Liquid velocity (m/s)			
		0.7	1.0	1.5	2.0
Oil percentage in tank (%)	0	1.09 (0%*)	1.25 (0%)	1.63 (0%)	1.84 (0%)
	25	1.01 (1.8%)	1.10 (3.9%)	1.45 (16.5%)	1.79 (22.0%)
	75	0.84 (9.1%)	0.99 (14.6%)	1.09 (56.0%)	1.41 (71.9%)

*: *in-situ* oil percentage.

2.0 m/s. These data correspond to an *in situ* oil percentage at the bottom of pipe of 1.8%, 3.9%, 16.5%, and 22.0 %, respectively.

In situ oil percentage was calculated by the volume of water/oil mixture sampled from a valve at the bottom of the pipeline. A Pyrex® cylinder with 100 ml volume was used to sample the water/oil mixture. The in situ oil percentage was calculated after the oil and water volumes were measured. The measurement error of in situ oil percentage is about 2%, corresponding to the accuracy of cylinder. In situ oil percentages at the bottom of the pipe below 1 m/s (e.g. 1.8% and 3.9%) are negligible compared to that at 1.5 m/s and higher (e.g. 16.5% and 22.0%). Similar trends are seen for 75% oil in the tank. The results confirm the studies of Shi et al. (1999) in which it was shown that below 1 m/s, oil and water flow in stratified layers with little mixing. Above 1.5 m/s, there is considerable mixing of oil and water.

The relation between mass transfer coefficient and in situ oil percentage derived from Figure 4.2.4 is shown in Figure 4.2.5. Comparison of mass transfer coefficient under different in situ oil percentages at same velocity in Figure 4.2.5

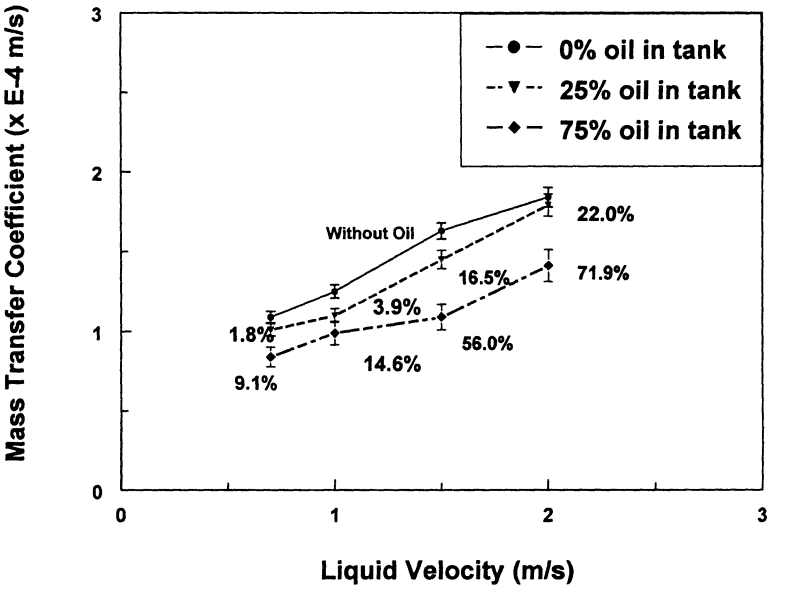

Figure 4.2.4 Average mass transfer coefficient of five electrodes vs liquid velocity in full pipe flow with different in situ oil percentage

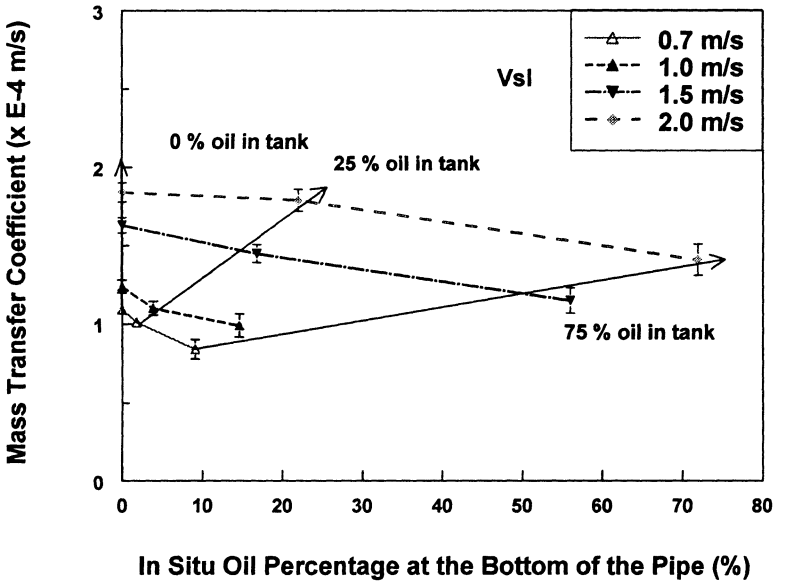

Figure 4.2.5 Average mass transfer coefficient vs in situ oil percentage in full pipe flow

shows that mass transfer coefficient decreases with increase of in situ oil percentage. At 1.5 m/s liquid velocity the mass transfer coefficient decreases from 1.63×10^{-4} to 1.45×10^{-4} and then to 1.09×10^{-4} m/s as in situ oil percentage increases from 0 to 16.5% and then to 56.0%. At 2.0 m/s liquid velocity the mass transfer coefficient does not decrease significantly for an increase in in situ oil percentage from 0 to 22.0%. Only a slight change from 1.84×10^{-4} m/s to 1.79×10^{-4} m/s is observed. The mass transfer coefficient, however, decreases significantly at a higher in situ oil percentage. For example, at 71.9% in situ oil percentage the mass transfer coefficient is 1.41×10^{-4} m/s, which amounts to a 21.2% drop from the value at in situ oil percentage of 22.0%. This is due to the increase in oil phase, which decreases ionic mass transfer coefficient. At 1.5 m/s, 1.0 m/s, and 0.7 m/s the corresponding reductions are 24.8%, 10.0%, and 16.8%, respectively when the oil percentage in the tank increases from 25% to 75%.

Furthermore, it is found that at a higher liquid velocity (e.g. 1.5 m/s and 2.0 m/s) there is a large decrease of average mass transfer coefficient when oil percentage in the tank increases from 25 % to 75% while there is only a small decrease when it increases from 0% to 25%. At low liquid velocity (e.g. 0.7 m/s and 1.0 m/s) there is always a small decrease of average mass transfer coefficient when oil percentage in the tank increases from 0% to 25% and then to 75% as shown in Figure 4.2.4 and Figure 4.2.5. This result indicates that a phase inversion resulting in a change in the continuous phase from water to oil occurs at a higher velocity ($\geq$ 1.5 m/s) when oil percentage in the tank increases from 25% to 75%. At a lower liquid velocity the flow

is semi-mixed. With an increase in oil percentage, there is more oil reaching the bottom resulting in lower values for mass transfer coefficient.

The difference of mass transfer coefficient between oil-in-water and water-in-oil is not significant in full pipe flow because of two possible physical reasons: conductivity and viscosity effect. The viscosity of oil (3 cp) in the experiment is close to the viscosity of water (1 cp) at 25 °C. In the production of oil and gas, the crude oil usually has much high viscosity, e.g. 10-10000 cp (Speight, 1999). Then there will be probably a larger decrease of mass transfer coefficient when phase changes from oil-in-water to water-in-oil flow in full pipe flow, thus leading to a large decrease of corrosion rate of carbon steel pipeline.

4.2.1.2 Water/Gas and Water/Gas/Oil Slug Flow

The average mass transfer coefficient is calculated from local mass transfer coefficients obtained from five electrodes. There is approximately 5.0% measurement error for the average mass transfer coefficient in slug flow with and without oil. The average mass transfer coefficients under slug flow at various oil percentages are shown in Figure 4.2.6 and Table 4.2.4. It shows that mass transfer coefficient increases with increase in superficial gas velocity. Also, with an increase in the oil percentage in the tank from 0% to 25% and then to 75%, the mass transfer coefficients decrease at the same superficial gas velocity. Figure 4.2.6 indicates that gas causes more uniform mixing of water and oil compared to full pipe water/oil flow. At 75%

input oil percentage the in situ oil percentage at the bottom changes from 63.3% to 70.6% when the superficial gas velocity is increased from 1.4 m/s to 4.8 m/s.

Figure 4.2.7 shows the effect of in situ oil percentage at the bottom of pipe on average mass transfer coefficient in slug flow. The mass transfer coefficient increases with increase in superficial gas velocity at constant in situ oil percentage. The superficial gas velocity has a smaller effect on mass transfer at low oil percentage than at high oil percentage. For instance, the average mass transfer coefficient in slug flow in the absence of oil at superficial gas velocities of 1.4, 2.4, 3.6, and 4.8 m/s are 2.04×10^{-4}, 2.14×10^{-4}, 2.24×10^{-4}, and 2.30×10^{-4} m/s, respectively. The largest value 2.30×10^{-4} m/s is 1.13 times the lowest value 2.04×10^{-4} m/s. However, at 75% oil percentage condition the largest value 1.99×10^{-4} at 4.8 m/s superficial gas velocity is 1.21 times of lowest value 1.64×10^{-4} at 1.4 m/s superficial gas velocity. This trend is clear when the left and right sides of curves in Figure 4.2.7 are compared. The average mass transfer coefficient decreases with increase in in situ oil percentage. At 3.6 m/s superficial gas velocity the mass transfer coefficient decreases gradually from 2.24×10^{-4} m/s to 1.74×10^{-4} m/s while in situ percentage increases from 0 to 68.7%. Similar trends are observed at other superficial gas velocities.

Slug characteristics such as slug length, velocity, frequency, void fraction, and pressure drop are very important parameters in investigating the mass transfer features in slug flow (Gopal and Jepson, 1998 a, b). The initial study of instantaneous mass transfer coefficient has shown 10-1000 times enhancement of instantaneous mass transfer coefficient, which is caused by the gas bubble collapse at the bottom of pipe

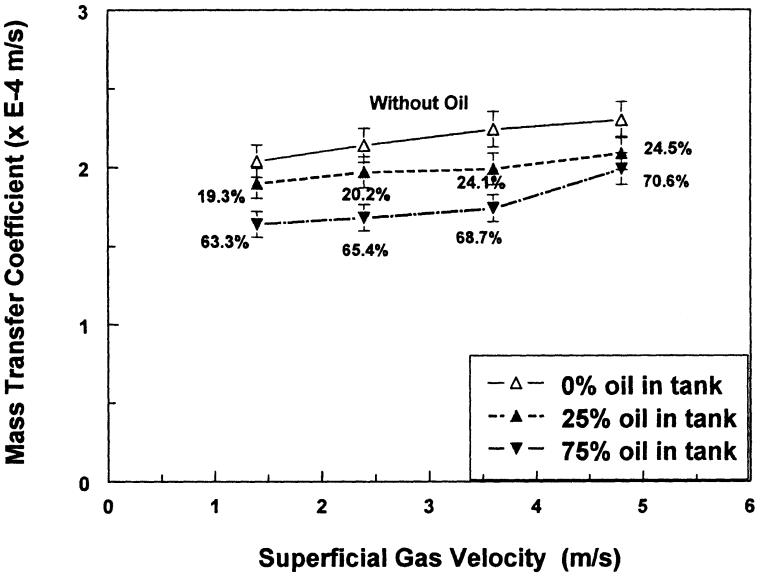

Figure 4.2.6 Average mass transfer coefficient vs superficial gas velocity in slug flow with different in situ oil percentage

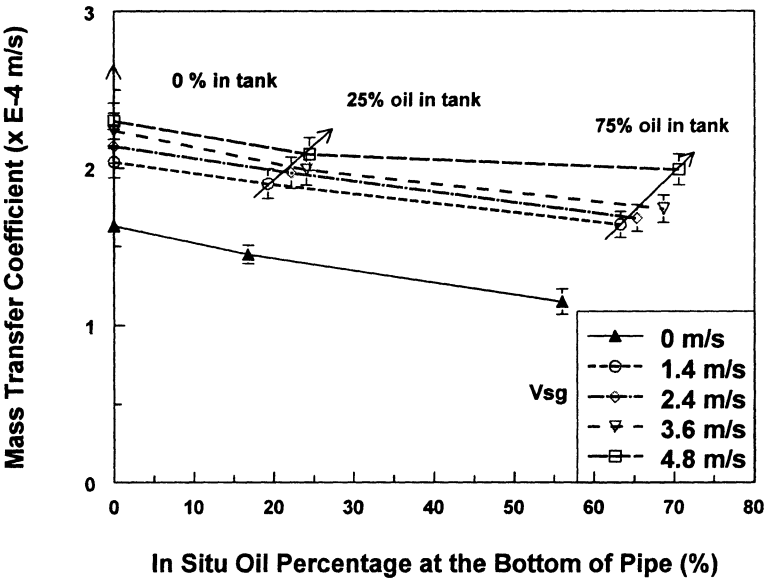

Figure 4.2.7 Comparison of average mass transfer in slug flow and full pipe flow at 1.5 m/s liquid velocity

Table 4.2.4 Average mass transfer coefficients in slug flow (Vsl=1.5 m/s)

Mass transfer coefficient (m/s)		Superficial gas velocity (m/s)			
		1.4	2.4	3.6	4.8
Oil percentage in tank (%)	0	2.04 (0%*)	2.14 (0%)	2.24 (0%)	2.30 (0%)
	25	1.90 (19.3%)	1.97 (20.2%)	1.99 (24.1%)	2.09 (24.5%)
	75	1.64 (63.3%)	1.68 (65.4%)	1.74 (68.7%)	1.99 (70.6%)

*: *in-situ* oil percentage.

wall (Wang et al. 1999). It has been found that the instantaneous mass transfer coefficient in each slug zone, e.g. slug mixing zone, slug body, slug tail, and slug film are different. This section only addresses the average mass transfer in slug flow at 1.5 m/s superficial liquid velocity. The mass transfer study in slug flow at other superficial liquid velocities will be reported later. The relationships among average mass transfer coefficient, instantaneous mass transfer coefficient, and slug flow parameters will be studied further.

4.2.1.3 Comparison between Full Pipe Flow and Slug Flow

The mass transfer coefficient at 1.5 m/s full pipe flow is compared with the results in slug flow where the superficial liquid velocity is set at 1.5 m/s. It is known that the in situ liquid velocity in slug flow is usually higher than 1.5 m/s because of the presence of gas. This analysis aims to give a qualitative comparison of mass transfers in full pipe flow and slug flow. Figure 4.2.7 already shows the difference of mass transfer coefficient in full pipe flow and slug flow. The mass transfer coefficient at 1.5

m/s full pipe flow without oil is 1.63×10^{-4} m/s. The mass transfer coefficients in slug flow without oil at superficial gas velocities of 1.4, 2.4, 3.6, and 4.8 m/s are 2.04×10^{-4}, 2.14×10^{-4}, 2.24×10^{-4}, and 2.30×10^{-4} m/s, respectively. Therefore slug flow enhances the average mass transfer coefficient by 25.3%, 31.8%, 37.8%, and 41.6%, respectively.

When in situ oil percentage increases, the enhancement factors will increase appreciably. As shown in Figure 4.2.7, the mass transfer coefficient is 1.19×10^{-4} at 50% in situ oil percentage in 1.5 m/s full pipe flow. The mass transfer coefficients in slug flow at the different superficial gas velocities of 1.4, 2.4, 3.6, and 4.8 m/s are 1.71×10^{-4}, 1.79×10^{-4}, 1.83×10^{-4}, and 2.02×10^{-4} m/s, respectively. Thus the mass transfer enhancement factors in slug flow are 43.2%, 49.7%, 53.2%, and 69.6%, respectively compared to the mass transfer coefficient in 1.5 m/s full pipe flow. This indicates that the enhancement factors have increased with the addition of oil. The increase of in situ oil percentage results in a lower increase in turbulence intensity in full pipe flow than in slug flow, where mixing of gas and liquid significantly increases the turbulence. Thus there is a higher enhancement of mass transfer in slug flow compared to full pipe flow with the addition of oil.

In a summary, experiments showed that the average mass transfer coefficient increases with increasing liquid velocity in full pipe flow. The average mass transfer coefficient will decrease with increasing in situ oil percentage, e.g. the mass transfer coefficient decreases 21.2% at 2.0 m/s liquid velocity when in situ oil percentage

increases from 22.0% to 71.9%. This is due to the increase in oil phase, which decreases the ionic mass transfer coefficient.

In slug flow, a similar conclusion is obtained that the average mass transfer coefficient increases with the increase of superficial gas velocity because of enhancement of turbulence. Superficial gas velocity has a higher enhancement effect on mass transfer at high oil percentage than at low oil percentage. At the same gas velocities, increasing the in situ oil percentage results in the decreasing of the mass transfer coefficient. This decrease of average mass transfer coefficient in slug flow is considerably less than in full pipe flow because gas causes more uniform mixing of the water and oil phases in slug flow.

The mass transfer coefficient in slug flow is higher than in full pipe flow because gas intensifies turbulence and mixing of the water and oil phases. With increasing in situ oil percentage, the mass transfer coefficient in full pipe flow shows a larger drop than in slug flow. Therefore, the difference between mass transfer in full pipe flow and slug flow is further increased.

In this study the mass transfer coefficient clearly shows the existence of phase inversion when the oil percentage increases from 25% to 75% at higher liquid velocity (1.5 m/s and 2.0 m/s) in full pipe flow.

4.2.2 Instantaneous Mass Transfer Coefficient in Water/Oil Flow

Since the $Fe(CN)_6^{4-}$ was not soluble in LVT 200 oil, its concentration was not corrected for the volume fraction of the oil when calculating the mass transfer

coefficient. According to the results obtained by Shi et al. (1999) in water/oil flows in large diameter horizontal pipelines, the emulsion of water/oil does not exist at low velocities less than 2.6 m/s. Therefore, it can be considered that, in case of this work, there should be no emulsion at the velocity of 1 m/s.

Figure 4.2.8 shows the polarization curves obtained from potentiodynamic measurements in water flow and water/oil two-phase flow. Limiting current densities were observed on the two curves after 0.25 V (point A). The values are nearly equal at 1.10×10^{-2} A/cm^2. According to Equation 2.31, the mass transfer coefficient is 6.30×10^{-5} m/s.

Kanwar and Jepson (1994) observed that the corrosion rate unexpectedly increases with the increment of oil from 0% to 60% (v./v.) at low velocities. However, the mechanistic reason was not explained completely. In general, fluid velocity has two effects on corrosion, the mass transfer effect and the surface shear stress effect (Heitz, 1991, Poulson, 1993).

The experimental results from Figure 4.2.8 show that the measured time-averaged mass transfer coefficient is nearly the same in water and water/oil. Zhang et al. (1997) showed that the CO_2 corrosion rate is mass transfer controlled in low velocities ranging from 0 to 3 m/s through experimental studies. It is unlikely that the mass transfer coefficients are the same between water and water/oil flows because the corrosion rates are different in these two kinds of fluids. Thus, the difference in the instantaneous mass transfer coefficient in water and water/oil can be considered as a main reason for the different corrosion rates. In this work, the instantaneous limiting

current density was measured to determine the instantaneous mass transfer coefficient. The potential in the middle of the limiting current plateau (E_A = 0.25 V), as shown in Figure 4.2.8, was selected for making the potentiostatic measurements to record the instantaneous limiting current density shown in Figures 4.2.9 and 4.2.10 for water and water/oil flows, respectively. Under these conditions the surface concentration is expected to be close to zero. The responses in Figure 4.2.8 show that the limiting current density has some small fluctuations, which have been amplified in the potentiostatic experiments shown in Figure 4.2.9a and 4.2.10a. The response between limiting current density and time in water flow in Figure 4.2.9a shows a relatively flat baseline, although there is a low level of fluctuation. These fluctuations may have resulted from a surface oxidation film on the electrode. However, large current spikes.

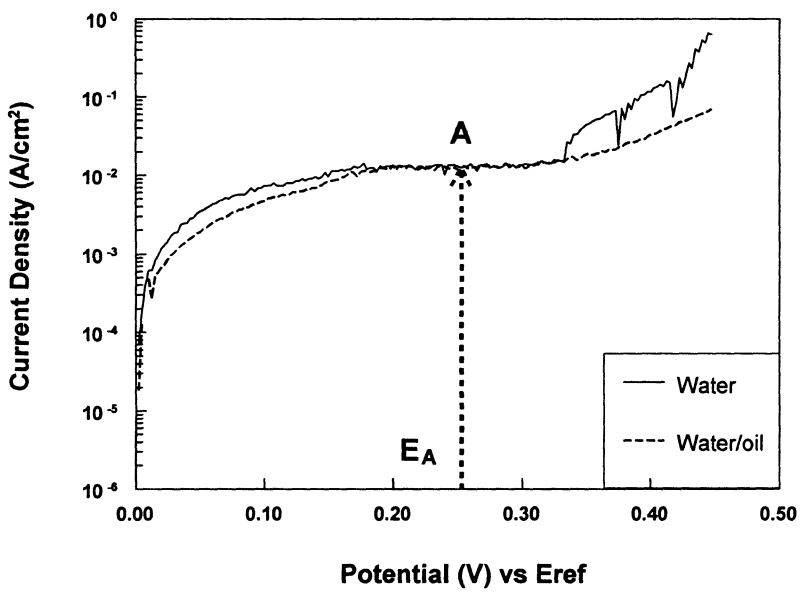

Figure 4.2.8 Limiting current density in water and water/oil flow at velocity 1 m/s. Point A is in the middle of the limiting current plateau. E_A (0.25V) is the applied potential in the potentiostatic experiments

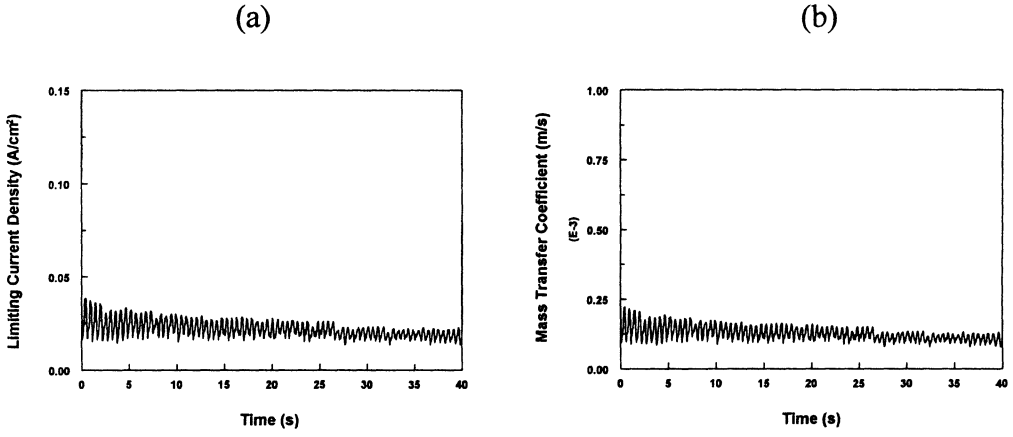

Figure 4.2.9 Instantaneous limiting current density (a) and instantaneous mass transfer coefficient (b) in water flow at velocity 1 m/s

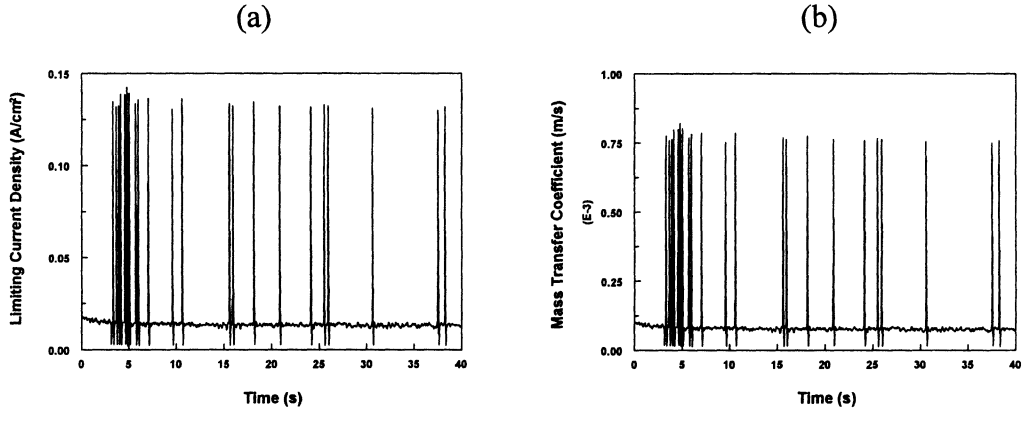

Figure 4.2.10 Instantaneous limiting current density (a) and instantaneous mass transfer coefficient (b) in water/oil flow at velocity 1 m/s

in water/oil flow are observed as shown in Figure 4.2.10a. If it is assumed that these spikes are only a short fraction of the whole time period tested, then it can still be considered that the zero surface concentration is valid

Based on Equation 2.31, the instantaneous mass transfer coefficient can be obtained, and the results for water and water/oil phases are shown in Figure 4.2.9b and 4.2.10b, respectively. The average value of the instantaneous mass transfer coefficient

in water flow is 1.10×10^{-4} m/s. The average value of the instantaneous mass transfer coefficient at the spikes in water/oil flow is 7.65×10^{-4} m/s and the average value of the baseline instantaneous mass transfer coefficient in water/oil flow is 8.06×10^{-5} as shown in Figure 4.2.10b. Adding oil to water flow enhanced the instantaneous mass transfer coefficient about 7 times. Kanwar and Jepson (1994) had considered that shear forces and the effects of turbulence contribute to enhanced corrosion rates under water/oil flow. The former includes a scouring type of corrosion while the latter can account for the increase in mass transfer rate to and from the pipeline wall. They concluded that the effect of each component could not be distinguished at that time. Therefore, the high frequency and high magnitude instantaneous mass transfer coefficient found in the present study may answer this question and may result in the enhancement of the corrosion rate in water/oil flow (Wang et al. 2000b).

4.2.3 Mechanism of Mass Transfer Oscillation by Oil Droplets

Through the comparison, the impingement of an occasional oil droplet corresponds to the spikes of limiting current density and may have increased the mass transfer in this study. Following the mechanism of mass transfer enhancement by entrained gas bubbles, a similar qualitative explanation may be given, as follows, after considering the influence of an oil droplet and revising Li's bistability theory. When a constant voltage (V) is imposed in the circuit in Figure 4.1.19, it is divided into two parts: one part $I \times (R_e + R_s)$, where I is the circuit current, R_e is the external series resistance, and R_s is the solution resistance and another is E, the potential of the cell.

At the beginning of the imposition of the potential, E will drive the current over the limiting value of the $Fe(CN)_6^{4-}$ anions in a stationary state, so the surface concentration of the anions is depleted and maintained at zero because this potentiostatic experiment is carried out at the selected voltage E_A. The movement of oil droplets produces a forced convection, which replenishes the surface concentration of the $Fe(CN)_6^{4-}$ anions, and raises the limiting current plateau over the stationary one to the spiked level. This may be called a positive feedback because it increases the current. In the meanwhile, a negative feedback comes from two aspects: one is the depletion of the surface concentration of the $Fe(CN)_6^{4-}$ anions by oxidation; and the other is a decrease in E because of the increase of I and so I $(R_e + R_s)$ under constant voltage. This reduces the current to the minimum until the oil droplet influences it again. It is believed that the combination of positive feedback and negative feedback accounts for the oscillation of the instantaneous limiting current.

In a summary, the effect of oil droplets on mass transfer in a large diameter pipeline has been discussed in this section. A high frequency and high magnitude instantaneous mass transfer coefficient found in water/oil flow may explain the enhancement of the corrosion rate in a low fluid velocity (1 m/s).

The current oscillations are explained by the influence of oil droplets in water/oil flow. The combination of positive and negative feedback results in the current oscillations and the spikes in the instantaneous mass transfer coefficient.

4.3 Effect of Flow Regime on Mass Transfer in Multiphase Flow

4.3.1 Water/Gas Two-Phase Flow

4.3.1.1 Average Mass Transfer Coefficient in Different Flow Regimes

Table 4.3.1.1 shows the test matrix for the mass transfer measurements in single and multiphase flows. Table 4.3.1.2 collects the flow regime information at different superficial liquid velocities from 0.2 to 1.5 m/s and superficial gas velocity from 0 to 4.8 m/s. Three kinds of flows were examined, full pipe flow, plug flow at a lower superficial gas velocity, e.g. 0.4, 0.6, 0.8, and 1.0 m/s, and slug flow at a higher superficial gas velocity, e.g. 1.4, 2.4, 3.0, 3.6, and 4.8 /s. Table 4.3.1.3 indicates the plug and slug frequency for each flow condition.

Figure 4.3.1.1 gives the relationship between the slug frequency and the superficial gas velocity. For the superficial gas velocities studied, i.e. below 5 m/s, the slug frequency does not change much with an increase in the superficial gas velocity. For example, at a 0.5 m/s superficial liquid velocity, the slug frequency increases from 14 slug/min at a 1.4 m/s superficial gas velocity to 17 slug/min at a 4.8 m/s superficial gas velocity.

Figure 4.3.1.2 shows the relationship between the slug frequency and the superficial liquid velocity. This indicates the small effect of the superficial gas velocity on the slug frequency. The slug frequency increases with the increases of the superficial liquid velocity. For example, at a 2.4 m/s superficial gas velocity, the slug frequency will increase from 12 slug/min at a 0.2 m/s superficial liquid velocity to 15, 35, 46, 58, 84 slug/min at 0.5, 0.8, 1.0, 1.2, and 1.5 m/s superficial liquid velocity,

Table 4.3.1.1 Experimental test matrix for multiphase flow without oil

Superficial liquid velocity (m/s)	0.2, 0.5, 0.8, 1.0, 1.2, 1.5
Superficial gas velocity (m/s)	0, 0.4, 0.6, 0.8, 1.0 1.4, 2.4, 3.0, 3.6, 4.8
Gas	Nitrogen
Liquid	0.01 M potassium ferro-ferricyanide, 1.0 N sodium hydroxide
Temperature (°C)	20

Table 4.3.1.2 Flow regimes corresponding to different gas and liquid velocities

Flow regime	Vsg (m/s)										
Vsl (m/s)		0	0.4	0.6	0.8	1.0	1.4	2.4	3.0	3.6	4.8
	0.2	FF*	PF*	PF	PF	PF	SF*	SF	SF	SF	SF
	0.5	FF	PF	PF	PF	PF	SF	SF	SF	SF	SF
	0.8	FF	PF	PF	PF	PF	SF	SF	SF	SF	SF
	1.0	FF	PF	PF	PF	PF	SF	SF	SF	SF	SF
	1.2	FF	PF	PF	PF	PF	SF	SF	SF	SF	SF
	1.5	FF	PF	PF	PF	PF	SF	SF	SF	SF	SF

* FF: Full pipe flow; PF: Plug flow; SF: Slug flow

Table 4.3.1.3 Comparison of slug frequency in different flows

Frequency (Hz)	Vsg (m/s)					
Vsl (m/s)		1.4	2.4	3.0	3.6	4.8
	0.2	12	12	13	13	17
	0.5	14	15	14	16	17
	0.8	33	35	40	38	38
	1.0	47	46	49	42	41
	1.2	62	58	65	52	52
	1.5	75	84	84	72	68

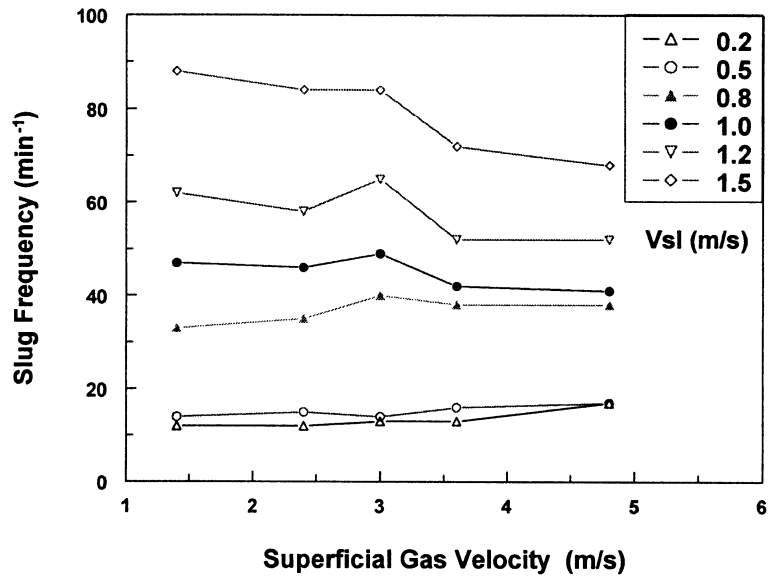

Figure 4.3.1.1 Effect of superficial gas velocity on the slug frequency

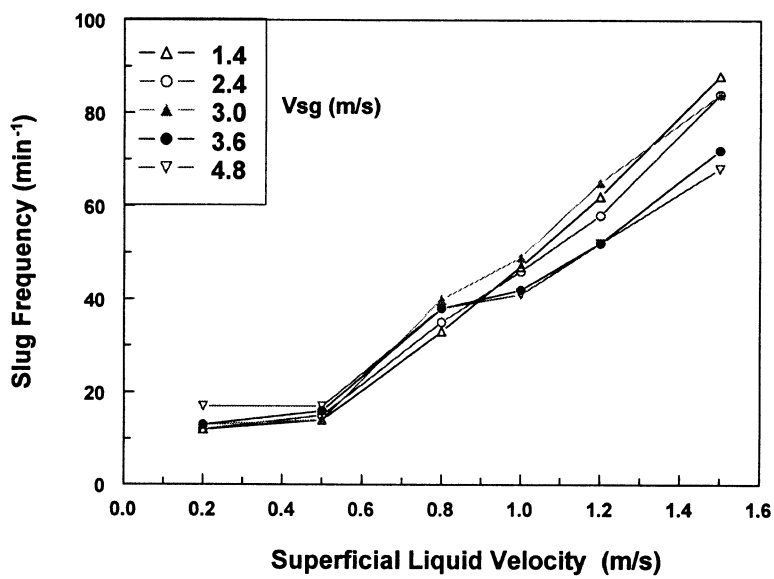

Figure 4.3.1.2 Effect of superficial liquid velocity on the slug frequency

respectively. It again proves that liquid velocity has a determined effect on the slug frequency (Wilkens, 1997). At each superficial liquid velocity, the frequencies at different superficial gas velocities are very similar.

At each flow condition, potentiodynamic measurements were taken to determine the average mass transfer coefficient (K). Figure 4.3.1.3 shows the effect of the superficial gas velocity on the average mass transfer coefficient. At a lower superficial gas velocity (<1.0 m/s), the average mass transfer coefficient increases with an increase in the superficial gas velocity. However, at a higher superficial velocities (>1 m/s), the average mass transfer coefficient does not change much. For instance, at a 0.8 m/s full pipe flow, the average mass transfer coefficient is 4.45×10^{-5} m/s. With an increase in the superficial gas velocity from 0 through 1 m/s, the average mass transfer coefficient increases from 4.45×10^{-5} to 5.17×10^{-5}, 5.58×10^{-5}, 6.17×10^{-5}, and 7.03×10^{-5} m/s and then remains constant. This is because the slug flow produces a highly turbulent flow and the average mass transfer coefficient becomes almost constant no matter how high the superficial gas velocity. It will not change until the annual flow is reached at a higher superficial gas velocity over 10 m/s. These results also indicate that it is hard to find a clear relationship between the average mass transfer coefficient and the slug flow characteristic parameters, such as the slug frequency and the Froude number.

Figure 4.3.1.4 indicates the effect on the superficial liquid velocity on the average mass transfer coefficient. It proves that the liquid velocity has a pronounced

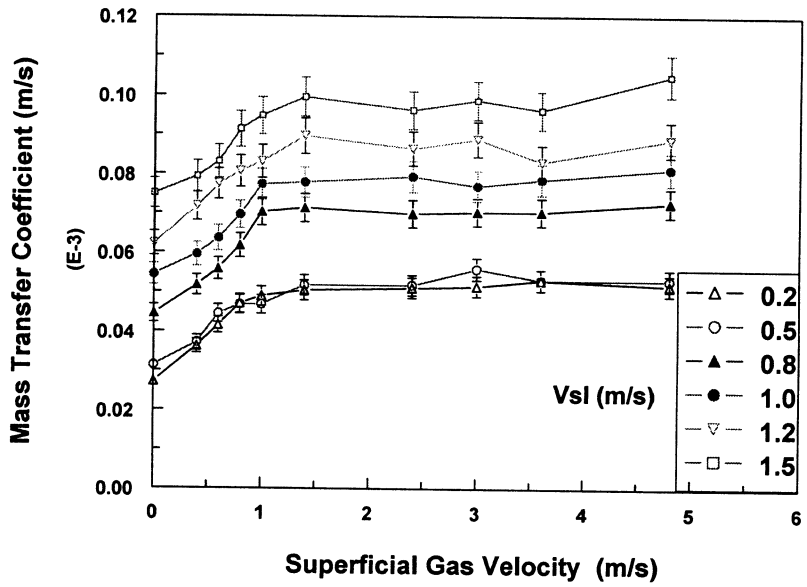

Figure 4.3.1.3 Effect of superficial gas velocity on the average mass transfer coefficient in slug flow and other flows

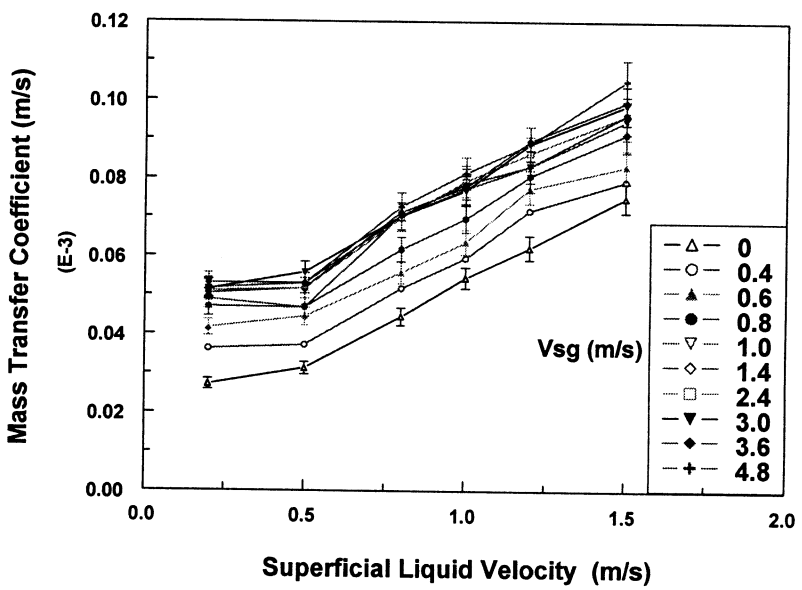

Figure 4.3.1.4 Effect of superficial liquid velocity on the average mass transfer coefficient in slug flow and other flows

effect on the average mass transfer coefficient. The mass transfer coefficient always gradually increases with the increase of the superficial liquid velocity at each superficial gas velocity. For example, at a 0.4 m/s superficial gas velocity, the mass transfer coefficient increases from 3.62×10^{-5} m/s at a 0.2 m/s superficial liquid velocity to 7.93×10^{-5} m/s at a 1.5 m/s superficial liquid velocity.

4.3.1.2 Instantaneous Mass Transfer Coefficient in Moving Slug Flow

4.3.1.2.1 Mass Transfer Characteristics in Time Domain

Table 4.3.1.4 indicates instantaneous mass transfer coefficient at specific flow conditions, e.g. Figure 4.3.1.7-d will show instantaneous mass transfer coefficient at a 0.8 m/s superficial liquid velocity and a 0.8 m/s superficial gas velocity.

Figures 4.3.1.5 to 4.3.1.10 present the instantaneous mass transfer coefficient in slug flow and other flow regimes. Figures 4.3.1.5-a to j examine the instantaneous mass transfer coefficient in the flow at a 0.2 m/s superficial liquid velocity at different superficial gas velocities. Figure 4.3.1.5-a shows the instantaneous mass transfer coefficient in a full pipe flow. The fluctuations reflect just the nature of the turbulence and the mass transfer coefficient is almost constant at about 2.6×10^{-5} m/s. When the superficial gas velocity is increased to 0.4 m/s (Figure 4.3.1.5-b), the fluctuations are enhanced due to the formation of slow moving lumps of liquid or plugs. The mass transfer coefficient is increased to about 3.2×10^{-5} m/s with fluctuations between 0.25×10^{-5} and 4.0×10^{-5} m/s. The fluctuation of instantaneous mass transfer coefficient is increased further at a superficial gas velocity of 0.6 m/s as shown in Figure 4.3.1.5-c.

Much higher peaks now appear and the plug flow can be divided into two zones, that is, the plug itself and the film between the plugs as shown in Figure 1.1.

Table 4.3.1.4 Index of the instantaneous mass transfer coefficient figures in different flows

Figure No:	Vsg (m/s)										
Vsl (m/s)		0	0.4	0.6	0.8	1.0	1.4	2.4	3.0	3.6	4.8
	0.2	Fig. 4.3.1. 5-a	Fig 4.3.1. 5-b	Fig. 4.3.1. 5-c	Fig. 4.3.1. 5-d	Fig. 4.3.1. 5-e	Fig. 4.3.1. 5-f	Fig. 4.3.1. 5-g	Fig 4.3.1. 5-h	Fig. 4.3.1. 5-I	Fig 4.3.1. 5-j
	0.5	Fig. 4.3.1. 6-a	Fig 4.3.1. 6-b	Fig. 4.3.1. 6-c	Fig. 4.3.1. 6-d	Fig. 4.3.1. 6-e	Fig. 4.3.1. 6-f	Fig. 4.3.1. 6-g	Fig 4.3.1. 6-h	Fig. 4.3.1. 6-I	Fig 4.3.1. 6-j
	0.8	Fig. 4.3.1. 7-a	Fig 4.3.1. 7-b	Fig. 4.3.1. 7-c	Fig. 4.3.1. 7-d	Fig. 4.3.1. 7-e	Fig. 4.3.1. 7-f	Fig. 4.3.1. 7-g	Fig 4.3.1. 7-h	Fig. 4.3.1. 7-I	Fig 4.3.1. 7-j
	1.0	Fig. 4.3.1. 8-a	Fig 4.3.1. 8-b	Fig. 4.3.1. 8-c	Fig. 4.3.1. 8-d	Fig. 4.3.1. 8-e	Fig. 4.3.1. 8-f	Fig. 4.3.1. 8-g	Fig 4.3.1. 8-h	Fig. 4.3.1. 8-I	Fig 4.3.1. 8-j
	1.2	Fig. 4.3.1. 9-a	Fig 4.3.1. 9-b	Fig. 4.3.1. 9-c	Fig. 4.3.1. 9-d	Fig. 4.3.1. 9-e	Fig. 4.3.1. 9-f	Fig. 4.3.1. 9-g	Fig 4.3.1. 9-h	Fig. 4.3.1. 9-I	Fig 4.3.1. 9-j
	1.5	Fig. 4.3.1. 10-a	Fig 4.3.1. 10-b	Fig. 4.3.1. 10-c	Fig. 4.3.1. 10-d	Fig. 4.3.1. 10-e	Fig. 4.3.1. 10-f	Fig. 4.3.1. 10-g	Fig 4.3.1. 10-h	Fig. 4.3.1. 10-i	Fig 4.3.1. 10-j

The amplitude of these peaks becomes more and more significant with an increase in the superficial gas velocity, e.g. to 0.8, 1.0, 1.4 m/s (Figure 4.3.1.5-d, e, f). A comparison of Figures 4.3.1.5-b, c, d, e, f, which correspond to the plug flow, show that the frequency of these is equal to the frequency of the plug flow.

When the superficial gas velocity is increased to 2.4 m/s, slug flow is now present and two large amplitude peaks appear in Figure 4.3.1.5-g. This is due to the formation of the mixing zone, which produces high-energy bubbles, which can hit the bottom of the pipe. The magnitude of the peaks is much higher than the plug flow. The

instantaneous mass transfer coefficient in the slug is 1.0×10^{-3} m/s which is about 10 times higher than that in the slug film zone.

With a further increase of the superficial gas velocity to 3.6 m/s (Figure 4.3.1.5-i), more high-energy bubbles are formed and the instantaneous mass transfer peak increases correspondingly. The magnitude of the fluctuations reaches 8.0×10^{-3} m/s which is about 160 times the film value. The peaks appear at a frequency equal to the frequency of the slug flow (Refer to Table 4.3.1.3). Figures 4.3.1.5-i and 4.3.1.5-j show similar results.

When the superficial liquid velocity increases, the frequency of the plug flow or slug flow increases significantly as shown by Table 4.3.1.3. Similar results are seen for the full pipe flow and for the plug flow except that the plug frequency increases with an increase in the superficial liquid velocity. More differences in the slug frequency are noted. By examining the g, h, i, and j parts of each of the Figures 4.3.1.5 to 4.3.1.10, it is seen that the slug frequency has increased from about 12/min to a range of 70-90/min. It becomes difficult to determine the frequency of the slug flow from the peaks of the instantaneous mass transfer coefficient visually.

As the superficial liquid velocity is increased, the number of large peaks within the slug also increases. This may be linked to the fact that the Froude number may be higher at higher liquid rates. The magnitude of the fluctuations is similar to those described earlier and ranges from 10 to 100 times that of the liquid film.

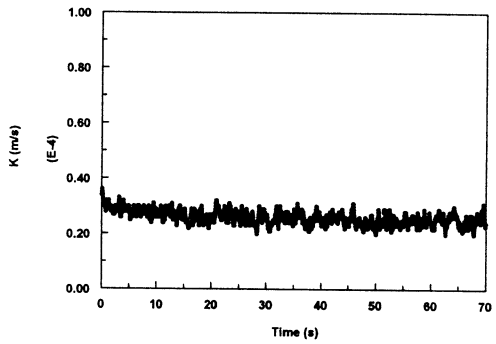

Figure 4.3.1.5-a Instantaneous mass transfer coefficient at Vsl=0.2 m/s and Vsg=0 m/s in water/gas flow

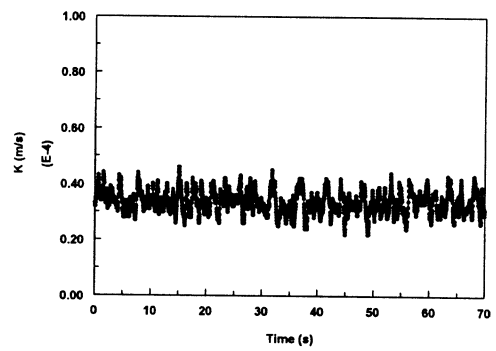

Figure 4.3.1.5-b Instantaneous mass transfer coefficient at Vsl=0.2 m/s and Vsg=0.4 m/s in water/gas flow

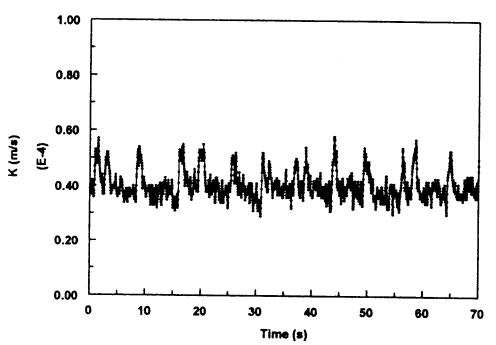

Figure 4.3.1.5-c Instantaneous mass transfer coefficient at Vsl=0.2 m/s and Vsg=0.6 m/s in water/gas flow

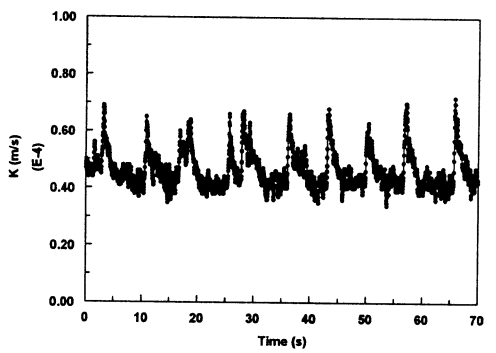

Figure 4.3.1.5-d Instantaneous mass transfer coefficient at Vsl=0.2 m/s and Vsg=0.8 m/s in water/gas flow

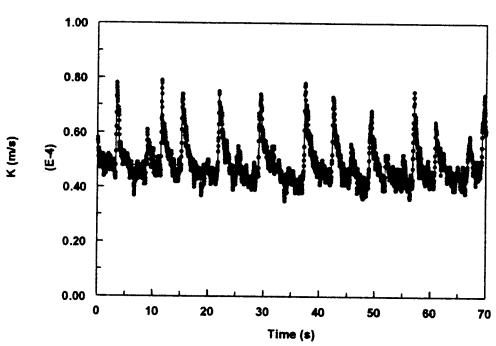

Figure 4.3.1.5-e Instantaneous mass transfer coefficient at Vsl=0.2 m/s and Vsg=1.0 m/s in water/gas flow

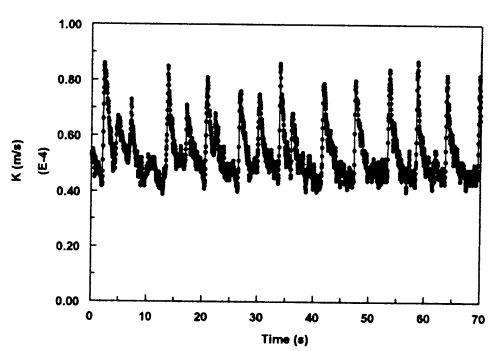

Figure 4.3.1.5-f Instantaneous mass transfer coefficient at Vsl=0.2 m/s and Vsg=1.4 m/s in water/gas flow

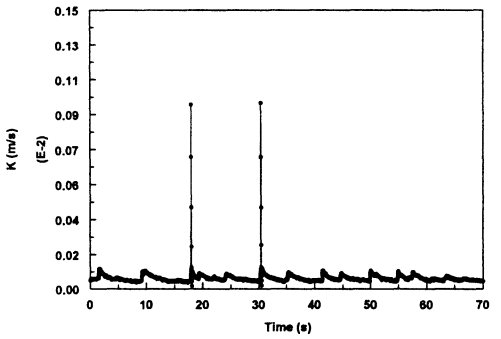

Figure 4.3.1.5-g Instantaneous mass transfer coefficient at Vsl=0.2 m/s and Vsg=2.4 m/s in water/gas flow

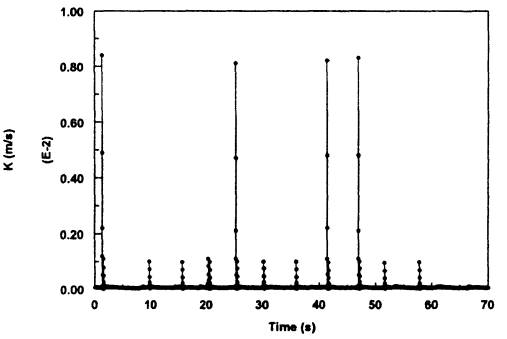

Figure 4.3.1.5-j Instantaneous mass transfer coefficient at Vsl=0.2 m/s and Vsg=4.8 m/s in water/gas flow

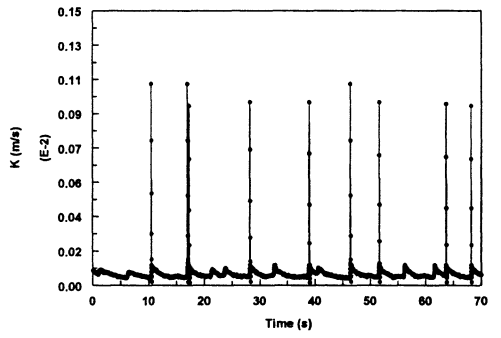

Figure 4.3.1.5-h Instantaneous mass transfer coefficient at Vsl=0.2 m/s and Vsg=3.0 m/s in water/gas flow

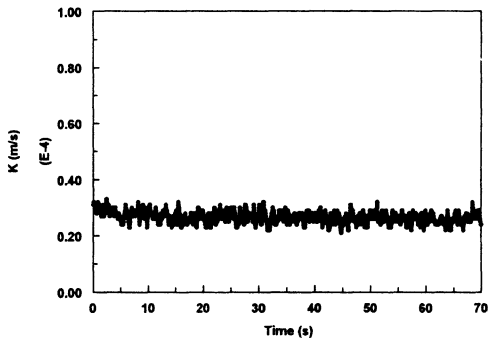

Figure 4.3.1.6-a Instantaneous mass transfer coefficient at Vsl=0.5 m/s and Vsg=0 m/s in water/gas flow

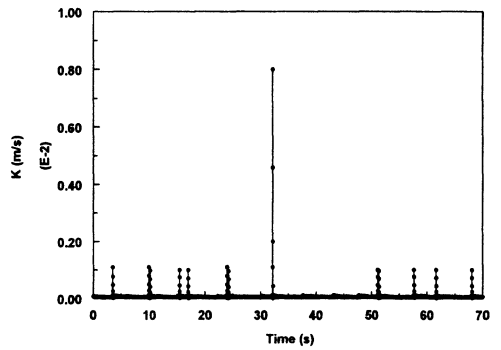

Figure 4.3.1.5-i Instantaneous mass transfer coefficient at Vsl=0.2 m/s and Vsg=3.6 m/s in water/gas flow

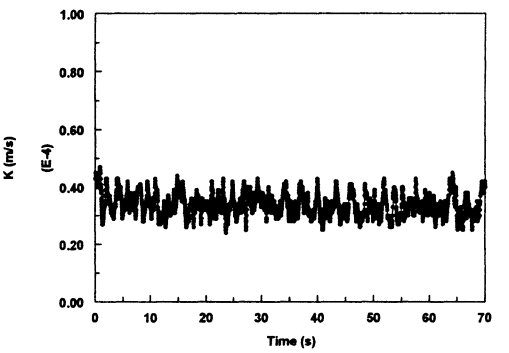

Figure 4.3.1.6-b Instantaneous mass transfer coefficient at Vsl=0.5 m/s and Vsg=0.4 m/s in water/gas flow

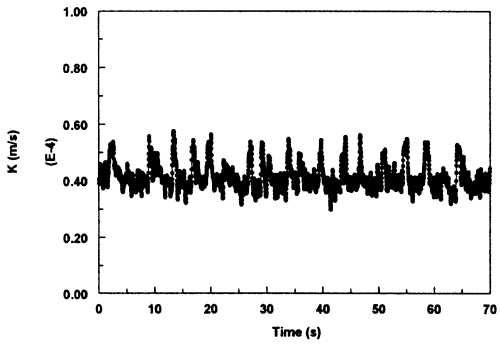

Figure 4.3.1.6-c Instantaneous mass transfer coefficient at Vsl=0.5 m/s and Vsg=0.6 m/s in water/gas flow

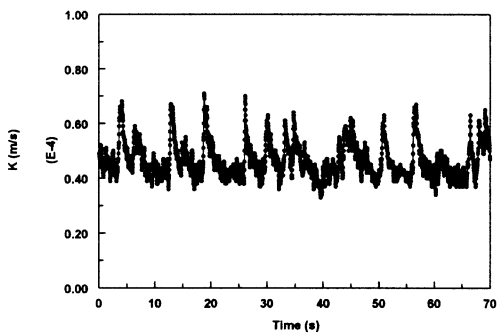

Figure 4.3.1.6-d Instantaneous mass transfer coefficient at Vsl=0.5 m/s and Vsg=0.8 m/s in water/gas flow

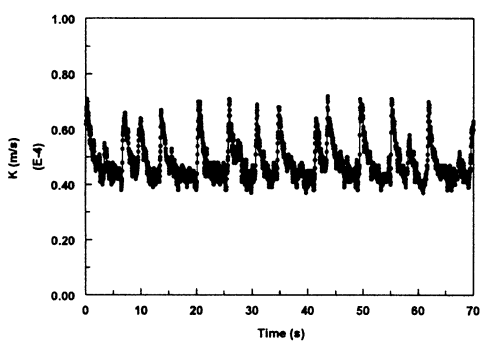

Figure 4.3.1.6-e Instantaneous mass transfer coefficient at Vsl=0.5 m/s and Vsg=1.0 m/s in water/gas flow

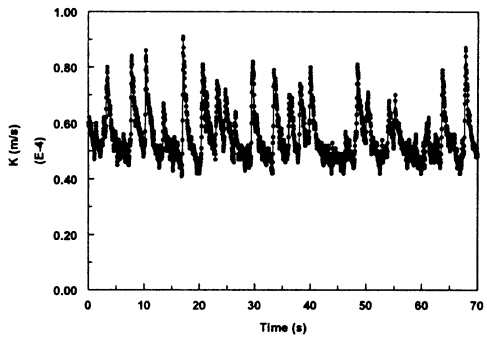

Figure 4.3.1.6-f Instantaneous mass transfer coefficient at Vsl=0.5 m/s and Vsg=1.4 m/s in water/gas flow

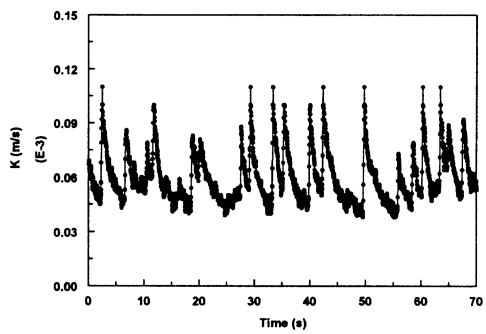

Figure 4.3.1.6-g Instantaneous mass transfer coefficient at Vsl=0.5 m/s and Vsg=2.4 m/s in water/gas flow

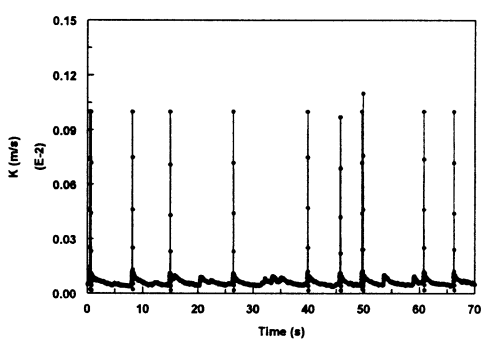

Figure 4.3.1.6-h Instantaneous mass transfer coefficient at Vsl=0.5 m/s and Vsg=3.0 m/s in water/gas flow

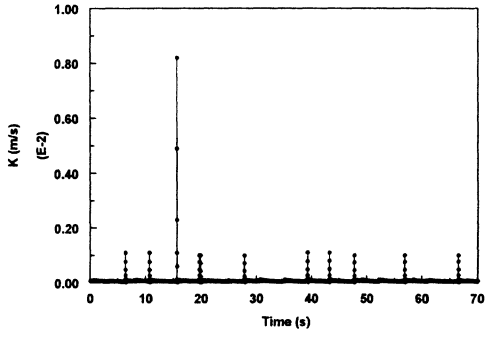

Figure 4.3.1.6-i Instantaneous mass transfer coefficient at Vsl=0.5 m/s and Vsl=3.6 m/s in water/gas flow

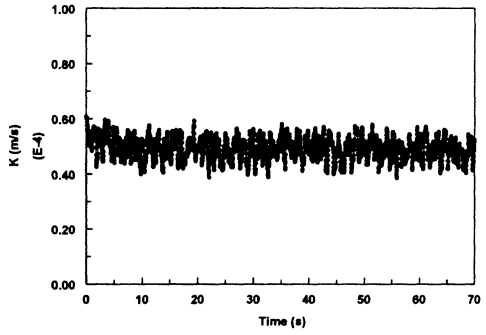

Figure 4.3.1.7-b Instantaneous mass transfer coefficient at Vsl=0.8 m/s and Vsg=0.4 m/s in water/gas flow

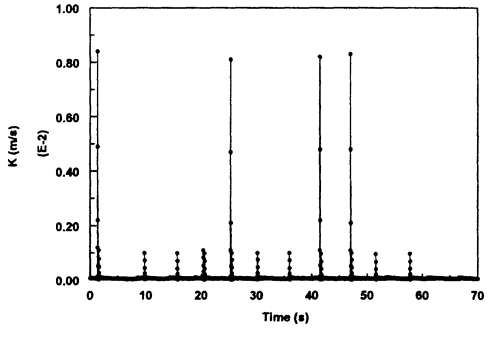

Figure 4.3.1.6-j Instantaneous mass transfer coefficient at Vsl=0.5 m/s and Vsg=4.8 m/s in water/gas flow

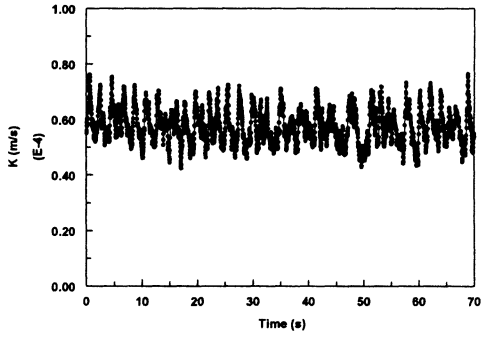

Figure 4.3.1.7-c Instantaneous mass transfer coefficient at Vsl=0.8 m/s and Vsg=0.6 m/s in water/gas flow

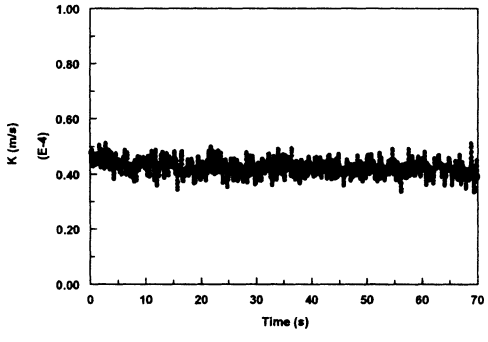

Figure 4.3.1.7-a Instantaneous mass transfer coefficient at Vsl=0.8 m/s and Vsg=0 m/s in water/gas flow

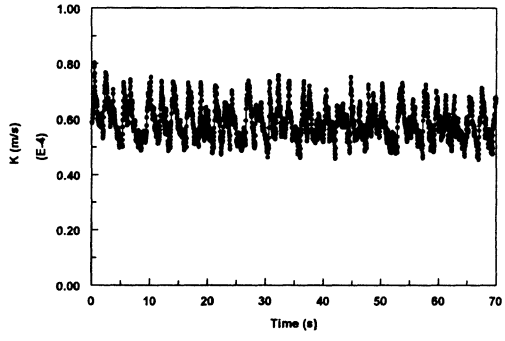

Figure 4.3.1.7-d Instantaneous mass transfer coefficient at Vsl=0.8 m/s and Vsg=0.8 m/s in water/gas flow

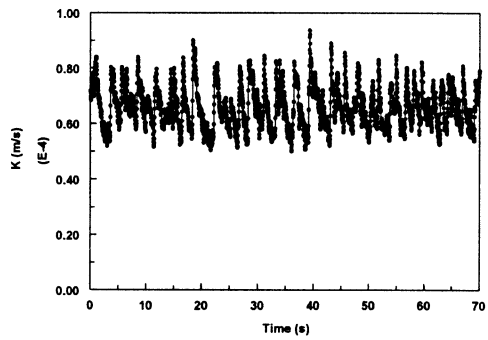

Figure 4.3.1.7-e Instantaneous mass transfer coefficient at Vsl=0.8 m/s and Vsg=1.0 m/s in water/gas flow

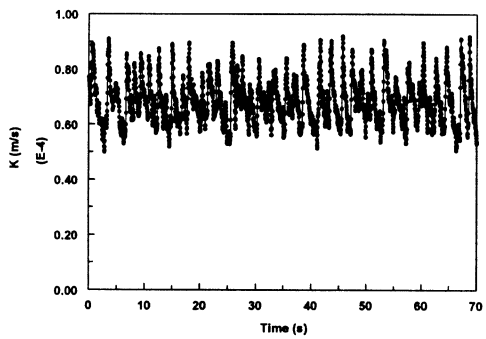

Figure 4.3.1.7-f Instantaneous mass transfer coefficient at Vsl=0.8 m/s and Vsg=1.4 m/s in water/gas flow

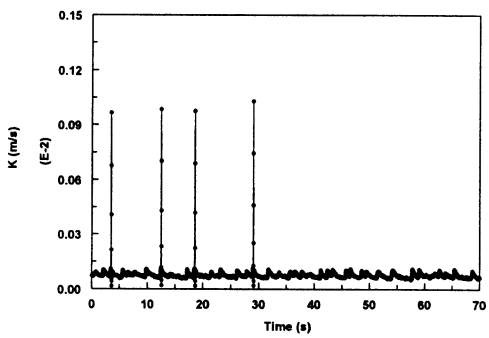

Figure 4.3.1.7-g Instantaneous mass transfer coefficient at Vsl=0.8 m/s and Vsg=2.4 m/s in water/gas flow

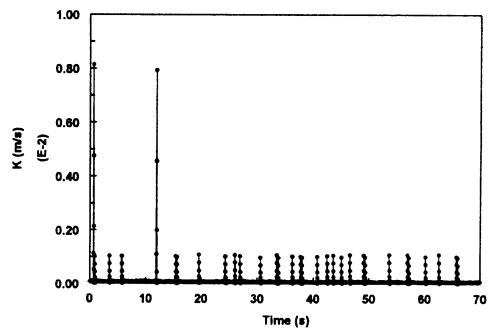

Figure 4.3.1.7-h Instantaneous mass transfer coefficient at Vsl=0.8 m/s and Vsg=3.0 m/s in water/gas flow

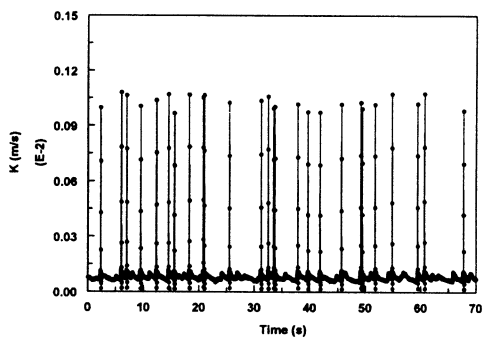

Figure 4.3.1.7-i Instantaneous mass transfer coefficient at Vsl=0.8 m/s and Vsg=3.6 m/s in water/gas flow

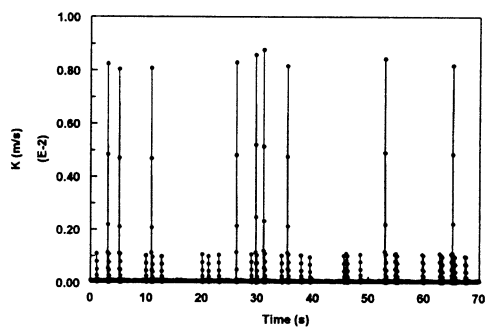

Figure 4.3.1.7-j Instantaneous mass transfer coefficient at Vsl=0.8 m/s and Vsg=4.8 m/s in water/gas flow

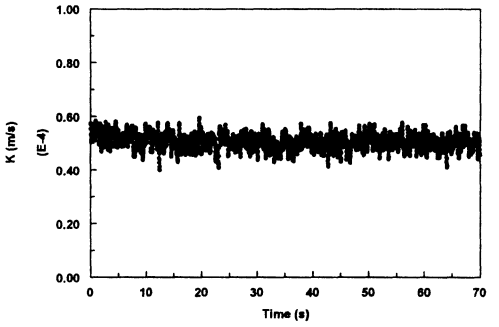

Figure 4.3.1.8-a Instantaneous mass transfer coefficient at Vsl=1.0 m/s and Vsg=0 m/s in water/gas flow

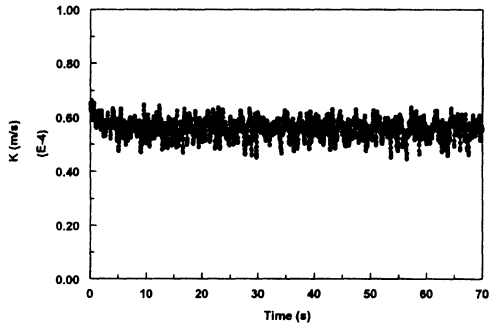

Figure 4.3.1.8-b Instantaneous mass transfer coefficient at Vsl=1.0 m/s and Vsg=0.4 m/s in water/gas flow

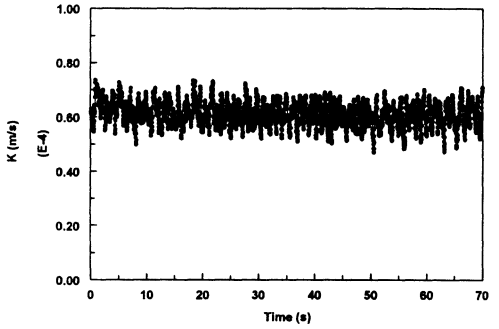

Figure 4.3.1.8-c Instantaneous mass transfer coefficient at Vsl=1.0 m/s and Vsg=0.6 m/s in water/gas flow

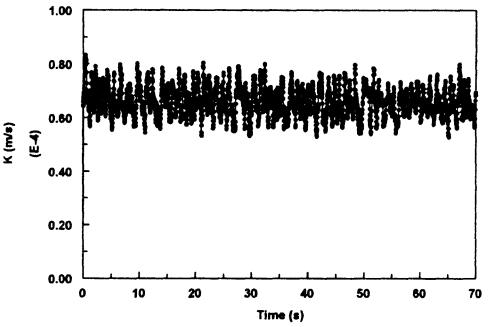

Figure 4.3.1.8-d Instantaneous mass transfer coefficient at Vsl=1.0 m/s and Vsg=0.8 m/s in water/gas flow

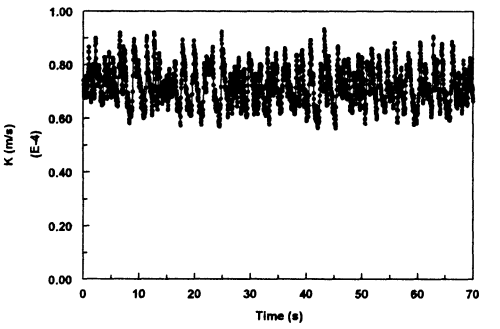

Figure 4.3.1.8-e Instantaneous mass transfer coefficient at Vsl=1.0 m/s and Vsg=1.0 m/s in water/gas flow

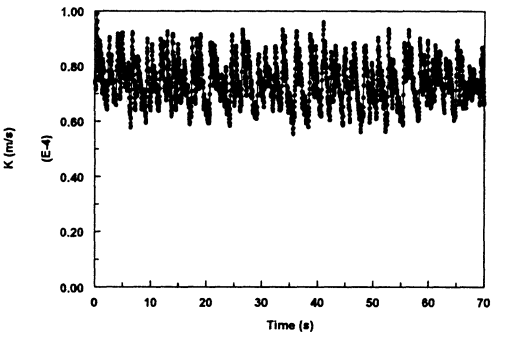

Figure 4.3.1.8-f Instantaneous mass transfer coefficient at Vsl=1.0 m/s and Vsg=1.4 m/s in water/gas flow

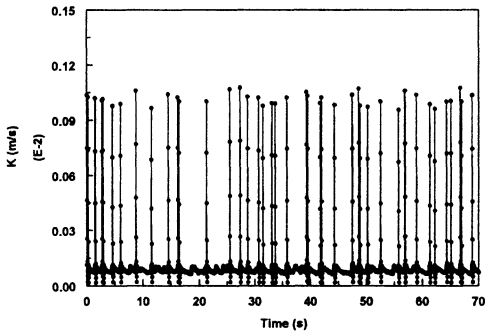

Figure 4.3.1.8-g Instantaneous mass transfer coefficient at Vsl=1.0 m/s and Vsg=2.4 m/s in water/gas flow

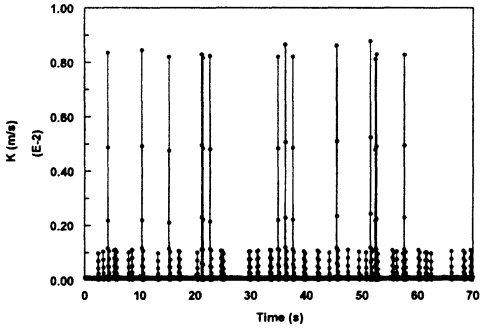

Figure 4.3.1.8-j Instantaneous mass transfer coefficient at Vsl=1.0 m/s and Vsg=4.8 m/s in water/gas flow

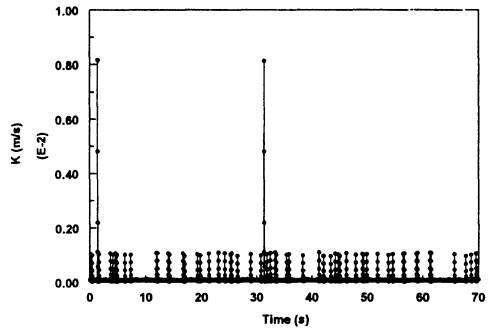

Figure 4.3.1.8-h Instantaneous mass transfer coefficient at Vsl=1.0 m/s and Vsg=3.0 m/s in water/gas flow

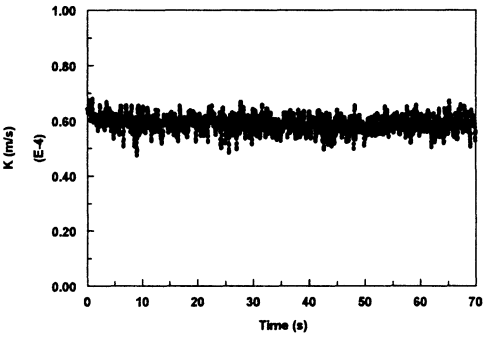

Figure 4.3.1.9-a Instantaneous mass transfer coefficient at Vsl=1.2 m/s and Vsg=0 m/s in water/gas flow

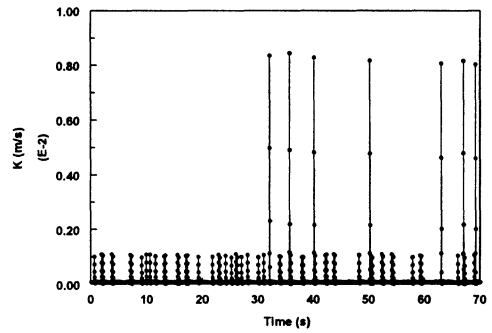

Figure 4.3.1.8-i Instantaneous mass transfer coefficient at Vsl=1.0 m/s and Vsg=3.6 m/s in water/gas flow

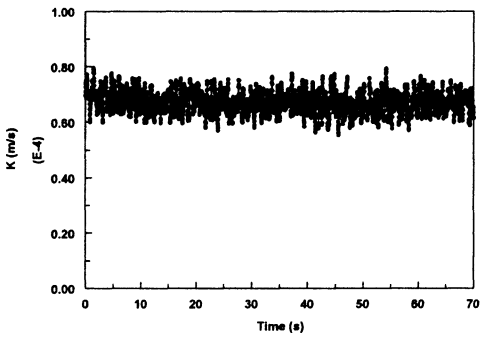

Figure 4.3.1.9-b Instantaneous mass transfer coefficient at Vsl=1.2 m/s and Vsg=0.4 m/s in water/gas flow

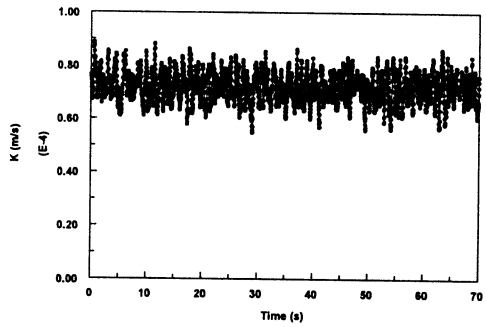

Figure 4.3.1.9-c Instantaneous mass transfer coefficient at Vsl=1.2 m/s and Vsg=0.6 m/s in water/gas flow

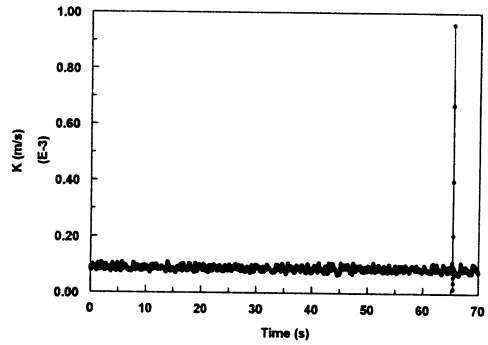

Figure 4.3.1.9-f Instantaneous mass transfer coefficient at Vsl=1.2 m/s and Vsg=1.4 m/s in water/gas flow

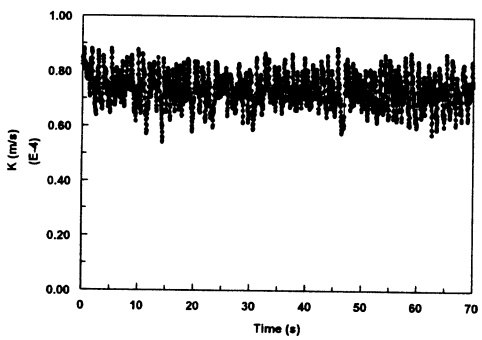

Figure 4.3.1.9-d Instantaneous mass transfer coefficient at Vsl=1.2 m/s and Vsg=0.8 m/s in water/gas flow

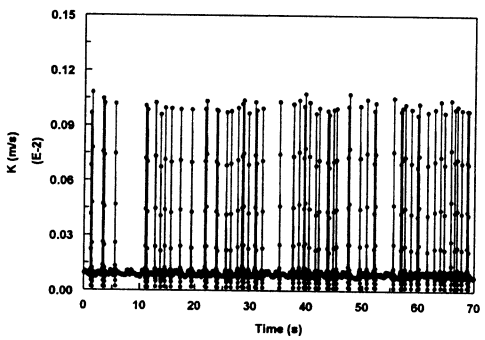

Figure 4.3.1.9-g Instantaneous mass transfer coefficient at Vsl=1.2 m/s and Vsg=2.4 m/s in water/gas flow

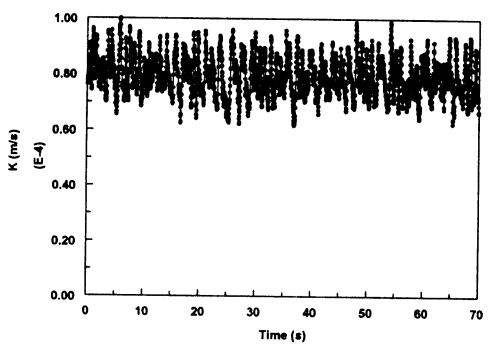

Figure 4.3.1.9-e Instantaneous mass transfer coefficient at Vsl=1.2 m/s and Vsg=1.0 m/s in water/gas flow

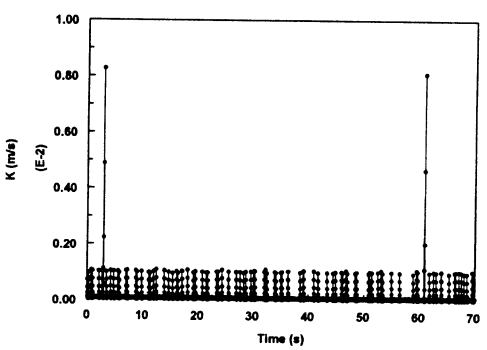

Figure 4.3.1.9-h Instantaneous mass transfer coefficient at Vsl=1.2 m/s and Vsg=3.0 m/s in water/gas flow

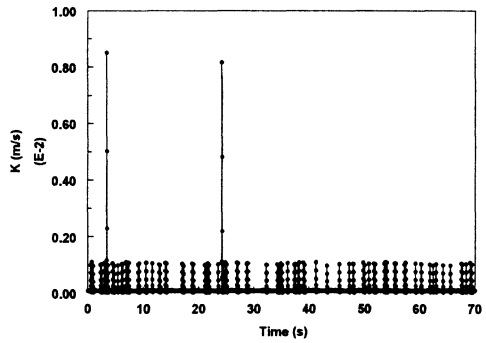

Figure 4.3.1.9-i Instantaneous mass transfer coefficient at Vsl=1.2 m/s and Vsg=3.6 m/s in water/gas flow

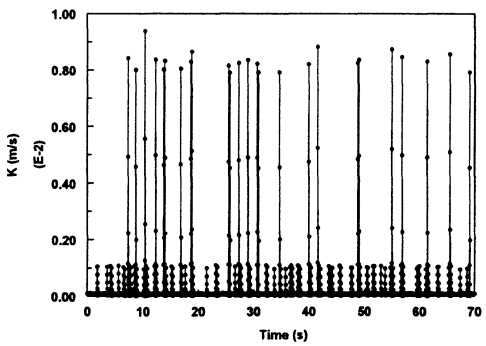

Figure 4.3.1.9-j Instantaneous mass transfer coefficient at Vsl=1.2 m/s and Vsg=4.8 m/s in water/gas flow

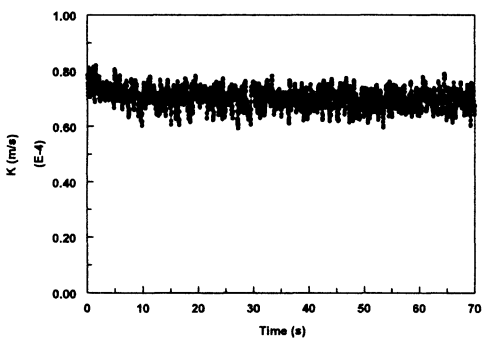

Figure 4.3.1.10-a Instantaneous mass transfer coefficient at Vsl=1.5 m/s and Vsg=0 m/s in water/gas flow

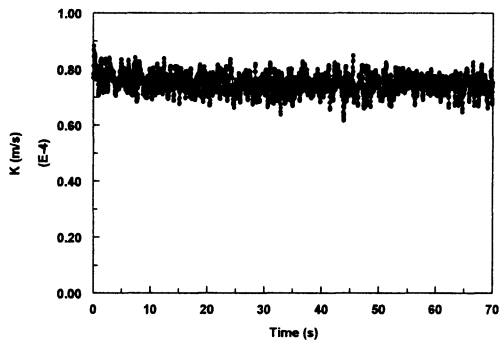

Figure 4.3.1.10-b Instantaneous mass transfer coefficient at Vsl=1.5 m/s and Vsg=0.4 m/s in water/gas flow

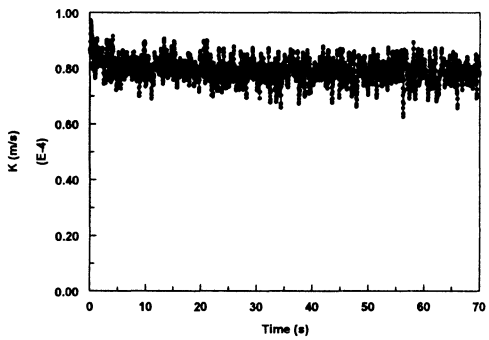

Figure 4.3.1.10-c Instantaneous mass transfer coefficient at Vsl=1.5 m/s and Vsg=0.6 m/s in water/gas flow

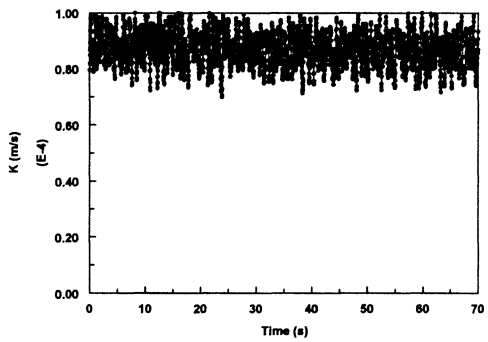

Figure 4.3.1.10-d Instantaneous mass transfer coefficient at Vsl=1.5 m/s and Vsg=0.8 m/s in water/gas flow

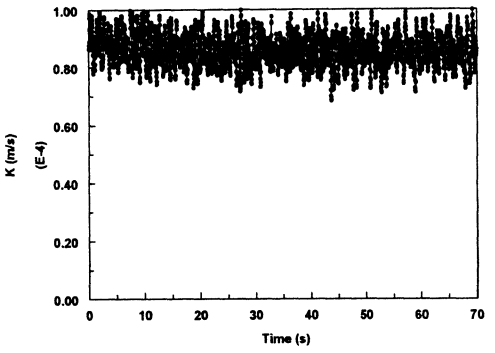

Figure 4.3.1.10-e Instantaneous mass transfer coefficient at Vsl=1.5 m/s and Vsg=1.0 m/s in water/gas flow

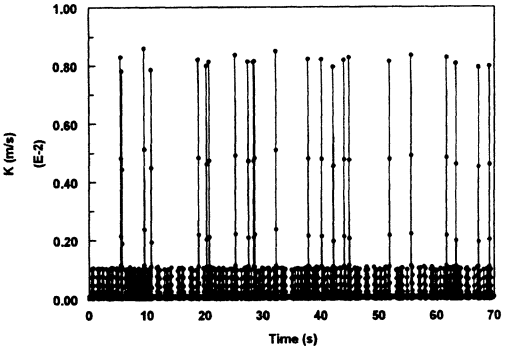

Figure 4.3.1.10-h Instantaneous mass transfer coefficient at Vsl=1.5 m/s and Vsg=3.0 m/s in water/gas flow

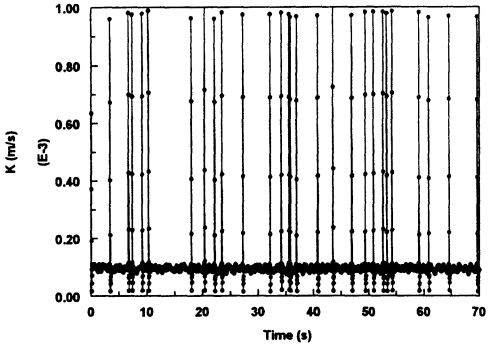

Figure 4.3.1.10-f Instantaneous mass transfer coefficient at Vsl=1.5 m/s and Vsg=1.4 m/s in water/gas flow

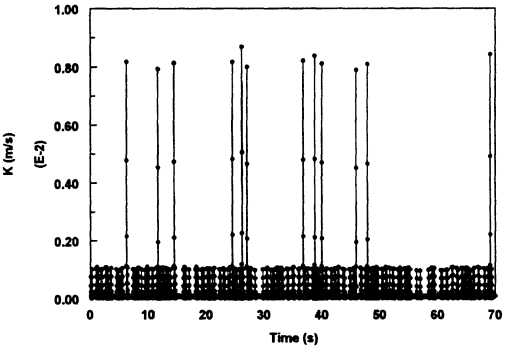

Figure 4.3.1.10-i Instantaneous mass transfer coefficient at Vsl=1.5 m/s and Vsg=3.6 m/s in water/gas flow

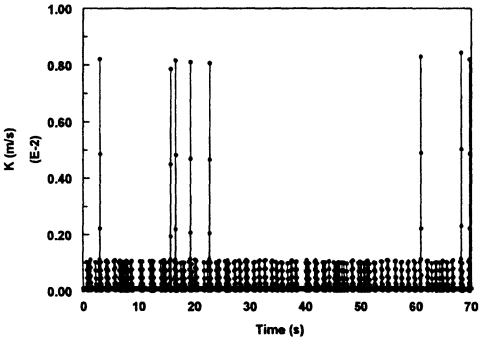

Figure 4.3.1.10-g Instantaneous mass transfer coefficient at Vsl=1.5 m/s and Vsg=2.4 m/s in water/gas flow

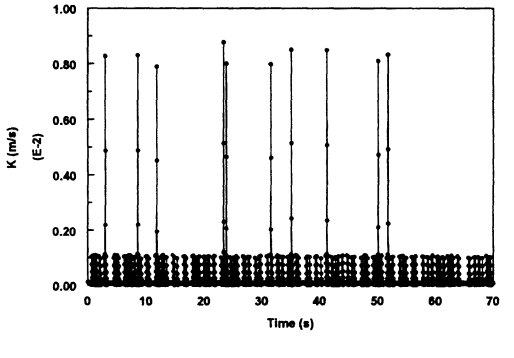

Figure 4.3.1.10-j Instantaneous mass transfer coefficient at Vsl=1.5 m/s and Vsg=4.8 m/s in water/gas flow

It can be concluded that for the plug flow and the transition from the plug flow to the slug flow, the frequency (f1) of large fluctuations in the instantaneous mass transfer coefficient is equal to the frequency (f2) of the plug flow or the slug flow obtained visually. The mixing zone does not produce multiple bubble impacts. However, f1 will be higher than f2 in a stronger slug flow regime since f1 corresponds to the frequency of bubble impact at the bottom of the pipe when each mixing zone produces the pulses of bubbles and than the multiple bubble impacts.

For example, at a slug flow with Vsl=1.5 m/s and Vsg=3.0 m/s, we can obtain the following data from Figure 4.3.1.10-h and Figure 4.3.1.16-h.

f1 = dominant frequency = 4.5 Hz = 270 /min.

f2 = slug frequency = 84 /min (visually counting)

f1 > f2 (270/84 = 3.21)

This means that it may be possible that 3 bubble impacts or collapses appear during the period of one slug mixing zone.

At a slug flow with Vsl = 0.2 m/s and Vsg = 3.0 m/s, it is found from Figures 4.3.1.5-h and 4.3.1.11-h:

f1 = dominant frequency = 0.2 Hz = 12 /min

f2 = slug frequency = 12 /min (visually counting)

f1 = f2

This suggests that only one bubble impact on the bottom appears during the period of one slug mixing zone.

The mass transfer enhancement (E) is defined to describe the effect of the bubble impacts on the mass transfer coefficient in the slug flow:

$$E = Kp/Km \tag{4.1}$$

Where,

Kp = peak mass transfer coefficient (m/s)

Km = mean mass transfer coefficient (m/s)

Table 4.3.1.5 compares the mass transfer enhancement (E) in different flow conditions. In full pipe flow the instantaneous mass transfer coefficient only has small oscillations because of natural fluctuations in the turbulent flow. At a lower superficial gas velocity (<1.0 m/s) corresponding to the plug flow, the enhancement is usually around 1.5. Since the plug flow can be divided into two zones, that is, the plug itself and the film between the plugs, the plug usually has a higher velocity than the film. It is this higher velocity that causes the 1.5 times enhancement of the instantaneous mass transfer coefficient.

With the further increase of the superficial gas velocity (≥2.4 m/s) at each superficial liquid velocity, the enhancement has significant changes. For example, at a 0.8 m/s superficial liquid velocity, the enhancement can reach approximately 17 at 2.4, 3.0, and 3.6 m/s superficial gas velocity, and maximum 135 at a 4.8 m/s superficial gas velocity (Table 4.3.1.5). The corresponding peak instantaneous mass transfer coefficients are approximately 1.0×10^{-3}, 1.0×10^{-3}, 1.0×10^{-3}, and 8.1×10^{-3} m/s at superficial gas velocity of 2.4, 3.0, 36, and 4.8 m/s, respectively (Figure 4.3.1.7). At

each of these four superficial gas velocities the corresponding mean mass transfer coefficients Km do not change much and have a value of around 6×10^{-5} m/s.

In another example, at a 1.2 m/s superficial liquid velocity, there are two mass transfer enhancements, 13 and 104 at 3.0, 3.6, and 4.8 m/s (Table 4.3.1.5). These two enhancements represent two kinds of bubble contacts on the bottom of the pipe. This may be the bubble impact, and latterly, the bubble collapse. These two kinds of bubble impacts have large differences in terms of energy and will cause different mass transfer coefficients and mechanical effects. This is closely related to the power spectrum of the instantaneous mass transfer coefficient in the slug mixing zone, and this relationship will be now discussed.

Table 4.3.1.5 Mass transfer enhancement in different flows

E	Vsg (m/s)										
Vsl (m/s)		0	0.4	0.6	0.8	1.0	1.4	2.4	3.0	3.6	4.8
	0.2	1	1	1.5	1.6	1.7	1.9	2.2, 20	2.4, 20	20, 160	20, 160
	0.5	1	1	1.5	1.8	1.7	1.7	2.2	2.2, 20	20, 164	20, 164
	0.8	1	1	1	1.5	1.5	1.6	2.0, 17	2.0, 17	2.0, 17	17, 135
	1.0	1	1	1	1	1.5	1.5	14	14, 112	14, 120	14, 120
	1.2	1	1	1	1	1	12	13	13, 104	13, 104	13, 104
	1.5	1	1	1	1	1	11	11, 92	11, 92	11, 92	11, 92

4.3.1.2.2 Mass Transfer Characteristics in Frequency Domain

A Fast Fourier Transform (FFT) method is used to compare these instantaneous mass transfer coefficient signals in the frequency domain and the results are given in Table 4.3.1.6.

Table 4.3.1.6 Index of FFT analysis of the instantaneous mass transfer coefficient

Figure No:	Vsg (m/s)					
Vsl (m/s)		1.4	2.4	3.0	3.6	4.8
	0.2	Fig. 4.3.1.11-f	Fig. 4.3.1.11-g	Fig. 4.3.1.11-h	Fig. 4.3.1.11-i	Fig. 4.3.1.11-j
	0.5	Fig. 4.3.1.12-f	Fig. 4.3.1.12-g	Fig. 4.3.1.12-h	Fig. 4.3.1.12-i	Fig. 4.3.1.12-j
	0.8	Fig. 4.3.1.13-f	Fig. 4.3.1.13-g	Fig. 4.3.1.13-h	Fig. 4.3.1.13-i	Fig. 4.3.1.13-j
	1.0	Fig. 4.3.1.14-f	Fig. 4.3.1.14-g	Fig. 4.3.1.14-h	Fig. 4.3.1.14-i	Fig. 4.3.1.14-j
	1.2	Fig. 4.3.1.15-f	Fig. 4.3.1.15-g	Fig. 4.3.1.15-h	Fig. 4.3.1.15-i	Fig. 4.3.1.15-j
	1.5	Fig. 4.3.1.16-f	Fig. 4.3.1.16-g	Fig. 4.3.1.16-h	Fig. 4.3.1.16-i	Fig. 4.3.1.16-j

The FFT analysis can identify the characteristics of a complex signal. A brief discussion of Figure 4.3.1.11 that corresponds to Figure 4.3.1.5 series is given. Figures 4.3.1.5-a to e are indicative of a full pipe flow and a slow moving plug flow, and have very small amplitude oscillations, which is similar to Figure 4.3.1.5-f. Therefore, only the FFT results in Figure 4.3.1.11-f onwards are shown. Figure 4.3.1.11-f indicates that the dominant frequency is 0.2 Hz. As we have discussed in previous section, the dominant frequency 0.2 Hz is equivalent to the visual slug frequency (12 slug/min).

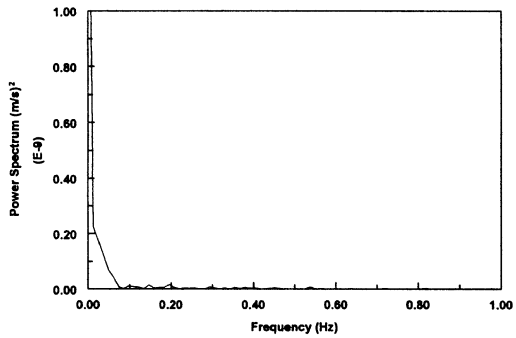

Figure 4.3.1.11-f Power spectrum of the instantaneous mass transfer coefficient at Vsl=0.2 m/s, Vsg=1.4 m/s in water/gas flow

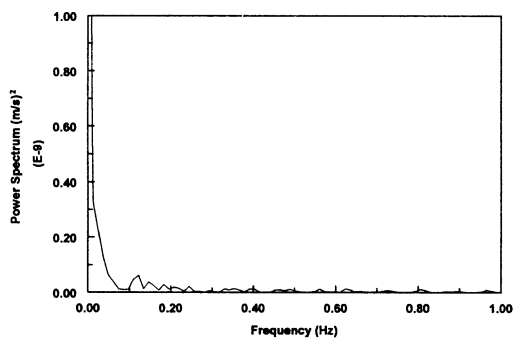

Figure 4.3.1.11-g Power spectrum of the instantaneous mass transfer coefficient at Vsl=0.2 m/s, Vsg=2.4 m/s in water/gas flow

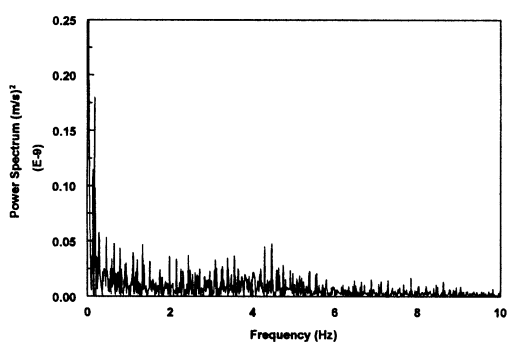

Figure 4.3.1.11-h Power spectrum of the instantaneous mass transfer coefficient at Vsl=0.2 m/s, Vsg=3.0 m/s in water/gas flow

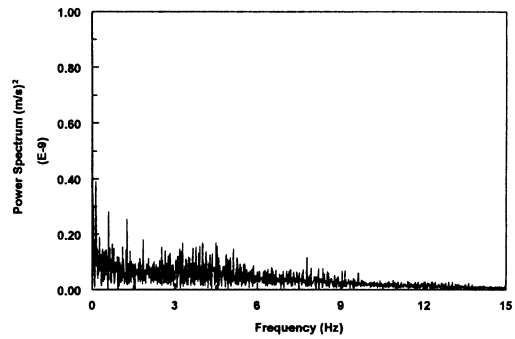

Figure 4.3.1.11-i Power spectrum of the instantaneous mass transfer coefficient at Vsl=0.2 m/s, Vsg=3.6 m/s in water/gas flow

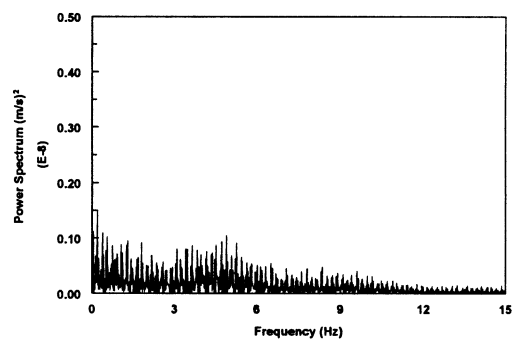

Figure 4.3.1.11-j Power spectrum of the instantaneous mass transfer coefficient at Vsl=0.2 m/s, Vsg=4.8 m/s in water/gas flow

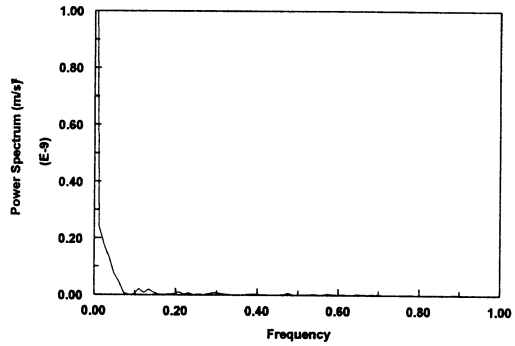

Figure 4.3.1.12-f Power spectrum of the instantaneous mass transfer coefficient at Vsl=0.5 m/s and Vsg=1.4 m/s in water/gas flow

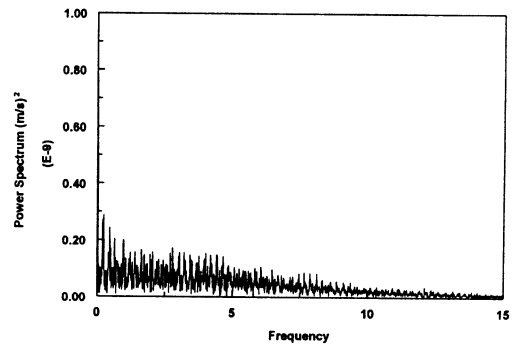

Figure 4.3.1.12-i Power spectrum of the instantaneous mass transfer coefficient at Vsl=0.5 m/s and Vsg=3.6 m/s in water/gas flow

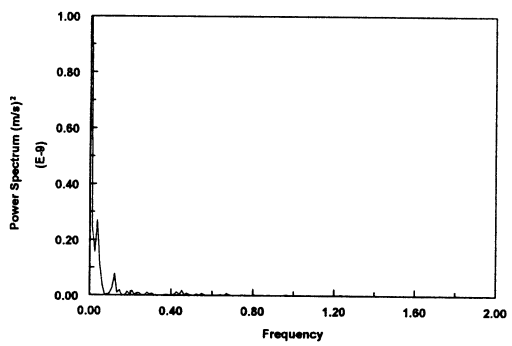

Figure 4.3.1.12-g Power spectrum of the instantaneous mass transfer coefficient at Vsl=0.5 m/s and Vsg=2.4 m/s in water/gas flow

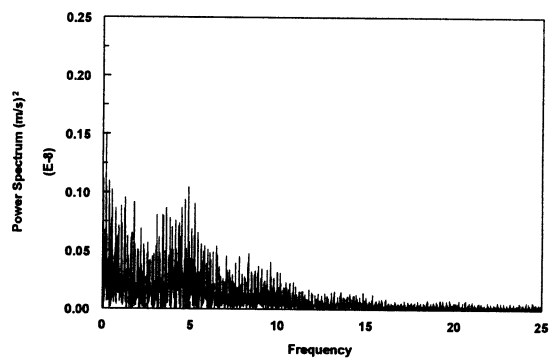

Figure 4.3.1.12-j Power spectrum of the instantaneous mass transfer coefficient at Vsl=0.5 m/s and Vsg=4.8 m/s in water/gas flow

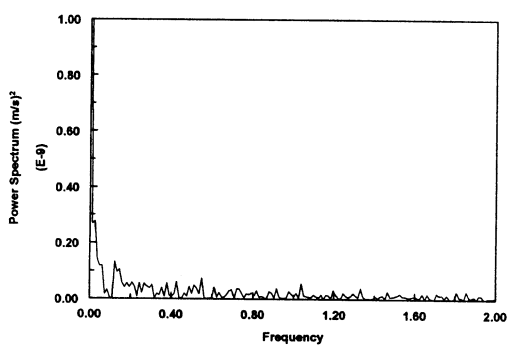

Figure 4.3.1.12-h Power spectrum of the instantaneous mass transfer coefficient at Vsl=0.5 m/s and Vsg=3.0 m/s in water/gas flow

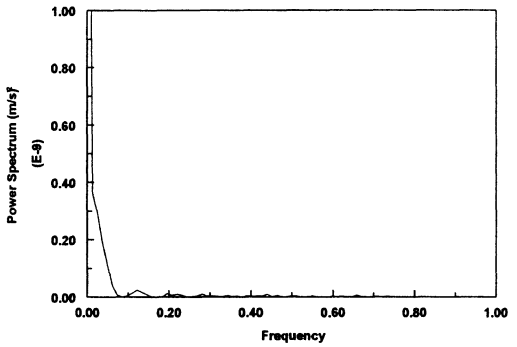

Figure 4.3.1.13-f Power spectrum of the instantaneous mass transfer coefficient at Vsl=0.8 m/s and Vsg=1.4 m/s in water/gas flow

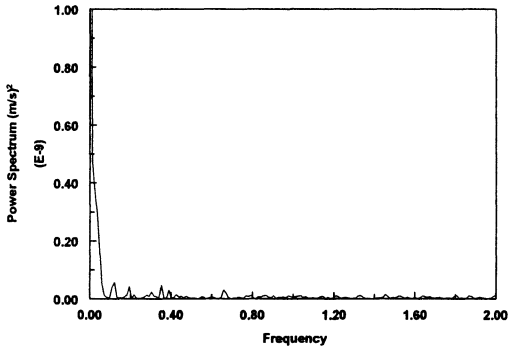

Figure 4.3.1.13-g Power spectrum of the instantaneous mass transfer coefficient at Vsl=0.8 m/s and Vsg=2.4 m/s in water/gas flow

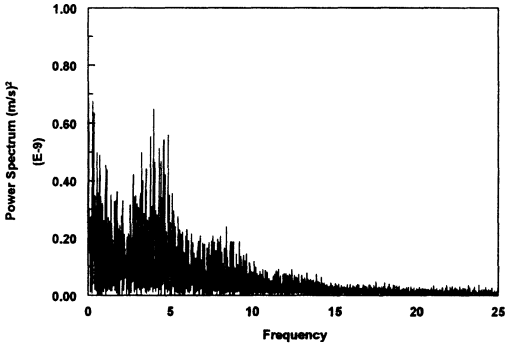

Figure 4.3.1.13-h Power spectrum of the instantaneous mass transfer coefficient at Vsl=0.8 m/s and Vsg=3.0 m/s in water/gas flow

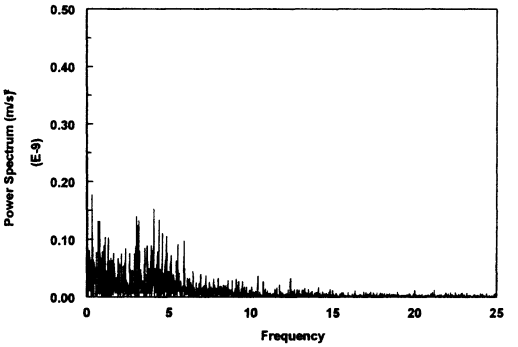

Figure 4.3.1.13-i Power spectrum of the instantaneous mass transfer coefficient at Vsl=0.8 m/s and Vsg=3.6 m/s in water/gas flow

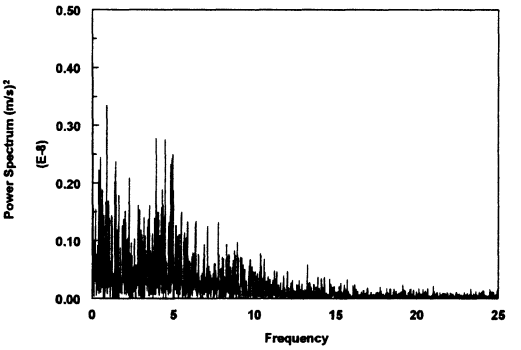

Figure 4.3.1.13-j Power spectrum of the instantaneous mass transfer coefficient at Vsl=0.8 m/s and Vsg=4.8 m/s in water/gas flow

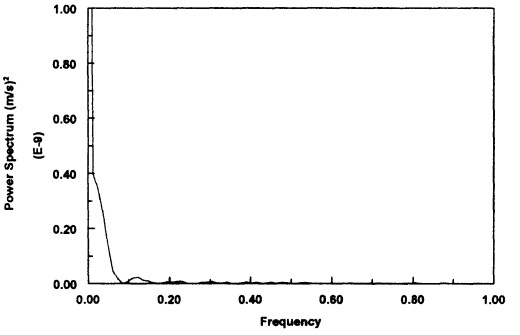

Figure 4.3.1.14-f Power spectrum of the instantaneous mass transfer coefficient at Vsl=1.0 m/s and Vsg=1.4 m/s in water/gas flow

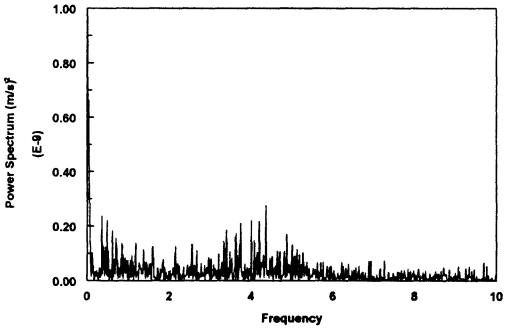

Figure 4.3.1.14-g Power spectrum of the instantaneous mass transfer coefficient at Vsl=1.0 m/s and Vsg=2.4 m/s in water/gas flow

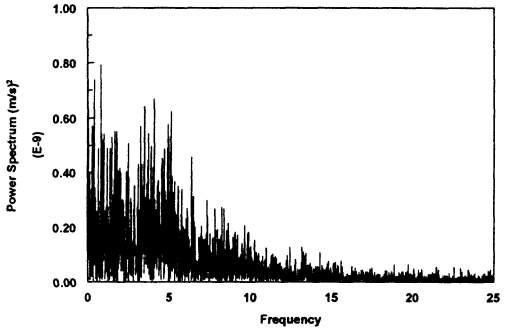

Figure 4.3.1.14-h Power spectrum of the instantaneous mass transfer coefficient at Vsl=1.0 m/s and Vsg=3.0 m/s in water/gas flow

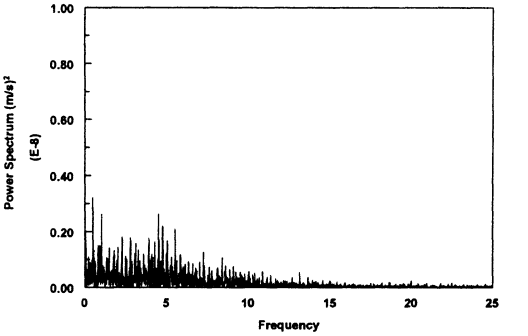

Figure 4.3.1.14-i Power spectrum of the instantaneous mass transfer coefficient at Vsl=1.0 m/s and Vsg=3.6 m/s in water/gas flow

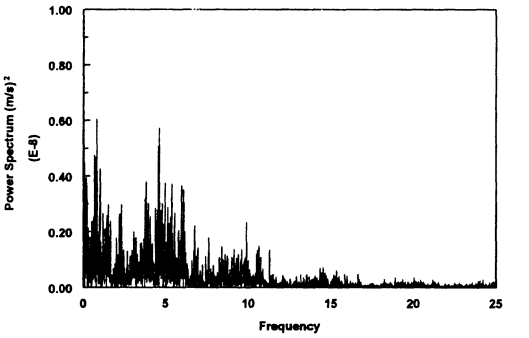

Figure 4.3.1.14-j Power spectrum of the instantaneous mass transfer coefficient at Vsl=1.0 m/s and Vsg=4.8 m/s in water/gas flow

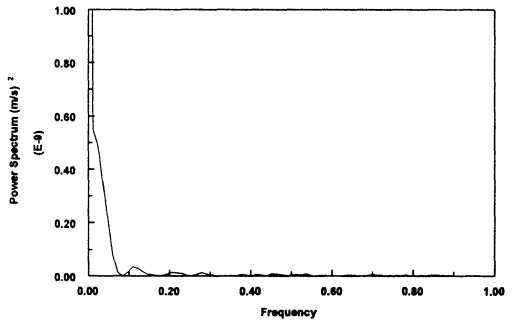

Figure 4.3.1.15-f Power spectrum of the instantaneous mass transfer coefficient at Vsl=1.2 m/s and Vsg=1.4 m/s in water/gas flow

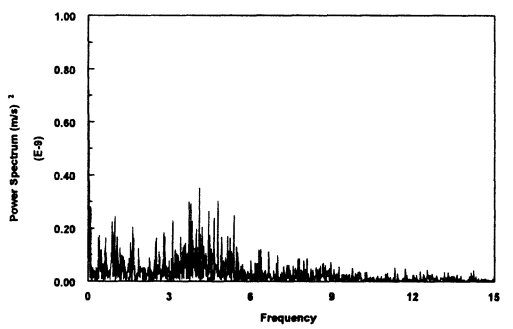

Figure 4.3.1.15-g Power spectrum of the instantaneous mass transfer coefficient at Vsl=1.2 m/s and Vsg=2.4 m/s in water/gas flow

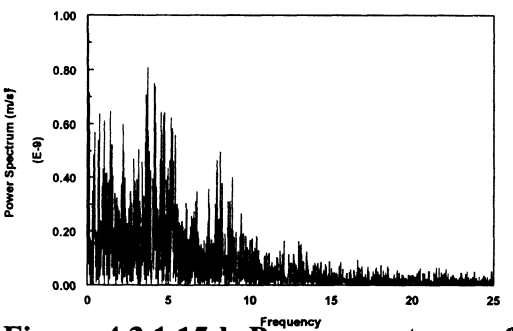

Figure 4.3.1.15-h Power spectrum of the instantaneous mass transfer coefficient at Vsl=1.2 m/s and Vsg=3.0 m/s in water/gas flow

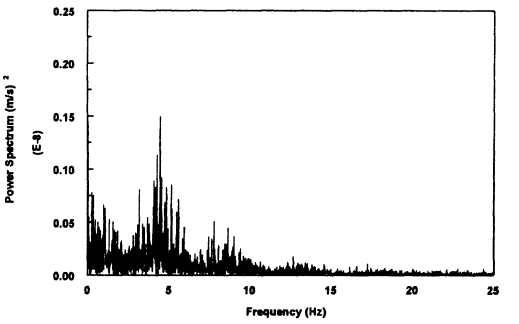

Figure 4.3.1.15-i Power spectrum of the instantaneous mass transfer coefficient at Vsl=1.2 m/s and Vsg=3.6 m/s in water/gas flow

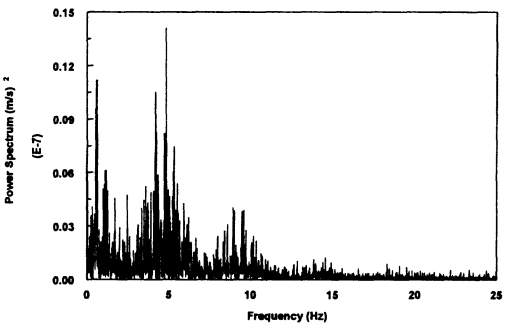

Figure 4.3.1.15-j Power spectrum of the instantaneous mass transfer coefficient at Vsl=1.2 m/s and Vsg=4.8 m/s in water/gas flow

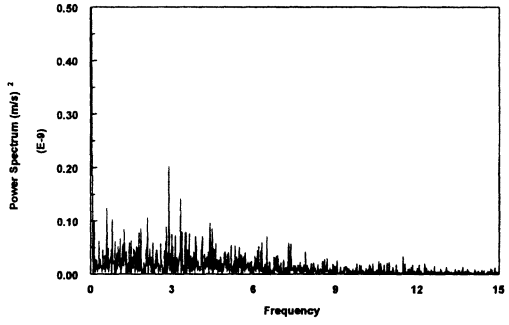

Figure 4.3.1.16-f Power spectrum of the instantaneous mass transfer coefficient at Vsl=1.5 m/s and Vsg=1.4 m/s in water/gas flow

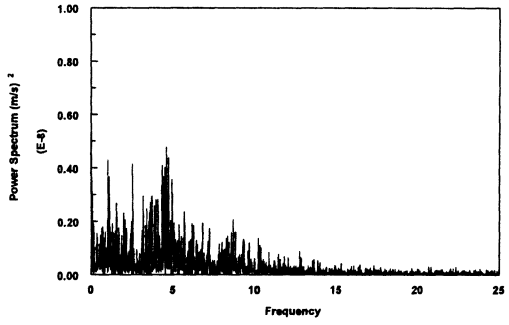

Figure 4.3.1.16-i Power spectrum of the instantaneous mass transfer coefficient at Vsl=1.5 m/s and Vsg=3.6 m/s in water/gas flow

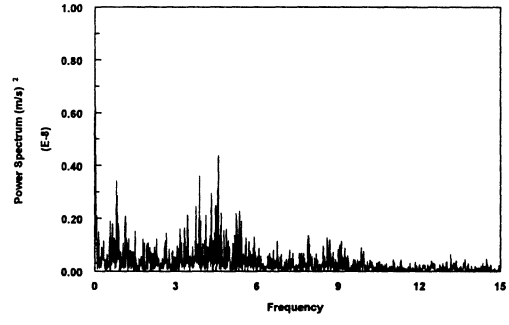

Figure 4.3.1.16-g Power spectrum of the instantaneous mass transfer coefficient at Vsl=1.5 m/s and Vsg=2.4 m/s in water/gas flow

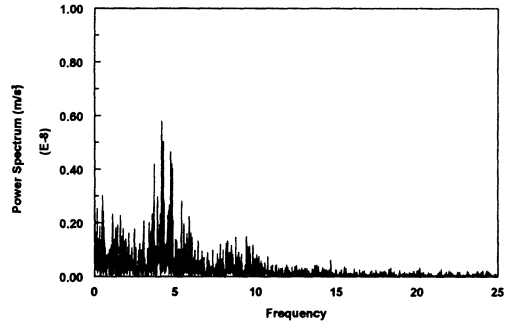

Figure 4.3.1.16-j Power spectrum of the instantaneous mass transfer coefficient at Vsl=1.5 m/s and Vsg=4.8 m/s in water/gas flow

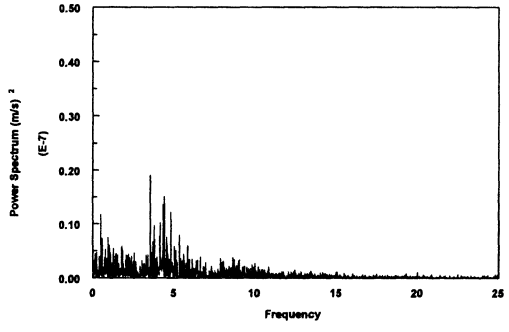

Figure 4.3.1.16-h Power spectrum of the instantaneous mass transfer coefficient at Vsl=1.5 m/s and Vsg=3.0 m/s in water/gas flow

Figure 4.3.1.11-g corresponds to the instantaneous mass transfer coefficient in Figure 4.3.1.5-g. Since the differences between Figure 4.3.1.5-f and Figure 4.3.1.5-g are very small, the FFT results also show only a small change in the FFT.

Figures 4.3.1.11-h, i, j just reflect the FFT information of Figures 4.3.1.5-h, i, j, respectively. The differences between Figures 4.3.1.5-h and 4.3.1.5-i are small except for the fact that one high amplitude peak appears in Figure 4.3.1.5-i. Their dominant frequencies are 4.4 and 4.5 respectively (also refer to Table 4.3.1.7), which are very close. The average power spectrum in Figure 4.3.1.11-i is 0.17×10^{-9} $(m/s)^2$, which is much greater than the 0.04×10^{-9} $(m/s)^2$ shown in Figure 4.3.1.13-h. It is the only high amplitude peak appearing on Figure 4.3.1.5-i that increases the power spectrum significantly.

After the superficial gas velocity is further increased from 3.6 to 4.8 m/s, more peaks appear, and the dominant frequency increases from 4.5 to 5.0 Hz as shown in Figures 4.3.1.11-i and j. The power spectrum in Figure 4.3.1.11-j is 1.2×10^{-9} $(m/s)^2$, much higher than the 0.17×10^{-9} $(m/s)^2$ in Figure 4.3.1.11-i. Similar results are noted in Figures 4.3.1.12 to 4.3.1.16.

Table 4.3.1.7 compares the dominant frequency and the power spectrum of the instantaneous mass transfer coefficient in different flow conditions. The dominant frequency represents the frequency of pulses of bubble collapsing in the slug mixing zone. The dominant frequency gradually reaches 4.5~5.0 Hz with the increase of superficial liquid velocity and superficial gas velocity. For example, at a low superficial gas velocity, e.g. 2.4 m/s, the dominant frequency is 0.12 Hz at a 0.2 m/s

superficial liquid velocity. With the increase of the superficial liquid velocity, it increases to 0.1, 0.1, 4.2, 4.0, 4.5 Hz at 0.5, 0.8, 1.0, 1.2, and 1.5 m/s superficial liquid velocity, respectively. This points out that more and more pulses of bubbles have collapsed at the bottom of the pipe with the increase of the superficial liquid velocity. It is observed that there is a transition point where the dominant frequency surges from 0.1 to 4.2 Hz as shown in Figure 4.3.1.17 and Table 4.3.1.7. This occurs about 42 times when the superficial liquid velocity changes from 0.8 m/s to 1.0 m/s. It means that there are fewer pulses of bubble in the mixing zone at 0.8 m/s superficial liquid velocity than at the 1.0 m/s superficial liquid velocity with 2.4 m/s superficial gas velocity. Similar results are observed between the 1.2 m/s and the 1.5 m/s superficial liquid velocities at the 1.4 m/s superficial gas velocity, where the dominant frequency changes about 25 times, from 0.03 to 0.21 Hz.

Table 4.3.1.7 Power spectrum analysis of the instantaneous mass transfer coefficients in different slug flows

	Vsg (m/s)									
	1.4		2.4		3.0		3.6		4.8	
Vsl (m/s)	F* (Hz)	P* $\times 10^{-9}$	F (Hz)	P $\times 10^{-9}$	F (Hz)	P $\times 10^{-9}$	F (Hz)	P $\times 10^{-9}$	F (Hz)	P $\times 10^{-9}$
0.2	0.20	0.02	0.12	0.07	4.4	0.04	4.5	0.17	5.0	1.2
0.5	0.14	0.02	0.1	0.08	4.4	0.05	4.3	0.15	5.0	1.1
0.8	0.12	0.03	0.1	0.06	4.5	0.66	4.0	0.16	5.0	2.6
1.0	0.12	0.02	4.2	0.28	5.0	0.63	4.5	2.60	4.8	5.8
1.2	0.12	0.03	4.0	0.35	4.0	0.80	4.2	1.5	4.6	13.8
1.5	3.0	0.21	4.5	4.5	4.5	15	4.5	4.8	4.5	5.8

* F: dominant frequency of the instantaneous mass transfer coefficient (Hz)
* P: power spectrum of the instantaneous mass transfer coefficient $((m/s)^2)$

Figure 4.3.1.18 shows the corresponding power spectrum of the instantaneous mass transfer coefficients at each flow condition. The power spectrum refers to the energy level and the amplitude of the instantaneous mass transfer coefficient. Through this figure, the energy level of the bubbles in the slug flow can be identified.

At a 1.4 m/s superficial gas velocity, the power spectrum is low compared to that at a higher superficial gas velocity. This means that the bubbles have less energy when they hit the bottom of the pipe, which leads to a lower enhancement of the mass transfer coefficient.

However, the power spectrum in other superficial gas velocities, e.g. 2.4, 3.0, 3.6, and 4.8 m/s, begins to show the existence of bubble collapse. For example, at a 2.4 m/s superficial gas velocity, a significant surge in the power spectrum appears at a 1.5 m/s superficial liquid velocity (refer to Table 4.3.1.7). It has changed from 0.35×10^{-9} to 4.5×10^{-9} $(m/s)^2$ when the superficial liquid velocity increases from 1.2 m/s to 1.5 m/s.

It is noticed that the dominant frequency and power spectrum should be evaluated together when the influence of bubble is to be investigated. For example, at a 2.4 m/s superficial gas velocity, the dominant frequency of pulses of bubbles reaches around 4.2, 4.0, and 4.5 Hz at 1.0, 1.2, and 1.5 m/s superficial liquid velocity, respectively. These dominant frequencies in the same 4.0 Hz level indicate that the pulses of bubble appear stable. However, a lower power spectrum of 0.28×10^{-9} and

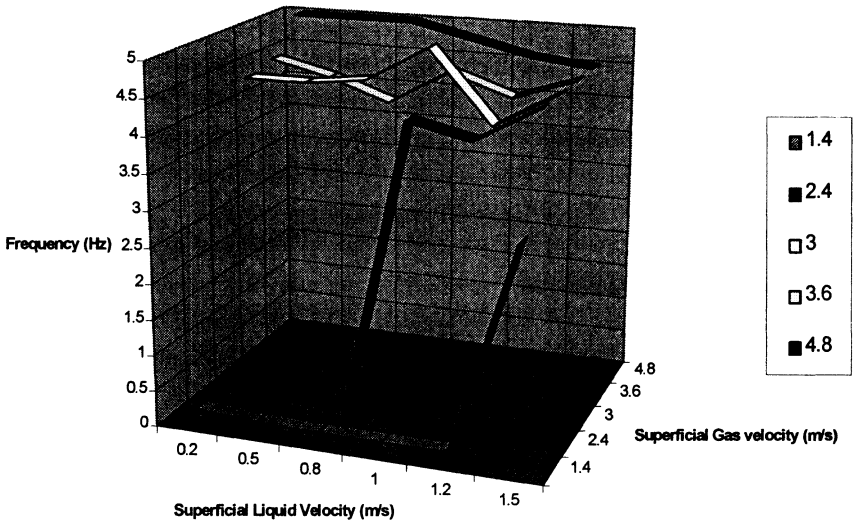

Figure 4.3.1.17 Dominant frequency of the instantaneous mass transfer coefficients in different slug flows

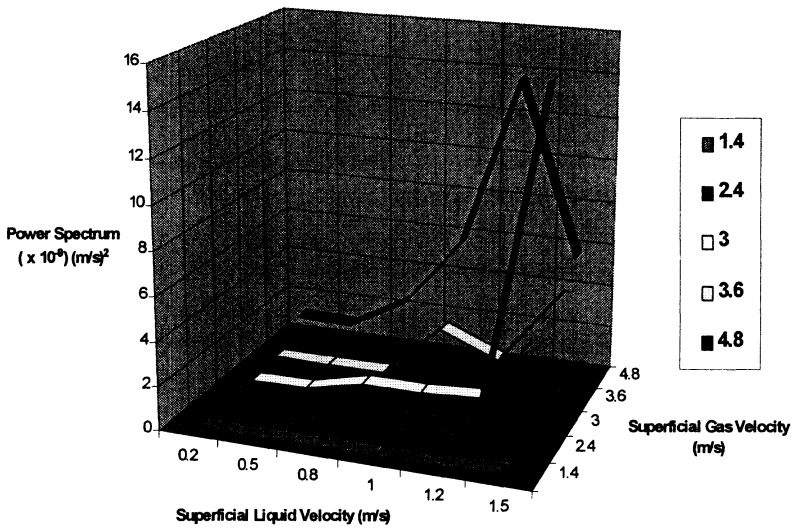

Figure 4.3.1.18 Power spectrum of the instantaneous mass transfer coefficients in different slug flows

0.35×10^{-9} $(m/s)^2$ at a 1.0 m/s and a 1.2 m/s superficial liquid velocity, respectively in comparison with a higher power spectrum of 4.5×10^{-9} $(m/s)^2$ at 1.5 m/s means that the contribution of bubble collapsing at 1.0 m/s and 1.2 m/s superficial liquid velocity can be negligible.

A new parameter, power spectrum index (PSI) is tentatively proposed as a criterion to evaluate the energy level of bubble collapsing on the bottom of the pipe. It further points out the mass transfer enhancement effect and the potential mechanical effect of bubble impact in slug flow.

$PSI = (0, 1.0 \times 10^{-8})$	energy level one PSI1
$PSI = [1.0 \times 10^{-8}, 1.0 \times 10^{-9}]$	energy level two PSI2
$PSI = (1.0 \times 10^{-9}, \infty)$	energy level three PSI3

In Figure 4.3.1.18, it is observed that two peaks of power spectrum (PSI3) exist. Mass transfers at a 1.2 m/s superficial liquid velocity with a 4.8 m/s superficial gas velocity, a 1.5 m/s superficial liquid velocity with a 3.6 m/s superficial gas velocity have the highest power spectrum, 13.8×10^{-9} and 15.0×10^{-9} $(m/s)^2$, respectively. It may be predicted that the bubble collapsing in the above two flow conditions have the highest contribution to the instantaneous mass transfer coefficient enhancement and to the mechanical effect on the metal surface or the corrosion product layer of the pipe. These conclusions cannot be drawn from the comparison of the average mass transfer coefficients. Therefore, the analysis of the instantaneous mass transfer coefficients becomes critical to identify the effect of multiphase flow on the mass transfer in corrosion.

4.3.2 Water/Gas/Oil Three-Phase Slug Flow with 20% LVT oil

4.3.2.1 Average Mass Transfer Coefficient in Different Flow Regimes

Table 4.3.2.1 shows the test matrix for the mass transfer measurements in single and multiphase flows. Table 4.3.2.2 collects the flow regime information at different superficial liquid velocities from 0.2 to 1.5 m/s and superficial gas velocity from 0 to 4.8 m/s. Three kinds of flow were examined, full pipe flow, plug flow at a lower superficial gas velocity, e.g. 0.4, 0.6, 0.8, and 1.0 m/s, and slug flow at a higher superficial gas velocity, e.g. 1.4, 2.4, 3.0, 3.6, and 4.8 /s. Table 4.3.2.3 indicates the plug and slug frequency for each flow condition in the presence of 20% input oil.

Table 4.3.2.1 Experimental test matrix for multiphase flow with 20% input oil

Superficial liquid velocity (m/s)	0.2, 0.5, 0.8, 1.0, 1.2, 1.5
Superficial gas velocity (m/s)	0, 0.4, 0.6, 0.8, 1.0 1.4, 2.4, 3.0, 3.6, 4.8
Gas	Nitrogen
Liquid	0.01 M potassium ferro-ferricyanide, 1.0 N sodium hydroxide, and 20% input LVT oil
Temperature (°C)	20

Figure 4.3.2.1 gives the relationship between the superficial gas velocity and the slug frequency. For the superficial gas velocities studied, i.e. below 5 m/s, the slug frequency does not change much with the increase in the superficial gas velocity. For example, at a 0.5 m/s superficial liquid velocity the slug frequency decreases from 13 slug/min at a 1.4 m/s superficial gas velocity to 10 slug/min at a 4.8 m/s superficial gas velocity.

Table 4.3.2.2 Flow regimes corresponding to different gas and liquid velocities with 20 % input oil

Flow regime		Vsg (m/s)									
		0	0.4	0.6	0.8	1.0	1.4	2.4	3.0	3.6	4.8
Vsl (m/s)	0.2	FF*	PF*	PF	PF	PF	SF*	SF	SF	SF	SF
	0.5	FF	PF	PF	PF	SF	SF	SF	SF	SF	SF
	0.8	FF	PF	PF	PF	SF	SF	SF	SF	SF	SF
	1.0	FF	PF	PF	PF	SF	SF	SF	SF	SF	SF
	1.2	FF	PF	PF	PF	SF	SF	SF	SF	SF	SF
	1.5	FF	PF	SF	SF	SF	SF	SF	SF	SF	SF

* FF: Full pipe flow, PF: Plug flow, SF: Slug flow

Table 4.3.2.3 Plug and slug frequency comparison in the flow with 20 % input oil

Frequency (/min)		Vsg (m/s)								
		0.4	0.6	0.8	1.0	1.4	2.4	3.0	3.6	4.8
Vsl (m/s)	0.2	15	8	9	9	10	13	12	13	11
	0.5	17	12	11	13	13	12	12	13	10
	0.8	36	38	31	32	36	35	34	37	36
	1.0	66	55	54	60	52	52	52	50	52
	1.2	81	82	75	68	72	70	69	67	65
	1.5	102	117	105	90	90	92	90	90	88

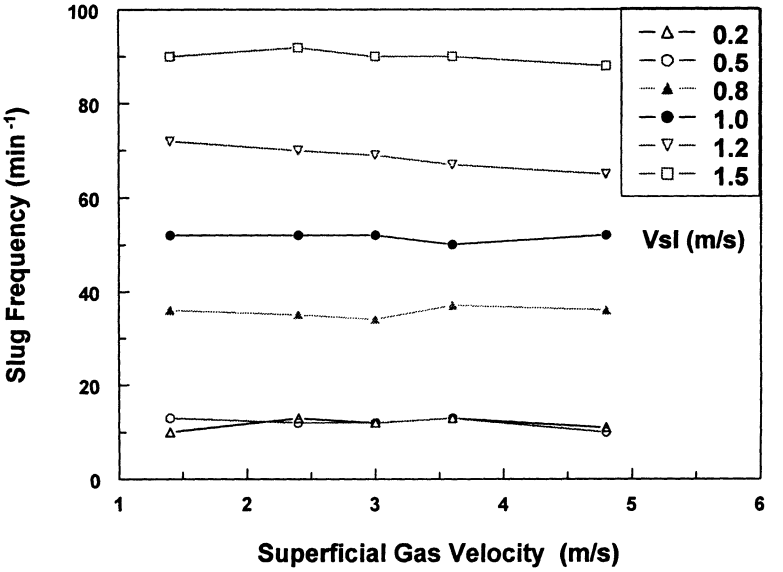

Figure 4.3.2.1 Effect of superficial gas velocity on the slug frequency with 20% input oil

Figure 4.3.2.2 shows the relationship between the superficial liquid velocity and the slug frequency. At each superficial liquid velocity, the frequencies at different superficial gas velocities are very similar. This indicates the small effect of superficial gas velocity on the slug frequency. The slug frequency usually increases with the increase in the superficial liquid velocity. For example, at 2.4 m/s superficial gas velocity, the slug frequency will change from 13 slug/min at 0.2 m/s superficial liquid velocity to 12, 35, 52, 70, 92 slug/min at 0.5, 0.8, 1.0, 1.2, and 1.5 m/s superficial liquid velocity, respectively. It again proves that the liquid velocity has a determined effect on the slug frequency (Wilkens, 1997).

At each flow condition, potentiodynamic measurements were taken to determine the average mass transfer coefficient. Figure 4.3.2.3 shows the effect of superficial gas velocity on the average mass transfer coefficient. At a lower superficial gas velocity (Vsg<3.0 m/s), it clearly shows that the average mass transfer coefficient increases with an increase in the superficial gas velocity. However, above this critical velocity (Vsg>3 m/s) the average mass transfer coefficient does not change much with a further increase of the superficial gas velocity. For instance, at 0.8 m/s full pipe flow the mass transfer coefficient is 8.7×10^{-5} m/s. With the increase of the superficial gas velocity from 0 through 3 m/s to 4.8 m/s, the mass transfer coefficient increases from 8.7×10^{-5} to 1.45×10^{-4} m/s and then remains constant. This is because the slug flow produces a highly turbulent flow and the average mass transfer coefficient becomes almost constant when the superficial gas velocity is above the critical velocity. In addition, this critical superficial gas velocity has increased from 1.0 m/s in the slug

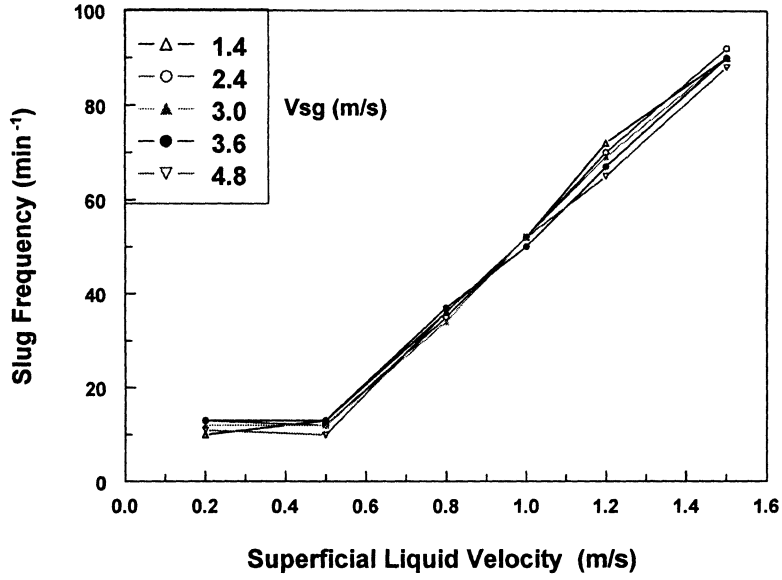

Figure 4.3.2.2 Effect of superficial liquid velocity on the slug frequency with 20% input oil

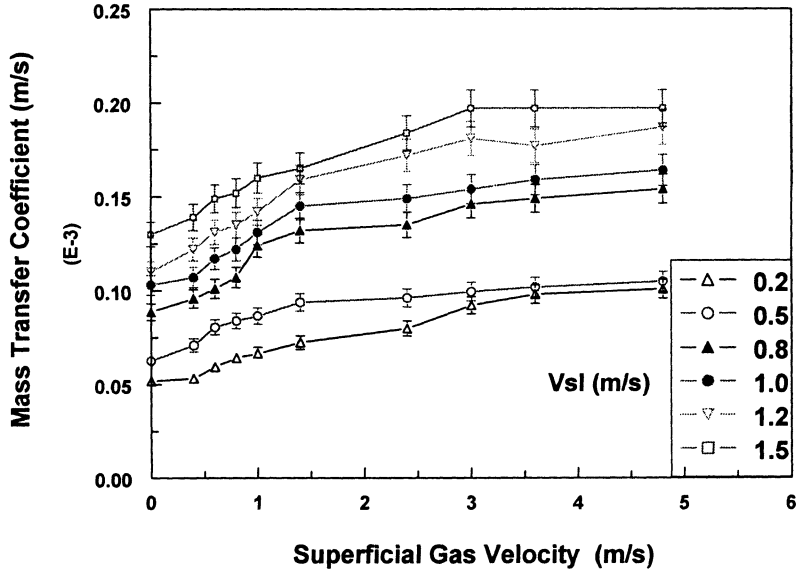

Figure 4.3.2.3 Effect of superficial gas velocity on the average mass transfer coefficient in slug flow and other flows with 20% input oil

flow without input oil to 3.0 m/s in this study with 20 % input oil. This shift proves that the mixing of oil and water is not complete until 3 m/s superficial gas velocity as shown in Figures 4.3.2.5 and 4.3.2.6. The mass transfer coefficients do not change significantly until the annual flow is reached at a high superficial gas velocity above 10 m/s.

Figure 4.3.2.4 indicates the effect of the superficial liquid velocity on the average mass transfer coefficient. It proves that the liquid velocity has a pronounced effect on the average mass transfer coefficient. The mass transfer coefficient always gradually increases with an increase of the superficial liquid velocity at each superficial gas velocity. For example, at 0.6 m/s superficial gas velocity the mass transfer coefficient increases from 6.0×10^{-5} m/s at 0.2 m/s superficial liquid velocity to 1.48×10^{-4} m/s at 1.5 m/s superficial liquid velocity.

Figure 4.3.2.5 shows the effect of the superficial gas velocity on the in situ oil percentage at the bottom of pipe. At a lower superficial gas velocity from 0 to 3 m/s, the in situ oil percentage increases from the minimum value to the plateau value. For instance, at the superficial liquid velocity of 1.2 m/s it increases from 8.5 % at full pipe flow to 15.4% at a 1.0 m/s superficial gas velocity. When the superficial gas velocity increases further, the in situ oil percentage has a small increase. Therefore, the influence of the superficial gas velocity on the in situ oil percentage becomes negligible when it is above the critical superficial gas velocity. It is also observed that this critical superficial gas velocity changes with different superficial liquid velocities as shown in Figure 4.3.2.5. The significant influence of the superficial liquid velocity

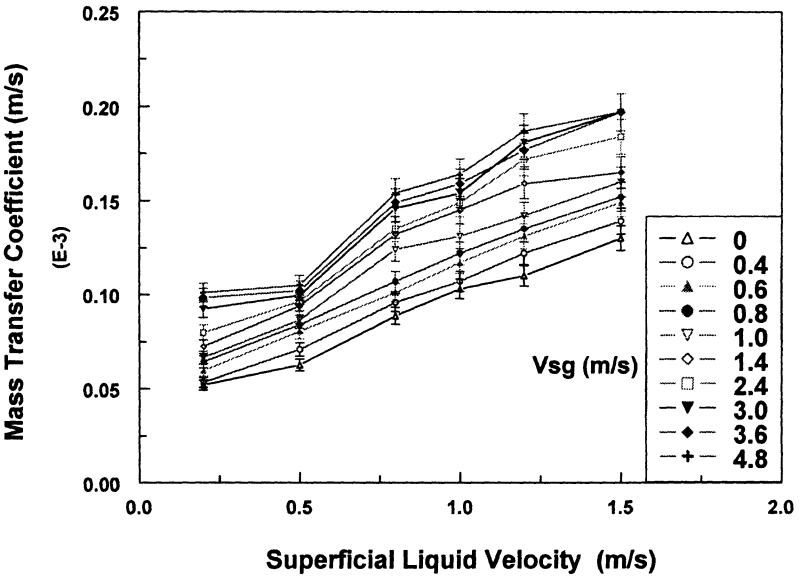

Figure 4.3.2.4 Effect of superficial liquid velocity on the average mass transfer coefficient in slug flow and other flows with 20% input oil

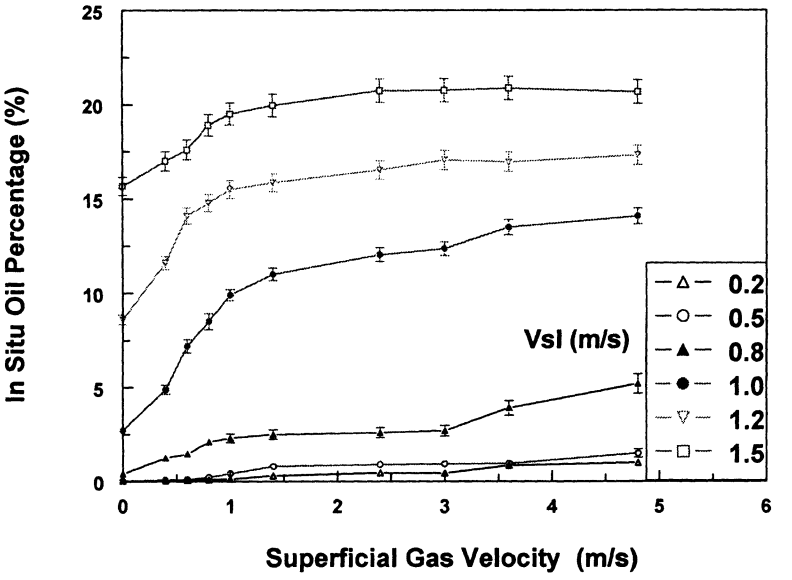

Figure 4.3.2.5 Effect of superficial gas velocity on the in situ oil percentage at the bottom of pipe in water/gas/oil three-phase flow with 20% input oil

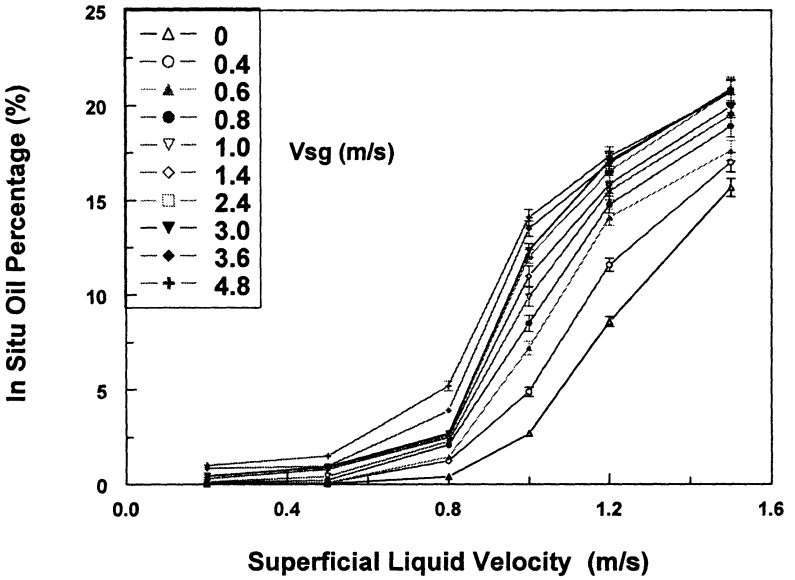

Figure 4.3.2.6 Effect of superficial liquid velocity on the in situ oil percentage at the bottom of pipe in water/gas/oil three-phase flow with 20% input oil

on the in situ oil percentage is noticed in Figure 4.3.2.6. When the superficial liquid velocity is lower than 0.8 m/s, the oil percentage is below 5% because there is small turbulence in plug flow. The water layer and the oil layer are separate in the pipe. A small amount of oil enters the water layer occasionally. When the superficial liquid velocity is above 0.8 m/s, the in situ oil percentage increases quickly with the increase of the superficial liquid velocity.

From these results it is concluded that the average mass transfer coefficient is directly related to the superficial liquid velocity, the superficial gas velocity, and the oil percentage. However, other characteristics of the slug flow, such as slug frequency and slug length, are not available from the above analysis. The analysis of the instantaneous mass transfer coefficient becomes necessary and is discussed next.

4.3.2.2 Instantaneous Mass Transfer Coefficient in Moving Slug Flow

It is observed that the instantaneous mass transfer coefficient in the water/gas/oil three-phase flow has the same characteristics as when it is in water/gas two-phase multiphase flow as discussed in the previous section. Therefore, only one set of experimental results at Vsl=1.0 m/s and difference superficial gas velocity are discussed in this section.

Figures 4.3.2.7-a to j examine the flow at a 1.0 m/s superficial liquid velocity and at different superficial gas velocities. Figure 4.3.2.7-a shows the instantaneous mass transfer coefficient in the full pipe flow. The fluctuations reflect just the nature of the turbulence and the mass transfer coefficient is almost constant at about 9.6×10^{-5} m/s.

When the superficial gas velocity is increased to 0.4 m/s (Figure 4.3.2.7-b), the fluctuations are enhanced due to the formation of slow moving lumps of liquid or plugs. The average mass transfer coefficient is increased to about 1.0×10^{-5} m/s with fluctuations between 1.0×10^{-5} and 2.7×10^{-5} m/s. The fluctuation of the instantaneous mass transfer coefficient is increased further at a superficial gas velocity of 0.6 m/s (Figure 4.3.2.7-c). A comparison of Figures 4.3.2.7-b and c, which correspond to the plug flow, show that the frequency of these fluctuations is equal to the frequency of the plug flow.

The amplitude of these fluctuations becomes more and more significant with an increase in the superficial gas velocity, e.g. to 0.8, 1.0 m/s as shown in Figures 4.3.2.7-d and e. When the superficial gas velocity is increased to 1.0 m/s, slug flow

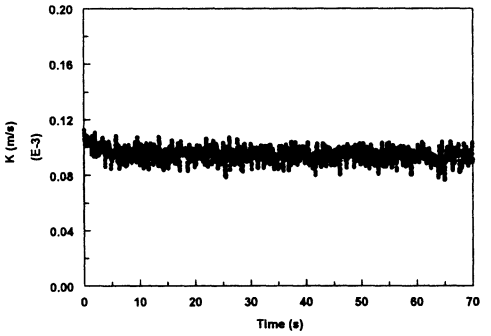

Figure 4.3.2.7-a Instantaneous mass transfer coefficient at Vsl=1.0 m/s and Vsg=0 m/s in water/gas/oil flow with 20% oil

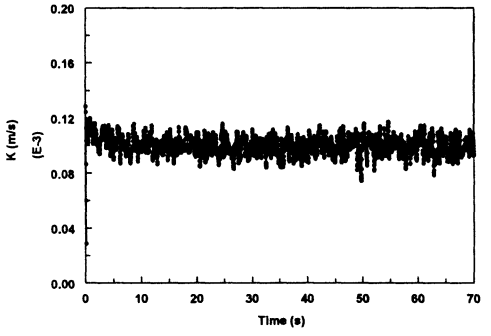

Figure 4.3.2.7-b Instantaneous mass transfer coefficient at Vsl=1.0 m/s and Vsg=0.4 m/s in water/gas/oil flow with 20% oil

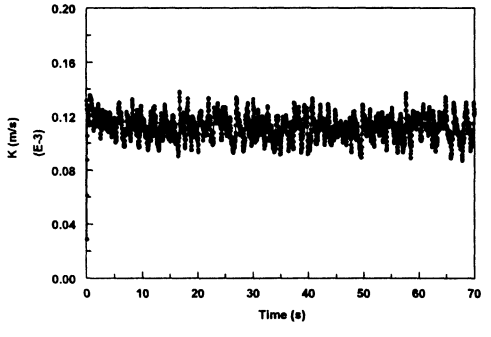

Figure 4.3.2.7-c Instantaneous mass transfer coefficient at Vsl=1.0 m/s and Vsg=0.6 m/s in water/gas/oil flow with 20% oil

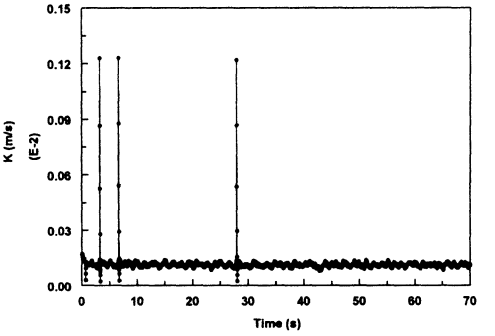

Figure 4.3.2.7-d Instantaneous mass transfer coefficient at Vsl=1.0 m/s and Vsg=0.8 m/s in water/gas/oil flow with 20% oil

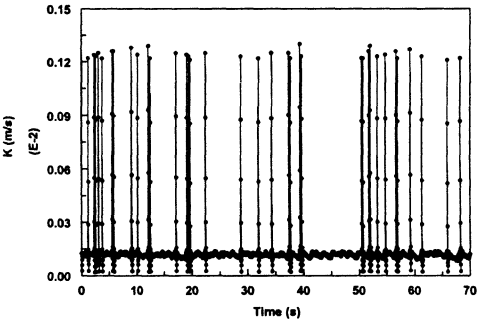

Figure 4.3.2.7-e Instantaneous mass transfer coefficient at Vsl=1.0 m/s and Vsg=1.0 m/s in water/gas/oil flow with 20% oil

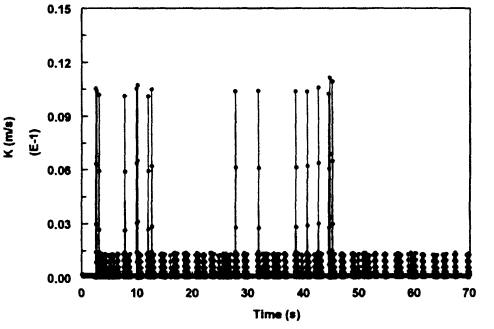

Figure 4.3.2.7-f Instantaneous mass transfer coefficient at Vsl=1.0 m/s and Vsg=1.4 m/s in water/gas/oil flow with 20% oil

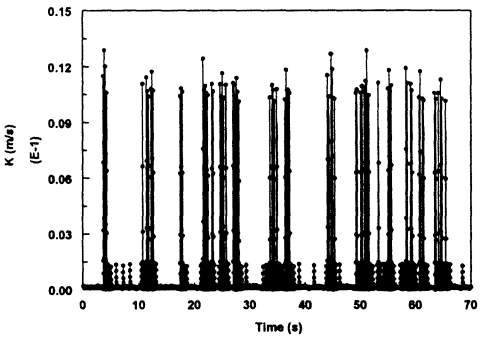

Figure 4.3.2.7-g Instantaneous mass transfer coefficient at Vsl=1.0 m/s and Vsg=2.4 m/s in water/gas/oil flow with 20% oil

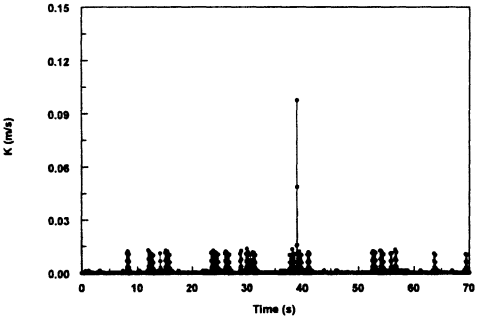

Figure 4.3.2.7-i Instantaneous mass transfer coefficient at Vsl=1.0 m/s and Vsg=3.6 m/s in water/gas/oil flow with 20% oil

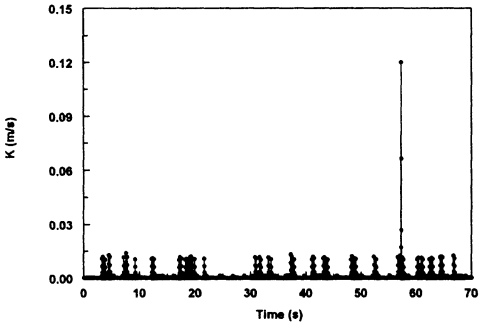

Figure 4.3.2.7-h Instantaneous mass transfer coefficient at Vsl=1.0 m/s and Vsg=3.0 m/s in water/gas/oil flow with 20% oil

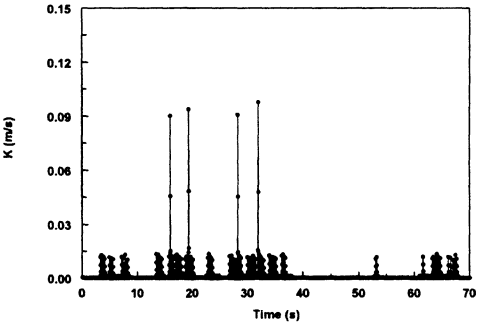

Figure 4.3.2.7-j Instantaneous mass transfer coefficient at Vsl=1.0 m/s and Vsg=4.8 m/s in water/gas/oil flow with 20% oil

appears and several large amplitude peaks appear in Figure 4.3.2.7-e. This is due to the formation of the mixing zone which produces high-energy bubbles which can hit the bottom of the pipe. The magnitude of the peaks is much higher than the plug flow. The instantaneous value in the slug is about 1.3×10^{-3} m/s which is about 12 times higher than that in the film region with a mass transfer coefficient of approximately 1.1×10^{-4} m/s.

With a further increase of the superficial gas velocity to 1.4 m/s (Figure 4.3.2.7-f), more high-energy bubbles appear and the instantaneous mass transfer peak increases correspondingly. The magnitude of the fluctuations reaches 1.05×10^{-3} m/s, about 110 times the value in the slug film. Figures 4.3.2.7-i and 4.3.2.7-j show similar results.

When the superficial liquid velocity increases, the frequency of the plug flow or the slug flow increases significantly. It is seen that the slug frequency has increased from about 12/min to a range of 90-120/min. It is difficult to visually determine the frequency of slug flow from the peaks of the instantaneous mass transfer coefficient.

Table 4.3.2.4 compares the mass transfer coefficient enhancement (E) at different flow conditions. The mass transfer enhancement has a similar trend as in a water/gas multiphase flow. The major difference in the water/gas/oil three-phase flow is that some high mass transfer enhancement, e.g. E=750, appears in some slug flow conditions. With the further increase of the superficial gas velocity (≥0.8 m/s) at each superficial liquid velocity, the mass transfer enhancement (E) has a significant change. For example, at a 1.0 m/s superficial liquid velocity the enhancement transfer enhancement can reach approximately 110 at 2.4 and 3.0 m/s superficial gas velocity and 750 at 3.6 and 4.8 m/s superficial gas velocity (Table 4.3.2.4). The corresponding peak instantaneous mass transfer coefficients are approximately 1.2×10^{-2}, 1.2×10^{-2}, 9×10^{-2}, and 9×10^{-2} m/s at superficial gas velocity 2.4, 3.0, 36, and 4.8 m/s, respectively. At these four superficial gas velocities, the corresponding mean mass transfer coefficients of Km do not change much and they have a value around $1.2 \times$

10^{-4} m/s. It is shown that at a superficial gas velocity of 3.6 m/s and 4.8 m/s under a superficial liquid velocity of 1.0 m/s there are three E factors, 12, 110, and 750 (Table 4.3.2.4). These three factors can represent three kinds of bubble impacts on the bottom of the pipe. This may be the bubble impact, and latterly, the bubble collapse and the strong collapse. These three kinds of bubbles have large differences in energy and will cause different mass transfer coefficients and shear stresses. Table 4.3.2.5 shows the power spectrum analysis of the instantaneous mass transfer coefficients in different slug flows with the 20% input oil. The analysis is similar to the discussion in Chapter 4.3.1.2.2. Therefore, further discussion is not necessary.

Table 4.3.2.4 Mass transfer coefficient enhancement in different flows with 20 % input oil

E*		Vsg (m/s)									
		0	0.4	0.6	0.8	1.0	1.4	2.4	3.0	3.6	4.8
Vsl (m/s)	0.2	1	1.5	1.8	1.8	1.9	2.2, 16	20, 160	20, 160	20, 160	20, 160
	0.5	1	1.4	1.5	2.2, 20	2.2, 20	2.2, 20	20, 160	20, 160	20, 160	20, 160
	0.8	1	1	1.2	1.5, 12	1.5, 12	12, 110	12, 110	12, 110	12, 110, 750	12, 110, 750
	1.0	1	1	1.2	1.3, 12	1.5, 12	12, 110	14, 110	14, 110	14, 110, 750	14, 110, 750
	1.2	1	1	12	12	12, 100	12, 110	12, 110	12, 110	12, 110	12, 110
	1.5	1	10	10, 85	10, 85	10, 85	10, 85	1.6	1.6	1.6	1.6

Jepson and Menezes in 1995 studied the effect of the viscosity of oil on corrosion in a three-phase flow. Oils with 2 cp and 96 cp have been used in experiments. The water cut ranged from 0 to 100 %. It was found that the oil with low

viscosity entrains more gas in the slug than the higher viscosity oil. The pressure drop across the slug is larger for the higher viscosity oil. It was also found that the corrosion rate in 96 cp oil/water mixture is higher than in the 2 cp oil/water mixture in the slug flow. In the study of cavitation pitting and erosion of aluminum 6061-T6 in mineral oil and water, it was found that the cavitation effect is stronger in the higher viscosity liquid (Rao and Buckley, 1983). Hence, it is concluded that the higher liquid viscosity and the higher cavitation increase the corrosion rate. It further confirms that a cavitation type phenomenon probably exists in the slug flow since the mass transfer enhancement caused by bubble impact increases with the increase of oil phase percentage in the slug flow.

Table 4.3.2.5 Power spectrum analysis of the instantaneous mass transfer coefficients in different slug flows with 20% input oil

	Vsg (m/s)									
	1.4		2.4		3.0		3.6		4.8	
Vsl (m/s)	F* (Hz)	P* $\times 10^{-9}$	F (Hz)	P $\times 10^{-9}$	F (Hz)	P $\times 10^{-9}$	F (Hz)	P $\times 10^{-9}$	F (Hz)	P $\times 10^{-9}$
0.2	0.16	0.07	5.0	2.0	5.0	1.0	5.0	32	5.0	1.0
0.5	4.0	0.1	4.9	14	5.0	14	5.0	30	4.8	7
0.8	4.1	2.2	4.6	16.4	4.5	33	4.6	52	4.8	100
1.0	4.9	5	4.9	32	4.9	58	4.9	71	4.8	91
1.2	4.4	25	4.7	1.3	4.7	5.0	0.9	0.03	5.0	0.5
1.5	4.8	30	0.9	0.006	1.0	0.01	1.3	0.006	1.2	0.007

* F: dominant frequency of the instantaneous mass transfer coefficient (Hz)
* P: power spectrum of the instantaneous mass transfer coefficient $((m/s)^2)$

4.3.3 Water/Gas/Oil Three-Phase Slug Flow with 40% LVT oil

4.3.3.1 Average Mass Transfer Coefficient in Different Flow Regimes

Table 4.3.3.1 shows an experimental test matrix for a multiphase flow with 40% input oil. Table 4.3.3.2 shows the flow regimes at different superficial gas velocity and superficial liquid velocity in the presence of 40% input oil. Three kinds of flow regimes were examined, full pipe flow, plug flow at a lower superficial gas velocity, e.g. 0.4, 0.6, 0.8, 1.0 m/s and slug flow at a higher superficial gas velocity, e.g. 1.4 to 4.8 m/s.

Table 4.3.3.1 Experimental test matrix for multiphase flow with 40% input oil

Superficial liquid velocity (m/s)	0.2, 0.5, 0.8, 1.0, 1.2, 1.5
Superficial gas velocity (m/s)	0, 0.4, 0.6, 0.8, 1.0 1.4, 2.4, 3.0, 3.6, 4.8
Gas	Nitrogen
Liquid	0.01 M potassium ferro-ferricyanide, 1.0 N sodium hydroxide, and 40% input LVT oil
Temperature (°C)	20

Table 4.3.3.3 indicates that plug and slug frequency for each flow condition in the presence of 40% input oil. Figures 4.3.3.1 and 4.3.3.2 show the effect of the superficial gas velocity and the superficial liquid velocity on the slug frequency respectively. The superficial liquid velocity has a determined influence on the slug frequency, which is the same as the conclusion drawn from experimental results in two phase slug flow and three-phase slug flow with the 20% input oil. There are some minor differences between the 20% oil and the 40 % oil. At a mediate superficial

Table 4.3.3.2 Flow regimes corresponding to different gas and liquid velocities with 40 % input oil

Flow regime		Vsg (m/s)									
		0	0.4	0.6	0.8	1.0	1.4	2.4	3.0	3.6	4.8
Vsl (m/s)	0.2	FF*	PF*	PF	SF	SF	SF*	SF	SF	SF	SF
	0.5	FF	PF	PF	SF	SF	PF	SF	SF	SF	SF
	0.8	FF	PF	PF	SF	SF	PF	SF	SF	SF	SF
	1.0	FF	PF	PF	SF	SF	SF	SF	SF	SF	SF
	1.2	FF	PF	PF	SF	SF	SF	SF	SF	SF	SF
	1.5	FF	PF	PF	SF	SF	SF	SF	SF	SF	SF

* FF: Full pipe flow, PF: Plug flow, SF: Slug flow

Table 4.3.3.3 Plug and slug frequency comparison in the flow with 40% input oil

Frequency (/min)		Vsg (m/s)								
		0.4	0.6	0.8	1.0	1.4	2.4	3.0	3.6	4.8
Vsl (m/s)	0.2	14	10	10	9	9	10	7	8	7
	0.5	16	10	10	8	10	8	10	7	8
	0.8	44	39	25	23	28	26	25	26	26
	1.0	65	70	45	45	44	43	44	44	42
	1.2	90	78	82	76	74	72	67	68	66
	1.5	130	120	108	108	96	96	96	96	94

liquid velocity (0.5 – 1.0 m/s), the system with the 40% input oil usually has a lower slug frequency. At a higher superficial liquid velocity (>1.2 m/s), the slug frequency is the same in both flow conditions.

Figures 4.3.3.3 and 4.3.3.4 show the effect of the superficial liquid velocity and the superficial gas velocity on the average mass transfer coefficient. The effect of the superficial liquid velocity on the average mass transfer coefficient is the same as in the 20% and the 0% oil system. The average mass transfer coefficient increases with

the increase of the superficial liquid velocity. However, the differences between these two systems are significant. First, there is no plateau in Figure 4.3.3.3. The average mass transfer coefficient continuously increases with the increase of the superficial gas velocity at the specific superficial liquid velocity, especially at a higher superficial liquid velocity (> 0.8 m/s) in the 40% oil system. Secondly, at a higher superficial liquid velocity (>0.8 m/s), the value of the average mass transfer coefficient in the system with the 40% input oil is higher than in the system with the 20% input oil. For example, at the superficial gas velocity of 4.8 m/s and the superficial liquid velocity of 1.0 m/s, the mass transfer coefficient is about 2.1×10^{-4} in the 40% system and 1.6×10^{-4} in the 20% system. The difference reason is caused by the stronger turbulence due to the mixing of water, oil droplets, and gas bubbles although the void fraction decreases with the increases of input oil percentage (Zhou and Jepson, 1994). It is predicted that the influence in oil droplets on the mass transfer is enhanced at this condition.

The study without the presence of oil has indicated that the effect of gas on the average mass transfer coefficient is negligible when the superficial gas velocity is above the critical superficial gas velocity of 1.4 m/s. In the 20% input oil system this critical superficial gas velocity increases to 3 m/s. And it increases to a higher value in the 40% oil system which is out of the measurement range and not shown in Figure 4.3.3.3. This change indicates that the influence of oil on the average mass transfer coefficient is significant.

Figure 4.3.3.5 and 4.3.3.6 shows the effect of the superficial gas velocity and

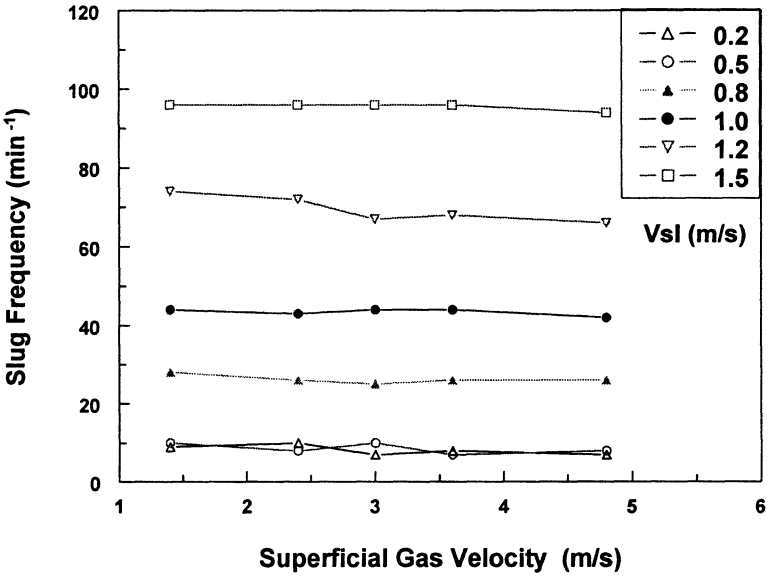

Figure 4.3.3.1 Effect of superficial gas velocity on the slug frequency with 40% input oil

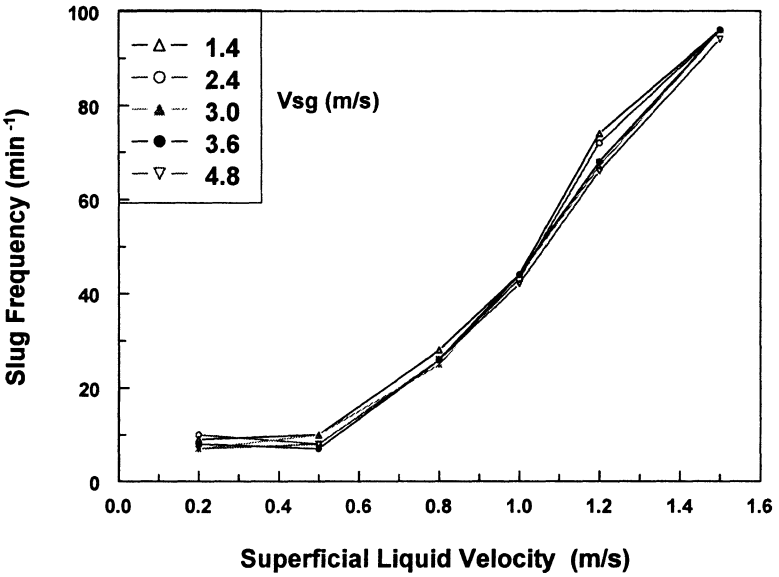

Figure 4.3.3.2 Effect of superficial liquid velocity on the slug frequency with 40% input oil

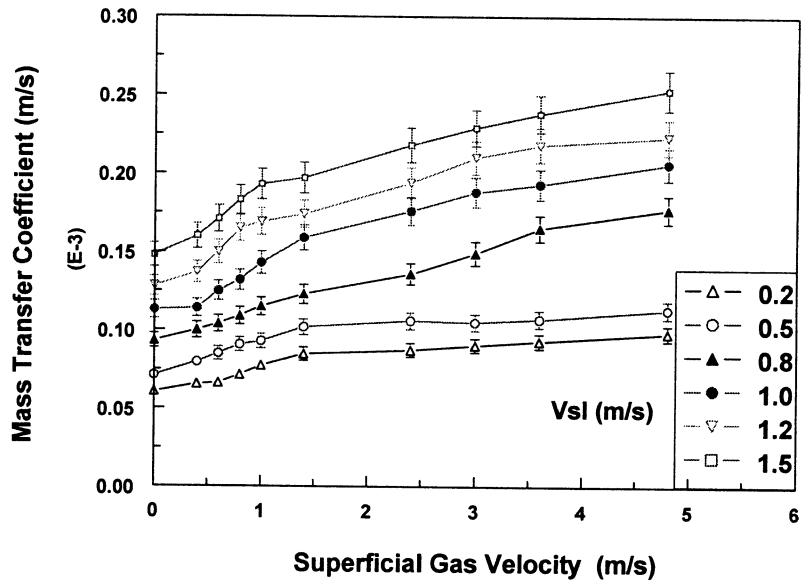

Figure 4.3.3.3 Effect of superficial gas velocity on the average mass transfer coefficient in slug flow and other flows with 40% input oil

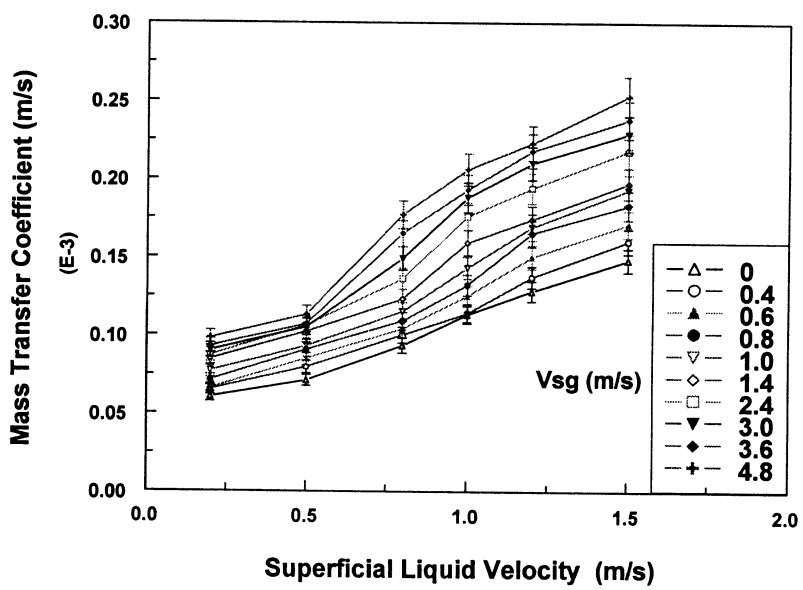

Figure 4.3.3.4 Effect of superficial gas velocity on the average mass transfer coefficient in slug flow and other flows with 40% input oil

the superficial liquid velocity on the in situ oil percentage at the bottom of the pipe in the slug flow system with the 40% input oil. The same conclusions could be drawn as in the slug flow with the 20% input oil. First, the superficial liquid velocity has a major influence on the in situ oil percentage because it directly changes the velocity gradient in the mass transfer boundary layer. Secondly, the influence of the superficial gas velocity on the in situ oil percentage varies with the specific superficial liquid velocity. For instance, at the superficial liquid velocity of 1.0 m/s the in situ oil changes from 7% to 38 % when the superficial gas velocity increases from 0 to 4.8 m/s. At the superficial liquid velocity of 1.5 m/s, it changes from 32.5% to 42.5%. However, at a 0.5 m/s low superficial liquid velocity, it only has a minor increase from 1% to 5.2% as shown in Figure 4.3.3.5. These differences in the in situ oil percentage will further determine the instantaneous mass transfer coefficient. However, the water layer at the bottom of the pipe acts like a filter that decreases the oil influence.

4.3.3.2 Instantaneous Mass Transfer Coefficient in Moving Slug Flow

The instantaneous mass transfer coefficient in the slug flow in the presence of the 40% oil is similar to that in the presence of the 20% oil. Here only the results obtained at superficial liquid velocity of 1.0 m/s and at multiple superficial gas velocities are shown in the Figures 4.3.3.7-a to j. A comparison of Figure 4.3.3.7 and Figure 4.3.2.7 indicates some differences between these two slug flow systems. First, the peak appears earlier at a 0.6 m/s superficial gas velocity in the 40% oil system. One reason is that in the presence of a higher percentage oil phase some oil droplets,

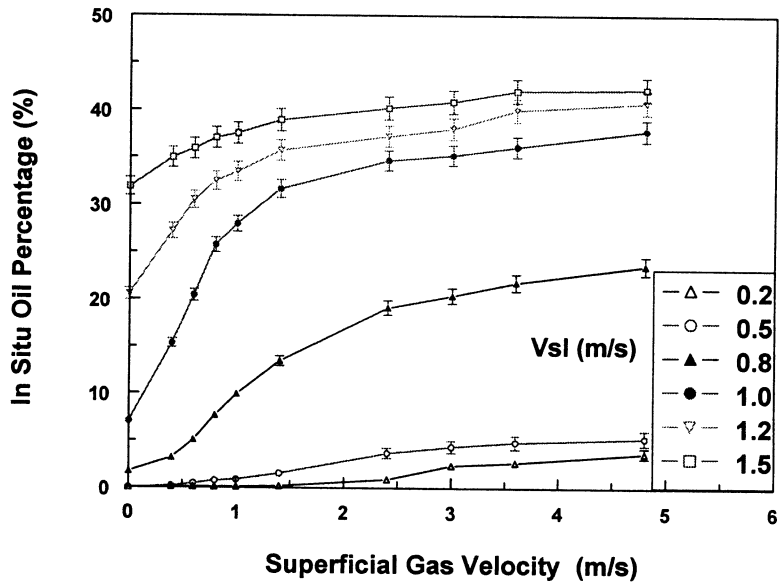

Figure 4.3.3.5 Effect of superficial gas velocity on the in situ oil percentage at the bottom of pipe in water/gas/oil three-phase flow with 40% input oil

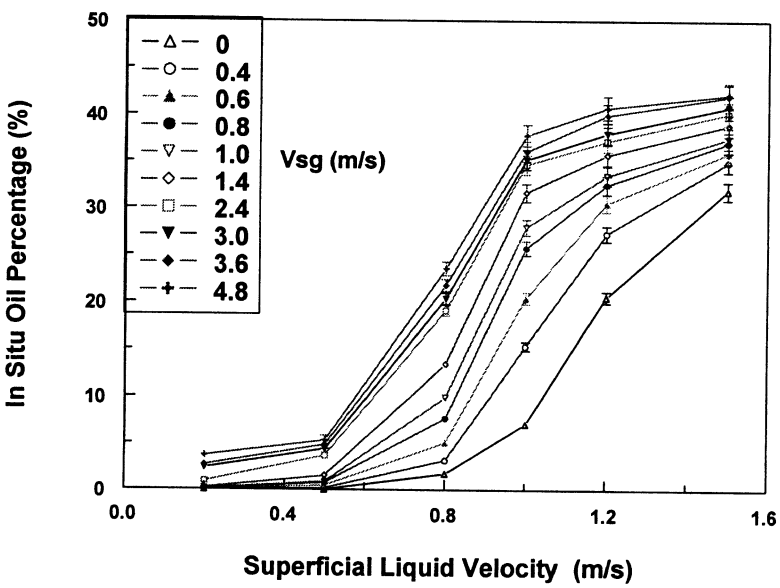

Figure 4.3.3.6 Effect of superficial liquid velocity on the in situ oil percentage at the bottom of pipe in water/gas/oil three-phase flow with 40% input oil

together with gas bubbles, can enter the mass transfer boundary layer easier. The void fraction in mixing zone in the 40% oil system also decreases (Zhou and Jepson, 1994), thus the possibility of oil droplet influence is enhanced. If the critical superficial gas velocity is defined as the point where the mass transfer peak begins to appear. Comparison of the instantaneous mass transfer results in slug flow without oil, with the 20% input oil, and the 40% input oil shows that this critical velocity has decreased from 2.4 m/s (Figure 4.3.1.8-g), to 0.8 m/s (Figure 4.3.2.7-d), then to 0.6 m/s (Figure 4.3.3.7-c) when the superficial liquid velocity is kept constant at 1.0 m/s. This shows that the oil phase has a significant contribution to the enhanced instantaneous mass transfer coefficient.

The analysis of the instantaneous mass transfer coefficient in slug flow in the presence of the 40% oil also gives a similar conclusion as previously drawn for it in slug flow in the presence of the 20% oil in Chapter 4.3.2.2. Therefore, the detailed discussion is not repeated here.

The power spectral density (p.s.d.) analysis can give a clear comparison of each signal in the frequency spectrum. Therefore, p.s.d. analysis of the instantaneous mass transfer coefficients was carried out to examine how turbulence at different frequency influences mass transfer.

Figure 4.3.3.8 gives a comparison of the p.s.d. of different superficial gas velocities at 1.0 m/s superficial liquid velocity in the slug flow with the 20% input oil. The curve for the full pipe flow has the lowest power spectral density ($(m/s)^2/Hz$). Its slope is also the biggest one among these five curves. It indicates that the turbulence

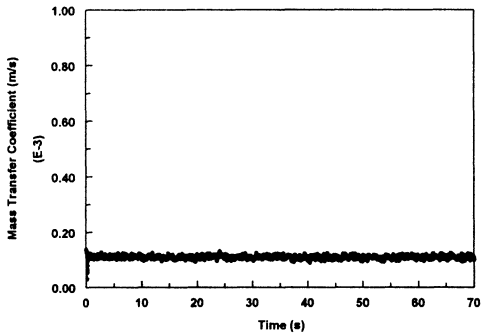

Figure 4.3.3.7-a Instantaneous mass transfer coefficient at Vsl=1.0 m/s and Vsg=0 m/s in water/gas/oil three-phase flow with 40% oil

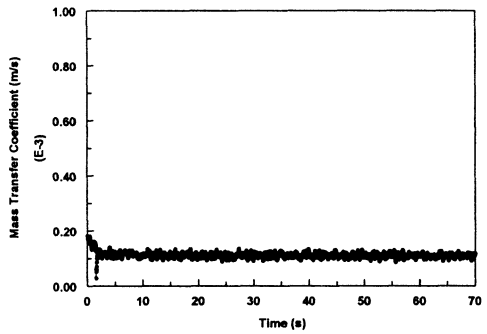

Figure 4.3.3.7-b Instantaneous mass transfer coefficient at Vsl=1.0 m/s and Vsg=0.4 m/s in water/gas/oil three-phase flow with 40% oil

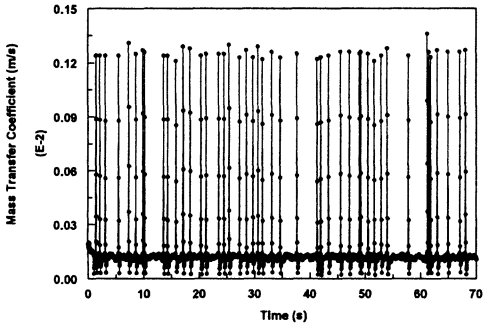

Figure 4.3.3.7-c Instantaneous mass transfer coefficient at Vsl=1.0 m/s and Vsg=0.6 m/s in water/gas/oil three-phase flow with 40% oil

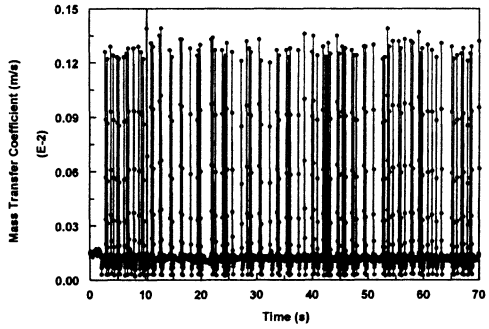

Figure 4.3.3.7-d Instantaneous mass transfer coefficient at Vsl=1.0 m/s and Vsg=0.8 m/s in water/gas/oil three-phase flow with 40% oil

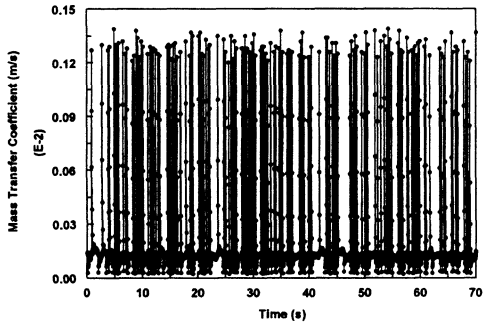

Figure 4.3.3.7-e Instantaneous mass transfer coefficient at Vsl=1.0 m/s and Vsg=1.0 m/s in water/gas/oil three-phase flow with 40% oil

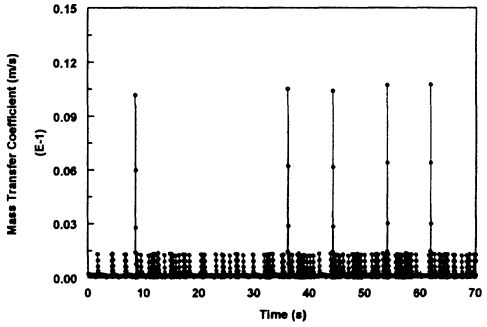

Figure 4.3.3.7-f Instantaneous mass transfer coefficient at Vsl=1.0 m/s and Vsg=1.4 m/s in water/gas/oil three-phase flow with 40% oil

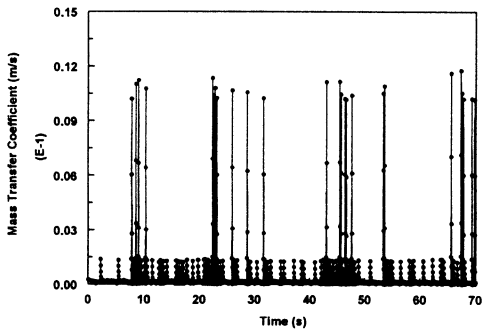

Figure 4.3.3.7-g Instantaneous mass transfer coefficient at Vsl=1.0 m/s and Vsg=2.4 m/s in water/gas/oil three-phase flow with 40% oil

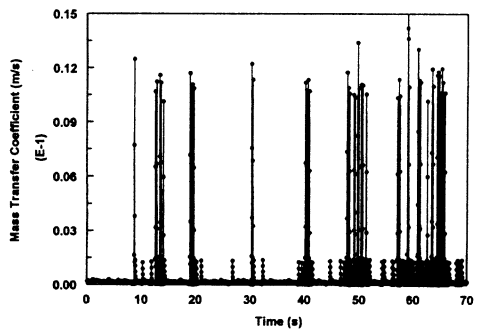

Figure 4.3.3.7-i Instantaneous mass transfer coefficient at Vsl=1.0 m/s and Vsg=3.6 m/s in water/gas/oil three-phase flow with 40% oil

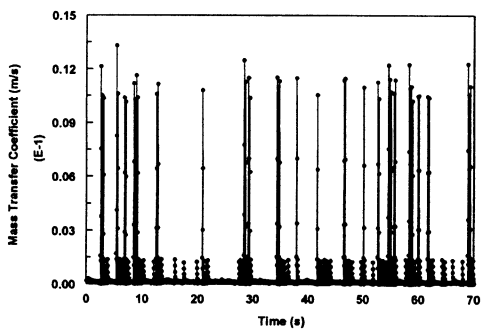

Figure 4.3.3.7-h Instantaneous mass transfer coefficient at Vsl=1.0 m/s and Vsg=3.0 m/s in water/gas/oil three-phase flow with 40% oil

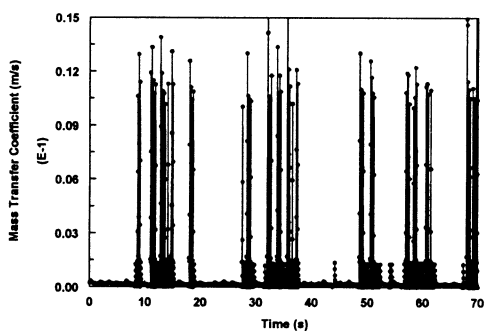

Figure 4.3.3.7-j Instantaneous mass transfer coefficient at Vsl=1.0 m/s and Vsg=4.8 m/s in water/gas/oil three-phase flow with 40% oil

with frequency lower than about 5 Hz dominates the mass transport in the full pipe flow. When the slug flow appears with the increase of the superficial gas velocity, the interaction of gas and liquid enhances the turbulence significantly. When gas bubbles collapse on the pipe wall, they can destroy the mass transfer boundary layer completely. This enhanced turbulence includes some higher frequency micro turbulence besides the low frequency micro turbulence near the liquid-solid surface. It is shown that the higher frequency micro turbulence in the slug flow influences the

p.s.d. significantly. As shown in Figure 4.3.3.8, for example, the curve for superficial gas velocity=4.8 m/s slug flow becomes close to a straight line. This figure confirms that superficial gas velocity can enhance the mass transfer significantly in high frequency spectrum, further more, it also supports the fact that slug flow has important differences when compared with the full pipe turbulent flow in high frequency micro turbulence.

Figure 4.3.3.9 gives a similar comparison of the influence of the superficial gas velocity on the power spectral density of the instantaneous mass transfer coefficient in the slug flow with the 40% input oil as being shown in Figure 4.3.3.8. The same conclusion could be drawn. However, there is only a very small difference between the slug flow with the 20% input oil and the slug flow with the 40% input oil.

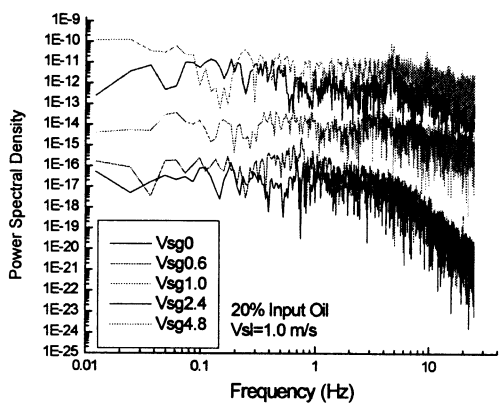

Figure 4.3.3.8 Comparison of p.s.d. at different superficial gas velocities and 1.0 m/s superficial liquid velocity with 20% input oil

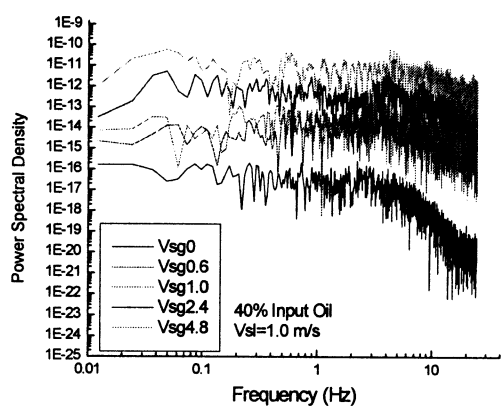

Figure 4.3.3.9 Comparison of p.s.d. at different superficial gas velocities and 1.0 m/s superficial liquid velocity with 40% input oil

Figure 4.3.3.10 shows that the influence of the superficial liquid velocity on the power spectral density of the instantaneous mass transfer coefficient in the full pipe flow is negligible. However, when the flow becomes a slug flow with 1.4 m/s superficial gas velocity, the influence of the superficial liquid velocity on the p.s.d. of the instantaneous mass transfer coefficient becomes significant. The higher the superficial liquid velocity, the higher the power spectral density, as shown in Figure 4.3.3.11. The p.s.d. analysis provides an excellent method to evaluate mass transfer characteristics and shear rate in multiphase flow as shown in the introduction section. More detailed and sophisticated analysis can be carried out to better quantify the characteristics of mass transfer and shear rate in slug flow. However, it is beyond the scope of this dissertation since it might become a separate study in the future.

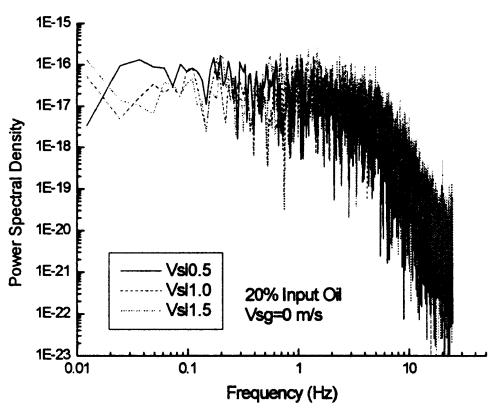

Figure 4.3.3.10 Comparison of p.s.d. at different superficial liquid velocities and 0 m/s superficial gas velocity with 20% input oil

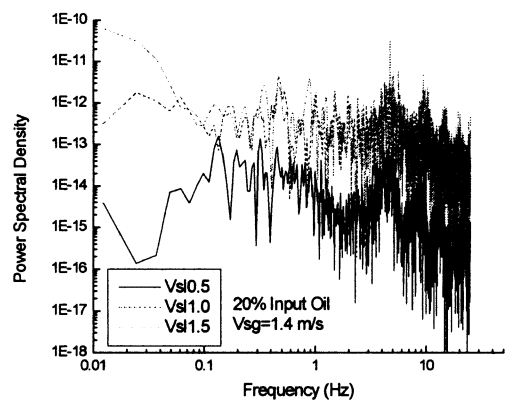

Figure 4.3.3.11 Comparison of p.s.d. at different superficial liquid velocities and 1.4 m/s superficial gas velocity with 20% input oil

4.4 Mass Transfer Correlation Development and Shear Stress Analysis

4.4.1 Mass Transfer Measurement in Single-Phase Full Pipe Flow

In the multiphase flow loop shown in Figure 3.1, mass transfer measurements were carried out initially in a single-phase full pipe flow. The measured limiting currents (I_L) were converted into the mass transfer coefficient (K) by the Equation 3.3. The results of these measurements in single-phase full pipe flow are shown in Figure 4.4.1. A dimensionless mass transfer correlation in Equation 4.2 is developed and the results are not dependent on the properties of the solution or the species involved.

$$Sh' = 0.089\ Re^{0.78}\ Sc^{0.33} \tag{4.2}$$

The mass transfer coefficients obtained with the small circular electrode need to be converted into actual mass transfer coefficients, which correspond to a fully developed concentration boundary layer. A mass transfer correlation has been well established in single-phase flow with a fully developed boundary layer by Berger & Hau (1977):

$$Sh = 0.0165\ Re^{0.86}\ Sc^{0.33} \tag{4.3}$$

Where,

$$\text{Sh} = \text{Sherwood number} = \frac{Kd_e}{D}$$

$$\text{Re} = \text{Reynolds number} = \frac{\rho_L V\, d_e}{\mu}$$

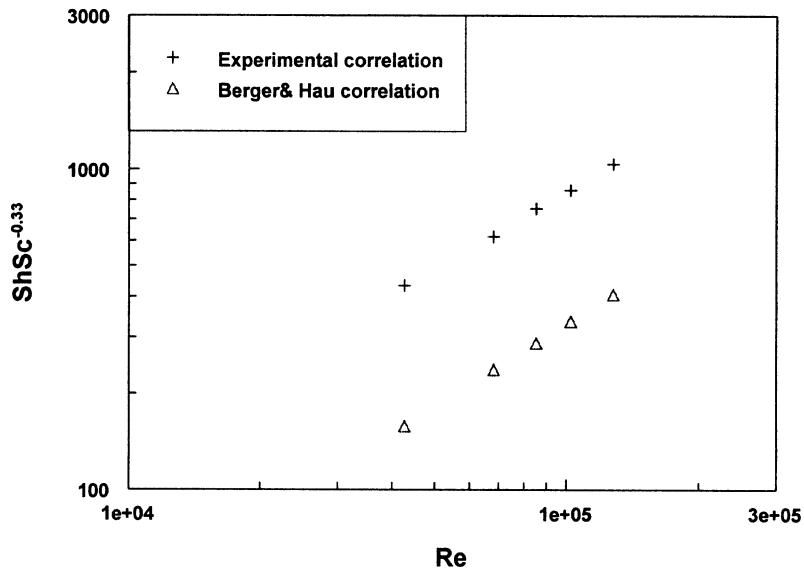

Figure 4.4.1 Experimental mass transfer correlation and Berger & Hau mass transfer correlation

Sc = Schmidt number = $\frac{\upsilon}{D}$

K = mass transfer coefficient (m/s)

d_e = equivalent hydraulic pipe diameter (m)

ρ_L = density (kg/m^3)

V = liquid velocity (m/s)

μ = dynamic viscosity (cP)

υ = kinematic viscosity (m^2/s)

D = diffusion coefficient (m^2/s)

We find the following equation to correct the measured mass transfer, Sh′, to actual mass transfer, Sh, in the two-phase flow.

$$Sh = 0.225\ Sh'^{\,1.08}\ Sc^{\,-0.027} \tag{4.4}$$

From the analogy of mass and momentum transfer and the fact that for large Schmidt numbers the mass transfer boundary layer is embedded in the viscous sub layer it can be shown, Nakoryakov et al. (1983), that the wall shear stress τ and the Sherwood number are related:

$$\tau = \frac{1.9\mu D}{l^2} Sh^3 \tag{4.5}$$

Where,

τ = shear stress (Pa)

μ = dynamic viscosity (cP)

D = diffusion coefficient (m^2/s)

l = electrode diameter (m)

Sh = Sherwood number

Thus one can obtain the wall shear stress by conducting the mass transfer measurements.

4.4.2 Mass Transfer Measurement in Horizontal Slug Flow

4.4.2.1 Average Mass Transfer Coefficient

Figure 4.4.2 shows the average mass transfer coefficients in single and multiphase flows by conducting the potentiodynamic experiment. It shows the different effects of superficial gas velocity and superficial liquid velocity on the average mass transfer coefficients. It indicates that superficial liquid velocity has a pronounced effect on the average mass transfer coefficient. The mass transfer coefficient always gradually increases with the increase of superficial liquid velocity at each superficial gas velocity.

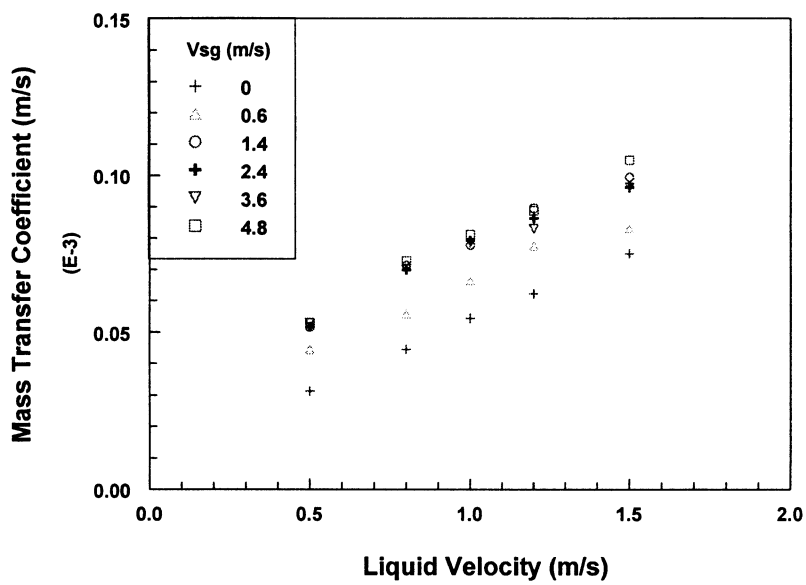

Figure 4.4.2 Average mass transfer measurement in water/gas two-phase flow

It is also observed that the mass transfer coefficient increases with increasing superficial gas velocity, the increasing being more remarkable at relatively low

superficial gas velocities (< 1.4 m/s). When superficial gas velocity further increases, its influence on average mass transfer is negligible. For instance, at a 0.8 m/s full pipe flow, the mass transfer coefficient is 4.45×10^{-5} m/s. With the increase of the superficial gas velocity from 0 through 1.4 m/s, the mass transfer coefficient increases from 4.45×10^{-5} to 5.58×10^{-5}, and 7.13×10^{-5} m/s and then remains almost constant. A similar phenomenon was also observed in a bubble column (Zaki et al. 1997). This may be explained by the fact that the gas holdup which represents the concentration of the turbulence promoting bubbles increases substantially at a relatively lower gas velocity than at a higher gas velocity.

4.4.2.2 Instantaneous Mass Transfer Coefficient

Chapter 4.3.1 already discussed the influence of multiphase flow on the instantaneous mass transfer coefficient. Figures 4.4.3 to 4.4.8 show Figure 4.3.1.8-a to j in a larger scale obtained in slug flow with a 1.0 m/s superficial liquid velocity and different superficial gas velocities. Figure 4.4.3 shows the instantaneous mass transfer coefficient in full pipe flow. The fluctuations reflect just the nature of the turbulence and the mass transfer coefficient is almost constant at about 5.44×10^{-5} m/s.

When the superficial gas velocity is increased to 0.6 m/s as shown in Figure 4.4.4, the fluctuations are enhanced due to the formation of slow moving lumps of liquid or plugs. The mass transfer coefficient is increased to about 6.36×10^{-5} m/s with fluctuations between 5.0×10^{-5} and 7.3×10^{-5} m/s. The fluctuation of the instantaneous mass transfer coefficient is increased further with the superficial gas velocity 1.4 m/s

shown in Figure 4.4.5. Much higher peaks now appear and the plug flow can be divided into two zones, the plug itself and the film between plugs as shown in Figure 1.1.

When the superficial gas velocity is increased to a 2.4 m/s a slug flow appears and large amplitude peaks appear in Figure 4.4.6. This is due to the formation of the mixing zone, which produces high-energy bubbles collapsing on the bottom of the pipe. The magnitude of the peaks is much higher than the plug flow. The instantaneous mass transfer coefficient in the slug is 1.08×10^{-3} m/s about 10 times higher than that in the film region. Figure 4.4.7 shows a similar phenomenon when the superficial gas velocity increases to 3.6 m/s.

With a further increase of the superficial gas velocity to 4.8 m/s shown in Figure 4.4.8, the instantaneous mass transfer increases significantly because the amount and energy level of bubbles are increased. The amplitude of the fluctuations reaches 8.8×10^{-3} m/s, about 160 times higher than it in the slug film zone. The previous study [Wang, 2000a] has shown that the gas bubble collapsing can enhance the mass transfer coefficient in the electrochemical cell and the stationary slug. Therefore, it is derived that the bubble collapsing in the slug flow also causes these high amplitude mass transfer spikes.

The mass transfer enhancement (E) has been introduced in Chapter 4.3.1.2.1 in order to effectively describe the bubbles' contribution to the mass transfer enhancement. In full pipe flow the instantaneous mass transfer coefficient only has small oscillations because of the natural fluctuations in turbulent flow. At a lower

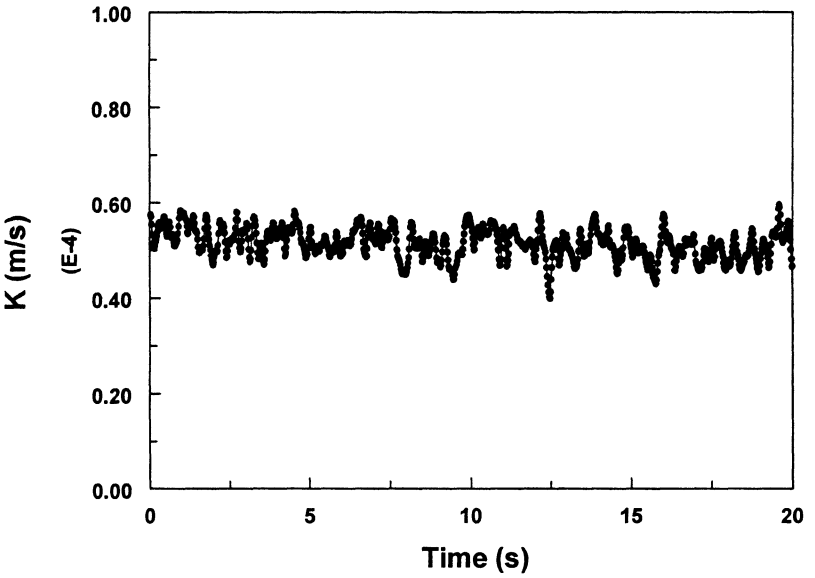

Figure 4.4.3 Instantaneous mass transfer coefficient in water full pipe flow with Vsl=1.0 m/s

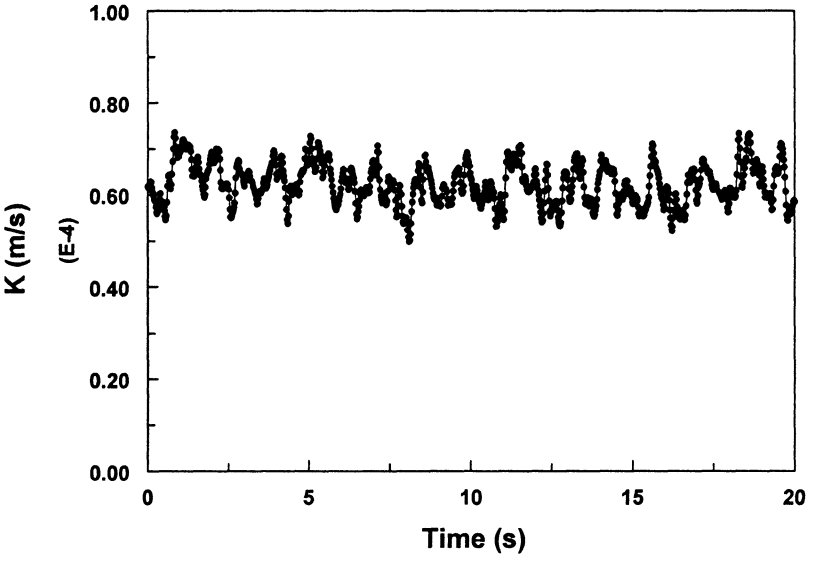

Figure 4.4.4 Instantaneous mass transfer coefficient in water/gas two-phase flow with Vsl=1.0 m/s and Vsg=0.6 m/s

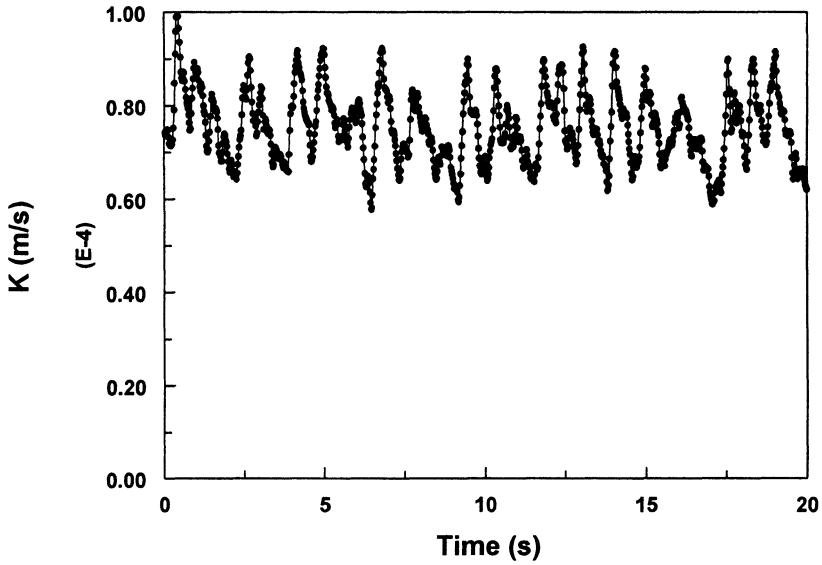

Figure 4.4.5 Instantaneous mass transfer coefficient in water/gas two-phase flow with Vsl=1.0 m/s and Vsg=1.4 m/s

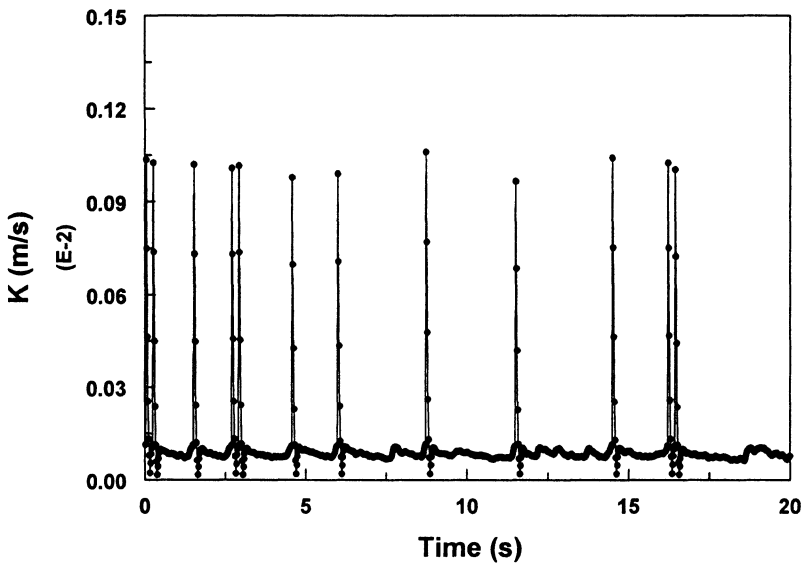

Figure 4.4.6 Instantaneous mass transfer coefficient in water/gas two-phase flow with Vsl=1.0 m/s and Vsg=2.4 m/s

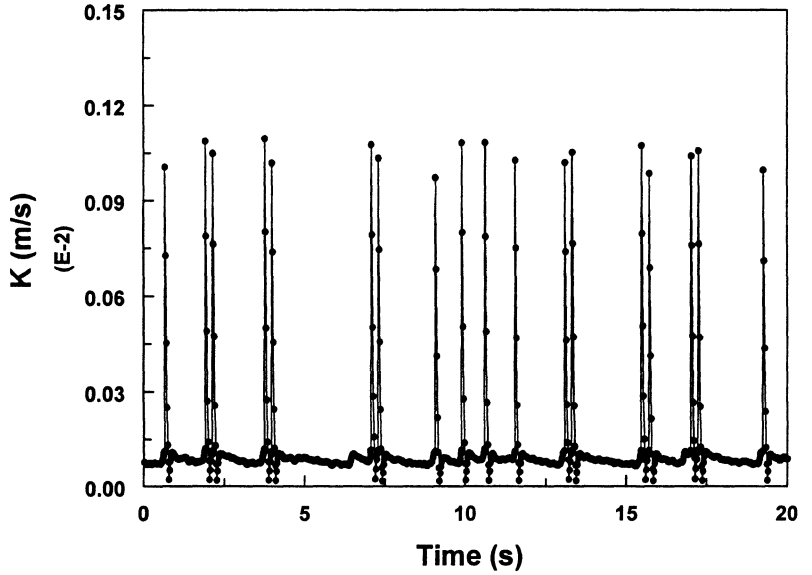

Figure 4.4.7 Instantaneous mass transfer coefficient in water/gas two-phase flow with Vsl=1.0 m/s and Vsg=3.6 m/s

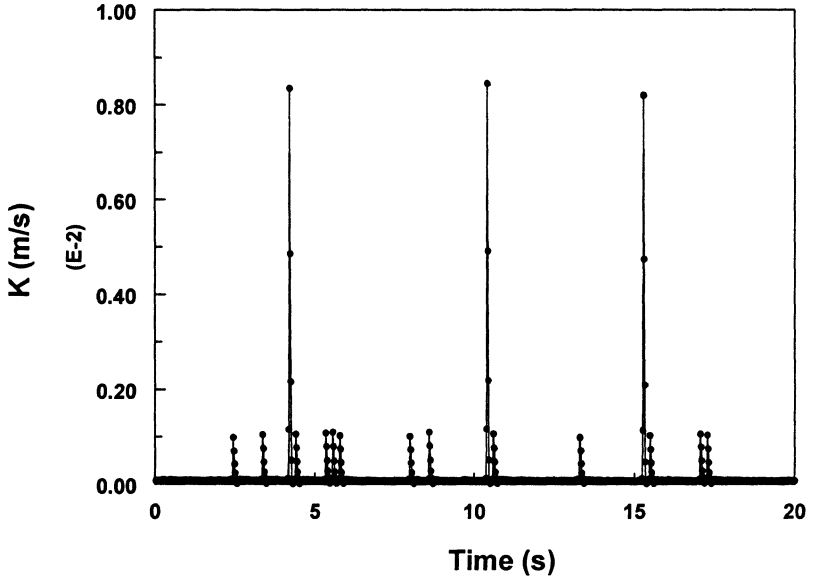

Figure 4.4.8 The Instantaneous mass transfer coefficient in water/gas two-phase flow with Vsl=1.0 m/s and Vsg=4.8 m/s

superficial gas velocity (<1.4 m/s) the enhancement is usually around 1.5. Since the plug flow can be divided into two zones, that is, the plug itself and the film between th plugs, the plug usually has a higher velocity than the film. It is this higher velocity that causes the 1.5 times enhancement of the instantaneous mass transfer coefficient.

With the further increase of the superficial gas velocity (≥2.4 m/s) at each superficial liquid velocity, the mass transfer enhancement (E) has a significant change. For example, at a 1.0 m/s superficial liquid velocity the enhancement can reach approximately 14 at a 2.4 and a 3.6 m/s superficial gas velocity, and a maximum 120 at a 4.8 m/s superficial gas velocity as shown in Table 4.4.1. The corresponding peak instantaneous mass transfer coefficients are approximately 1.1×10^{-3}, 1.1×10^{-3}, and 8.8×10^{-3} m/s at a superficial gas velocity of 2.4, 3.6, and 4.8 m/s, respectively.

These mass transfer enhancements represent two kind of bubble contact on the bottom of the pipe shown in Figure 4.4.8. This may be the bubble impact, and latterly, the bubble collapse. These two kinds of bubbles have large differences of energy and will cause different mass transfer coefficients and shear stress.

Jepson (1989) has proposed a dimensionless parameter, Froude number (Fr), to describe the turbulence magnitude in the slug flow as shown in Equation 2.23. In a slug flow with a higher Fr, more gas is entrained in the mixing zone while the amount and energy of bubbles will be increased. It further enhances the mass transfer coefficient as the Table 4.4.1 indicates. Figure 4.4.9 shows that the following results, which can be used in the mass transfer correlation development.

$$E = 1.5 \quad \text{for} \quad Fr \leq 4$$
$$E = 15 \quad \text{for} \quad 4 < Fr < 9 \qquad (4.6)$$
$$E = 120 \quad \text{for} \quad Fr \geq 9$$

Equation 4.6 only gives a simple and a discrete relation between the Froude number and the mass transfer enhancement. Another continuous model is further developed for an easy application in the corrosion modeling. We assume the following correlation for E and Froude:

$$E = a\, Fr^{b} \qquad (4.7)$$

Where,

E = mass transfer enhancement

Fr = Froude number of slug flow

a, b = constants of equation

Table 4.4.1 Mass transfer enhancement in water/gas two-phase flow

E		Vsl (m/s)						
		0	0.6	1.4	2.4	3.0	3.6	4.8
Vsl (m/s)	0.5	1	1.5	1.7	2.2	2.2	20	164
	0.8	1	1.5	1.6	17	17	17	135
	1.0	1	1.5	2	14	14, 112	14, 120	14, 120
	1.2	1	1.5	12	13	13, 104	13, 104	13, 104
	1.5	1	1.5	11	11, 92	11, 92	11, 92	11, 92
Froude number (Vsl=1.0)		0	2	4	6	8	10	12

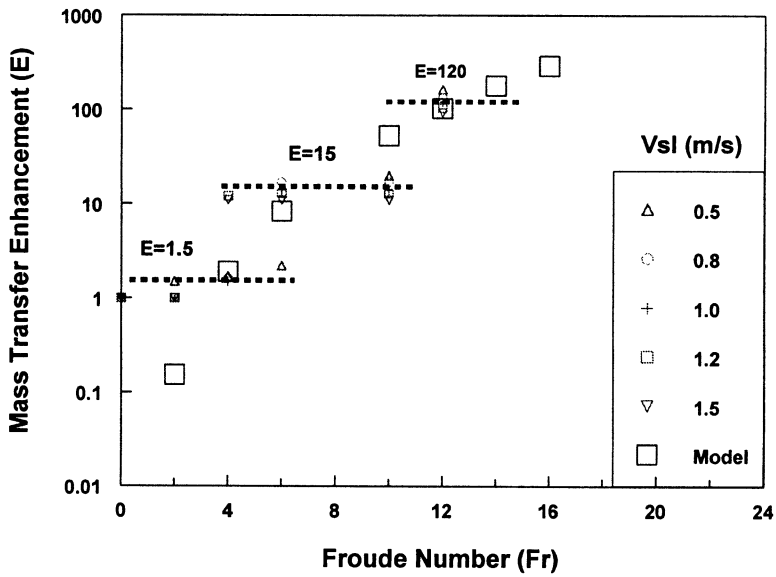

Figure 4.4.9 Relationship between mass transfer enhancement and Froude number

Table 4.4.1 shows that both the superficial liquid velocity and the superficial gas velocity have influence on the mass transfer enhancement. However, the influence of the superficial gas velocity is much more significant. Therefore, the influence of the superficial liquid velocity on E is neglected. The mass transfer enhancement data at a 1.0 m/s superficial liquid velocity and at different superficial gas velocity was used to solve the equation constants a and b.

$$\text{LOG}(E) = \text{LOG}(a) + b\,\text{LOG}(Fr) \qquad (4.8)$$

$$a = 0.0124$$

$$b = 3.63$$

Thus we have developed the correlation as:

$$E = 0.0124\ Fr^{3.63} \qquad (4.9)$$

Figure 4.4.9 compares the Equations 4.6 and 4.9 with the mass transfer coefficient data. It shows that Equation 4.9 basically reflects the relationship between E and the Froude number and can be applied to the mass transfer correlation development.

4.4.3 Mass Transfer Correlation Development in Slug Flow

Following the above conclusions, the average mass transfer correlation can be developed, which neglects the bubble collapsing in slug flow. This correlation could be used for the slug film zone. Then the mass transfer enhancement (E) will be used to correct the developed mass transfer correlation in the slug film, thus the mass transfer correlation in the slug mixing zone is obtained.

The average mass transfer coefficient in a superficial gas velocity 4.8 m/s and in different superficial liquid velocities will be used to develop the mass transfer correlation in the slug film.

$$Sh' = 1.806\ Re^{0.56}\ Sc^{\ 0..33} \qquad (4.10)$$

Inserting Equation 4.10 into Equation 4.4, gives the mass transfer correlation 4.11, from which the actual mass transfer coefficients of reactant species can be calculated

in the slug film with the input of the superficial liquid velocity and the equivalent liquid diameter in the slug film zone.

$$Sh = 0.544\ Re^{0.61}\ Sc^{0.33} \tag{4.11}$$

Now the mass transfer correlation for the slug mixing zone will be developed from the above average mass transfer correlation corrected by the mass transfer enhancement, E, as shown in Equation 4.9.

$$Sh = 0.544\ E\ Re^{0.61}\ Sc^{0.33} \tag{4.12}$$

$$Sh = 0.00675\ Fr^{3.63}\ Re^{0.61}\ Sc^{0.33} \tag{4.13}$$

These mass transfer correlations can be used in the CO_2 corrosion mechanistic modeling next.

4.4.4 Wall Shear Stress Analysis

The classic mechanism of flow induced localized corrosion (FILC) starts with the scaled metal surface as shown in Figure 2.3. The roughness of the scale gives rise to microturbulences which cause local thinning of the scale with subsequent formation of pores. Higher corrosion activities at these porous sites result in further local destruction of the scale followed by a localized attack at this local anode where the scale re-formation is hindered by high local flow intensities, thus stabilizing the local anode.

If hydrodynamic forces are responsible for the local destruction of corrosion product scales these forces must be high enough to overcome the binding forces in the crystal agglomerates of the scale and the adhesion forces between the metal substrate and the scale [Schmitt et al. 1999]. Table 4.4.2 compares the hydrodynamics and the fracture mechanics. Usually the hydrodynamic forces are several orders of magnitude too small to cause destruction and spalling of protective corrosion product scales, and thus should not be able to initiate the FILC.

On the other hand, there is no doubt of the existence of the critical flow intensities above which corrosion product scales are hydrodynamically destroyed. Equation 4.3, 4.11, and 4.13 are used to calculate the wall shear stress in multiphase flow. The results are shown in Table 4.4.3. The comparison of the predicted maximum wall shear stress and the measured shear stress shows the significance of investigating the maximum shear stress. Gopal et al. (1995, 2000) found that the slug flow can thin the corrosion product scale and remove the corrosion inhibitor film through surface analysis. Their study confirms the above shear stress calculation in slug flow based on the following hypothesis.

The proposed hypothesis is that the slug flow produces a strong cavitation type bubble collapsing and it is able to directly destroy the corrosion product scales. This bubble collapsing has been validated in the electrochemical cell, the stationary slug flow, and the slug flow. The calculated maximum wall shear stress in the slug flow shows that its hydrodynamics is enough higher to destruct the corrosion product

Table 4.4.2 Hydromechanics vs. fracture mechanics

Forces	Magnitude (Pa)
Wall shear stress • In typical technical systems • In regions of high flow intensities, e.g. at flow disturbance • In slug flow with strong bubble collapsing (cavitation type)	 10^0 --- 10^2 10^4 --- 10^5 10^5 --- 10^8
Adherence of corrosion product scales to the metal substrate	10^6 --- 3×10^7
Fracture stress of corrosion product scales • High porosity scales • Low porosity scales	 10^7 --- 10^8 10^8 --- 10^9

scales. For example, the slug flow with a superficial gas velocity of 4.8 m/s and a superficial liquid velocity of 1.0 m/s is able to produce a high maximum shear stress up to 7.4×10^7 Pa. This critical value is close to the range of the adherence force of corrosion product scales to the metal substrate between [1×10^6, 3×10^7] Pa and fracture stress of corrosion product scales high porosity scales between [1×10^7, 1×10^8] Pa. Gouglas et al. observed that when a cavitation bubble grows and collapses, the local pressures during the few milliseconds may be up to 4,000 atm. It could be predicted that this extremely high shear stress induced by cavitation type bubble collapsing can overcome the binding forces in the crystal agglomerates of the scale and the adhesion forces between the metal substrate.

Table 4.4.3 Theoretical calculation of shear stress in slug flow under the assumption of cavitation type bubble collapsing

Vsl (m/s)	1.0					
Vsg (m/s)	0	0.6	1.4	2.4	3.6	4.8
E	1	1	1.5	14	14	120
Fr	0	2	4	6	9	12
Equations	4.4.5, 4.4.2	4.4.5, 4.4.13	4.4.5, 4.4.13	4.4.5, 4.4.13	4.4.5, 4.4.13	4.4.5, 4.4.13
Maximum Shear Stress (Pa)	6.0	42	140	1.4×10^5	$1.4E \times 10^5$	$7.4E \times 10^7$
Average Shear Stress Measured (Pa) (Gopal et al. 1995)	5	10	50	80	100	150-160

The following conclusions can be drawn from the above analysis.

1. The cavitation type bubble collapsing in slug flow not only enhances the mass transfer coefficient, but also produces very high instantaneous magnitude wall shear stress. Therefore, the slug flow is able to cause a much higher corrosion rate than a full pipe flow because these two effects enhance the corrosion process together.
2. The above derived mass transfer correlations for slug flow can be further used in the CO_2 corrosion mechanistic modeling in the following Chapters 5 and 6.

CHAPTER 5

CO_2 CORROSION MECHANISTIC MODELING IN HORIZONTAL SLUG FLOW

Metallic corrosion can be defined as the destructive attack of a metal by chemical and electrochemical reaction with its environment. An overall corrosion reaction is composed of at least one anodic reaction of metal and one cathodic reaction of oxidant. Since both reactions involve transport processes, a typical corrosion process can be divided into three basic steps:

1. Transport of oxidants (e.g. H^+) from bulk solution to metal/solution interface.
2. Surface electrochemical reactions during which the metal corrodes and dissolves into solution and oxidants are reduced on the corroding surface.
3. Transport of dissolved corrosion products from metal/solution interface to bulk solution.

The corrosion rate may be controlled or affected by any one of the above steps. The first step and the third step are directly affected by the mass transfer rate of the oxidants to be reduced on the metal surface and the dissolved corrosion product. As mentioned in Chapter 2, in this study, this model only considers two reactions: the reduction of the hydrogen ion as the cathodic reaction and the oxidation of iron to the ferrous ion as the anodic reaction as shown in Equation 2.4 and 2.5. Initially the anodic dissolution of iron and cathodic reduction of hydrogen will be assumed to proceed in the absence of a corrosion product layer. Once a model has been

developed for this scenario, the effect of the corrosion product layer will be incorporated.

CO_2 corrosion mechanistic model is developed for the water/gas two-phase and water/oil/gas three-phase slug flow based on the development strategy as shown in Figure 5.1. The model incorporates the chemistry of the salt solution, thermodynamics of carbon dioxide dissolution and dissociation, enhanced solid/liquid mass transfer, electrochemical kinetics on the metal surface, and the presence of a corrosion product film.

5.1 Calculation of Bulk Concentrations

The pH is an essential parameter in the calculation of the corrosion rate. It is assumed that the dissolution reaction of iron into the solution does not significantly affect the bulk solution pH. For sweet corrosion, the pH is found by calculating the concentration of all the ions present in the bulk of the flowing solution.

5.1.1 Electroneutrality

Electroneutrality is the fact that the sum of the charges in a solution is zero. The composition of ASTM D1152 substitute seawater used in the corrosion experiments are shown in Table 5.1 (Pitzer, 1991). There are 11 major constituents including, NaCl, Na_2SO_4, $NaHCO_3$, NaF, KCl, KBr, $MgCl_2$, $CaCl_2$, $SrCl_2$, and H_3BO_3. In solution, these compound dissociate into their constituent ions. The dissolved carbon dioxide reacts with water to form carbonic acid and carbonic acid dissociates to form bicarbonate and hydrogen ions. The bicarbonate ions further dissociate to form

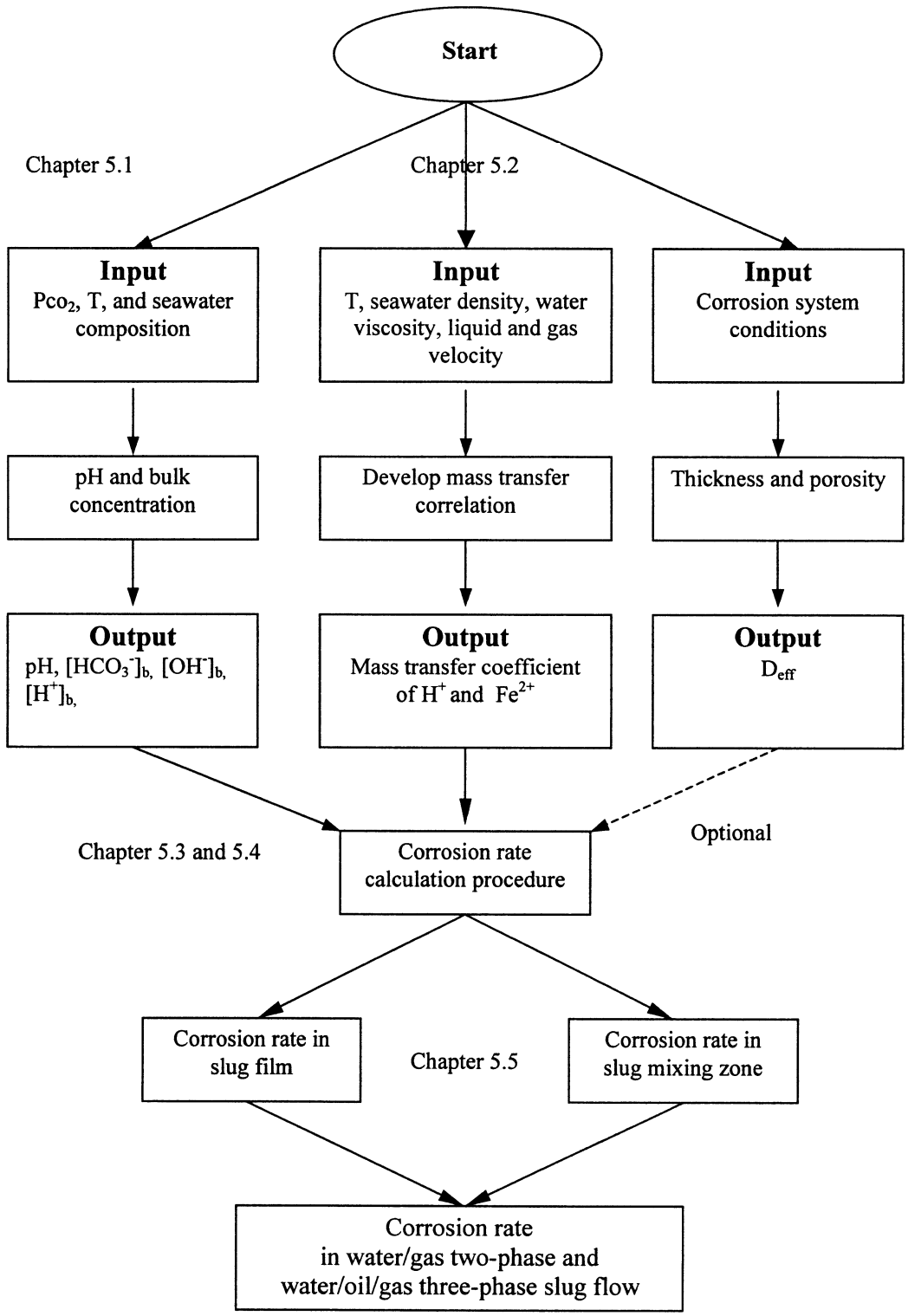

Figure 5.1 Calculation algorithm of corrosion rate in slug flow

carbonate ions and hydrogen ions. The hydrogen ions and hydroxide ions are also involved in another equilibrium reactions namely dissociation of water. Hence, the ionic concentrations of sea salt along with HCO_3^-, CO_3^{2-}, H^+, and OH^-, cannot be varied independently, due to electroneutrality requirements. This may be written as follows:

Table 5.1 The Composition of ASTM Grade D1141-52 Synthetic Sea Salt

Compound Name	Concentration (wt%)
NaCl	58.49
$MgCl_2 \cdot 6H_2O$	26.46
Na_2SO_4	9.75
$CaCl_2$	2.765
KCl	1.450
$NaHCO_3$	0.477
KBr	0.238
H_3BO_3	0.071
$SrCl_2 \cdot 6H_2O$	0.095
NaF	0.007

$$\lambda + [H^+] = [HCO_3^-] + [OH^-] + 2\,[CO_3^{2-}] \qquad (5.1)$$

Where, "[ ]" represents the concentration of each ion.

$$\lambda = [Na^+] + [Mg^{2+}] + 2\,[Ca^{2+}] + [K^+] + 2\,[Sr^{2+}] - [Cl^-] - [Br^-] - [BO_4^-] - 2[SO_4^{2-}] - [F^-]$$

Dayalan et al. (1995) showed that the concentration of CO_3^{2-} does not significantly affect the overall corrosion reaction; therefore, the concentration of CO_3^{2-} ions can be neglected in pH calculations. Equation 5.1 then becomes:

$$\lambda + [H^+] = [HCO_3^-] + [OH^-] \quad (5.2)$$

The ionic association is described by the ionic interaction. Physical interactions are weak at a large distance, but may become quite strong for a short distance. The association of all the ionic components of sea salt except H^+ ion is neglected for the purpose of pH calculations. Their coefficients can be taken as $\gamma_i = 1$. Equation 5.2 can be expressed in terms of activity coefficients as follows:

$$\lambda + \frac{a_{H^+}}{\gamma_{H^+}} = \frac{a_{HCO_3^-}}{\gamma_{HCO_3^-}} + \frac{a_{OH^-}}{\gamma_{OH^-}} \quad (5.3)$$

Where,

a_i = activity of ion i (mol/m^3)

γ_i = activity coefficient of ion i

The activity a_i of a component i in a solution is a convenient alternative means of describing its chemical potential:

$$\mu_i = \mu_i^0 + RT \ln a_i \quad (5.4)$$

Where,

μ_i = chemical potential of components i (J/mol)

μ_i^0 = standard chemical potential of component i (J/mol)

The activity coefficient γ_i is defined as the ratio a_i/m_i where m_i is the molality. γ_i is a dimensionless quantity, tending to 1 at infinite dilution.

5.1.2 Carbon Dioxide Solubility

It is assumed that the entire CO_2 in solution dissolves to form carbonic acid. The dissolution of carbon dioxide in solution is given by Henry's law as follow:

$$\alpha_{CO_2} = f_{CO_2} K_H \tag{5.5}$$

Where,

a_{co_2} = activity of CO_2 in the liquid phase (mol/m^3)

f_{co_2} = fugacity of CO_2 in the gas phase (atm) = $\Phi_{co_2}\ y_{co_2}\ P_T$

Φ_{co_2} = fugacity coefficient of CO_2 in the gas phase

y_{co_2} = mole fraction of CO_2 in the gas phase

P_T = total pressure of the system (atm)

K_H = Henry's law constant (mol/g/atm)

The fugacity coefficient of carbon dioxide is nearly 1 for pressures less than 25 bars, which is the range of interest for this study.

5.1.3 Carbon Dioxide Ionization

The equilibrium thermodynamic constant for the dissociation of H_2CO_3 is given by:

$$K_{HCO_3^-}^{*} = K_{CO_2} = \frac{a_{H^+} a_{HCO_3^-}}{a_{CO_2}} \quad (5.6)$$

Where,

$K_{HCO_3^-}^{*}$ = equilibrium constant for the dissociation of H_2CO_3 (mol/m^3)

K_{CO_2} = equilibrium constant for the dissociation of H_2CO_3 (mol/m^3)

a_{H^+} = activity of H^+ ion (mol/m^3)

$a_{HCO_3^-}$ = activity of HCO_3^- ion (mol/m^3)

a_{CO_2} = activity of CO_2 in the liquid phase (mol/m^3)

5.1.4 Dissociation of Water

Concentration of free H^+ and OH^- ions are related by the ionic product of water as: $H_2O = OH^- + H^+$ (5.7)

$$K_w = \frac{a_{H^+} a_{OH^-}}{a_{H_2O}} \quad (5.8)$$

Where,

K_w = equilibrium constant for the dissociation of H_2O (mol/m^3)

a_{H^+} = activity of H^+ ion (mol/m^3)

a_{OH^-} = activity of OH^- ion (mol/m^3)

a_{H_2O} = activity of H_2O (mol/m^3)

5.1.5 Activity of Hydrogen

From Pitzer (1991), the activity of water under standard conditions is equal to 1. In addition, for dilute aqueous solutions the activity coefficient of water can be taken as unity. Equation 5.3 can then be written in terms of a_{H^+}, a_{CO_2}, the ionization constants, and activity coefficients as:

$$\frac{1}{\gamma_{H^+}} a_{H^+}{}^2 + \lambda\, a_{H^+} + \left[-\frac{K_{CO_2} a_{CO_2}}{\gamma_{HCO_3^-}} - \frac{K_W}{\gamma_{OH^-}} \right] = 0 \qquad (5.9)$$

Equation 5.9 can be solved for a_{H^+}, if all the ionization constants can be estimated as functions of temperature and pressure as given below.

5.1.6 Equilibrium Constants

Pitzer (1991) suggested that the chemistry of carbon dioxide is controlled by the following equilibrium:

$CO_2(g) = CO_2(aq)$ $\qquad K_H$ $\qquad (5.10)$

$CO_2(g) + H_2O = H_2CO_3$ $\qquad K_{H_2CO_3}$ $\qquad (5.11)$

$H_2CO_3 = H^+ + HCO_3^-$ $\qquad K_{HCO_3^-}$ $\qquad (5.12)$

Combining Equations 5.11 and 5.12

$$CO_2(g) + H_2O = H^+ + HCO_3^- \qquad K_{HCO_3^-}^* \qquad (5.13)$$

Pitzer proposed the following correlation for HCO_3^- equilibrium constant $K_{HCO_3^-}^*$

$$p K_{HCO_3^-}^* = 6320.81/T - 126.3405 + 19.568 \ln T \qquad (5.14)$$

Henry's law has:

$$\log(K_H) = 108.3865 + 0.01985076/T - 6919.3/T - 40.45154\log(T) + 669365/T \qquad (5.15)$$

The dissociation constant of water is given by Wagman et al. (1982) as:

$$\log(K_{H_2O}) = -283.971 + 13323/T - 0.05069842T + 102.24447\log(T) - 1119669/T^2 \qquad (5.16)$$

5.1.7 Activity Coefficients

The Debye Huckel equation was modified by Davies for the mean activity coefficient as:

$$\log \gamma_{\pm} = -Az_+|z_-|\left(\frac{\mu^{1/2}}{1+\mu^{1/2}} - 0.3\mu\right) \qquad (5.17)$$

Where,

$\gamma_{\pm}$ = ionic activity coefficient

μ = ionic strength on the molality scale (mol/m^3)

z = ionic charge

$A = 1.82\times 10^{6} (\varepsilon T)^{-3/2}$

ε = dielectric constant

T = temperature (K)

In this study the activity coefficients for H^+, HCO_3^-, and OH^- are obtained by Equation 5.17. Ionic strength is determined as:

$$\mu = \frac{1}{2}\sum_j z_j^{\,2} m_j \qquad (5.18)$$

Where, m_j = molality of ion j with charge z (kg/mol)

In using the Davies equation in a solution containing several electrolytes all the ions in the solution contribute to μ. However, z in Equation 5.17 refers to the ionic charge of the particular electrolyte for which $\gamma_{\pm}$ is calculated. Moreover, the Davies Equation for $\log\gamma_{\pm}$ is obtained by replacement of $z_+|z_-|$ in Equation 5.17 by z^2.

5.1.8 Dielectric Constant for Water

Pitzer (1991) has suggested the following correlation for evaluating the dielectric constant for water. This is dependent on pressure and temperature:

$$\varepsilon = \varepsilon_{1000} + C \ln [(B+P)/(B+100)] \qquad (5.19)$$

Where,

$$\varepsilon_{1000} = U_1 \exp(U_2 T + U_3 T^2) \quad (5.20)$$

$$C = U_4 + U_5/(U_6 + T) \quad (5.21)$$

$$B = U_7 + U_8/T + U_9 T \quad (5.22)$$

P = total pressure (bar)

T = temperature (K)

$U_1 = 342.79$

$U_2 = -5.0866 \times 10^{-3}$

$U_3 = 9.469 \times 10^{-7}$

$U_4 = -2.0525$

$U_5 = 3115.9$

$U_6 = -182.89$

$U_7 = -8032.5$

$U_8 = 4.2142 \times 10^{+6}$

$U_9 = 2.1417$

5.1.9 Calculation Procedure

The following equations represent the relation obtained for the dissociation of carbonic acid, activity of CO_2 in liquid phase, ionic phase, ionic product of water, and electroneutrality as discussed.

$$K_{CO_2} = \frac{a_{H^+} a_{HCO_3^-}}{a_{CO_2}} \quad (5.23)$$

$$a_{CO_2} = f_{CO_2} K_H \tag{5.24}$$

$$K_W = \frac{a_{H^+} a_{OH^-}}{a_{H_2O}} \tag{5.25}$$

$$\frac{1}{\gamma_{H^+}} a_{H^+}{}^2 + \lambda a_{H^+} + \left[-\frac{K_{CO_2} a_{CO_2}}{\gamma_{HCO_3^-}} - \frac{K_W}{\gamma_{OH^-}} \right] = 0 \tag{5.26}$$

Equations 5.26 is a quadratic equation with one unknown a_{H^+}, hence equation 5.26 can be solved for a_{H^+}, then pH can be obtained by the following equation:

$$pH = -\log[a_{H^+}] \tag{5.27}$$

When a_{H^+} is substituted into Equations 5.23 and 5.25, $a_{HCO_3^-}$ and a_{OH^-} can be solved. Finally the bulk concentrations for H^+, HCO_3^-, and OH^- can be determined by using the ratio of the activity over the activity coefficient ($m_i = a_i/\gamma_i$), respectively.

5.2 Calculation of Mass Transfer Coefficients

Mass transfer plays an important role in the corrosion process. Due to electrochemical reactions taking place on the metal surface, the concentrations of various species at the metal surface are different from those in the bulk. As a result of this concentration gradient in the fluid, there is movement of the species from bulk solution to the pipe wall and vice versa. In order to calculate the mass transfer rate of

the species it is necessary to compute the mass transfer coefficients of the species. In this study the developed mass transfer correlations in Equations 4.11 and 4.13 are used to determine the mass transfer coefficients for corrosion reactive species in slug film and slug mixing zone, respectively.

The diffusion coefficients of ions can be calculated with the aid of the Nerst-Einstein relation:

$$D_i = \frac{\lambda_i RT}{F^2 Z_i^2} \tag{5.28}$$

Where,

D_i = diffusion coefficient (m^2/s)

λ = ionic conductivity (S/m)

R = universal gas constant (=8.134 J/mol-K)

T = temperature (K)

Z = charge of the ion

The values of equivalent conductance of ions are at the infinite dilution in water (Newman, 1991). For seawater and oil/saltwater mixtures, the value of ionic conductivity is not available but may be much greater than suggested by Newman. Hence using the value of ionic conductivity from Newman may lead to loss of accuracy. From recent experiments on conductivity (Xie, 1997), it is found that the diffusivity was 2 to 3 times that given above. Therefore, in this study diffusivities of D, 2 × D, and 3 × D were used for 40, 60, and 80 °C, respectively, for brine and

oil/water flow conditions, to predict corrosion rate since mass transfer rate increases greatly with temperature.

An approximate guide to the temperature dependence of ionic diffusion coefficients is provided by the relationship according to Newman (1991):

$$\frac{D\mu}{T} = \text{constant} \tag{5.29}$$

Where,

μ = viscosity of the solution (cP)

D = ionic diffusion coefficient (m^2/s)

T = temperature (K)

The conductance of ions is used for the determination of the diffusivity, but the values of conductance are at infinite dilution in water at 25 °C. If the studied temperature is different, this modification needs to be involved.

5.3 Modeling of CO_2 Corrosion without Corrosion Product Layer

5.3.1 Fundamental Theory

After the reactants reach the metal surface, various electrochemical reactions take place between the metal surface and the species. The model assumes that the following reactions take place at the surface.

Cathodic reaction:

$$2H^+ + 2e^- \rightarrow H_2 \tag{2.4}$$

Anodic reaction:

$$Fe \rightarrow Fe^{2+} + 2e^- \tag{2.5}$$

The current densities i_a, i_c due to the above electrochemical reactions are given by the Butler-Volmer equation, and can be written as:

$$i_a = 2FK_{e,Fe^{2+}}[Fe^{2+}]_s \exp[\frac{2(1-\alpha)F(E_{corr} - E_{Fe^{2+}})}{RT}] \tag{5.30}$$

$$i_c = 2FK_{e,H^+}[H^+]_s \exp[\frac{-2\alpha F(E_{corr} - E_{H^+})}{RT}] \tag{5.31}$$

Where,

i_a = anodic current density (A/m^2)

i_c = cathodic current density (A/m^2)

$[Fe^{2+}]_s$ = surface concentration of Fe^{2+} (mol/m^3)

$[H^+]_s$ = surface concentration of H^+ (mol/m^3)

E_{corr} = corrosion potential (V)

α = transfer coefficient (=0.5 for most cases)

F = Faraday's constant (=96500 C/mol)

R = universal gas constant (=8.314 J/mol-K)

T = temperature (K)

$E_{Fe^{2+}}$ = potential for the anodic reaction (V)

$E_{H^{2+}}$ = potential for the cathodic reaction (V)

$K_{e,Fe^{2+}}$ = rate constants for the anodic reaction (m/s)

K_{e,H^+} = rate constants for the cathodic reaction (m/s)

The values of the rate constants are not available readily in the literature at all temperatures and for all material types. From Tanaka and Tamamushi (1964), the rate constant increases with temperature and is about one order magnitude higher for every 20 °C. In this study, the values for the rate constants ($K_{e,H^+}, K_{e,Fe^{2+}}$) are 2×10^{-3} and 2.59 cm/s, respectively, for hydrogen ion reduction and iron dissolution reactions at 80 °C, which are suggested by Dayalan et al. (1995). At 60 °C, the values for the rate constants ($K_{e,H^+}, K_{e,Fe^{2+}}$) are 2×10^{-4} and 0.259 cm/s, respectively, while they are 2×10^{-5} and 0.0259 cm/s respectively at 40 °C.

The equilibrium potentials E_{H^+} and $E_{Fe^{2+}}$ are given by the Nernst equations:

$$E_{H^+} = E^0{}_{H^+} + \frac{RT}{nF} \ln \frac{[H^+]_s^2}{[H_2]} \tag{5.32}$$

$$E_{Fe^{2+}} = E^0{}_{Fe^{2+}} + \frac{RT}{nF} \ln [Fe^{2+}]_s \tag{5.33}$$

Where,

H_2 = surface concentration of H_2 (mol/m^3)

$E^0{}_{H^+}$ = standard potential for the cathodic reactions (V)

$E^0_{Fe^{2+}}$ = standard potential for the anodic reactions (V)

Assuming steady state, the sum of the currents due to the cathodic reactions should be equal to the sum of the currents due to the anodic reactions, which in turn is equal to the corrosion current.

$$i_c = i_a = i_{corr} \tag{5.34}$$

For ion, corrosion rate is calculated by:

$$CR = \frac{i_a}{2F}\frac{M_{Fe}}{\rho_{Fe}} \times 3600 \times 24 \times 365 = 1.16 i_a \tag{5.35}$$

Where,

CR = corrosion rate (mm/year)

i_a = anodic current density (A/m^2)

F = Faraday's constant (=96500 C/mol)

M_{Fe} = iron molecular weight (=55.85 kg/kmol)

ρ_{Fe} = iron mass density (=7800kg/m^3)

Under steady state conditions it is assumed the sum of the mass transfer rates of the reactant are equal to the sum of the electrochemical reaction rates. Hence we can write,

$$2FK_{mt,Fe^{2+}}([Fe^{2+}]_s - [Fe^{2+}]_b) = i_a \tag{5.36}$$

$$FK_{mt,H^+}([H^+]_b - [H^+]_s) = i_c \tag{5.37}$$

The subscripts s and b represents the surface and bulk, respectively. The three unknowns are surface concentrations of Fe^{2+} and H^+, along with the corrosion potential $E_{corr.}$ Three Equations 5.34, 5.35, 5.36 and 5.37 are used to solve these three unknowns; finally, the corrosion rate can be determined.

5.3.2 Numerical Solution of Corrosion Rate

As we have discussed in section 5.3.1, three unknowns, which are surface concentration of ferrous ion, surface concentration of hydrogen ion, and corrosion potential, can be solved by a set of three nonlinear equations. These three nonlinear equations are linearized and are solved by using the Newton-Raphson method as described below. In this method the three equations are written in the form of $F_i(x_j)=0$, where x_j is the variable vector and F_i is the residual vector as shown below with i and j ranging from 1 to 3. Equations 5.30, 5.31, 5.34, 5.36, and 5.37 after rearranging gives,

$$F_1 = K_{mt,Fe^{2+}}(x_1 - [Fe^{2+}]_b) - K_{e,Fe^{2+}} x_1 \exp\left[\frac{2(1-\alpha)F\left(x_3 - E^0_{Fe^{2+}} - \frac{RT}{2F}\ln(x_1)\right)}{RT}\right] = 0 \tag{5.38}$$

$$F_2 = K_{mt,H^+}([H^+]_b - x_2) - 2K_{e,H^+}x_2 \exp\left[\frac{-2\alpha F\left(x_3 - E^0{}_{H^+} - \frac{RT}{2F}\ln\left(\frac{x_2{}^2}{H_2}\right)\right)}{RT}\right] = 0 \quad (5.39)$$

$$F_3 = K_{e,H^+}x_2 \exp\left[\frac{-2\alpha F(x_3 - E^0{}_{H^+} - \frac{RT}{2F}\ln(\frac{x_1{}^2}{H_{21}}))}{RT}\right] - K_{e,Fe^{2+}}x_1 \exp\left[\frac{2(1-\alpha)F(x_3 - E^0{}_{Fe^{2+}} - \frac{RT}{2F}\ln(x_1))}{RT}\right] = 0 \quad (5.40)$$

Where,

x_1 = surface concentration of Fe^{2+} (mol/m^3)

x_2 = surface concentration of H^+ (mol/m^3)

x_3 = corrosion potential (V)

α = transfer coefficient (=0.5 for most cases)

F = Faraday's constant (=96500 C/mol)

R = universal gas constant (=8.314 J/mol-K)

T = temperature (K)

$K_{mt,Fe^{2+}}$ = mass transfer coefficient for Fe^{2+} (m/s)

K_{mt,H^+} = mass transfer coefficient for H^+ (m/s)

K_{e,H^+} = rate constant for cathodic reaction (m/s)

$K_{e,Fe^{2+}}$ = rate constant for anodic reaction (m/s)

H_2 = surface concentration of H_2 gas (mol/m^3)

$E^0{}_{H^+}$ = standard potential for the cathodic reaction (V)

$E^0_{Fe^{2+}}$ = standard potential for the anodic reaction (V)

$[Fe^{2+}]_b$ = bulk concentration for Fe^{2+} (mol/m^3)

$[H^+]_b$ = bulk concentration for H^+ (mol/m^3)

The equations are of the following form,

$$F_i(x_j^*) = 0, \qquad i, j = 1 \rightarrow 3 \tag{5.41}$$

Taylor series expansion about (x_j') ignoring the higher order terms,

$$F_i(x_j^*) = F_i(x_j') + \left.\frac{\partial F_i}{\partial x_j}\right|_{x_j'} (x^* - x_j') \tag{5.42}$$

Where,

x^* = final converged solution

x_j' = initial estimation

Combining Equation 5.41 and 5.42 and solving for ($x^* - x_j'$) = Δx_j

$$\left.\frac{\partial F_i}{\partial x_j}\right|_{x_j'} (\Delta x_j) = -F_i(x_j') \tag{5.43}$$

Hence, this set of three non-linear equations is linearized to the form

$$[J(i, j)](\Delta x_j) = - F_i(x_j') \tag{5.44}$$

Where [J(i, j)] is the Jacobian matrix whose (i, j) th element is obtained by taking partial derivative of F_i with respect to x_j (for i=1 to 3 and j = 1 to 3). The elements of the Jacobian matrix for the system of Equations 5.38, 5.39, and 5.40 are:

$$A(1,1) = K_{mt,Fe^{2+}} - 0.5K_{e,Fe^{2+}} \exp[\frac{F(x_3 - E^0{}_{Fe^{2+}} - \frac{RT}{2F}\ln(x_1))}{RT}] \tag{5.45}$$

$$A(1,2)=0 \tag{5.46}$$

$$A(1,3) = -K_{e,Fe^{2+}} x_1 \exp[\frac{F(x_3 - E^0{}_{Fe^{2+}} - \frac{RT}{2F}\ln(x_1))}{RT}]\frac{F}{RT} \tag{5.47}$$

$$A(2,1)=0 \tag{5.48}$$

$$A(2,2) = -K_{mt,H^+} - 4K_{e,H^+} \exp[\frac{-F(x_3 - E^0{}_{H^+} - \frac{RT}{2F}\ln(\frac{x_2{}^2}{H_2}))}{RT}] \tag{5.49}$$

$$A(2,3) = -2K_{H^+} x_2 \exp[\frac{-F(x_3 - E^0{}_{H^+} - \frac{RT}{2F}\ln(\frac{x_2{}^2}{H_2}))}{RT}]\frac{-F}{RT} \tag{5.50}$$

$$A(3,1) = -0.5K_{e,Fe^{2+}} \exp[\frac{F(x_3 - E^0{}_{Fe^{2+}} - \frac{RT}{2F}\ln(x_1))}{RT}] \tag{5.51}$$

$$A(3,2) = 2K_{e,H^+} \exp[\frac{-F(x_3 - E^0{}_{H^+} - \frac{RT}{2F}\ln(\frac{x_2^{\,2}}{H_2}))}{RT}] \tag{5.52}$$

$$A(3,3) = K_{e,H^+}x_2 \exp[\frac{-F(x_3 - E^0{}_{H^+} - \frac{RT}{2F}\ln(\frac{x_2^{\,2}}{H_2}))}{RT}]\frac{-F}{RT} - K_{e,Fe^{2+}}x_1 \exp[\frac{F(x_3 - E^0{}_{Fe^{2+}} - \frac{RT}{2F}\ln(x_1))}{RT}]\frac{F}{RT} \tag{5.53}$$

The system of equations given by Equation 5.43 is solved by Gauss elimination method. Then the value of (x_j') is updated to (x_j' +Δx_j) and iterated again until the system of equations converges to the solution. In order to get started with Newton's method, initial estimations for three unknowns must be provided.

5.4 Modeling of CO_2 Corrosion with Corrosion Product Layer

5.4.1 Fundamental Theory

The earlier studies show that a thinner corrosion product layer (6 to 14 μm) exists in the slug flow with a lower Froude number (<12) while corrosion product layer disappears in the slug flow with a higher Froude number (>12) compared to the corrosion product layer in the full pipe flow. This corrosion product film will influence the corrosion rate through the transfer of reactive species and its protective effect from the fluid. Figure 5.4.1 shows the mass transfer where a corrosion film forms. There is a corrosion product layer, which is composed of the porous media between the metal surface and the bulk solution. The reactant (H^+) passes from the

bulk solution to the metal surface through a mass transfer region with a thickness of δ, and the product (Fe^{2+}) move from the metal surface toward the bulk solution. Since only two reactions (2.4) and (2.5) are considered in this model, only the movement of the ferrous ion and hydrogen ion will be considered in this layer.

Assuming no chemical reaction, applying a mass balance over the differential region of corrosion product layer or film from z to z+Δz gives that at steady state:

$$N_{Az}\big|_{z+\Delta z} 2\pi(r-z-\Delta z)l - N_{Az}\big|2\pi(r-z)l = 0 \qquad (5.54)$$

Where,

N_{Az} = molar flux of species A at z direction (mol/m^2/s)

r = radius of the pipe (m)

l = pipe length (m)

Rearranging gives:

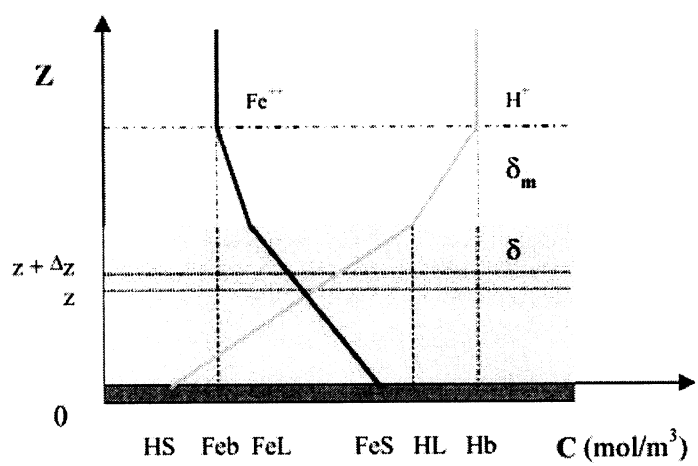

Figure 5.4.1 Schematic of mass transfer with the presence of corrosion product film

$$\frac{N_{Az}\big|_{z+\Delta z} - N_{Az}\big|_{z}}{\Delta z} = \frac{N_{Az}\big|_{z+\Delta z}}{r-z} \tag{5.55}$$

Taking the limit as Δz approaches zero gives:

$$\frac{dN_{Az}}{dz} = \frac{N_{Az}}{r-z} \tag{5.56}$$

Integrating with respect to z gives:

$$N_{Az} = \frac{C}{r-z} \tag{5.57}$$

Where, C = constant

At steady state the rate of mass transfer is equal to the electrochemical reaction rate at the metal surface. The boundary condition is described as following:

At z=0, $N_{Az} = C/r = R_A$

Where, R_A = electrochemical reaction rate of species A ($mol/m^2/s$)

Hence, $C = R_A r$

$$N_{Az} = \frac{R_A r}{r-z} \tag{5.58}$$

For Fe^{2+}:

$$N_{Fe^{2+}_z} = \frac{R_{Fe^{2+}} r}{r - z} \tag{5.59}$$

Where,

$N_{Fe^{2+}_z}$ = molar flux of Fe^{2+} ($mol/m^2/s$)

$R_{Fe^{2+}}$ = electrochemical reaction rate of Fe^{2+} ($mol/m^2/s$) = $i_a/2F$

i_a = anodic current density (A/m^2)

F = Faraday's constant (=96500 C/mol)

Similarly for H^+:

$$N_{H^+_z} = -\frac{R_{H^+} r}{r - z} \tag{5.60}$$

Where,

$N_{H^+_z}$ = molar flux of H^+ ($mol/m^2/s$)

R_{H^+} = electrochemical reaction rate of H^+ ($mol/m^2/s$) = i_c/F

i_c = cathodic current density (A/m^2)

F = Faraday's constant (=96500 C/mol)

For steady state, $i_a = i_c$, and gives:

$$N_{H^+_z} = -2N_{Fe^{2+}_z} \tag{5.61}$$

The ratio of molar flux of H^+ and Fe^{2+} is –2. From the anodic and cathodic reactions, it can be seen that 1 mol Fe^{2+} needs 2 mols H^+ to react each other and the ionic molar fluxes of H^+ and $Fe^{2+}$are in the opposite directions.

According the Fogler (1986), the total molar flux of A, N_{Az}, is the result of two contributions, the molecular diffusion flux produced by a concentration gradient and the flux resulting from the convection of the fluid.

$$N_{A_z} = -cD_{AB}\frac{dx_A}{dz} + x_A(N_{A_z} + N_{B_z}) \tag{5.62}$$

Where,

N_{A_z} = molar flux of A (mol/m^2/s)

N_{B_z} = molar flux of B (mol/m^2/s)

D_{AB} = diffusivity of A in a binary system (m^2/s)

X_A = mole fraction of A

c = molar density of solution (mol/m^3) =ρ/M

ρ = density of solution (kg/m^3)

M = molecular weight of solution (kg/kmol)

For Fe^{2+}:

$$N_{Fe^{2+}{}_z} = -cD_{Fe^{2+}} \frac{dx_{Fe^{2+}}}{dz} + x_{Fe^{2+}}(N_{Fe^{2+}{}_z} + N_{H^+{}_z}) \tag{5.63}$$

When Equation 5.61 are substituted into Equation 5.63, the following expressions are obtained:

$$N_{Fe^{2+}{}_z} = -cD_{Fe^{2+}} \frac{dx_{Fe^{2+}}}{dz} - x_{Fe^{2+}} N_{Fe^{2+}{}_z} \tag{5.64}$$

Hence,

$$N_{Fe^{2+}{}_z} dz = -\frac{cD_{Fe^{2+}}}{(1+x_{Fe^{2+}})} dx_{Fe^{2+}} \tag{5.65}$$

When Equation 5.59 are substituted into Equation 5.65, the following equation are obtained:

$$\frac{i_a r}{2F(r-z)} dz = -\frac{cD_{Fe^{2+}}}{(1+x_{Fe^{2+}})} dx_{Fe^{2+}} \tag{5.66}$$

Integrating with respect to z from o to δ, and the boundary conditions are described as following,

At z = 0, $x_{Fe^{2+}} = FeS/c$

At z = δ, $x_{Fe^{2+}} = FeL/c$

Integrating with respect to $x_{Fe^{2+}}$ from metal surface to the edge of the corrosion film gives:

$$\frac{i_a r}{2F}\ln(1-\frac{\delta}{r}) = cD_{Fe^{2+}}[\ln(1+\frac{FeL}{c}) - \ln(1+\frac{FeS}{c})] \qquad (5.67)$$

Where,

δ = thickness of the corrosion film (m)

FeL = layer concentration of Fe^{2+} (mol/m^3)

FeS = metal surface concentration of Fe^{2+} (mol/m^3)

$D_{Fe^{2+}}$ = diffusion coefficient of Fe^{2+} through corrosion film (m^2/s)

c = molar density of solution (mol/m^3) =ρ/M

ρ = density of solution (kg/m^3)

M = molecular weight of solution (kg/kmol)

Similarly for H^+,

$$N_{H^+_z} = -cD_{H^+}\frac{dx_{H^+}}{dz} + \frac{1}{2}x_{H^+}(N_{Fe^{2+}_z} + N_{H^+_z}) \qquad (5.68)$$

Substitute Equation 5.61 into Equation 5.68, gives:

$$N_{H^+_z} = -cD_{H^+}\frac{dx_{H^+}}{dz} + \frac{1}{2}x_{H^+}N_{H^+_z} \tag{5.69}$$

Hence,

$$N_{H^+_z}dz = -\frac{cD_{H^+}}{(1-0.5x_{H^+})}dx_{H^+} \tag{5.70}$$

Substitute Equation 5.60 into Equation 5.70, gives:

$$\frac{i_c r}{F(r-z)}dz = -\frac{cD_{H^+}}{(1-0.5x_{H^+})}dx_{H^+} \tag{5.71}$$

Integrating with respect to z from o to δ, and the boundary conditions are described as following,

At z = 0, $x_{H^+} = HS/c$

At z = δ, $x_{H^+} = HL/c$

Integrating with respect to x_{H^+} from metal surface to the edge of the corrosion film gives:

$$\frac{i_c r}{F}\ln(1-\frac{\delta}{r}) = 2cD_{H^+}[\ln(1-\frac{0.5HL}{c}) - \ln(1-\frac{0.5HS}{c})] \tag{5.72}$$

Where,

δ = thickness of the corrosion film (m)

HL = layer concentration of H^+ (mol/m^3)

HS = metal surface concentration of H^+ (mol/m^3)

D_{H^+} = diffusion coefficient of H^+ through corrosion film (m^2/s)

c = molar density of solution (mol/m^3) =ρ/M

ρ = density of solution (kg/m^3)

M = molecular weight of solution (kg/kmol)

Equations 5.67 and 5.72 are simplified by using the series expansions:

$$\ln(1+x) = x - \frac{x^2}{2} + \frac{x^3}{3} - \frac{x^4}{4} + \ldots + (-1)^{n+1}\frac{x^n}{n} + \ldots \tag{5.73}$$

$|x| < 1$

$$\ln(1-x) = -(x + \frac{x^2}{2} + \frac{x^3}{3} + \frac{x^4}{4} + \ldots + \frac{x^n}{n} + \ldots) \tag{5.74}$$

$|x| < 1$

For Fe^{2+}, $0<\delta/r<<1$, $0<FeL/c<<1$, and $0<FeS/c<<1$, so keeping only one term in series expansion, Equation 5.67 gives:

$$-\frac{i_a}{2F}\delta = D_{Fe^{2+}}(FeL - FeS) \tag{5.75}$$

Hence,

$$FeL = FeS - \frac{i_a\delta}{2FD_{Fe^{2+}}} \tag{5.76}$$

For H^+, $0<\delta/r<<1$, $0<HL/c<<1$, and $0<HS/c<<1$, so keeping only one term in series expansion, Equation 5.72 gives:

$$\frac{i_c}{F}\delta = D_{H^+}(HL - HS) \tag{5.77}$$

Hence,

$$HL = HS + \frac{i_c\delta}{FD_{H^+}} \tag{5.78}$$

Rates of Electrochemical Reactions:

The current densities i_a, i_c are given as before in Equations 5.30 and 5.31. The equilibrium potentials E_{H^+} and $E_{Fe^{2+}}$ are given by the Nerst equations as before in Equations 5.32 and 5.33.

The sum of the currents due to the cathodic reactions should be equal to the sum of the currents due to the anodic reactions, which in turn is equal to the corrosion current as mentioned in Equation 5.34. Under steady state conditions it is assumed that the sum of the mass transfer rates of the reactions are equal to the sum of the electrochemical reaction rates. Hence we can write,

$$2FK_{mt,Fe^{2+}}(FeL - Feb) = i_a \tag{5.79}$$

$$FK_{mt,H^+}(Hb - HL) = i_c \tag{5.80}$$

Where,

Feb = bulk concentration of Fe^{2+} (mol/m^3)

FeL = layer concentration of Fe^{2+} (mol/m^3)

Hb = bulk concentration of H^+ (mol/m^3)

HL = layer concentration of H^+ (mol/m^3)

The three equations 5.34, 5.35, 5.79, and 5.80 are used for corrosion rate calculation by adding the effect of corrosion film.

5.4.2 Diffusivity in Porous Corrosion Film

According to Scatterfield (1980), pore diffusion may occur by bulk diffusion. Pore diffusion is shown in Figure 5.4.2 He suggested that the bulk diffusion coefficient for pore media, $D_{12,\,eff}$, can be expressed as

$$D_{12,eff} = \frac{D_{12}\theta}{\tau} \tag{5.81}$$

Where,

θ = void fraction

τ = tortuosity factor

Experimental measurements on a variety of commercial catalysts observe that in many cases, values of τ is in the range of 2 to 7, while values of θ vary from about 0.3 to 0.7.

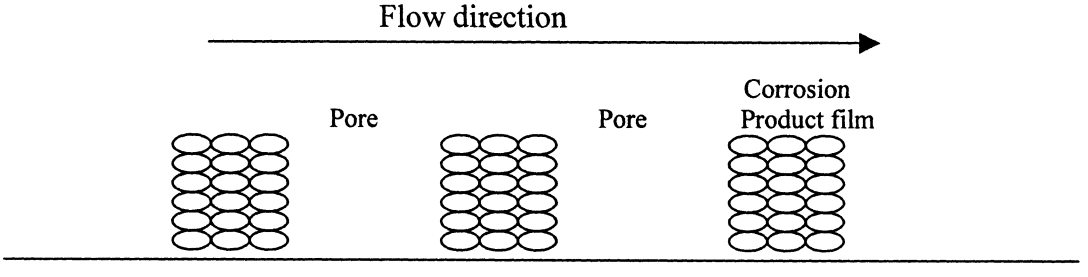

Figure 5.4.2 Pore diffusion in porous corrosion film

If the pores are large, the process is that of bulk diffusion. In this study, the pores of corrosion product film are large and the corrosion film are not composed of the traditional crystals, hence, $\theta/\tau=1.0$ can be investigated for the porous corrosion film.

According to Fogler (1986), the total molar flux of A, N_{Az}, is the result of two contributions: the molecular diffusion flux produced by a concentration gradient, and the flux resulting from the convection of the fluid. If the pores of corrosion product film are wide and the film is thick, the second contribution can not be neglected. In addition to natural convection, forced convection exists and plays an important role in fully developed turbulent pipe flow and multiphase flow conditions.

The mass transfer in large pores is the combination of mass transfers by diffusion (including diffusion through liquid and solid) and convection (combination of natural and forced convection). Incorporating mass transfer by the effects of forced convection and diffusion through solid into the total molar flux, $\theta/\tau=5$, 10, and 15 can be tested for the corrosion film through increasing the rate of mass transfer by diffusion through liquid.

5.4.3 Numerical Solution of Corrosion Rate

From Equations 5.76 and 5.78, we know the relations between the surface concentrations and layer concentrations. As we discussed in section 5.3, three unknowns, which are surface concentration of ferrous ion, surface concentration of hydrogen ion, and corrosion potential, can be solved by a set of three nonlinear

equations. These three nonlinear equations are linearized in terms of the unknown quantities and are solved by using the Newton-Raphson method as described in section 5.3.2. When Equation 5.76 and 5.78 are substituted into Equation 5.79 and 5.80, Equations 5.30, 5.31, 5.34, 5.79, and 5.80 gives,

$$F_1 = K_{mt,Fe^{2+}}(x_1 - [Fe^{2+}]_b) - \left(\frac{K_{mt,Fe^{2+}}\delta}{D_{Fe^{2+}}} + 1\right)K_{e,Fe^{2+}}x_1 \exp\left[\frac{2(1-\alpha)F(x_3 - E^0_{Fe^{2+}} - \frac{RT}{2F}\ln(x_1))}{RT}\right] = 0 \quad (5.82)$$

$$F_2 = K_{mt,H^+}([H^+]_b - x_2) - 2\left(\frac{K_{mt,H^+}\delta}{D_{H^+}} + 1\right)K_{e,H^+}x_2 \exp\left[\frac{-2\alpha F(x_3 - E^0_{H^+} - \frac{RT}{2F}\ln(\frac{x_2^2}{H_2}))}{RT}\right] = 0 \quad (5.83)$$

$$F_3 = K_{e,H^+}x_2 \exp\left[\frac{-2\alpha F(x_3 - E^0_{H^+} - \frac{RT}{2F}\ln(\frac{x_2^2}{H_2}))}{RT}\right] - K_{e,Fe^{2+}}x_1 \exp\left[\frac{2(1-\alpha)F(x_3 - E^0_{Fe^{2+}} - \frac{RT}{2F}\ln(x_1))}{RT}\right] = 0 \quad (5.84)$$

Where,

x_1 = surface concentration of Fe^{2+} (mol/m^3)

x_2 = surface concentration of H^+ (mol/m^3)

x_3 = corrosion potential (V)

δ = thickness of the corrosion product film (m)

$D_{Fe^{2+}}$ = diffusion coefficient of Fe^{2+} through corrosion film (m^2/s)

D_{H^+} = diffusion coefficient of H^+ through corrosion film (m^2/s)

α = transfer coefficient (=0.5 for most cases)

F = Faraday's constant (=96500 C/mol)

R = universal gas constant (=8.314 J/mol-K)

T = temperature (K)

$K_{mt,Fe^{2+}}$ = mass transfer coefficient for Fe^{2+} (m/s)

K_{mt,H^+} = mass transfer coefficient for H^+ (m/s)

K_{e,H^+} = rate constant for cathodic reaction (m/s)

$K_{e,Fe^{2+}}$ = rate constant for anodic reaction (m/s)

H_2 = surface concentration of H_2 gas (mol/m^3)

$E^0_{H^+}$ = standard potential for the cathodic reaction (V)

$E^0_{Fe^{2+}}$ = standard potential for the anodic reaction (V)

$[Fe^{2+}]_b$ = bulk concentration for Fe^{2+} (mol/m^3)

$[H^+]_b$ = bulk concentration for H^{2+} (mol/m^3)

The elements of the Jacobian matrix for the system of Equations 5.82, 5.83, and 5.84 are:

$$A(1,1) = K_{mt,Fe^{2+}} - 0.5(\frac{K_{mt,Fe^{2+}}\delta}{D_{Fe^{2+}}} + 1)K_{e,Fe^{2+}} \exp[\frac{F(x_3 - E^0{}_{Fe^{2+}} - \frac{RT}{2F}\ln(x_1))}{RT}]$$

(5.85)

A(1, 2)=0 (5.86)

$$A(1,3) = -(\frac{K_{mt,Fe^{2+}}\delta}{D_{Fe^{2+}}} + 1)K_{e,Fe^{2+}}x_1 \exp[\frac{F(x_3 - E^0{}_{Fe^{2+}} - \frac{RT}{2F}\ln(x_1))}{RT}]\frac{F}{RT}$$

(5.87)

A(2, 1)=0 (5.88)

$$A(2,2) = -K_{mt,H^+} - 4(\frac{K_{mt,H^+}\delta}{D_{H^+}} + 1)K_{e,H^+} \exp[\frac{-F(x_3 - E^0{}_{H^+} - \frac{RT}{2F}\ln(\frac{x_2{}^2}{H_2}))}{RT}]$$

(5.89)

$$A(2,3) = -2(\frac{K_{mt,H^+}\delta}{D_{H^+}} + 1)K_{e,H^+}x_2 \exp[\frac{-F(x_3 - E^0{}_{H^+} - \frac{RT}{2F}\ln(\frac{x_2{}^2}{H_2}))}{RT}]\frac{-F}{RT}$$

(5.90)

$$A(3,1) = -0.5K_{e,Fe^{2+}} \exp[\frac{F(x_3 - E^0{}_{Fe^{2+}} - \frac{RT}{2F}\ln(x_1))}{RT}] \quad (5.91)$$

$$A(3,2) = 2K_{e,H^+} \exp[\frac{-F(x_3 - E^0{}_{H^+} - \frac{RT}{2F}\ln(\frac{x_2{}^2}{H_2}))}{RT}] \quad (5.92)$$

$$A(3,3) = K_{e,H^+} x_2 \exp\left[\frac{-F\left(x_3 - E^0{}_{H^+} - \frac{RT}{2F}\ln\left(\frac{x_2^{\,2}}{H_2}\right)\right)}{RT}\right]\frac{-F}{RT} - K_{e,Fe^{2+}} x_1 \exp\left[\frac{F\left(x_3 - E^0{}_{Fe^{2+}} - \frac{RT}{2F}\ln(x_1)\right)}{RT}\right]\frac{F}{RT} \quad (5.93)$$

5.5 Development of CO_2 Corrosion Mechanistic Model in Slug Flow

A development flow sheet of the corrosion mechanistic model in slug flow is given in Figure 5.5.1. The prospective model includes two phases. Phase one develops the model for corrosion without the corrosion product film. Phase two will develop the model for corrosion with the presence of corrosion product film.

Earlier studies (Gopal, 1995, and Maley, 1997) prepare a plenty of information on the slug flow, such as slug length, slug frequency, height of film, holdup, mixture velocity, film velocity, and Froude number. These parameters could be used to calculate the corresponding corrosion rate in slug zones as indicated below.

To calculate the overall corrosion rate, the slug unit can be split into four separate components, slug film, slug mixing zone, slug body, and slug tail, as shown in Figure 5.5.2(a). If the slug and film characteristics are known, then the corrosion in each section can be calculated. Finally, the overall corrosion rate can be determined as given in Equations 5.94 and 5.95.

$$C_R = C_{sf}(t_{sf}/t) + C_{sm}(t_{sm}/t) + C_{sb}(t_{sb}/t) + C_{st}(t_{st}/t) \quad (5.94)$$

$$t = t_{sf} + t_{sm} + t_{sb} + t_{st} \quad (5.95)$$

Where,

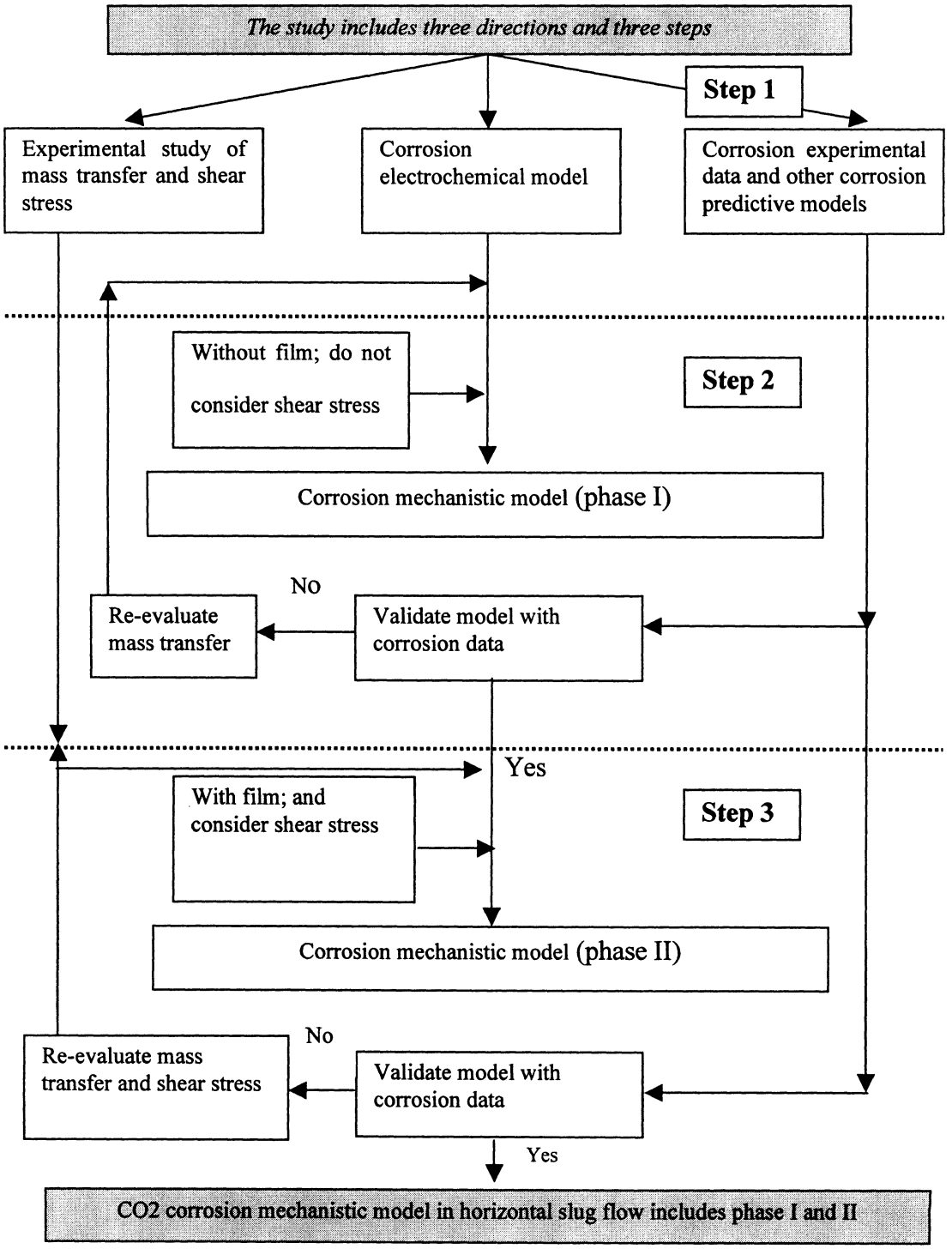

Figure 5.5.1 Development of corrosion mechanistic model for slug flow

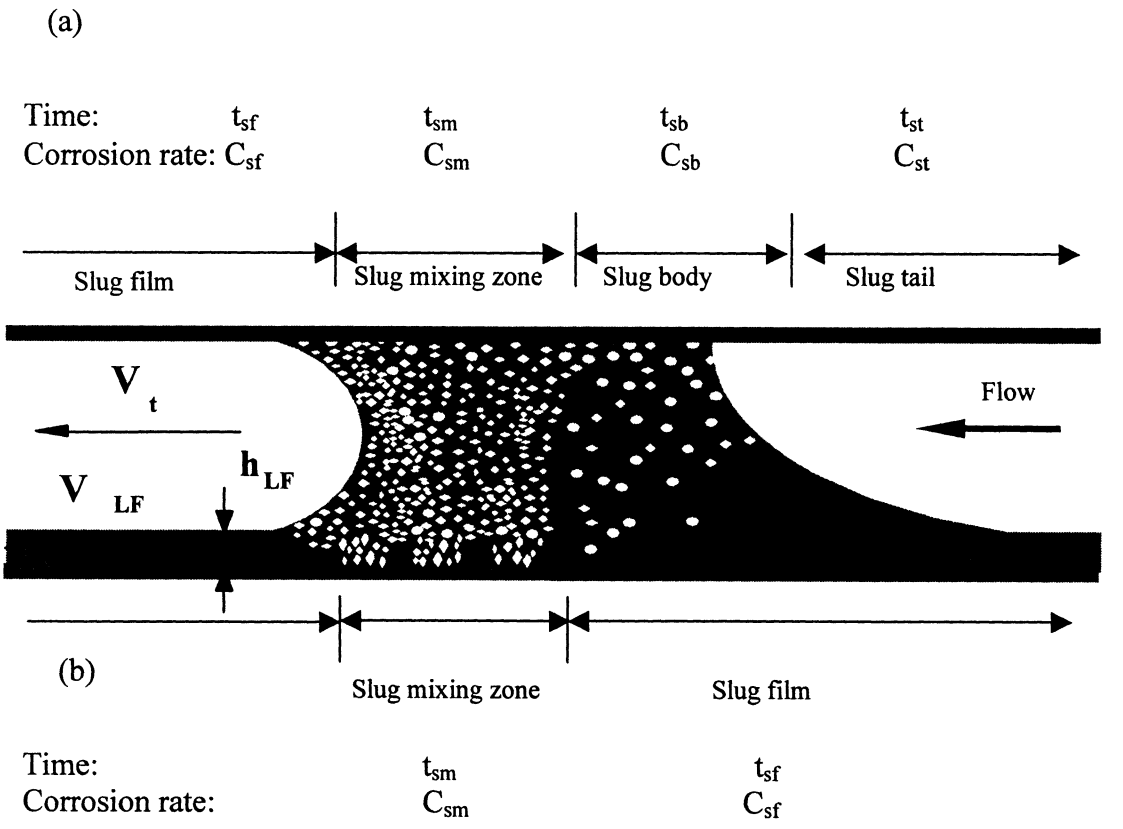

Figure 5.5.2 Calculation of overall corrosion rate by (a) four parts and (b) two parts in slug flow

C_R = corrosion rate (mm/yr)

t = time for one slug (s)

t_{sf} = time for one slug film (s)

t_{sm} = time for one slug mixing zone (s)

t_{sb} = time for one slug body (s)

The experimental studies of the instantaneous mass transfer coefficient in slug flow have shown that equation 5.94 can be simplified. An example is shown in

Figures 5.5.3. Figure 5.5.3 (a) is typical in that the peaks of the instantaneous mass transfer coefficient appear when the slug mixing zone exists. The base value is for the slug film. This is further shown in an enlarged Figure 5.5.3 (b).

The mass transfer coefficient modeling in slug flow can be simplified through an assumption that slug flow is composed of only two distinctive parts: the mixing zone and the slug film. The slug film also includes the slug body and the slug tail where there is much less influence from gas bubbles. The mixing zone includes the gas bubble entrainment region and the gas redistribution region (Maley and Jepson, 1998). This is shown in Figure 5.5.2 (b). Each mixing zone correponds to the peak instantaneous mass transfer coefficient while each slug film has the base instantaneous mass transfer coefficient.

It is also noticed that the mixing zone does not always create high peaks of instantaneous mass transfer coefficient even in the same slug flow condition. Some slugs are well developed and produce a strong mixing zone where the bubbles can collapse on the wall in the form of pulses. Some slugs are not well developed and thus no pulses of bubbles collapse on the wall. This has been confirmed by observing videos.

The following calculation method is proposed:

$$C_R = C_{sf}\,(t_{sf}/t) + C_{sm}(t_{sm}/t) \qquad (5.96)$$

or

(a)

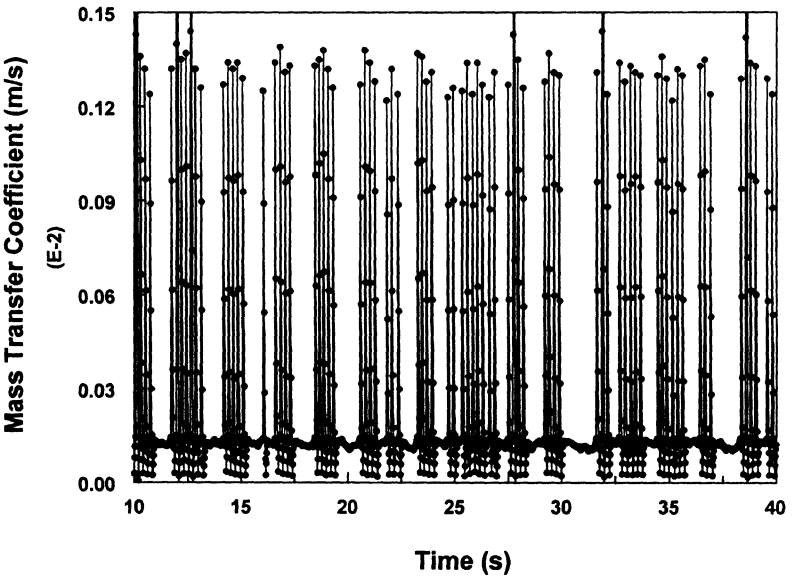

(b)

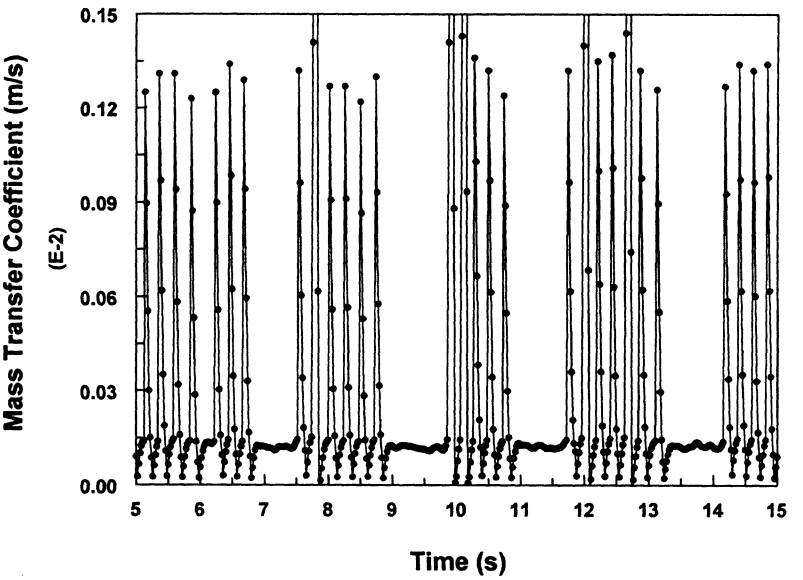

Figure 5.5.3 Instantaneous mass transfer coefficient at Vsl=1.0 m/s and Vsg=1.4 m/s in water/oil/gas slug flow with 20% input oil (a) 10 – 40 s (b) 5 – 15 s

$$C_R = C_{sf}(1 - R_m) + C_{sm} R_m \quad (5.97)$$

$$t = t_{sf} + t_{sm} \quad (5.98)$$

$$R_m = t_{sm}/t \quad (5.99)$$

Where,

t_{sf} = time for one slug film (s)

t_{sm} = time for one slug mixing zone (s)

R_m = ratio of mixing zone time over one slug time

C_{sf} = corrosion rate in slug film (mm/yr)

C_{sm} = corrosion rate in slug mixing zone (mm/yr)

The developed mass transfer correlation Equation 4.11 is used to calculate the mass transfer coefficient of reactive species in slug film. For the slug mixing zone, the mass transfer enhancement (E) shall be taken into consideration. In Chapter 4.4. the mass transfer correlation in Equation 4.13 has been developed for this purpose.

The whole calculation is shown as follows:

Average slug time (s):

$$t = 1/f \quad (5.100)$$

$$\text{Log}(f \times D/V_{sl}) = m \times V_m + b \quad (2.28)$$

$$m = 4 \times 10^{-5}\theta^3 + 5 \times 10^{-4}\theta^2 - 2.5 \times 10^{-2}\theta + 0.7 \quad (2.29)$$

$$b = -4 \times 10^{-4}\theta^3 - 4.1 \times 10^{-3}\theta^2 + 2\theta - 1.7 \quad (2.30)$$

Where,

f = slug frequency (s)

V_m = total gas/oil/water velocity (m/s)

V_{sl} = superficial liquid velocity (m/s)

D = pipeline diameter (m)

θ = pipeline inclination (degree)

Average mixing zone time (s):

$$t_{sm} = LMZ/ V_t \tag{5.101}$$

Average length of mixing zone (m) (Lisa, 1997):

By correlation

$$LMZ = 0.051\ Fr + 0.18 \tag{2.24}$$

or by mechanistic model

$$LMZ = 1.5D + \frac{h_{ls} \times Fr_s \times \sqrt{gD}}{v_b} \tag{2.25}$$

$$v_b = 1.53\left[\frac{\sigma \times g \times \Delta\rho}{\rho^2}\right]^{1/4} \tag{2.26}$$

Where,

v_b = rise velocity of a moderate bubble calculated from equations (m/s)

h_{ls} = liquid height to gas/liquid interface (m)

v_m = mixture velocity with respect to pipe wall (m/s)

V_t = transitional mixing zone velocity (m/s) =1.25 (Vsl+ Vsg) (5.102)

V_{LF} = slug film Velocity (m/s) =Vsl (Gopal, 1994) (5.103)

Fr_s = slug Froude number $= \frac{v_t - v_m}{\sqrt{g \times D}}$ (5.104)

Fr = film Froude number $= \frac{V_t - V_{LF}}{\sqrt{(gh_{EF})}}$ (2.23)

h_{EF} = effective film height obtained from the experiment measurement (m)

The detail computation and discussion of the corrosion mechanistic model is reported in Chapter 6.

CHAPTER 6

CO_2 CORROSION MECHANISTIC MODELING

RESULTS AND DISCUSSION

A CO_2 corrosion mechanistic model has been proposed for the prediction of sweet corrosion rate in two-phase water/gas and three-phase water/oil/ gas slug flow in the previous chapter. Extensive results on corrosion and multiphase flow have been produced at the NSF, I/UCRC Corrosion in Multiphase Systems Center at Ohio University. A database was generated by 1999 at the center. Corrosion and flow data have been measured in 10 cm diameter pipes at temperatures ranging from 30 °C to 90 °C, carbon dioxide partial pressure from 0.13 MPa to 0.79 MPa, using oil/saltwater mixtures in the liquid phase and carbon dioxide as the gas. Oil/saltwater mixtures with a water cut ranging from 100% to 20% have been investigated. ASTM substitute seawater has been used for the aqueous phase. Oils of viscosities 2 and 100 cP have been studied. The computational results from the model are compared with the experimental data from the center's database. The corrosion experimental setup and measurement procedures have been discussed extensively in a previous study (Jepson et al., 1996). This chapter includes a detailed discussion and analysis of the corrosion modeling results.

6.1 Bulk Concentration and pH Results

Figure 6.1.1 shows the predicted values of pH for various conditions of pressure and temperature for saltwater solutions. It is shown that the pH of the solution

decreases with an increase in the carbon dioxide partial pressure. At each pressure, the pH increases with increasing temperature. Both results are expected since the dissolution of carbon dioxide in the aqueous solutions increase with pressure, but decreases with increasing temperature.

Predicted values of pH are compared with experimental results at various temperatures and pressures in Figure 6.1.2. It shows a reasonable agreement at all temperatures and pressures. Further, it has been noticed that the pH does not change when oil is added to solution. Hence the results from the pH calculations are used for water/gas/oil multiphase flows as well.

6.2 Mass Transfer Coefficients

Several mass transfer correlations are used to calculate mass transfer coefficient in turbulent full pipe flow. Chilton and Colburn (1934), Vieth et al. (1963), Berger and Hau (1977), and Equation 4.2 are used to calculate the mass transfer coefficients and corrosion rates. The results are shown in Tables 6.2.1, 6.2.2, 6.2.3, and 6.2.4 for brine. The resulting corrosion rates predicted from the models are compared with experimental results at 40 °C, and are shown in Figure 6.2.1.

The Berger & Hau correlation was developed using electrochemical limiting current technique and large pipe electrode, which are able to provide a fully developed mass transfer layer in the pipeline. It has become the most reliable correlation for the mass transfer in horizontal pipelines. Its predicted values of mass transfer coefficients are about five times lower than those predicted from the Vieth et al. correlation. The Berger and Hau (1977) correlation gives a similar estimation of mass transfer

coefficients as the Chilton and Colburn (1934) correlation does. The Vieth et al. correlation predicts a much higher mass transfer coefficient than the other correlations shown in Table 6.2.1. Figure 6.2.1 shows that the Vieth expression gives reasonable corrosion rates compared to experimental results. This is because the Vieth et al. expression includes the turbulence effects through the ratio V_{max}/V_{avg} that is related to the Reynolds number. This turbulence effects coincide with the in situ flow condition where the corrosion rate are measured in a large diameter multiphase flow loop. In another word, the measured corrosion rate in the flow loop is always higher than the theoretical predicted rate.

$$\text{If } \mathrm{Re} \leq 3200, \ \frac{V_{max}}{V_{avg}} = \frac{1}{0.0425 \log \mathrm{Re} + 0.6172} \tag{6.1}$$

$$\text{If } \mathrm{Re} > 3200, \ \frac{V_{max}}{V_{avg}} = \frac{1}{1.0319 \log \mathrm{Re} - 2.8880} \tag{6.2}$$

In Chapter 4.4, mass transfer correlations for multiphase slug flow have been developed from experimental data based on the Berger and Hau (1977) correlation since both studies use similar technique. The above corrosion calculations indicate that both correlations underrate the corrosion rates in full pipe flow.

It is seen from Table 6.2.1 that the mass transfer coefficients in all cases increase with velocity as expected. However, the predicted values of the mass transfer

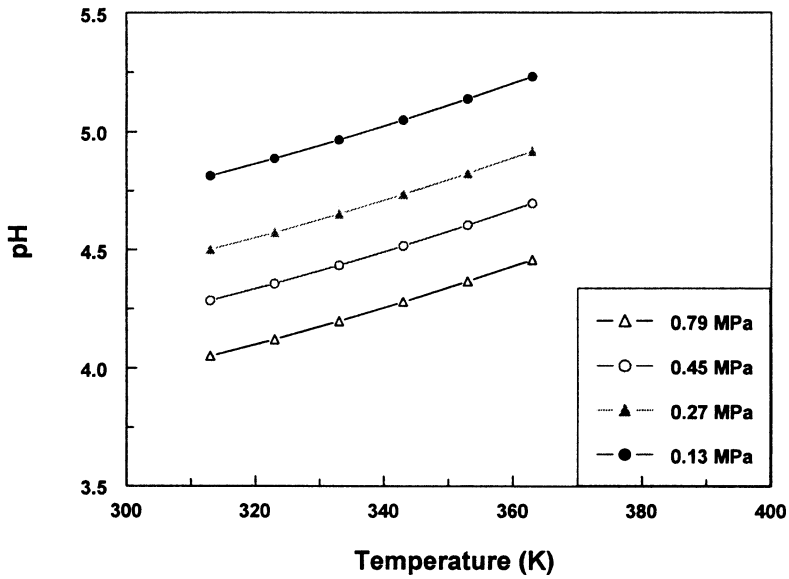

Figure 6.1.1 Predicted pH vs temperature and pressure for brine

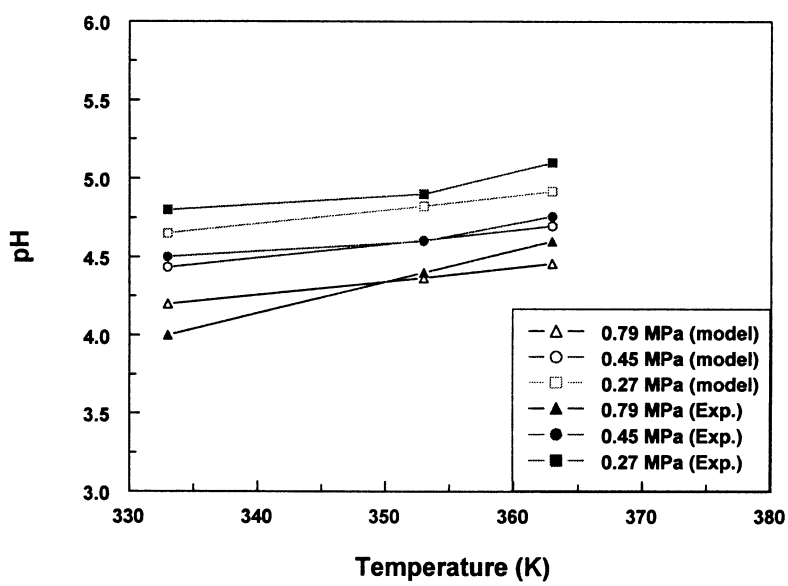

Figure 6.1.2 Comparison of experimental data and predicted pH values for brine

Table 6.2.1 Using Chilton and Colburn expression for fully developed turbulent mass transfer to predict corrosion rates for brine at 40 °C

P (MPa)	U (m/s)	KmtFe (m/s)	KmtH (m/s)	$[H^+]$ (mol/m^3)	CR (pred.) (mm/yr)	CR (exp.) (mm/yr)
0.136	1.0	3.77E-05	2.07E-04	1.428E-02	0.33	0.88
0.27	1.0	3.77E-05	2.07E-04	2.814E-02	0.65	4.25
0.45	1.0	3.77E-05	2.07E-04	4.644E-02	1.08	8.6
0.79	1.0	3.77E-05	2.07E-04	8.008E-02	1.86	11.4

Table 6.2.2 Using Vieth et al. expression for fully developed turbulent mass transfer to predict corrosion rates for brine at 40 °C

P (MPa)	U (m/s)	KmtFe (m/s)	KmtH (m/s)	$[H^+]$ (mol/m^3)	CR (pred.) (mm/yr)	CR (exp.) (mm/yr)
0.136	1.0	2.05E-04	1.13E-03	1.428E-02	1.80	0.88
0.27	0.28	6.99E-05	3.84E-04	2.814E-02	1.21	3.0
0.27	1.0	2.05E-04	1.13E-03	2.814E-02	3.55	4.25
0.45	1.0	2.05E-04	1.13E-03	4.644E-02	8.60	8.6
0.79	1.0	2.05E-04	1.13E-03	8.008E-02	10.11	11.4

Table 6.2.3 Using Berger & Hau expression for fully developed turbulent mass transfer to predict corrosion rates for brine at 40 °C

P (MPa)	U (m/s)	KmtFe (m/s)	KmtH (m/s)	$[H^+]$ (mol/m^3)	CR (pred.) (mm/yr)	CR (exp.) (mm/yr)
0.136	1.0	4.91E-05	2.70E-4	1.428E-02	0.43	0.88
0.27	1.0	4.91E-05	2.70E-4	2.814E-02	0.85	4.25
0.45	1.0	4.91E-05	2.70E-4	4.644E-02	1.40	8.6
0.79	1.0	4.91E-05	2.70E-4	8.008E-02	2.42	11.4

Table 6.2.4 Using Equation 4.2 Expression for fully developed turbulent mass transfer to predict corrosion rates for brine at 40 °C

P (MPa)	U (m/s)	KmtFe (m/s)	KmtH (m/s)	$[H^+]$ (mol/m^3)	CR (pred.) (mm/yr)	CR (exp.) (mm/yr)
0.136	1.0	9.99E-05	5.50E-04	1.428E-02	0.88	0.88
0.27	1.0	9.99E-05	5.50E-04	2.814E-02	1.73	4.25
0.45	1.0	9.99E-05	5.50E-04	4.644E-02	2.86	8.6
0.79	1.0	9.99E-05	5.50E-04	8.008E-02	4.92	11.4

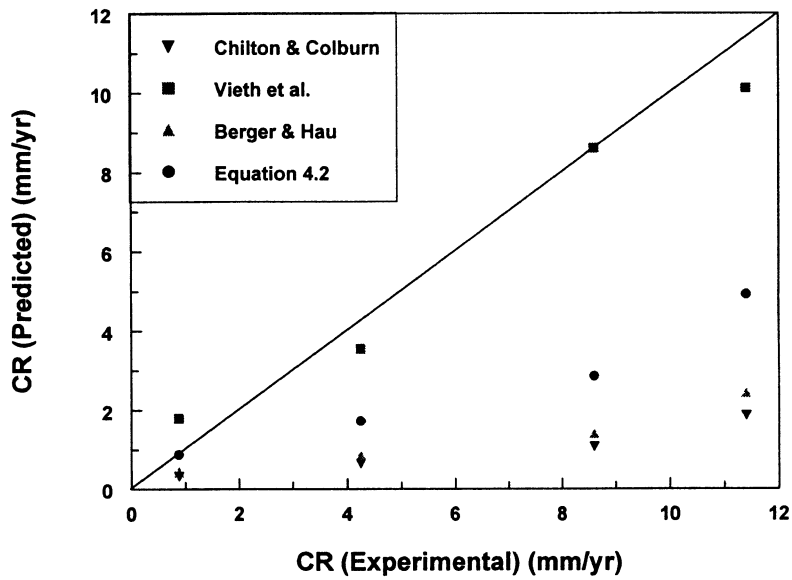

Figure 6.2.1 Predicted vs experimental corrosion rates for brine by using several mass transfer correlations in full pipe flow

coefficients are different. For example, at a velocity of 1.0 m/s, a pressure of 0.79 MPa, the mass transfer coefficient for hydrogen ion is 2.07×10^{-4} m/s by using the Chilton and Colburn expression, 1.13×10^{-4} m/s by using the Vieth expression, 2.70×10^{-4} m/s by using the Berger and Hau expression, and 5.50×10^{-4} by Equation 4.2 developed in this study. The corresponding corrosion rates are 1.86, 10.11, 2.42, 4.92 mm/yr, respectively. The experimental corrosion rate is 11.4 mm/yr at this condition. It is shown that the corrosion rates in all cases increase proportionally to the calculated mass transfer coefficient with the increase of CO_2 partial pressure.

6.3 Water/Gas/Oil Multiphase Slug Low

6.3.1 Water/Gas Slug Flow

The mass transfer correlations (4.11) and (4.13) are developed just for the slug film zone and the slug mixing zone, respectively. Therefore these correlations are used to calculate the mass transfer coefficient in the CO_2 corrosion mechanistic model. The water physical properties are directly used in the calculations of Reynolds and Schmidt numbers in the water/gas two-phase slug flow.

6.3.2 Water/Gas/Oil Slug Flow

Zhang (1997) has suggested two methods to calculate the mass transfer coefficient for water/oil flow. Both involved in situ water velocity and pipe diameter. In the first method mixture density and mixture viscosity, averaged on a volumetric basis, were used in the definitions of Reynolds and Schmidt numbers. In the second method, only the saltwater density and viscosity were used.

The in situ oil percentages in three-phase slug flow have been discussed in Chapter 4.2 and 4.4. These studies prove that the oil phase mixed very well with the water phase because of the enhanced turbulence induced by the gas phase in the slug flow. Therefore, water/oil mixture properties will be used in the definition of Reynolds and Schmidt numbers in the liquid phase under water/gas/oil three-phase slug flow.

6.4 Temperature Dependence of Corrosion Rate

All the previous results discussed are for 40 °C. Computation is further carried out for 60 °C and 80 °C. The developed correlations Equation 4.11 and 4.13 are used to predict the mass transfer coefficients in the slug film and the slug mixing zone.

These results are shown in Figure 6.4.1 and Table 6.4.1 for 40, 60 and 80 °C, respectively, for brine and 20% oil testing conditions. Comparisons with experimental observations at slug with Froude 13.1 are shown in Table 6.4.1.

It shows that the predicted corrosion rate increases greatly with the temperature at a high-pressure condition. For example, in Table 6.4.1 for brine, at a pressure of 0.79 MPa, the predicted corrosion rates are 11.9, 92.1, 143.3 mm/yr for 40, 60, and 80 °C, respectively, while the corresponding experimental results are 13.3, 37.8, and 58.5 mm/yr. It indicates that the model gives a higher corrosion rate than the experimental value. The main reason is that the highest mass transfer coefficient is assumed in the whole slug mixing zone as shown in Figure 5.5.3. This means that the ratio of mixing zone time over one slug time obtained in Equation 5.99 may be overestimated. Without the consideration of corrosion film in the model would be another possible reason since the corrosion film usually decreases the corrosion rates.

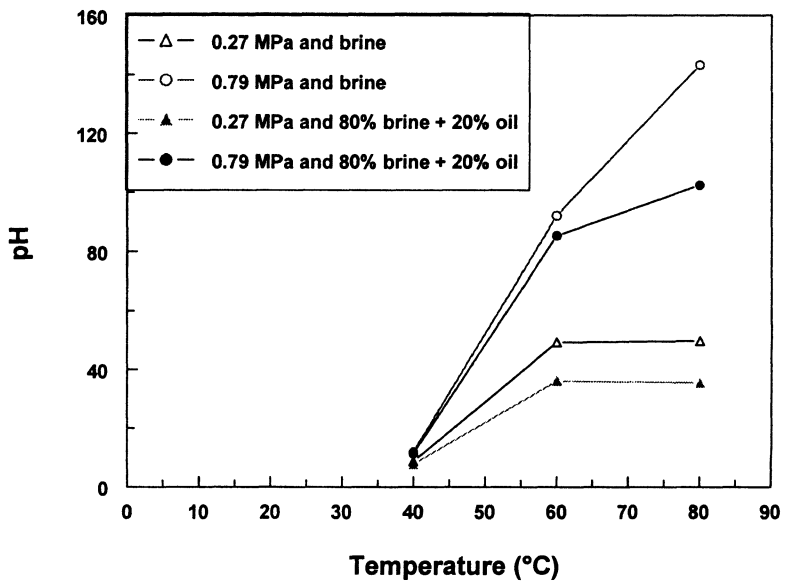

Figure 6.4.1 Influence of temperature on corrosion rates in multiphase slug flow

Table 6.4.1 Using the developed mass transfer correlation to predict corrosion rates in two-phase and three-phase slug flow at temperature of 40, 60, and 80 °C and pressure of 0.27 and 0.79 MPa

T (°C)	CR (mm/yr)															
	Water/gas (Vsl=1 m/s, Vsg=6 m/s) Fr=13.1 (13.1 is my calculation results)															
	Brine								20% Oil -80% Brine							
	0.27 (MPa)				0.79 (MPa)				0.27 (MPa)				0.79 (MPa)			
	Exp.	Mod.	Ohio	Shell	Exp.	Mod.	Ohio	Shell	Exp.	Mod.	Ohio	Shell	Exp.	Mod.	Ohio	Shell
40	10.6	8.8	8.7	1.5	13.3	11.9	20.4	2.1	7.8	7.8	8.1	1.1	11.2	11.3	19.1	3.1
60	18.4	49.2	15.4	2.0	37.8	92.1	36.3	5.8	17.0	36.2	14.4	1.4	34.4	85.4	33.9	4.1
80	24.6	49.7	25.7	1.9	58.5	143.3	60.6	5.3	22.0	35.6	24.0	1.3	53.2	102.4	56.7	3.8

6.5 Comparison with Shell Model and Ohio Model

Table 6.4.1 also compares three models, the Shell model, the Ohio model, and the current mechanistic model to predict the corrosion rate in multiphase slug flow. Figure 6.5.1 further compares the results given by these three models with the experimental corrosion rate. The comparison directly indicates the Shell model seriously underestimates the corrosion rate for slug flow since it neglects the bubble collapsing in the slug mixing zone as discussed in Table 2.3 of Chapter 2.2.2.

Gunaltun (1996) suggested that high accuracy in corrosion prediction is neither required nor possible because of the complexity involved in the production, corrosion control, and engineering design. Only the "order of magnitude" of the corrosion rate has a practical meaning. Therefore, the current mechanistic model is better than the previous mechanistic models in predicting the corrosion rates in slug flow.

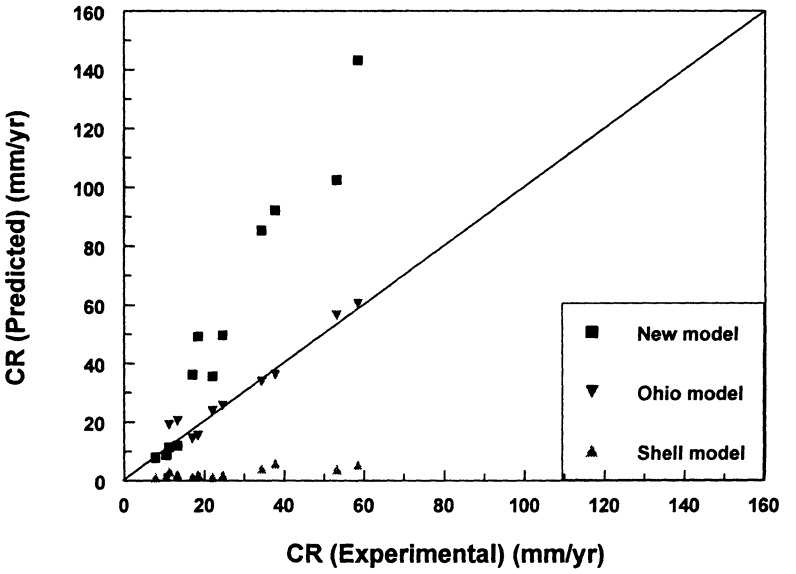

Figure 6.5.1 Comparison of three corrosion models with experimental data

6.6. Effect of Slug Flow on Corrosion Rate

6.6.1 Effect of Superficial Gas Velocity and Froude number

Table 6.6.1 shows the calculation procedure in this mechanistic model. The variables follow the definition mentioned in Chapter 5.5. For example, at 60 °C, 6 m/s superficial gas velocity, and 1 m/s superficial liquid velocity, the Froude number 13.1 is first calculated based on the Equation 2.23. Then, the length of the slug mixing zone (LMZ) is obtained by Equations 2.24 or 2.25. The average mixing zone time (t_{sm}) of 0.097 is calculated by Equation 5.101. On the other hand, the average slug time (t) can be calculated from the slug frequency (f) in Equation 5.101. The ratio of the mixing zone time over the one slug time (R_m) is then obtained as 0.058 from Equation 5.99. The mechanistic model predicts a corrosion rate of 816.93 mm/yr in the mixing zone using the mass transfer correlation in Equation 4.13. It gives a corrosion rate of only 1.75 mm/yr in the slug film using the mass transfer correlation in Equation 4.11. The significant difference in the corrosion rate is a result of the enhanced mass transfer rate in the slug mixing zone. In the end Equation 5.97 is applied to calculate the average corrosion rate (C_R) of 49.16 mm/yr in the slug flow.

Figure 6.6.1 directly presents the influence of superficial gas velocity and temperature on the corrosion rate in the slug flow. At a temperature of 40 °C, the corrosion process is mass transfer controlled at low velocities (from 0 to 4 m/s or from Froude zero to 10.8), while it becomes reaction controlled at high velocities (above 4 m/s). The transition velocity is called the limiting velocity, and it continues to go up with an increasing temperature since the reaction rate increases much more quickly

Table 6.6.1 Calculation of corrosion rate in two-phase slug flow using the mechanistic model at 0.27 MPa

Temp (°c)	Vsg (m/s)	Vsl (m/s)	Fr	LMZ (m)	T_{sm} (s)	f (1/s)	T (s)	R_m	Vt (m/s)	C_{sm} (mm/yr)	V_{lf} (m/s)	C_{sf} (mm/yr)	C_r (mm/yr)
40	6	0.5	14.4	0.914	0.113	24	2.500	0.045	8.125	128.69	0.5	0.88	6.63
60	6	0.5	14.4	0.914	0.113	24	2.500	0.045	8.125	1053.6	0.5	1.15	48.53
80	6	0.5	14.4	0.914	0.113	24	2.500	0.045	8.125	1103.6	0.5	1.05	50.68
40	6	1	13.1	0.848	0.097	36	1.667	0.058	8.75	128.95	1.0	1.34	8.76
60	6	1	13.1	0.848	0.097	36	1.667	0.058	8.75	816.93	1.0	1.75	49.16
80	6	1	13.1	0.848	0.097	36	1.667	0.058	8.75	827.82	1.0	1.61	49.66
40	6	1.5	14	0.894	0.095	60	1.000	0.095	9.375	128.78	1.5	1.71	13.83
60	6	1.5	14	0.894	0.095	60	1.000	0.095	9.375	1040.52	1.5	2.25	101.26
80	6	1.5	14	0.894	0.095	60	1.000	0.095	9.375	1087.84	1.5	2.06	105.60

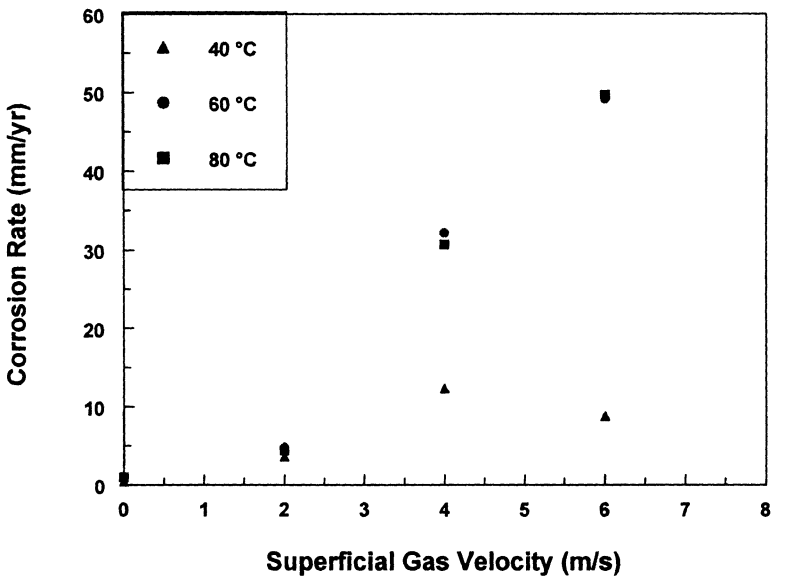

Figure 6.6.1 Predicted corrosion rate vs superficial gas velocity for 40, 60, and 80 °C in ASTM seawater/gas slug flow at 0.27 MPa

compared to the mass transfer rate when the temperature increases. At a higher temperature, e.g. 60 or 80 °C, the reaction speed increases significantly compared to 40 °C. The reaction rate constants increase about 10 times, but the mass transfer coefficients increase only about 2 times. Therefore, the mass transfer controlled flow region extends to a superficial velocity of 6 m/s or higher. This proves that the effect of multiphase flow on corrosion is important, as is this study in general.

There is a close relation between the Froude number and the superficial gas velocity as shown in Equation 2.23. Table 6.6.2 shows that the Froude number dominantly influences the corrosion rate. For example, at 60 °C when the Froude number increases from 6 to 10.8 and 13.1, the corrosion rate increases significantly from 4.80 to 32.19 and 49.16 mm/yr although the slug frequency decreases slightly.

Table 6.6.2 Predicted corrosion at various superficial gas velocities and 1.0 m/s superficial liquid velocity in water/gas slug flow at 0.27 MPa

Vsg (m/s)	Froude	Slug frequency (Hz)	CR (mm/yr) at 0.27 MPa, water/gas slug flow, Vsl =1.0 m/s		
			Temperature (°C)		
			40	60	80
0	-	-	0.45	0.75	1.02
2	6	46	3.64	4.80	4.42
4	10.8	44	12.33	32.19	30.69
6	13.1	36	8.76	49.16	49.66

This trend is also observed at other temperatures. This also confirms the significance of introducing the dimensionless Froude number into the mass transfer correlation as shown in Equation 4.13.

6.6.2 Effect of Superficial Liquid Velocity and Slug Frequency

Table 6.6.3 shows the predicted corrosion rates at various superficial liquid velocities and at a 1.0 m/s superficial liquid velocity in water/gas slug flow at 0.27 MPa. These three flow conditions have similar Froude numbers, but have significant differences in the slug frequency since the slug frequency is mainly influenced by the superficial liquid velocity as shown in Equation 2.28.

Figure 6.6.2 indicates that the slug frequency and the liquid velocity have an important impact on the corrosion rate. Under a low superficial liquid velocity (e.g. 1 m/s), the slug frequency is quite small, and the corrosion rate does not change much. However, a significant change in the slug frequency causes the corrosion rates to increase quickly when the superficial liquid velocity increases to 1.5 m/s. It is also

noticed that the corrosion is reaction controlled under the temperature of 40 °C. Under a higher temperature, e.g. 60 or 80 °C, the corrosion becomes mass transfer controlled because the reaction rate increases faster than the mass transfer rate.

Table 6.6.3 Predicted corrosion at various superficial liquid velocities and 1.0 m/s superficial liquid velocity in water/gas slug flow at 0.27 MPa

Vsl (m/s)	Slug frequency (Hz)	Froude	CR (mm/yr) at 0.27 MPa, water/gas slug flow, Vsg =6.0 m/s		
			Temperature (°C)		
			40	60	80
0.5	24	14.4	6.63	48.53	50.68
1.0	36	13.1	8.76	49.16	49.66
1.5	60	14	13.83	101.26	105.60

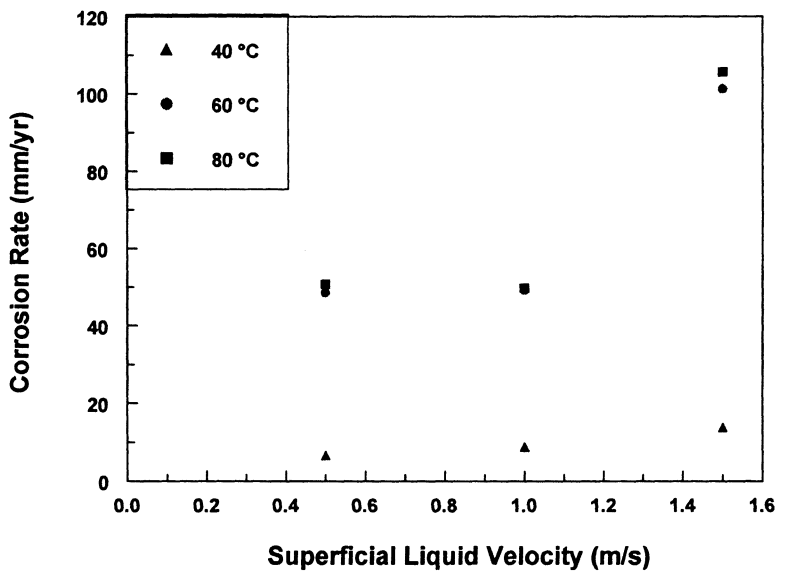

Figure 6.6.2 Predicted corrosion rate vs superficial liquid velocity for 40, 60, and 80 °C in ASTM seawater/gas slug flow at 0.27 MPa

6.7 Effect of Corrosion Film on Corrosion Rate

Chapter 5.5 already discussed the mechanistic model in the presence of the corrosion product film. The earlier studies by Heuer and Stubbins (1999) and Seal et al. (2000) found that the thickness of the corrosion film in the slug flow (corrosion product layer or corrosion scale) is around 6 to 14 μm, which is much lower than the 30-40 μm produced in full pipe flow. This thin film is a direct result of the high shear stress and the scouring action of the slug flow. The analysis in Chapter 4.5 already shows that in the slug flow at Froude 12 the instantaneous shear stress can compete with the adherence of corrosion product scales to the metal substrate and the internal fracture stress of the corrosion film. Therefore, the corrosion product film can be completely destroyed in a slug flow with a higher Froude (>12) and there is no need to consider the influence of the corrosion product film in the corrosion mechanistic model. The previously developed CO_2 corrosion mechanistic model without the corrosion product film is able to predict the worst corrosion rate in a multiphase horizontal slug flow.

The influence of the corrosion film on mass transfer can be modeled by the following Equations 6.4 and 6.5, which appeared in Equations 5.82 and 5.83. Analysis of the corrosion film in the slug flow can become a separate research topic in the future.

$$B_1 = \frac{K_{mt,Fe^{2+}}\delta}{D_{Fe^{2+}}} + 1 \qquad (6.4)$$

$$B_2 = \frac{K_{mt,H^+}\delta}{D_{H^+}} + 1 \qquad (6.5)$$

Where:

$K_{mt,Fe^{2+}}$ = mass transfer coefficient for Fe^{2+} (m/s)

K_{mt,H^+} = mass transfer coefficient for H^+ (m/s)

$D_{Fe^{2+}}$ = diffusion coefficient of Fe^{2+} through corrosion film (m^2/s)

D_{H^+} = diffusion coefficient of H^+ through corrosion film (m^2/s)

δ = thickness of the corrosion product film (m)

CHAPTER 7

CONCLUSIONS

Based on the results from the experimental measurements, observations, and mathematical models, the following conclusions are made.

The mass transfer and the wall shear stress characteristics in the horizontal slug flow have been studied and modeled for two-phase gas/liquid and three-phase gas/liquid/liquid systems. Experimental conditions maintained in this study were in the full pipe flow, the plug flow, and the slug flow regime. The liquid velocity ranged from 0.2 to 1.5 m/s for a water or a water/oil mixture. The superficial gas velocity ranged from 0 to 4.8 m/s. The slug flow was observed within this broad range of velocities in a 10 cm I.D. pipe.

The advanced electrochemical limiting current technique has been applied to study the detailed characteristics of the mass transfer and the shear stress in the electrochemical cell, the stationary slug, and the moving slug flow conditions. It successfully validates the effect of bubble collapsing on the enhancement of the mass transfer. It further confirms the cavitation type collapsing exists in the stationary slug flow and the moving slug flow, which can cause an increase of up to several hundreds times in the instantaneous mass transfer coefficient. A mechanistic model is proposed to explain the oscillation phenomenon of the limiting current density in these multiphase systems.

The oil phase also has an important influence on the mass transfer coefficient. It was found that the oil phase decreases the average mass transfer coefficient with an

increase of the oil percentage in the fluid. The solution sample indicates that the multiphase slug flow can cause an extensive mixing of the water and the oil phase compared to the full pipe flow. This becomes a solid basis for the use of mixture properties in the mass transfer calculation in the slug flow. It was found that the random oil droplets also cause the oscillation of the instantaneous mass transfer coefficient in the water/oil flow. This feature might further enhance the gas bubble collapsing impact in the slug flow. When the oil phase and the cavitation type bubble collapsing coexists in the slug flow, the influence of bubble collapsing on the corrosion processes will be increased from the view of cavitation.

The influence of flow regimes on the mass transfer has been studied. It is found that the bubble collapsing can result in an increase of the mass transfer up to two hundreds times in the water/gas and the water/oil/gas slug flows. This feature distinguishes the slug flow from other flow regimes. In the slug flow the change of the average mass transfer coefficient is negligible in the high superficial gas velocity regions. This becomes theoretical evidence to develop the average mass transfer correlation in the slug film zone and the slug mixing zone.

From the mass transfer data obtained from the multiphase slug flow, the mass transfer correlations for the slug film zone and the slug mixing zone are first developed as the following equations:

$$Sh = 0.544\, Re^{0.61}\, Sc^{0..33}$$

$$Sh = 0.00675\, Fr^{3.6315}\, Re^{0.61}\, Sc^{0..33}$$

The second equation effectively considers the bubble collapsing effect in the

slug flow and becomes an important step to develop the CO_2 corrosion mechanistic model for the slug flow.

The maximum wall shear stress analysis exposes the energy of the slug flow. The instantaneous shear stress produced by the bubble collapsing can compete with two forces: the adherence force of the corrosion product scales to the metal substrate and the fracture stress of corrosion product scales. Therefore, this theoretical calculation matches the experimental investigation of the corrosion coupon that the slug flow can scrape away the corrosion product film and corrosion inhibitor from the pipe wall in the slug flow with a higher Froude number (>12). It may cause the corrosion scale to be much thinner in comparison to a full pipe flow condition in the slug flow with a lower Froude number (<12).

Finally, a CO_2 corrosion mechanistic model is developed for the prediction of the corrosion rate of a carbon steel pipeline under multiphase slug flow conditions. The model considers chemistry, thermodynamics, enhanced solid-liquid mass transfer, simplified electrochemical reaction kinetics, and corrosion film. It follows the principles proposed by Zhang (1997) for the study of a corrosion mechanistic model for water/oil two-phase flow. This model simplifies the complex reactions system into two electrochemical reactions: the oxidation of the iron to the ferrous ion and the reduction of the hydrogen ion.

For slug flow, no corrosion product film is assumed in the model since no film exists or only a thin film exists in most slug flow regimes. This model gives the

corrosion rate in the worst case. Analysis of the corrosion product film can be considered separately.

The corrosion mechanistic model gives a clear picture of the corrosion principle in multiphase slug flow. The computation of the model confirms that the temperature and the pressure have important influences on the corrosion rates. At a low temperature the corrosion process is reaction controlled. With the increase of the temperature, the corrosion process becomes mass transfer controlled or mix controlled. This proves the important effect of multiphase flow on corrosion and points out the practical meanings of this study.

The superficial gas velocity is strongly associated with the dimensionless Froude number of the slug flow. When the Froude number increases, its significant contribution to the mass transfer coefficient and to the shear stress are demonstrated by Equations 4.13 and 4.5, respectively. This determines the dominant influence of the Froude number on corrosion. On the other hand, the influence of the slug frequency on corrosion is much less. This knowledge is very helpful in the design of a multiphase flow system. A comparison of the laboratory corrosion database and other models proposed for the slug flow indicates that the CO_2 mechanistic model developed in this study is able to predict the corrosion rate more effectively than the previous mechanistic model for slug flow.

BIBLIOGRAPHY

1. Ahmed, Z. and Abdul Aleem B. J., "Review and Application of Closed-Loop Systems in Flow-Induced Corrosion," *J. Materials Eng. & Performance*, **3**, 3 (1994)
2. Anderson, P. K., Muller, R. H., and Tobias, C. W., "The Effect of Suspended Solids on Mass Transfer to a Rotating Disk," *J. Electrochem. Soc.*, **136**, 390 (1989)
3. Apfel, R. E., "Acoustic Cavitation Inception," *Ultrasonics*, **22**, 25 (1984)
4. Ben Youssef, A., Haebel, U., Javet, P., "Local Enhancement of Liquid-to-Wall Mass Transfer by a Single Gas Bubble," *J. Appl. Electrochem.*, **24**, 658 (1994)
5. Berger, F. P., and Hau, K. -F.F.-L., "Mass Transfer in Turbulent Pipe Flow Measured by Electrochemical Method," *Int. J. Heat Mass Transfer*, **20**, 1185 (1977)
6. Berger, F. P. and Ziai A., "Optimization of Experimental Conditions for Electrochemical Mass Transfer Measurements," *Chem. Eng. Res. Des.*, **61**, 377 (1983)
7. Birkin, P. R., Silva-Martinez S., "The Effect of Ultrasound on Mass Transfer to a Microelectrode," *J. Chem. Soc. Chem. Commun.*, 1807 (1995)
8. Birkin, P. R., Silva-Martinez S., "A Study of the Effect of Ultrasound on Mass Transfer to a Microelectrode," *J. Electroanal. Chem.* **416**, 127 (1996)
9. Birkin, P. R., Silva-Martinez S., "A Study on the Effect of Ultrasound on Electrochemical Phenomena," *Ultrasonic Sonochem.*, **4**, 121 (1997)
10. Birkin, P. R., O'Connor R., Rapple, C., and Silva-Martinez, S., "Electrochemical Measurement of Erosion from Individual Cavitation Events Generated from Continuous Ultrasound," *J. Chem. Soc. Faraday Trans.*, **94**, 3365 (1998)
11. Bradley, H. B., Petroleum Engineering Handbook, Society of Petroleum Engineers, Richardson, TX, 1987
12. Bockris, J. O'M., Drazi, D. and Despic, A. R., "The Electrode Kinetics of the Deposition and Dissolution of Iron," *Electrochim. Acta,* **4**, 325 (1961)
13. Burke, P. A., Advances in CO_2 Corrosion, NACE, Houston, 1985
14. Chen, Y., Hong, T., and Jepson, W. P., "EIS Studies of a Corrosion Inhibitor Behavior under Multiphase Flow Conditions," *Corros. Sci.*, **42**, 979 (2000)
15. Chexal, B., Horowitz, J., Jones, R., Dooley, B., Wood, C., Bouchacourt, M., Remy, F., Nordmann, F., and Paul, P. S., Flow-accelerated Corrosion in Power Plants, Electric Power Research Institute (EPRI), 1996

16. Chilton, C.H., and Colburn, A.P., "Mass Transfer (Absorbtion) Coefficients Prediction from Data on Heat Transfer and Fluid Friction," *Ind. Eng. Chem.*, **26**, 1183 (1934)

17. Choi, H. J., Cepulis, R. L., and Lee, J. B., "Carbon Dioxide Corrosion of L-80 Grade Tubular in Flowing Oil-Brine Two-phase Environments," *Corrosion*, **45**, 667 (1989)

18. Copson, H. R., "Effects of Velocity on Corrosion," *Corrosion,* **16**, 861 (1960)

19. Crolet, J. L., Oslen, S., and Wilhelmsen, W., 'Influence of a Layer of Undissolved Cementite on the Rate of the CO_2 Corrosion of Carbon Steel." Corrosion/1993, Paper No. 42, (Houston, TX: NACE International, 1993)

20. Crowley, A. J., Sam, R. G., Wallis, G. B., and Mehta, D. C., "Slug Flow in a Large Diameter Pipe: I. Effect of Fluid Properties," AIChE Annual Meeting, San Francisco, CA, 1984

21. De Waard, C. and Williams, D. E., "Carbonic Acid Corrosion of Steel," *Corrosion*, **31**, 177 (1975)

22. De Waard, C., Lotz, U., and Milliams, D. E., "Predictive Model for CO_2 Corrosion Engineering in Wet Natural Gas Pipelines," *Corrosion*, **47**, 750 (1991)

23. De Waard, C., and Lotz, U., " Prediction of CO_2 Corrosion of Carbon Steel," Corrosion/1993, Paper No. 69, (Houston, TX: NACE International, 1993)

24. De Waard, C., Lotz, U., and Dugstad, A., " Influence of Liquid Flow Velocity on CO_2 corrosion: A Semi-empirical Model," Corrosion/1995, Paper No.128, (Orlando, FL: NACE International 1995)

25. Dayalan, E., Barrios, J. C., Shirazi, S. A., and Shadley, J. R., Influences of Flow Parameters on CO_2 Corrosion Behavior of Carbon Steels, Corrosion/1993, Paper No. 72, (Houston, TX: NACE International, 1993)

26. Dayalan, E., Vani, G., Shadley, J. R., Shirazi, S. A., and Rybicki, E. F., "Modeling CO_2 Corrosion of Carbon Steels," Corrosion/1995, Paper No. 118, (Orlando, FL: NACE International 1995)

27. Deissler, "Turbulent Fluid Motion," National Aeronautics and Space Administration (NASA), Report 1210, (Washington, DC, 1955)

28. Denpo, K. and Ogawa, H., "Fluid Flow Effects on CO_2 Corrosion Resistance of Oil Well Materials," *Corrosion*, **49**, 412 (1993)

29. Deslous, C., Gil, O., and Tribollet, B., "Frequency Response of Small Electrodes to Hydrodynamic or to Potential Perturbations," *Electrochim. Acta*, **38**, 1847 (1993)

30. Deslous, C., Gil, O. and Tribollet, B., "Frequency Response of Electrochemical Sensors to Hydrodynamic Fluctuations," *J. Fluid Mech.*, **215**, 85 (1990)

31. Dukler, A. E., and Hubbard, M. G., "A Model for Gas-Liquid Slug Flow in Horizontal and Near Horizontal Tubes," *Ind. Eng. Chem. Fundam.*, **14,** (4) 1975

32. Dugstad, R. P., Lunde, L., and Videm, K., "Parametric Study of CO_2 Corrosion of Carbon Steel," Corrosion/1994, Paper No. 14, (Baltimore, MD: NACE International, 1994)

33. Dumont, E., Fayolle, F., and Legrand, J., "Flow Regimes and Wall Shear Rates Determination within a Scraped Surface Heat Exchanger," *J. Food Eng.* **45**, 195 (2000a)

34. Dumont, E., Faylloe, F., Legrand, J., "Electrodiffusional Wall Shear Rate Analysis in Scraped Surface Heat Exchanger," *AIChE J.* **46**, 1138 (2000b)

35. Economou, D. J. and Alkire, R. C., "2-Phase Mass-Transfer in Channel Electrolyzes With Gas-Liquid Flow," *J. Electrochem. Soc.*, **132**, 601 (1985)

36. Efird K. D., "Effect of Fluid Dynamics on the Corrosion of Copper-base Alloys in Seawater," *Corrosion*, **33**, 3 (1977)

37. Efird, K. D., Wright, E. J., Boros, J. A. and Hailey, T.G., "Experimental Correlation of Steel Corrosion in Pipe Flow with Jet Impingement and Rotating Cylinder Laboratory Tests," *Corrosion*, **49**, 21 (1993)

38. Ellison, B. T. and Schmeal W. P., "Corrosion of Steel in Concentrated Sulfuric Acid," *J. Electrochem. Soc.*, **125**, 524 (1978)

39. Eriksrud, E., and Sontvedt, T., "Effect of Flow on CO_2 corrosion Rates in Real and Synthetic Formation Waters," Advances in CO_2 Corrosion, NACE, Houston, 1984

40. Fabre, J. and Line, A., " Modeling of 2-Phase Slug Flow," *Annu. Rev. Fluid Mech.*, **24**, 21 (1992)

41. Fenton, J. M., Alkire, R. C., "Mass Transfer in Flow-Through Porous Electrodes with Two-phase Liquid-Liquid Flow," *J. Electrochem. Soc.*, **135**, 2200 (1984)

42. Fogler, H. S., Elements of Chemical Reaction Engineering, Englewood Cliffs, New Jersey, 1986

43. Fu, S. L., and Bluth, M. J., "Study of Sweet Corrosion under Flowing Brine and/or Hydrocarbon Conditions," Corrosion/1994, Paper No. 31, (Baltimore, MD: NACE International, 1994)

44. Gopal M. "Visualization and Mathematical Modeling of Horizontal Multiphase Slug Flow, " Ph.D. Dissertation, Ohio University (1994)

45. Gopal, M., Kaul, A. and Jepson, W. P., " Mechanisms Contributing to Enhanced Corrosion in Three Phase Slug Flow in Horizontal Pipes," Corrosion/1995, Paper No. 105, (Orlando, FL: NACE International, 1995)

46. Gopal, M. and Jepson, W. P., "Development of Digital Image Analysis Techniques for the Study of Velocity and Void Profiles in Slug Flow," *Int. J. Multiphase Flow*, **23**, 945 (1997)

47. Gopal, M. and Jepson, W. P., "The Study of Dynamic Slug Flow Characteristics Using Digital Image Analysis – Part 1: Flow Visualization," *J. Energy Resour. Technol.*, **120**, 87 (1998a)

48. Gopal, M. and Jepson, W. P., "The Study of Dynamic Slug Flow Characteristics Using Digital Image Analysis – Part 2: Modeling Results," *J. Energy Resour. Technol.*, **120**, 92 (1998b)

49. Gopal, M., Satish, Rajappa, Jepson, W. P., "Corrosion Product Layer in Slug Flow," Corrosion/2000, Paper No. 35, (Orlando, FL: NACE International, 2000)

50. Gray, L. G.S., Anderson, B. G., Danysh, M. J., and Tremaine, O. G., " Mechanism of Carbon Steel Corrosion in Brines Containing Dissolved Carbon Dioxide at pH 4," Corrosion/1989. Paper No. 464, (Houston, TX: NACE International, 1989)

51. Gray, L. G.S., Anderson, B. G., Danish, M. J., and Tremaine, O. G., "Effect of pH and Temperature on The Mechanism of Carbon Steel Corrosion by Aqueous Carbon Dioxide," Corrosion/1990. Paper No. 40, (Houston, TX: NACE International, 1990)

52. Green, A.S., Johnson, B. V., and Choi, H., "Flow-related Corrosion in Large-Diameter Multiphase Flow Line," SPE, 20685, 677, (1990)

53. Gunaltun, Y. M., "Combine Research and Field Data for Corrosion Rate Prediction," Corrosion/1996, Paper No. 27, (Denver, CO, NACE International, 1996)

54. Hagenson, L. C., Doraiswamy, L. K., "Comparison of the Effects of Ultrasound and Mechanical Agitation on a Reacting Solid-liquid System," *Chem. Eng. Sci.*, **53**, 131 (1998)

55. Harmathy, T. Z., "Velocity of Large Drops and Bubbles in Media of Infinite or Restricted Extent," *AIChE J.*, **6**, 281 (1960)

56. Hausler, R. H., Advances in CO_2 Corrosion, NACE, Houston, 1984

57. Heitz, E. " Chemo-Mechanical Effects of Flow on Corrosion," *Corrosion*, **47**,135 (1991)

58. Herce, J. A., Wright, E. J., Efird, K. D., Boros, J. A., and Hailey, T. G., "Effects of Solution Chemistry and Flow on the Corrosion of Carbon Steel in Sweet Production," Corrosion/1995, Paper No. 111, (Orlando, FL: NACE International 1995)

59. Heuer, J. K., Stubbins, J. F., "An XPS Characterization of FeCO3 Films from CO2 Corrosion," *Corros. Sci.*, **41**, 1231 (1999)

60. High, M. S., Wagner, J., and Natarajan, S., "Mechanistic Modeling of Mass Transfer in the Laminar Sublayer in Downhole Systems," Corrosion/2000, Paper No. 62, (Orlando, FL: NACE, 2000)

61. Ikeda, A., Ueda, M., and Mukai, S., CO_2 Behavior of Carbon and Cr Steels, Advances in CO_2 Corrosion, NACE, Houston, 1984

62. Jandau, G. and Blasius E., "Einfuhrung in Das Anorganisch-chemische Praktikum," *Aufl.*, Julius Springer, Berlin, **10**, 317 (1977)

63. Jangama, V. R. and Srinivasan, S., "A Computer Model for Prediction of Corrosion of Carbon Steels," Corrosion/1997, Paper No. 318, (New Orleans, LA: NACE, 1997)

64. Jasinski, R. "Corrosion of N80-Type Steel by CO_2/Water Mixture," *Corrosion*, **43**, 214, (1987)

65. Jasinski, M. L. and Tomson, M. B., "Ferrous Carbonate Precipitation Kinetics and Its Impacts CO_2 corrosion," Corrosion/1991, Paper No. 268, (Cincinnati, OH: NACE International, 1991)

66. Laws, J. G. "Localized, Flow Dependent, Sweet Corrosion at Regions of Drastic Changes in Elevations: Hilly Terrain and River Crossings," M.S. Thesis, Ohio University, 1999

67. Jepson, W. P., "The Flow Characteristics in Horizontal Slug Flow," 3rd International Conference on Multiphase Flow, Paper F2, The Hague, Netherlands, 1987

68. Jepson, W. P., " Modeling the Transition to Slug Flow in Horizontal Conduit," *Can. J. Chem. Eng.*, **67**, 234 (1989)

69. Jepson, W. P. and Bhongale, S., "Effects of Pressure, Temperature and Oil Composition on Corrosion Rate in Horizontal Multiphase Slug Flow," NACE Middle East Conference, Paper No. 6, Bahrain, 1996

70. Jepson, W. P., Bhongale, S., and Gopal, M., "Predictive Model for Sweet Corrosion in Horizontal Multiphase Slug Flow," Corrosion/1996, Paper No. 19, (Denver, CO: NACE International, 1996)

71. Jepson, W. P., Krishnamoorthy, V., and Gopal, M., "Modeling of Multiphase Slug Flow Characteristics and Their influence on Corrosion in Large Diameter, High Pressure Horizontal Pipelines," NACE Middle East Conference, Paper No. 20, Bahrain, 1998

72. Jepson, W. P., and Menezes, R. J., "The Effect of Flow Characteristics on Sweet Corrosion in High-pressure, Three-phase, Oil/water/gas Horizontal Pipelines," Proceeding of Prevention of Pipeline Corrosion Conference, (Houston, TX, 1995)

73. Jepson, W. P., Stitzel, S., Kang, C., and Gopal, M., "Model for Sweet Corrosion in Horizontal Multiphase Slug Flow," Corrosion/1997, Paper No. 11, (New Orleans, LA: NACE International, 1997)

74. Jiang, L., Gopal, M., "Multiphase Flow-enhanced Corrosion Mechanisms in Horizontal Pipelines," *J. Energy Resour. Technol.*, **120**, 67 (1998)

75. Jones, D.A., Principles and Prevention of Corrosion, Macmillan Publishing Company, New York, 1991

76. Kang, C., Wilkens, R. and Jepson, W. P., "The Effect of Slug Frequency on Corrosion in High Pressure Inclined Pipelines," Corrosion/1996, Paper No. 20, (Denver, CO: NACE International, 1996)

77. Kanwar, S. and Jepson, W. P., " Effect of Pressure and Flow Velocity on Sweet Corrosion in High Pressure Horizontal Multiphase Pipelines," Proceedings of the bH^{r} Group Pipe Protection Conference, Paper No. 152, (Amsterdam, Netherlands, 1993)

78. Kanwar, S. and Jepson, W. P., "A Model to Predict Sweet Corrosion of Multiphase Flow in Horizontal Pipelines," Corrosion/1994, Paper No. 24, (Baltimore, MD: NACE International, 1994)

79. Kolthoff, I. M., and Sandell, B. E., Textbook of Quantitative Inorganic Analysis, 3rd Edition, New York, Macmillan, 1952

80. Kordyban, E. S., "Experimental Study of the Mechanism of Two-Phase Slug Flow in Horizontal Tubes," Winter Annual Meeting of the ASME, Philadelphia, Pennsylvania, 1963

81. Kouba, G. E. and Jepson, W. P. "The Flow of Slug in Horizontal, Two Phase Pipeline," Energy Sources Technology Conference and Exhibition, (Houston, TX, 1989)

82. Langsholt, M., Nordsveen, M., Lunde, K., Nesic, S., and Enerhaug, J., "Wall Shear Stress and Mass Transfer Rates – Important Parameters in CO_2 Corrosion," BHR Group, Multiphase, 1997

83. Laque, F. L., "Theoretical Studies and Laboratory Techniques in Sea Water Corrosion Testing Evaluation," *Corrosion*, **13**, 303 (1957)

84. Lee, A. H., A study of flow regime transitions for oil-water-gas mixtures in large diameter horizontal pipelines, M.S. Thesis, Ohio University, 1993

85. Legrand, L., Aouabed, H., Legentilhomme, P., Lefevre, G., and Huet, F., "Use of Electrochemical Sensors for the Determination of Wall Turbulence Characteristics in Annular Swirling Decaying Flows," *Exp. Therm. Fluid Sci.*, **15**, 125 (1997)

86. Levich, V. G., Physicochemical Hydrodynamics, Englewood Cliffs, NJ, Prentice-Hall, 1962

87. Li, Z., Cai, J., and Zhou, S., "Current Oscillation in the Reduction or Oxidation of Some Anions Involving Convection Mass Transfer," *J. Electroanal. Chem.*, **436,** 195 (1997a)

88. Li, Z., Cai, J., and Zhou, S., "Potential Oscillation during the Reduction of $Fe(CN)_6^{3-}$ Ions with Convection Feedback," *J. Electroanal. Chem.*, **432**, 111 (1997b)

89. Linter, B. R., and Burstein, G. T., "Reaction of Pipeline Steels in Carbon Dioxide Solutions," *Corros. Sci.*, ***41***, 117 (1999)

90. Lotz, U., Van Bodegom, and Ouwehand, C., "The Effect of Type of Oil or Gas Condensate on Carbon Acid Corrosion," *Corrosion,* **47,** 340 (1991)

91. Mahato, B. K., Voora, S. K., and Shemilt, L. W., "Steel Pipe Corrosion under Flow Conditions -I An Isothermal Correlation for a Mass Transfer Model," *Corros. Sci.*, **8**, 173 (1968)

92. Maley, L., Slug Flow Characteristics and Corrosion Rates in Inclined High Pressure Multiphase Flow Pipes, M.S. Thesis, Ohio University, 1997

93. Maley, L. C. and Jepson, W. P., "Liquid Holdup in Large-Diameter Horizontal Multiphase Pipeline," *J. Energy Resour. Technol.,* **120**, 185 (1998)

94. Mao, Z., and Hanratty, T. J., "Analysis of Wall Shear Stress Probes in Large Amplitude Unsteady Flows," *Intl. J. Heat Mass Transfer*, **34**, 281 (1991)

95. Mao, Z., and Hanratty, T. J., "Measurement of Wall Shear Rate in Large Amplitude Unsteady Reversing Flows," *Exp. Fluid*, **12**, 342 (1992)

96. Marken, F., Eklund, J. C., Compton, R. G., "Voltammetry in the Presence of Ultrasound: Can Ultrasound Modify Heterogeneous Electron Transfer Kinetics," *J. Electroanal. Chem.*, **395**, 335 (1995)

97. Mercier-Bonin, M., Marange C., Lafforgue, C., and Fondade, C., "Hydrodynamics of Slug Flow Applied to Cross-Flow Filtration in Narrow Tubes," *AIChE J.,* **46**, 476 (2000)

98. Mizushina, T., "Electrochemical Method in Transport Phenomena," in Advances in Heat Transfer, Academic Press, **7**, 1971

99. Nakoryakov, V. E., Kashinsky, O. N., Kozmenko, B. K., "Electrochemical Method for Measuring Turbulent Characteristics of Gas-Liquid Flows" in Measuring Techniques in Gas-Liquid Flows, Delhaye, H. H. M., Cognet, C., Springer Verlag, Heidelberg, 1984

100. Newman, J. S., Electrochemical Systems, 2nd Ed., Englewood Cliffs, New Jersey, 1991

101. Nesic, S. and Lunde, L., "CO_2 Corrosion of Carbon Steel in Two-Phase Flow," Corrosion/1993, Paper No 640, (Houston, TX: NACE International, 1993)

102. Nesic, S., Postlethwaite, J., and Olsen, S., " An Electrochemical Model for Prediction of Corrosion of Mild Steel in Aqueous Carbon Dioxide Solutions" *Corrosion*, **52,** 280 (1996)

103. Nishimura, T., Oka, N., Toshinaka, Y., Kunitsugu, K., "Influence of Imposed Oscillatory Frequency on Mass Transfer Enhancement of Grooved Channels for Pulsatile Flow," *Int. J. Heat Mass Transfer*, **43**, 2365 (2000)

104. Nyborg, R., Anderson, P., and Nordsveen, M., " Implementation of CO_2 Corrosion Models in a Three-Phase Fluid Flow Model," Corrosion/2000, Paper No. 48 (Orlando, FL: NACE, 2000)

105. Nyborg, R., Nordsveen, M., and Stangeland, A., "Kjeller Sweet Corrosion V, Final Report," Institute for Energy Technology, No. 75, (1998)

106. Ogundele, G. I., and White, W. E., "Some Observations on Corrosion of Carbon Steel in Aqueous Environments Containing Carbon Dioxide," *Corrosion,* **42**, 160 (1986)

107. Paisley, D., Barrett, N., and Wilson, O., "Pipeline Failure: the Roles Played by Corrosion, Flow and Metallurgy," Corrosion/1999, Paper No. 18, (San Antonio, TX: NACE International, 1999)

108. Perez-Herranz V., Guinon J. L., Garcia-Anton J., "Analysis of Mass and Momentum Transfer in an Annular Electrodialysis Cell in Pulsed Flow," *Chem. Eng. Sci.*, **54**, 1667 (1999)

109. Pitzer, K. S., Activity Coefficients in Electrolyte Solutions, CRC Press, Boca Raton, 1991

110. Pots, B. F. M.," Mechanistic Models for the Prediction of CO_2 Corrosion Rates under Multiphase Flow Conditions," Corrosion/1995, Paper No. 137, (Orlando, FL: NACE International, 1995)

111. Poulson, B., "Advances in Understanding Hydrodynamic Effects on Corrosion," *Corros. Sci.*, **35**, 655 (1993)

112. Rao, B. C. S. and Buckley, D. H., "Cavitation Pitting and Erosion of Aluminum 6061-T6 in Mineral Oil and Water," NASA-TP-2146, 1983

113. Reiss, L. P., and Hanratty, T. Z., " An Experimental Study of the Unsteady Nature of the Viscous Sublayer," *AIChE J.*, **8**, 154 (1963)

114. Rode, S., Latifi, M. A., Storck, A., and Midoux, N., "An Experimental Study of the Frequency Response of Electrochemical Sensors in Nonhomogenuous Flow in Packed Beds," *J. Appl. Electrochem.*, **24**, 639 (1994a)

115. Rode, S., Midoux, N., Latifi, M. A., Storck, A., and Saatdjian E., "Hydrodynamics of Liquid Flow in Packed Beds: An Experimental Study Using Electrochemical Shear Rate Sensors," *Chem. Eng. Sci.,* **49**, 889 (1994b)

116. Rode, S., Midoux, N., Latifi, M. A., Storck, A., "Hydrodynamics of Liquid Flow and Liquid-Solid Mass Transfer Mechanisms in Packed Beds: An Experimental Study Using Electrochemical Shear Rate Sensors," *Chem. Eng. Sci.*, **49**, 1383 (1994c)

117. Rosant, J. M., "Liquid-Wall Shear Stress in Stratified Liquid/Gas Flow," *J. Appl. Electrochem.*, **24**, 612 (1994)

118. Rosin, J., Reagent Chemicals and Standards, 5th Edition, Princeton, NJ, Van Nostrand, 1967

119. Ross, T. K. and Hitchen, B. P. L., "Some Effects of Electrolyte Motion During Corrosion," *Corros. Sci.*, **1**, 65 (1961)

120. Scatterfield, C.N., Heterogeneous Catalysis in Practice, Chemical Engineering Series, McGraw-Hill, New York, 1980

121. Schmitt, G, "CO_2 Corrosion of Steels - An Attempt to Range Parameters and Their Effects," Advances in CO_2 Corrosion, NACE, Houston, 1984a

122. Schmitt, G, "Fundamental Aspects of CO_2 Corrosion," Advances in CO_2 Corrosion, NACE, Houston, 1984b

123. Schmitt, G., Bosch, C., Mueller, M., "Modeling the Probability of Flow Induced Localized Corrosion From Critical Hydrodynamic Data and Fracture Mechanics Data of Scales from CO_2 Corrosion of Steel," in Advances in Corrosion Control and Materials in Oil and Gas Production, European Federation of Corrosion, The Institute of Materials, London, 1999

124. Schmitt, G., Bosch, C., Mueller, M., and Siegmund, G., "A Probabilistic Model for Flow Induced Localized Corrosion," Corrosion/2000, Paper No. 49, (Orlando, FL: NACE International, 2000)

125. Schmitt, G. and, Mueller, M., "Critical Wall Shear Stresses in CO_2 Corrosion of Carbon Steel," Corrosion/1999, Paper No. 44, (San Antonio, TX: NACE International 1999a)

126. Schmitt, G., Mueller, M., Papenfuss, M. and Strobel-Effertz, E., "Understanding Localized CO_2 Corrosion of Carbon Steel from Physical Properties of Iron Carbonate Scales," Corrosion/1999, Paper No. 38, (San Antonio, TX: NACE International 1999b)

127. Seal, S., Sapre, K., Kale, A., Desai, V., Gopla, M., Jepson, P., "Effect of Multiphase Flow on Corrosion of C-steel in Presence of Inhibitor: A Surface Morphological and Chemical Study," *Corros. Sci.*, **42**, 1623 (1999)

128. Sedahmed, G. H., Hosny, A. Y., Fadally, O. A., and El-Mekkawy, I. M., "Mass Transfer at Rough Gas-Sparged Electrodes," *J. Appl. Electrochem.*, **24**, 139 (1994)

129. Seguin, D., Montillet, A., and Comiti, J., "Experimental Characterization of Flow Regimes in Various Porous Media –I: Limit of Laminar Flow Regime," *Chem. Eng. Sci.*, **53**, 3751 (1998a)

130. Seguin, D., Montillet, A., Comiti J., and Huet, F., "Experimental Characterization of Flow Regimes in Various Porous Media –I: Transition to Turbulent Regime," *Chem. Eng. Sci.*, **53**, 3897 (1998b)

131. Selman, J.R. and Tobias, C.W., "Mass-Transfer Measurements by the Limiting –Current Technique," in Advances in Chemical Engineering, Academic Press, **11**, 1978

132. Shah, A., Jorne, J., "Mass Transfer under Bubble-Induced Convection in a Vertical Electrochemical Cell," *J. Electrochem. Soc.*, **136**, 144 (1989a)

133. Shah, A. Jorne, J., "Mass Transfer under Combined Gas Evolution and Forced Convection," *J. Electrochem. Soc.*, **136**, 153 (1989b)

134. Shi, H., Cai, J. Y., and Jepson, W. P., "The Effect of Surfactants on Flow Characteristics in Oil/Water Flows in Large Diameter Horizontal Pipelines," *Multiphase'99*, BHR Group, France, 1999

135. Speight, J. G. The Chemistry and Technology of Petroleum, 3rd Edition, Marcel Dekker Inc., New York, 1999

136. Sun, J. Y. and Jepson, W. P., "Slug Flow Characteristics and Their Effect on Corrosion Rates in horizontal Oil and Gas Pipelines," SPE 24787, (Washington, DC, 1992)

137. Sydberger, T., and Lotz U., "Relation Between Mass Transfer and Corrosion in a Turbulent Pipe Flow," *J. Electrochem. Soc.*, **129**, 276 (1982)

138. Tanaka, N., Tamamushi, R., "Kinetic Parameters of Electrode Reactions," *Electrochim. Acta*, **9**, 963 (1964)

139. Tomita Y., Shima A., "High-Speed Photographic Observations Of Laser-Induced Cavitation Bubbles In Water," *Acustica,* **71**,161 (1990)

140. Van Steenhoven, A. A., and Van De Beucken, F. J. H. M., "Dynamical Analysis of Electrochemical Wall Shear Rate Measurements," *J. Fluid Mech.*, **231**, 599 (1991)

141. Vieth, W.R., Porter, J.H., and Sherwood, T.K., "Mass Transfer and Chemical Reaction in a Turbulent Boundary Layer," *Ind. Eng. Chem. Fundam.*, **2**, 1 (1963)

142. Vlachos, N.A., Para, S. V., and Karabelas, A. J., "Liquid-To-Wall Shear Stress Distribution in Stratified/Atomization Flow," *Int. J. Multiphase Flow*, **23**, 845 (1997)

143. Vuppu, A. K. and Jepson, W. P., " Study of Sweet Corrosion in Horizontal Multiphase, Carbon Steel Pipelines," Offshore Technology Conference, (Houston, TX, 1994a)

144. Vuppu, A. K. and Jepson, W. P., " The Effect of Temperature in Sweet Corrosion of Horizontal Multiphase Carbon Steel Pipelines," SPE 28809, (Melbourne, Australia, 1994b)

145. Wagman, D. D., Evans, W. H., Parker, V. B., Schumm, I. H., Bailey, S. M., Churney, K. L., and Nuttall, R. L., "The NBS Tables of Chemical Thermodynamic Properties," *J. Phys. Chem. Ref. Data*, **11**, 1 (1982)

146. Wang, H., Cai, J. Y., Hong, T., and Jepson, W. P., "Current Oscillation of Oxidation of Ferrocyanide Anion in Two-Phase Slug Flow," 195th Meeting of The Electrochemical Society, Seattle, Washington, (1999)

147. Wang, H., Cai, J.Y., Hong, T., Gopal, M., Jepson, W. P., and Dewald, H. D., "Effect of Bubbles on Mass Transfer in Multiphase Flow," Corrosion/2000, Paper No. 50, (Orlando, FL: NACE International, 2000a)

148. Wang, H., Hong, T., Cai, J. Y., Dewald, H. D., and Jepson, W. P., "Enhancement of the Instantaneous Mass Transfer Coefficient in Large Diameter Pipeline under Water/Oil Flow," *J. Electrochem. Soc.*, **147**, 2552 (2000b)

149. Wang, H., Vedapuri, D., Cai, J. Y., Hong, T., and Jepson, W. P., "Mass Transfer Coefficient Measurement in Water/Oil Multiphase Flow, *J. Energy Resour. Technol.*, **23**, 144 (2001)

150. Whitey, G. M. and Tobias, C. W., "Mass Transfer Effects of Bubbles Streams Rising Near Vertical Electrodes," *AIChE J.*, **34**, 1981 (1989)

151. Wilkens, R., "Prediction of the Flow Regime Transitions in High Pressure Large Diameter, Inclined Multiphase Pipelines," Ph.D. Dissertation, Ohio University, 1997

152. Xie, Q. Q., Study on Mass Transfer and Turbulence in Large Pipe Flow Using Limiting Current Density Technique, M.S. Thesis, Ohio University, 1997

153. Zaki, M. M., Nirdosh, I., Sedahmed, G. H., "Forced Convection Mass Transfer Inside Large Hemispherical Cavities under Laminar Flow Conditions," *Can. J. Chem. Eng.*, **75,** 333 (1997)

154. Zhang, R., "Mechanistic Modeling of Sweet Corrosion in Horizontal Pipes," M.S. Thesis, Ohio University, 1997

155. Zhang, R., Gopal, M., and Jepson, W. P., Development of a Mechanistic Model for Predicting Corrosion Rate in Multiphase Oil/Water/Gas Flows, Corrosion/1997, Paper No 601, (New Orleans, LA: NACE International 1997)

156. Zhou, X. and Jepson, W. P., "Corrosion in Three-Phase Oil/Water/Gas Slug Flow in Horizontal Pipes," Corrosion/1994, Paper No. 26, (New Orleans, LA: NACE International, 1994)

APPENDIX A

Program for pH calculation

pH.for

```
      DOUBLE PRECISION T,P,RH,RHO,YCO2,FCCO2,FCO2,LKH, KH, ACO2,
      LK, K1CO2,E,MU,MU1,ZH,ZHCO3,ZOH,ACTH,ACTHCO,AH,AHCO3,H,
     * HCO3,LAMB, A2, A1, A0, AH1, PH1, TOL, KW, LKW, ACTOH,
     * LP,PCO2,AOH,TC,PC,PVP,VPA,VPB,VPC,VPD,TMAX,TMIN,
     * YH2O, TEMP, BB, SALT(10), IH,IHCO3
      REAL POSITIVE, NEGATIVE, DIFF, ADIFF

      INTEGER COUNT,I,J
      CHARACTER*135 DUMMY
      CHARACTER*32 OUT_FILE
      LOGICAL TP,PP

C     OPEN (90, FILE='PH_INPUT.DAT')
C     READ(90,11) (DUMMY, I=1, 14)
C     READ(90,*) T
      T=353.00
C     READ(90,11) (DUMMY, I=1,2)
C     READ(90,*) TP, PP
      TP=F
      PP=T
C     READ(90,11) (DUMMY, I=1,2)
C     READ(90,11) P
      P=0.13
C     READ(90,11) (DUMMY, I=1,2)
C     READ(90,11) RHO
      RHO=1000
C     READ(90,11) (DUMMY, I=1,2)
C     READ(90,11) RH
      RH=1250
C     READ(90,11) (DUMMY, I=1,2)
C     READ(90,11) FCCO2
      FCCO2=0.9
C     READ(90,11) (DUMMY, I=1,3)
C     READ(90,11) (SALT(J), J=1, 10)
      SALT(1)=0.483450
      SALT(2)=0.562381
      SALT(3)=0.055
      SALT(4)=0.029
```

```
      SALT(5)=0.010
      SALT(6)=0.00984
      SALT(7)=0.000839
      SALT(8)=0.000480
      SALT(9)=0.000150
      SALT(10)=0.00007
C     READ(90,11) (DUMMY, I=1,2)
C     READ(90,11) IHCO3, IH
      IHCO3=0.0023
      IH=0.00048
C     READ(90,11) (DUMMY, I=1,2)
C     READ(90,11) OUT_FILE
C     READ(90,11) DUMMY
C11   FORMAT(A132)
C12   FORMAT(A32)

      OPEN(60, FILE="OUT_DAT_2001.DAT")
C*****************************************************
C CHECK FOR THE BALANCE OF INPUT SEASALT
C*****************************************************
      POSITIVE=SALT(1)+2. *SALT(3) +2. *SALT(5) +
SALT(6)+2.*SALT(9)+IH
      NEGATIVE=SALT(2)+2.*SALT(4)+SALT(7)+SALT(8)+SALT(10)+IHCO3
      DIFF=POSITIVE-NEGATIVE
      IF (ABS(DIFF).LE. 1.0E-06) THEN
      WRITE(60,140)
140   FORMAT('*****THE INPUT SEASALT IS BALANCED *******')
      WRITE(60,150)
150   FORMAT ('*****************************************')
      ELSE
      WRITE(60,160)
160   FORMAT ('**THE INPUT SEASLT IS IMBALANCE ** ')
      IF (DIFF.GT.0) THEN
            WRITE (60, 120)
120         FORMAT ('CONCENTRATION OF POSITIVE IONS IS GREATER
                        THAN
  * CONCENTRATION OF NEGATIVE')
            WRITE (60,121) DIFF
121         FORMAT ('IONS BY',E10.4,'mol/l, BALANCE IS BROUGHT UP
BY
  * ADDITION OF CL- ION')
            WRITE(60, 124)
124         FORMAT ('************************')
            SALT(2)=SALT(2)+DIFF
```

```
      ELSE
            WRITE (60, 122)
122         FORMAT ('CONCENTRATION OF POSITIVE IONS IS GREATER
                        THAN
     * CONCENTRATION OF NEGATIVE')
            ADIFF=-DIFF
            WRITE(60, 123) ADIFF
123         FORMAT ('*IONS BY 'E10.4' MOL/L, BALANCE IS BROUGHT UP
                        BY
     * ADDITION OF Na+ ION *')
            WRITE(60, 125)
125         FORMAT ('******************')
            SALT(1)=SALT(1)-DIFF
      ENDIF
      ENDIF

C*****************************************************
C CONVERT INPUT DENSITIES FROM KG/M3 TO KG.LITER
C*****************************************************
      RH=RH/1000.0
      RHO=RHO/1000.0

C**************DEFINITION OF VARIABLES**************
C     T=TEMPERATURE K
C     P= PRESSURE, MPa
C     TC=CRITICAL TEMPERATURE
C     PC=CRITICAL PRESSURE, BAR
C     VPA, VPB, VPC, VPD=CONSTANTS IN VAPOUR PRRESSURE
C     CALCULATIONSTMIN,
C     TMAX, ARE TO GIVE TEMPERATURE RANGE WITHIN WHICH
VAPOUR
C     PRESSURE CORRELATION IS VALID
C     PCO2=PARTIAL PRESSURE OF CARBON DIOXIDE
C*****************************************************

      WRITE(60,3) T
3     FORMAT ('LIQUID TEMPERATURE OF CARBON STEEL', 32X, '=',
     * F8.1, 'K',/)
      COUNT=0

C************VAPOR PRESSURE OF WATER**************
C     PVC, PC ARE BARS
C*****************************************************
      VPA=-7.76451
```

```
      VPB=1.45838
      VPC=-2.7758
      VPD=-1.23303
      TC=647.3
      PC=221.2
      TMIN=275.0
      TMAX=TC

      IF(TP) THEN
            IF (T.LE. TMIN. OR. T. GE. TMAX) THEN
            WRITE(60, *) 'THE TEMP LIES OUTSIDE RANGE OF CALC'
            STOP
            ENDIF
            X=1.0-T/TC
            LP=(1.0/(1.0-X))*(VPA*X+VPB*X**1.5+VPC*x**3.0+VPD*x*6.0)
            PVP=DEXP(LP)*PC
            PVP=PVP*0.1
            PCO2=P-PVP
            WRITE(60,4) PCO2
4           FORMAT('CARBON DIOXIDE PARTIAL PRESSURE', 19X, '=',
     *            F8.4, 'Mpa')
            WRITE(60, 5) PVP
5           FORMAT(/,'VAPOR PRESSURE OF WATER', 27X,'=', F8.4,'MPA')
            WRITE(60, 6) P
6           FORMAT(/,'TOTAL PRESSURE', 36X, '=', F8.4,' MPA')
            YH2O=PVP/P
            WRITE(60,7) YH2O
7           FORMAT(/,'MOLE FRATION OF WATER IN VAPOR PHASE',
     *            12X, '=', F6.2)
            YCO2=1.0-YH2O
      ELSE
            PCO2=P
            X=1.0-T/TC
            LP=(1.0/(1.0-X))*(VPA*X+VPB*X**1.5+VPC*X**3.0+
     *      VPD*x**6.0)
            PVP=DEXP(LP)*PC
            PVP=PVP*0.1
            WRITE(60,5) PVP
            WRITE(60,4) PCO2
C           YCO2=1.0
            P=PCO2+PVP
            YCO2=PCO2/P
            WRITE(60,6) P
            WRITE(60,9) YCO2
```

```
9             FORMAT(/,'MOLE FRATION OF CO2 IN GAS PHASE', 12X,
     *              '=', F6.2)
      ENDIF

C*************CO2 SOLUBILITY CALCULATIONS**
C     YCO2=MOLE FRACTION OF CO2 IN THE GAS
C     FCCO2= FUGACITY COEFFICIENT OF CO2 IN THE GAS PHASE
C     FCO2=GAS FUGACITY
C     KH=HENRY'S LAW CONSTANT, MOL/(KG*ATM)
C     ACO2=ACTIVITY OF CO2, IN MOL/L
C     LKH=LOGARITHM OF KH
C     RHO=DENSITY OF SEAWATER IN KG/L
C     CORRELATION FROM REFERENCE: PITXER, SK,      ACTIVITY
C     COEFFICIENTS IN
C     ELECTROLYTE SOLUTIONS, 2ND EDITION, CRC PRESS, 1991
C*************************************************
      FCO2=YCO2*FCCO2*(P*9.86923)
      LKH=108.3865+(0.01985076)*T-(6919.53)/T - (40.4514)*DLOG10(T)+
     * (669365.0)/(T*T)
      KH=10**(LKH)
      WRITE(60, 8) KH
8     FORMAT(/,'HENRYS LAW CONSTANT', 31X,'=', F9.4,'mol/(Kg*atm)')

      ACO2=FCO2*KH*RH
      WRITE(60,29) ACO2
29    FORMAT(/,'ACTVITY OF CO2', 35X,'=', F8.4,'mol/liter')

C***********CO2 IONIZATION**********************
C
C     H2CO3-----àH+ + HCO3-
C     KICO2=AH+* AHCO3+/ACO2
C
C     CORRELATION FROM REFERENCE: SAEM AS ABOVE
C*************************************************
      LK=-6320.81/T+126.3405-19.568*LOG10(T)/LOG10(2.718282)
      K1CO2=(10.0)**(LK)*RH

C***********IONIZATION CONSTANT OF WATER***********
C CORRELATION FROM REFERENCE: ABOVE
C*************************************************

      LKW=-283.971+13323.0/T-0.05069842*T+102.24447*LOG10(T)-
     * 1119669.0/(T*T)
      KW=(10**(LKW))*RH
```

```
C******************DIEELECTRIC CONSTANT**********************
      CALL DIEL(T, P, E)

C************** ACTIVITY COEFFICIENT CALCULATION ************
C     MU=IONIC STRENGTH
C     Z= IONIC CHARGE
C     ACTH=ACTIVITY OF HYDROGEN ION
C     TOL=TOLERENCE
C*******************************************************************
      TOL=1.D-6
      ZH=1.0
      ZHCO3=-1.0
      ZOH=-1.0

      H=IH
      HCO3=IHCO3
      ACTH=1.0
      ACTHCO=1.0
      ACTOH=1.0
C     GOTO 400
200   COUNT=COUNT+1
      CALL IONST(RH, SALT, H, HCO3, MU, LAMB)
      MU1=MU
      CALL ACTCO(T, E, MU1, ZH, ACTH)
      CALL ACTCO(T, E, MU1, ZHCO3, ACTHCO)
      CALL ACTCO(T, E, MU1, ZOH, ACTOH)

C400  A2=1.0/ACTH
      A2=1.0/ACTH
      A1=LAMB
      A0=-((K1CO2*ACO2)/ACTHCO)-(KW/ACTOH)
      TEMP=A1*A1-4.0*A2*A0
      AH1=(-A1+(TEMP)**(0.5))/(2.0*A2)
      PH1=-DLOG10(AH1)
      IF ((PH1.GT.1.0).AND.(PH1.LE.14.0)) THEN
            IF((DABS((AH1-AH)/AH1)).GT.TOL) THEN
            AH=AH1
            AHCO3=K1CO2*(ACO2)/AH1
            AOH=KW/AH1
      ELSE
            H=AH/ACTH
            HCO3=AHCO3/ACTHCO
            OH=AOH/ACTOH
```

```
            GOTO 300
        ENDIF
        ENDIF

        H=AH/ACTH
        HCO3=AHCO3/ACTHCO
        OH=AOH/ACTOH
        GOTO 200

300     WRITE(60,16) MU
16      FORMAT(/,'IONIC STRENGTH OF SOLUTION', 24X,'=',E10.5)
        WRITE(60,17) OH
17      FORMAT(/,'THE ACTIVITY OF OH IONS', 27X,'=',E10.4,'MOL/L')
        WRITE(60,13) HCO3
13      FORMAT(/,'THE ACTIVITY OF HCO3 IONS', 25X,'=',E10.4,'MOL/L')
        WRITE(60,14) H
14      FORMAT(/,'THE ACTIVITY OF HYDROGEN', 26X,'=',E10.4,'MOL/L')
        WRITE(60,19) LAMB
19      FORMAT(/,'THE LAMB OF SEATWATER', 30X,'=',E10.4,'MOL/L',/)
        WRITE(60,18)
18      FORMAT(/,'*******************************************')
        WRITE(60,15) PH1
15      FORMAT('*', 6X,'CALCULATED pH of Solution', 18x, '=', f6.4,
     * 18x,'*')
        WRITE(60,18)
        CLOSE (60)

        STOP
        END
C*********************************************************************
C********** The end of main program ***********************************
C*********************************************************************



C*********SUBROUNTINE : DIELECTRIC CONSTANT OF WATER********
C       E=DIELECTRIC CONSTANT
C       E1000, C, B, U1-U9 ARE EMPIRICALPARAMETERS
C       USING PITZERS EQUATIONS
C       THE PRESSURE PB IS IN BARS AND IS CONVERTED FROM THE
C       INPUT PRESSURE P WHICH IS IN MPa
C
C       CORRELATION FROM REFERENCE: PITZER, SK, ACTIVITY
C       COEFFICIENTS  INELECTROLYTE SOLUTION, 2ND EDITION, crc
```

```
C       PRESS, 1991
C*****************************************************************

        SUBROUTINE DIEL(T, P, E)
        DOUBLE PRECISION T, P, E, PB, B, U, E1000, C
        DIMENSION U(9)
        U(1)= 3.4279D2
        U(2)= -5.0866D-3
        U(3)= 9.4690D-7
        U(4)= -2.0525
        U(5)= 3.1159D3
        U(6)= -1.8289D2
        U(7)= -8.0325D3
        U(8)= 4.2142D6
        U(9)= 2.1417
        PB=10.0*P
        E1000=U(1)*DEXP(U(2)*T+U(3)*T*T)
        C=U(4)+U(5)/(U(6)+T)
        B=U(7)+U(8)/T+U(9)*T
        E=E1000 + C*DLOG((B+PB)/(B+1000))
        RETURN
        END



C********* SUBROUNTINE: IONIC STRENGTH OF SOLUTION
C       CONCENTRATIONS ARE IN mol/litre
C*****************************************************************

        SUBROUTINE IONST(RH, SUBSALT, HS, HSCO3, TEMPMU, LAMB)
        DOUBLE PRECISION RH, HS, HSCO3, TEMPMU, LAMB, SUBSALT(10)
        REAL SALT(10)
        SALT(1)=0.483450
        SALT(2)=0.562381
        SALT(3)=0.055
        SALT(4)=0.029
        SALT(5)=0.010
        SALT(6)=0.00984
        SALT(7)=0.000839
        SALT(8)=0.000480
        SALT(9)=0.000150
        SALT(10)=0.00007
        TEMPMU=(0.5)*(SALT(1)+SALT(2)+4.0*SALT(3)+4.0*SALT(4)
     *  +4.0*SALT(5) +SALT(6)+HS+HSCO3+SALT(7)+SALT(8)+4.0*SALT(9)+
```

```
     *    SALT(10))*RH
          LAMB=SALT(1)+2.0*SALT(3)+2.0*SALT(5)+SALT(6)-SALT(2)-
     *    (2.0)*SALT(4)-SALT(7)-SALT(8)+2.0*SALT(9)-SALT(10)
          RETURN
          END

C******** SUBROUTINE: ACTIVITY COEFFICIENTS ******************
C
C         ACT=ACTIVITY OF ION IN SOLUTION
C         Z=CHARGE ON THE ION
C         M=IONIC STRENGTH OF SOLUTION
C
C***********************************************************************
          SUBROUTINE ACTCO(T, E, TEMPMU, Z, ACT)
          DOUBLE PRECISION T,E,TEMPMU,Z,ACT,A,LACT
          REAL I
          A=(1.820D6)*((E*T)**(-1.5))
C         OPEN (61, FILE="TEST.DAT")
C         CLOSE (61)
          LACT=-(A)*(Z*Z)*((TEMPMU**0.5)/(1.0+TEMPMU**(0.5))-
      *   0.3*TEMPMU)
          ACT=(10.0)**(LACT)
          I=I+1
          RETURN
          END
```

APPENDIX B

CO_2 Mechanistic Model for Slug Flow

Slug_corrosion_withoutfilm.for

```
C*****************************************************************
C
C       THIS PROGRAM CALCULATES THE SURFACE CONCENTRATION OF
C       HESPECIES CATHODIC AND ANODIC CURRENT, AND CORROSION
C       RATE THIS PROGRAM ASSUMES CORROSION RATE FOR NON
C       SCALING CONDITIONS. BY USING THE SALTWATER PROPERTIES
C       ONLY
C
C*****************************************************************

C************************ DIFINITION ******************************
C       X(1)=SURFACE CONCENTRATION OF FERROUS ION (mol/m3)
C       X(2)=SURFACE CONCENTRATION OF HYDROGEN ION (mol/m3)
C       X(3)=CORROSION POTENTIAL (Volt)
C       CR= CORROSION RATE (mm/year)
C       H_PLUSB=BULK CONCENTRATION OF HYDROGEN ION (mol/m3)
C       FEB=BULK CONCENTRATION OF FERROUS ION (mol/m3)
C       H2=SURFACE CONCENTRATION OF HYDROGEN (mol/m3)
C       H_PLUSS=SURFACE CONCENTRATION OF HYDROGEN (mol/m3)
C       FES=SURFACE CONCENTRATIONOF FERROUSION  (mol/m3)
C       E_FE=EQUILIBRIUM POTENTIAL OF IRON DISSOLUTION
C       REACTION(volts)
C       E_H= EQUILIBRIUM POTENTIAL OF HYDROGEN ION REDUCTION
C       EACTION (volts)
C       E_CORR=CORROSION POTENTIAL (volts)
C       E_FE0=STANDARD POTENTIAL OF IRON ION DISSOLUTION
C        REACTION
C       (volts)
C       E_H0= STANDARD POTENTIAL OF HYDROGEN ION REDUCTION
C       REACTION (volts)
C       I_FE=ANODIC CURRENT DUE TO IRON DISSOLUTIONREACTION
C       (amp/m2)
C       I_H=CATHODIC CURRENT DUE TO IRON DISSOLUTIONREACTION
C       (amp/m2)
```

```
C       BETA=TRANSFER COEFFICIENT (0.5 FOR MOST CASE)
C       S=FARADAY'S CONSTANT (96500 COLUMBS/GM EQUIVALENT)
C       R=UNIVERSAL GAS CONSTANT (J/K/mol)
C       T=TEMPERATURE (K)
C       KMTFE=MASS TRANSFER COEFFICIENT FOR FERROUS ION (M/S)
C       KMTH=MASS TRANSFER COEFFICIENT FOR HYDROGEN ION (M/S)
C       KFE=ELECTROCHEMICAL REACTION RATE CONSTANT FOR
C       ANODIC
C       REACTION (M/S)
C       Z=THE RESULT OF GAUSS-JORDAN ELIMINATION
C
C*****************************************************************

        DOUBLE PRECISION X(3), E(3), CR, Z(3), TOL, COE
        DOUBLE PRECISION H_PLUSB, FEB, H2, D, VISCP, WOR, QT
        DOUBLE PRECISION H_PLUSS, FES, T, P, RHO, TC
        DOUBLE PRECISION E_FE, E_H, ECORR, E_FE0, E_H0
        DOUBLE PRECISION I_FE, I_H, I_CORR, S
        DOUBLE PRECISION KMTFE, KMTH, RE, SC, HEIGTHT, VM
        DOUBLE PRECISION A(3,4), F(3), FF(3)
        DOUBLE PRECISION KFE, KH
        DOUBLE PRECISION EXP1, EXP2
        CHARACTER*135 DUMMY
        CHARACTER*32 OUT_FILE
        LOGICAL TP, PP
        INTEGER I, J, II
        INTEGER N, MIXTURE
        N=0

        S=96500.0
        R=8.314
        BETA=0.5
        E_FE0=-0.44
        E_H0=0.0

        FEB=0.0
        H2=1.0E-5

C*****************************************************************
C       READ DATA FOR CASE FROM INPUT FILE CR_INPUT.DAT
C*****************************************************************

C       WRITE(*,*)
C       WRITE(*,*) 'This program assumes cr for non scaling conditions'
```

```
C       WRITE(*,*)
C       OPEN(90, FILE='CR_INPUT.DAT')
C       READ(90,11) (DUMMY, I=1, 10)
C       WRITE (*, *) "DUMMY=", DUMMY
C       READ(90,*) T
C       WRITE(*,*) 'T =', T

        T=313.0
        P=0.27

        MIXTURE=1
        IF (MIXTURE.EQ.1) THEN
C       brine solution only
                RHO=1250.0
                VISCP=0.656
        ELSEIF (MIXTURE.EQ.2) THEN
C       brine and oil mixture for slug flow 20% OIL
                RHO=1250*0.80+825*0.20
                VISCP=0.656*0.80+2.0*0.20
        ELSEIF (MIXTURE.EQ.3) THEN
                RHO=1250*0.40+825*0.60
                VISCP=0.656*0.40+2.0*0.60
        ENDIF
        D=0.1016
C       for full pipe flow v=1.0 m/s
        QT=0.008107
C       for slug flow, transitional velocity Vt=8.75 m/s
C       QT=0.070939
        WOR=1.0

C***************************************
C       for temperature = 40 C
C       (1) for P=0.27 MPa
        H_PLUSB=2.814e-2
C       (2) for P=0.79 MPa
C       H_PLUSB=8.008E-2
C       (2) for P=0.45 MPa
C       H_PLUSB=4.644E-2
C       for p=0.136 MPa
C       H_PLUSB=1.428e-2

C***************************************
C       for temperature = 60 C
C       (1) for P=0.27 MPa
```

```
C       H_PLUSB=2.232e-2
C       (2) for P=0.79 MPa
C       H_PLUSB=6.345e-2

C***************************************
C       for temperature = 80 C
C       (1) for P=0.27 MPa
C       H_PLUSB=1.501e-2
C       (2) for P=0.79 MPa
C       H_PLUSB=4.302e-2

        TC=T-273.15
        IF(TC.GT.85.AND. TC.LE.95) THEN
              COE=3.5
        ELSEIF (TC.GT.75.AND. TC.LE.85) THEN
              COE=3.0
        ELSEIF (TC.GT.65.AND. TC.LE.75) THEN
              COE=2.5
        ELSEIF (TC.GT.55.AND. TC.LE.65) THEN
              COE=2.0
        ELSEIF (TC.GT.45.AND. TC.LE.55) THEN
              COE=1.5
        ELSEIF (TC.LE.45) THEN
              COE=1.0
        ENDIF

        IF(TC.GT.70. AND. TC.LE.90) THEN
              KFE=2.59E-02
              KH=2.0E-05
        ELSEIF (TC.GT.50. AND. TC.LE.70) THEN
              KFE=2.59E-02*0.1
              KH=2.0E-05*0.1
        ELSEIF (TC.GT.30. AND. TC.LE.50) THEN
              KFE=2.59E-02*0.01
              KH=2.0E-05*0.01
        ENDIF

C*********************************************************************
C
C       CALUCLATING THE MASS TRANSFER COEFFICIENTS FOR FERROUS
C       AND HYDROGEN IONS
C
C*********************************************************************
```

```
      CALL KMT(T,D,VISCP,RHO,QT,WOR,COE, KMTFE, KMTH, RE, SC)
      OPEN (60, FILE='OUTCORROSION.DAT')
      WRITE (60, *) "RE=", RE
      WRITE (60, *) "SC=", SC
      WRITE (60, *) "KMTH=", KMTH
      WRITE (60, *) "KMTFE=", KMTFE

C*****************************************************************
C     ENTER THE INITIAL VALUES FOR X(I)
C*****************************************************************
      IF (H_PLUSB.GE.3.0E-4) THEN
C     X(1)=SURFACE CONCENTRATION OF FERROUS ION (mol/m3)
C     X(2)=SURFACE CONCENTRATION OF HYDROGEN ION (mol/m3)
C     X(3)=CORROSION POTENTIAL (Volt)
            X(1)=0.46
            X(2)=2.0E-04
            X(3)=-0.46

C           X(1)=0.50
C           X(2)=3.0-04
C           X(3)=-0.48
      ELSE
            IF (H_PLUSB.GE.2.4E-4) THEN
            X(1)=3.0E-3
            X(2)=1.0E-05
            X(3)=-0.6
            ELSE
            X(1)=6E-05
            X(2)=2.0E-08
            X(3)=-0.76
            ENDIF
      ENDIF

C*****************************************************************
C     ELEMENT OF 3X3 JACOBIAN MATRIX GIVEN AS A(I, J)
C*****************************************************************

50    EXP1=EXP(S*(X(3)-E_FE0-R*T/(2.0*S)*LOG(X(1)))/R/T)
      EXP2=EXP(-S*(X(3)-E_H0-R*T/(2.0*S)*LOG(X(2)**2.0/H2))/(R*T))
      N=N+1
      A(1,1)=KMTFE-0.5*KFE*EXP1
      A(1,2)=0.0
      A(1,3)=-KFE*X(1)*EXP1*S/(R*T)
      A(2,1)=0.0
```

```
      A(2,2)=-KMTH-2.0*KH*EXP2*(1.0+H2)
      A(2,3)=-2.0*KH*X(2)*EXP2*(-S/(R*T))
      A(3,1)=-0.5*KFE*EXP1
      A(3,2)=KH*EXP2*(1.0+H2)
      A(3,3)=KH*X(2)*EXP2*(-S/(R*T))-KFE*X(1)*EXP1*S/(R*T)

C*********************************************************************
C     ANODIC:Fe =Fe++  +2E
C     CATHODIC: 2H+2E =H2
C*********************************************************************
      F(1)=KMTFE*(X(1)-FEB)-KFE*X(1)*EXP1
      F(2)=KMTH*(H_PLUSB-X(2))-2.0*KH*X(2)*EXP2
      F(3)=KH*X(2)*EXP2-KFE*X(1)*EXP1
      FF(1)=-F(1)
      FF(2)=-F(2)
      FF(3)=-F(3)
      TOL=1.0E-3
      CALL GAUSS(A,FF,Z)
      DO 800 II=1,3
            FF(II)=Z(II)
            X(II)=X(II)+FF(II)
            E(II)=ABS(FF(II)/X(II))
800   CONTINUE
666   IF (E(1).LT.TOL) THEN
            GOTO 1000
      ELSE
            GOTO 50
      ENDIF

1000  IF(E(2).LT.TOL) THEN
            GOTO 1100
      ELSE
            GOTO 50
      ENDIF
1100  IF(E(3).LT.TOL) THEN
            GOTO 1200
      ELSE
            GOTO 50
      ENDIF
1200  FES=X(1)
      H_PLUSS=X(2)
      ECORR=X(3)

C*********************************************************************
```

```
C       CORROSION RATE CALCULATION
C        1_CORR=1_FE (Amp/m**2)
C       CR IS CORROSION RATE IN mm/year
C*****************************************************************
        E_FE=E_FE0+R*T/(2.0*S)*LOG(FES)
        E_H=E_H0+R*T/(2.0*S)*LOG(X(2)**2.0/H2)

        I_FE=2.0*S*KFE*FES*EXP(2.0*(1.0-BETA)*S*(ECORR-E_FE)/(R*T))
        I_H=2.0*S*KH*H_PLUSS*EXP(-2.0*BETA*S*(ECORR-E_H)/(R*T))

        IF(ABS((I_FE-I_H)/I_FE).GT.1.E-06) THEN
              TOL=TOL*1E-03
              GOTO 666
        ELSE
              I_CORR=I_FE
        ENDIF
        CR=I_CORR*1.16

        WRITE(60,3) T
3       FORMAT('LIQUID TEMPERATURE', 32X,'=',F8.1,'K')
        WRITE(60,4) P
4       FORMAT('PRESSURE',42X,'=', F8.4,'MPa')
        WRITE(60,9)D
9       FORMAT('PIPE DIAMETER', 37X,'=',F8.4,'m')
        WRITE(60,21) WOR
21      FORMAT('INPIT WATER CUT', 35X, '=', F8.4)
        WRITE(60, 22) KMTFE
22      FORMAT ('MASS TRANSFER COEFFICIENT FOR FERROUS ION',
     *  9X,'=', E10.4,' m/s')
        WRITE(60,23) KMTH
23      FORMAT('MASS TRANSFER COEFFICIENT FOR HYDROGEN ION',
     *  5X,'=',  E10.4,'m/s')
        WRITE(60, 24) RE
24      FORMAT('REYNOLD NUMBER OF THE FLUID', 23X,'=', E10.4)
        WRITE(60,25) SC
25      FORMAT ('SCHMIDT NUMBER', 36X,'=', E10.4)
        WRITE(60,5) FES
5       FORMAT('SURFACE CONCENTRATION OF Fe ION', 19X, '=', E10.4,
     *   'mol/m3')
        WRITE(60, 6) H_PLUSS
6       FORMAT('SURFACE CONCENTRATION OF HYDROGEN ION', 17X,'=',
     *  E10.4, 'mol/m3')
        WRITE(60,7) ECORR
7       FORMAT('CORROSION POTENTIAL', 31X,'=',F8.4,'VOLTS')
```

```
      WRITE(60,28)
28    FORMAT('********************************')
      WRITE(60, 8) CR
8     FORMAT('CORROSION RATE', 36X,'=',F15.4,'mm/year')
      WRITE(60,28)
      CLOSE (60)
      STOP
      END


C*********************************************************************
C     THIS PROGRAM CALCULATES THE MASS TRANSFER COEFFICIENT
C     FOR THE FERROUS ION AND THE HYDROGEN ION
C***********DEFINITION OF VARIABLES ******************************
C     T=TEMPERATURE, K
C     D=DIAMETER OF THE PIPE, M
C     VISCP=VISCOSITY OF THE FLUID, CP
C     VISLIQ=DENSITY OF THE FLUID, Pa*S
C     RHO=DENSITY OF THE FLUID, Kg/m3
C     XLAMT=CONDUCTANCE OF THE IONS, MHO/EQUIVALENT
C     ROUGH=ROUGHNESS OF THE PIPR, M
C     U=VELOCITY OF THE FLUID, M/S
C     FF=MOODY FRICTION FACTOR
C     VINSW=INSITU WATER VELOCITY, M.S
C     QO=INPUT OIL FLOW RATE
C     WOR=WATER CUT
C     RE=REYNOLD'D NUMBER
C     DIFFUS_CEF=DIFFUSIVITY OF THE SPECIE IN THE FLUID, M2/S
C     MT_CEF=MASS TRANSFER COEFFICIENT OF THE SPECIES.
C     KMTH=MASS TRANSFER COEFFICIENT OF THE HYDROGEN ION,
C     M/S
C     KMTFE=MASS TRANSFER COEFFICIENT OF THE FERROUS ION, M/S
C*********************************************************************

      SUBROUTINE KMT(T,D,VISCP,RHO,QT,WOR,COE,KMTFE,KMTH,
     *  RE,SC)
      DOUBLE PRECISION T, D, ROUGH, RHO, VINSW, AP, QO, QT, QW,
     *  AW, SHELTA
      DOUBLE PRECISION KMTH, KMTFE, SC, FF, RE, HEIGHT, WOR, COE
      DOUBLE PRECISION DIFFUS_CEF(2), MT_CEF(2), XLAMT(2), VISLIQ,
     *  VISCP
      DOUBLE PRECISION CHARGE(2), FFFACTOR, Froude
      INTEGER INDEX
C     INDEX IS USED TO CHANGE THE CALCULATION METHOD OF MASS
```

```
C       TRANSFER CCOEFFICIENT
C
C       INDEX =1   VIETH METHOD
C             =2   SLUG FILM K CORRELATION
C             =3   SLUG MIXING ZONE K CORRELATION

        ROUGH=0.00004572
        VISLIQ=VISCP/1000.0
        FARADAY=96500.0
        Data XLAMT/349.8, 54.2/
        Data CHARGE/+1,+2/
        AP=3.1415926/4.0*(D**2.0)
        QO=QT*(1-WOR)
        QW=QT*WOR
        IF(WOR.EQ.1) THEN
                U=QT/AP
                RE=D*U*RHO/VISLIQ
        ELSE
                WRITE(*,*)
                WRITE(*,*) 'WARNING'
                WRITE(*,*) 'FOR OIL/WATER FLOW'
                WRITE(*,*) 'PLEASE INPUT WATER FILM HEIGHT IF KNOWN'
                WRITE(*,*)
                READ(*,*) HEIGHT
                HEIGHT=0.4
                IF (HEIGHT.LE.0.5*D) THEN
                        SHELTA=180.0/3.1415926*ACOS((0.5*D-HEIGHT)/(0.5*D))
                        AW=(2.0*SHELTA)/360.0*3.1415926*D**2.0/4.0-(0.5*D-
     *                  HEIGHT) *(0.25*D**2.0-(0.5*D-HEIGHT)**2.0)**0.5
                ELSE
                        SHELTA=180.0/3.1415926*ACOS((HEIGHT-0.5*D)/(0.5*D))
                        AW=(360.0-2.*SHELTA)/360.0*3.1415926*D**2.0/4.0+ (
     *                  HEIGHT-0.5*D)*(0.25*D**2.0 - (HEIGHT-0.5*D)**2.0)**0.5
                ENDIF
                WRITE(*,*) SHELTA, AW
                VINSW=QW/AW
                RE=D*VINSW*RHO/VISLIQ
        ENDIF

C***********************************************************************
C       CALCULATE THE FRICTION FACTOR BY THE CORRELATION OF
C       HAALAND
C***********************************************************************
CC      FFFACTOR=-1.8*LOG10(6.9/RE+(ROUGH/D)**1.11/3.7)
```

```
CC      FF=FFFACTOR**(-2.0)/4.0

        FF=(-1.8*LOG10((6.9/RE)+(ROUGH/(D*3.7))**1.11))**(-2.0)

C       INDEX =1  VIETH METHOD
C             =2  SLUG FILM K CORRELATION
C             =3  SLUG MIXING ZONE K CORRELATION
C             =4  DEVELOPED CORRELATION FOR FULL PIPE FLOW
C             =5  BERGER & HAU

        INDEX=2
        IF (INDEX.EQ.1) THEN
C*****************************************************************
C       CALCULATE THE MASS TRANSFER COEFFICIENTS BY VIETH
EXPRESSION
C*****************************************************************
        DO 20 K=1,2
              DIFFUS_CEF(K)=(8.314E-04)*T*XLAMT(K)/(FARADAY**2.0*
     *  ABS(CHARGE(K)))*COE
              DIFFUS_CEF(K)=DIFFUS_CEF(K)*(0.95/VISCP)
              SC=VISLIQ/RHO/DIFFUS_CEF(K)
              IF(RE.GE.3.2E+03) THEN
                    RATIO=0.0425*LOG10(RE)+0.6172
              ELSE
                    RATIO=1.0319*LOG10(RE)-2.888
              ENDIF
              MT_CEF(K)=(4.586/RATIO)*(FF/8.)*RE*(SC)**(1./3.)
     *                  *DIFFUS_CEF(K)/D
20    CONTINUE

        ELSEIF (INDEX.EQ.2) THEN
C*****************************************************************
C       CALCULATE THE MASS TRANSFER COEFFICIENTS using my
C       correlation for slug flow film zone
C       The pots method also uses this correlation
C*****************************************************************
              DO 30 K=1,2
                    DIFFUS_CEF(K)=(8.314E-04)*T* XLAMT(K) /(FARADAY
     *              ** 2.0* ABS(CHARGE(K)))*COE
                    DIFFUS_CEF(K)=DIFFUS_CEF(K)*(0.95/VISCP)
                    SC=VISLIQ/RHO/DIFFUS_CEF(K)
        MT_CEF(K)=0.544*(RE)**0.61*(SC)**(1./3.)*DIFFUS_CEF(K)/D
30            CONTINUE
        ELSEIF (INDEX.EQ.3) THEN
```

```
C*********************************************************************
C       CALCULATE THE MASS TRANSFER COEFFICIENTS using my
C        correlation for slug flow mixing zone
C*********************************************************************

        Froude=14.
        DO 40 K=1,2
              DIFFUS_CEF(K)=(8.314E-04)*T*XLAMT(K)/(FARADAY**2.0*
     *   ABS(CHARGE(K)))*COE
              DIFFUS_CEF(K)=DIFFUS_CEF(K)*(0.95/VISCP)
              SC=VISLIQ/RHO/DIFFUS_CEF(K)
              MT_CEF(K)=0.00675*(Froude)**3.6315*(RE)**0.61*(SC)**
     *        (1./3.)*DIFFUS_CEF(K)/D
40    CONTINUE

        ELSEIF (INDEX.EQ.4) THEN
C*********************************************************************
C       CALCULATE THE MASS TRANSFER COEFFICIENTS using my
C       correlation FOR FULL PIPE FLOW
C*********************************************************************
        DO 50 K=1,2
              DIFFUS_CEF(K)=(8.314E-04)*T*XLAMT(K)/(FARADAY**2.0*
     *   ABS(CHARGE(K)))*COE
              DIFFUS_CEF(K)=DIFFUS_CEF(K)*(0.95/VISCP)
              SC=VISLIQ/RHO/DIFFUS_CEF(K)
              MT_CEF(K)=0.089*(RE)**0.78*(SC)**(1./3.)*DIFFUS_CEF(K)/D
50    CONTINUE

        ELSEIF (INDEX.EQ.5) THEN
C*********************************************************************
C       CALCULATE THE MASS TRANSFER COEFFICIENTS By BERGER
C       &HAU (1977)
C*********************************************************************
        DO 60 K=1,2
              DIFFUS_CEF(K)=(8.314E-04)*T*XLAMT(K)/(FARADAY**2.0*
     *   ABS(CHARGE(K)))*COE
              DIFFUS_CEF(K)=DIFFUS_CEF(K)*(0.95/VISCP)
              SC=VISLIQ/RHO/DIFFUS_CEF(K)
              MT_CEF(K)=0.0165*(RE)**0.86*(SC)**(1./3.)*DIFFUS_CEF(K)/D
60    CONTINUE

C*********************************************************************
        ENDIF
```

```
C*********************************************************************
C       CALCULATE THE MASS TRANSFER COEFFICIENTS By BERGER
C       &HAU (1977) and test the enhancement E from
C       1, 5, 10, 40, 65.
C*********************************************************************
C       DO 20 K=1,2
C               DIFFUS_CEF(K)=(8.314E-04)*T*XLAMT(K)/(FARADAY**2.0*
C   *   ABS(CHARGE(K)))*COE
C               DIFFUS_CEF(K)=DIFFUS_CEF(K)*(0.95/VISCP)
C               SC=VISLIQ/RHO/DIFFUS_CEF(K)
C
        MT_CEF(K)=5*0.0165*(RE)**0.86*(SC)**(1./3.)*DIFFUS_CEF(K)/D
C 20    CONTINUE
C*********************************************************************

        KMTH=MT_CEF(1)
        KMTFE=MT_CEF(2)
        RETURN
        END

C*********************************************************************
C  GAUSS-JORDAN ELIMINATION METHOD
C*********************************************************************
        SUBROUTINE GAUSS (A,FF,Z)
        DOUBLE PRECISION A(3,4), FF(3), Z(3)

C***ENTER EQUATIONS  ******************************************
        DO 100 I=1,3
                A(I,4)=FF(I)
100     CONTINUE

C**** PIVOT EQUATIONS FROM FIRST TO LAST***********************
        DO 300 I=1,3
C**** FIND COEFFICIENT IN EQUATION I WITH LARGEST SQUARE
        P=0.0
                Q=0.0
                DO 400 J=1, 3
                        IF (A(I,J)*A(I,J).GT.(P*P)) THEN
                                Q=J
                                P=A(I,J)
                        ENDIF
400             CONTINUE
                IF((P*P).LT.1.0E-10) GOTO 300
C*** NORMALIZATION EQUATION1 **********************************
```

```
                DO 500 J=1,4
                        A(I,J)=A(I,J)/P
500             CONTINUE
C**********PIVOT ON COEFFICIENT NO. Q IN EQUATION I*************
                DO 600 K=1, 3
                        IF (K.EQ.I) GOTO 600
                        P=A(K,Q)
                        DO 700 J=1,4
                                A(K,J)=A(K,J)-P*A(I,J)
700                     CONTINUE
600             CONTINUE
300     CONTINUE
        DO 3000 I=1,3
        DO 3000 J=1,3
                IF(ABS(A(I,J)-1.0).LT. 1.0E-3) THEN
                        Z(I)=A(J,4)
                ENDIF
3000    CONTINUE
        RETURN
        END
```

NOMENCLATURE

English Letters

a	activity of ion (mol/m^3)
a_{co_2}	activity of CO_2 in the liquid phase (mol/m^3)
A	surface area of the electrode (m^2)
c	molar density of solution (mol/m^3) =ρ/M
C	constant
C_b	bulk concentration of the potassium ferrocyanide (mol/m^3)
C_{freq}	normalized factor to account for slug frequency and $0<C_{freq}<1$
C_{oil}	normalized factor to account for crude oil type and $0<C_{oil}<1$
C_R	corrosion rate (mm/yr)
C_{sf}	corrosion rate in slug film (mm/yr)
C_{sm}	corrosion rate in slug mixing zone (mm/yr)
C_w	concentration at the wall (mol/m^3)
d_e	hydraulic pipe diameter (m)
D	pipe diameter (m)
D	diffusional coefficient (m^2/s)
D	ionic diffusivity (m^2/s)
D_{AB}	diffusivity of A in a binary system (m^2/s)
$D_{Fe^{2+}}$	diffusivity of Fe^{2+} through corrosion film (m^2/s)
D_{H^+}	diffusivity of H^+ through corrosion film (m^2/s)

e	surface roughness
E	mass transfer enhancement
E_{corr}	corrosion potential (V)
$E_{Fe^{2+}}$	potential for the anodic reaction (V)
$E_{H^{2+}}$	potential for the cathodic reaction (V)
$E^0{}_{H^+}$	standard potential for the cathodic reactions (V)
$E^0{}_{Fe^{2+}}$	standard potential for the anodic reactions (V)
f	slug frequency (s)
f	Fanning friction factor
f_{co_2}	fugacity of CO_2 in the gas phase (atm)
F	Faraday's constant (=96500 C/mol)
Feb	bulk concentration of Fe^{2+} (mol/m^3)
FeL	layer concentration of Fe^{2+} (mol/m^3)
Fr	Froude number $= \frac{V_g^{\ 2}}{d_e g}$
Fr	Froude number of slug flow $= \frac{V_t - V_{LF}}{\sqrt{(g \cdot h_{EF})}}$
h_{EF}	effective liquid film height (m)
h_{ls}	liquid height to gas/liquid interface (m)
Hb	bulk concentration of H^+ (mol/m^3)
HL	layer concentration of H^+ (mol/m^3)

HS	metal surface concentration of H^+ (mol/m^3)
i_a	anodic current density (A/m^2)
i_c	cathodic current density (A/m^2)
i_{corr}	corrosion current density (A/m^2)
j	mass transfer factor = $StSc^{0.66}$
I_L	limiting current (A)
K	mass transfer coefficient (m/s)
K_{CO_2}	equilibrium constant for the dissociation of H_2CO_3 (mol/m^3)
K_{e,Fe^+}	rate constants for the anodic reaction (m/s)
K_{e,H^+}	rate constants for the cathodic reaction (m/s)
K_H	Henry law constant (mol/g/atm)
Km	mean mass transfer coefficient (m/s)
$K_{mt,Fe^{2+}}$	mass transfer coefficient for Fe^{2+} (m/s)
K_{mt,H^+}	mass transfer coefficient for H^+ (m/s)
Kp	peak mass transfer coefficient (m/s)
K_w	equilibrium constant for the dissociation of H_2O (mol/m^3)
l	diameter of circular pipe electrode (m) in Equation 4.4
L	pipeline length (m)
LMZ	mixing zone length (m)
m_j	molality of ion j with charge z (kg/mol)
M	molecular weight (kg/kmol)

n	number of moles reacted
N_{Ax}	molar flux of A (mol/m^2/s)
N_{Az}	molar flux of species A at z direction (mol/m^2/s)
N_{Bx}	molar flux of B (mol/m^2/s)
P_{CO2}	carbon dioxide partial pressure (MPa)
pH_{actual}	actual pH in the presence of dissolved salts
pH_{CO2}	pH of dissolved CO_2 in pure water
P_{CO_2}	partial pressure of CO_2 (MPa)
P_T	total pressure of the system (MPa)
ΔP	pressure drop through the slug flow (KPa/m)
r	radius of the pipe (m)
R	universal gas constant (= 8.314 J/mol-K)
Re	Reynolds number = $\frac{\rho_L V d_e}{\mu}$
$R_{Fe^{2+}}$	electrochemical reaction rate of Fe^{2+} (mol/m^2/s) = $i_a/2F$
R_{sm}	ratio of mixing zone time over one slug time
Sc	Schmidt number = $\frac{\upsilon}{D}$
Sh	Sherwood number = $\frac{Kd}{D}$
Sh_0	Sherwood number in steady state
Sh_p	time-averaged Sherwood number in pulsating flow
Sh'	Sherwood number calculated from experimental data

St	Stanton number = $\frac{Sh}{\mathrm{Re}\,Sc}$
t	time for one slug (s)
t_{sb}	time for one slug body (s)
t_{sf}	time for one slug film (s)
t_{st}	time for one slug tail (s)
t_{sm}	time for one slug mixing zone (s)
T	temperature (K)
U	liquid velocity (m/s)
v_b	rise velocity of a moderate bubble (m/s)
v_m	mixture velocity with respect to pipe wall (m/s)
V	liquid velocity (m/s)
V_{cor}	corrosion rate (mm/year)
V_{LF}	liquid film velocity
V_m	total gas/oil/water velocity (m/s)
V_m	mass transfer term (mm/year)
V_{sg}	superficial gas velocity
V_{sl}	superficial liquid velocity (m/s)
V_r	reaction rate term (mm/year)
V_t	translation velocity = $(1+ C)(V_{sl} + V_{sg})$
x_1	surface concentration of Fe^{2+} (mol/m^3)
x_2	surface concentration of H^+ (mol/m^3)
x_3	corrosion potential (V)

x_j^*	final converged solution
$x_j^{'}$	initial estimation
X_A	mole fraction of component A
y_{co_2}	mole fraction of CO_2 in the gas phase
z	ionic charge

Greek Letters

α	transfer coefficient (=0.5 for most cases)
γ	molar activity coefficient
δ	thickness of the corrosion film (m)
ε	dielectric constant
θ	pipeline inclination (degree)
θ	void fraction
λ	ionic conductivity (S/m)
μ	ionic strength on the molality scale (mol/m^3)
μ	dynamic viscosity (cP)
μ_i	chemical potential of components i (J/mol)
μ_i^0	standard chemical potential of component i (J/mol)
ν	the water cut, $0<\nu<1$
ν	kinematic viscosity (m^2/s)
ρ	density of solution (kg/m^3)

τ	the wall shear stress (Pa)
τ	tortuosity factor
Φ_{co_2}	fugacity coefficient of CO_2 in the gas phase

Subscripts

a	anodic reaction
A	component A
b	bulk
b	bubble
B	component B
c	cathodic reaction
cor	corrosion
i	component
j	number of iteration
LF	liquid film
m	mean
mt	mass transfer
p	peak
sb	slug body
sf	slug film
sg	superficial gas
sl	superficial liquid

sm	slug mixing zone
w	water
w	wall
x	direction
z	direction
0	steady state

Superscripts

*	final value
’	initial value
’	experimental value

ABSTRACT

WANG, HONGWEI. Ph.D. March 2002
Chemical Engineering

CO_2 Corrosion Mechanistic Modeling in Horizontal Slug Flow (289 pp.)

Director of Dissertation: W. Paul Jepson

Horizontal slug flow is the most common flow regime in oil and gas pipelines. Slug flow causes severe internal corrosion problems due to its high turbulence. There is a need to study the physics and chemistry of the influences of slug flow on flow-accelerated corrosion and corrosion models.

This dissertation first describes a systematically experimental investigation of mass transfer and wall shear stress in horizontal slug flow in two-phase water-gas and three-phase water-oil-gas mixtures using the Electrochemical Limiting Current technique. Water and an oil of viscosity of 2 cP were used for the liquid phase and nitrogen was used for the gas phase. Full pipe flow, plug flow, and slug flow in a 10 cm I.D. 15 m long Plexiglas^{TM} pipe was studied.

The effects of gas bubbles, the presence of an oil phase and droplets, and flow regime on average and instantaneous mass transfer coefficients in horizontal slug flow was studied. It is found that the cavitation type bubble collapsing exists in slug flow and causes an increase of up to several hundreds times the instantaneous mass transfer coefficient. The presence of the oil phase can further enhance the cavitation in slug flow. The analysis of the wall shear stress and the fracture mechanics indicates that the instantaneous wall shear stress produced by the cavitation can scrape away the